2011

A Detailed and Systematic Investigation of Personal Ventilation Systems

Jackie Russo
Syracuse University

Recommended Citation

Russo, Jackie, "A Detailed and Systematic Investigation of Personal Ventilation Systems" (2011). *Mechanical and Aerospace Engineering - Dissertations.* Paper 56.

Abstract

This research investigates the use of personal ventilation (PV) in a typical office space as a means of contaminant removal from ones breathing zone (BZ). For this work, a validated computational model was developed and used for PV assessment under different scenarios. Experimental data of Khalifa et al. (2009), Ito (2007) and Rim et al. (2009) were used to validate a computational model that is capable of simulating indoor chemical reactions with excellent agreement compared with the experiments. Through the validation process, various computational parameters were determined to be significant for producing accurate results. Grid resolution, geometry, far field BCs, turbulence model and radiation were shown to impact the solutions accuracy and care must be taken. However, it was found that adding complex, realistic features, such as unsteady breathing or sweating, does not improve the accuracy of the inhaled air quality results of the solution. With this knowledge, the benefits of two PV nozzles, a conventional round nozzle and a novel low-mixing Co-flow nozzle, were investigated for an array of scenarios including: non-reacting indoor sources, different office and PV configurations and indoor surface and volumetric reactions. Specifically, the use of PV to remove reaction products of the oxidation by Ozone of Squalene and D-Limonene were analyzed and compared to a conventional ventilation system. The Co-flow nozzle was shown to exhibit superior performance and robustness over a single jet PV system and both PV systems improved air quality in the BZ over conventional systems. It was found that well mixed behavior is not exhibited especially with large velocity and concentration gradients that are developed by the use of PV and/or when indoor sources or chemical reactions are present.

A Detailed and Systematic Investigation of Personal Ventilation Systems

Thesis

Jackie Russo

Advisor: Dr. H.E. Khalifa

May, 2010

Contents

List of Figures

List of Tables

Nomenclature

4-OPA	4-Oxopentanal
6-MHO	6-methyl-5-hepten-2-one
A_i	area of surface i
A_r	pre-exponential factor
Ar	Archimedes's Number
ACH	air change per hour
AQI	air quality index
BC	boundary conditions
BZ	breathing zone
C	refers to the Co-flow PV system.
CFD	computational fluid dynamics
C_b	species concentration at a point in the BZ
C_e	species concentration in the exhaust
$C_{j,r}$	molar concentration of species j in the reaction r
C_p	species concentration at the primary nozzle exit,
C_μ	eddy viscosity model constant
$C(\Delta y)$	concentration at 2/3 the mean molecular free path
CDesk	ClimaDesk
CMP	Computer Monitor Panel
CSP	computer simulated person
D	diameter
D_i	diffusion coefficient of species i in air,
D_t	turbulent diffusion coefficient
E_i	emissive power
E_r	activation energy for the reaction
F_{ij}	view factor
FSRM	Fictitious Surface Reaction Method
g	acceleration due to gravity
g_i	gravitational acceleration in direction i
G_i	irradiation
Gr	Grashoff number
h	mixture enthalpy
h_i	enthalpy of the species i
iF	intake fraction
J_i	radiosity
$J_{i,w}$	diffusive mass flux of species i at the wall,
k	turbulent kinetic energy
k_{eff}	effective thermal conductivity of the gas mixture
$k_{f,r}$	forward rate constant of the reaction
$k_{i,r}$	reaction rate constant
L	typical length scale of a person
LES	Large Eddy Simulation

LHS	left hand side
M_i	molecular weight of species *i*, and
M_w	molecular weight of the gas
N	number of species
O_3	Ozone
p	hydrostatic pressure
p_{op}	operating pressure
PEL	personal environmental laboratory
Pr	Prandtl number
Pr_t	turbulent Prandtl number
PV	personal ventilation
q_{conv}	convective heat flux
q_{rad}	radiative heat flux
R	universal gas constant
R	nozzle radius
R_i	net rate of production of species *i* by chemical reaction
$\hat{R}_{i,r}$	Arrhenius molar rate of creation/destruction of species in reaction *r*
$R_{i,w}$	molar surface reaction rate per unit area at the wall (*positive when i is produced at the wall*)
RANS	Reynolds Averaged Navier-Stokes
Re	Reynolds Number
RHS	right hand side
S	refers to the single (Primary) jet PV system
S	means strain rate
S_h	heat from any chemical reactions
S_i	source terms for species *i*
S_k	source term
Sc	Schmidt number
Sc_t	Turbulent Schmidt Number
SF_6	sulfur hexafluoride
SVOCs	semi-volatile organic compounds
T	temperature
T_{ref}	supply air temperature entering the domain
T_{wall}	typical skin temperature
ΔT	temperature difference between the human body and surrounding air
TAM	Task Air Module
Tu	turbulent intensity
u_j	mean velocity components
UDS	user defined scalar
UDSM	User Defined Scalar Method
$\langle v \rangle$	Boltzmann velocity for the chemical species
v_d	deposition velocity
v_{ir}'	stoichiometric coefficient of reactant *i*

v_{ir}''	stoichiometric coefficient of product *i*
v_t	transport limited deposition velocity
VDG	Vertical Desk Grill
VOCs	volatile organic compounds
w	skin wettedness
Y_i	mass fraction of species *i* in the air,

Greek Symbols

α	absorptivity
β	thermal expansion coefficient
β_r	temperature exponent
γ	mass accommodation coefficient or reaction probability
Γ	net effect of third bodies
ε	turbulent dissipation
ϵ	emissivity
$\eta_{j,r}'$	rate exponent for the reactant specie *j* in reaction *r*
$\eta_{j,r}''$	rate exponent for the product species *j* in the reaction *r*
κ	reflectivity
μ	molecular dynamic viscosity
μ_{eff}	effective viscosity of the mixture
μ_t	turbulent viscosity
ρ	fluid density
σ	Stephan-Boltzmann constant
σ_k	turbulent Prandtl numbers for *k*
σ_ε	turbulent Prandtl numbers for ε
ϕ_k	scalar
Γ_k	transport coefficient
$\overline{\Omega}_{ij}$	mean rate-of-rotation tensor viewed in a rotating reference frame
ω_k	angular velocity

Acknowledgements

I gained invaluable experience while working at Syracuse University. First and foremost I would like to thank my advisor, Dr. H. Ezzat Khalifa, for his support and guidance though the duration of this research project. Through our interactions and many discussions, I have learned an immeasurable amount about the topics within this dissertation and the thoughtful research process. I owe my academic success to Dr. Khalifa and, through his investment in my research and professional development, he has helped me enhance my skills and become the engineer I am today. I would also like to thank Dr. Thong Q. Dang for his collaborative efforts on the modeling of the complexities of fluid dynamics and his constant guidance through the duration of this dissertation research. His direction provided a greater depth to the quality of this research. I would like to thank Dr. John Dannenhoffer for providing direction on mesh generation and giving consistent feedback that shaped this research. I would like to extend my appreciation to the remaining committee members, Dr. Glauser, Dr. Tavlarides and Dr. Zhang. It was the combined efforts of these faculty members and other Syracuse University faculty and students who helped me complete this dissertation.

I have had the great opportunity to work with other faculty members outside of Syracuse University. Dr. Charles Weschler of Environmental & Occupational Health Sciences Institute ,University of Medicine & Dentistry of NJ and Rutgers University has given guidance and insight of chemical kinetics for chemical reaction modeling.

The research described in this article has been funded in part by the United States Environmental Protection Agency through grant/cooperative agreement under contract #CR-83269001-0 to Syracuse University. However, it has not been subjected to the Agency's peer and policy review; and therefore, does not necessarily reflect the views of the Agency, and no official endorsement should be inferred. Additional support has been received from the NYSTAR-awarded STAR Center for Environmental Quality Systems and the Syracuse Center of Excellence in Environmental and Energy Systems.

1 Introduction

For an average person, a significant portion of the day is spent indoors, about *90 %* (Klepeis et al., 2001), making indoor air quality vital to ones well being. To improve the quality of indoor air, fresh air from (~*7.5 l/s* per person) the outdoors is introduced to the indoor environment according to ASHRAE standards (ANSI/ASHRAE Standard 62.1-2004) through ventilation systems. As a constituent of outdoor air, Ozone also enters the indoor environment through the fresh air ventilation system, which can lead to indoor reactions with Terpenes and other indoor species. The oxidation of Terpenes has been shown to create harmful products with negative health effects for occupants. The transport of these reaction products to the breathing zone (BZ) of a human is not well documented and this research aims to determine the interactions between airflow, reactants, products and the human body in typical indoor settings with focus on the use of personal ventilation (PV) as a means to improve local air quality. Specifically, this research creates a validated computational model that is used to assess PV as a removal mechanism of contaminants from the BZ in the presence of chemically reacting flows.

1.1 Background and Problem Definition

The purpose of this research is to develop and validate a CFD model that 1) can be used for accurate inhalation exposure assessment, 2) takes into account the various exposure scenarios and chemical reactions in the indoor environment and 3) accounts for realistic energy, configurational and ergonomic constraints. Detailed calculations of concentration fields, especially in the personal microenvironment are required to resolve the spatial and temporal variation of contaminant concentrations, and to permit a more accurate assessment of inhalation exposure. When contaminants are formed as a result of chemical reactions of species emanating from different locations within the occupied space (e.g., O_3 from the supply diffuser and VOCs from the person and surroundings), exposure calculations become more complex, and the well-mixed assumption (used by many one compartment mass balance models) could be seriously in error. The validated CFD model, enhanced with surface and volumetric chemical reactions, is needed to predict the inhalation exposure of contaminants emitted from various indoor surfaces, or formed through chemical reactions of O_3 and emitted VOCs, especially within the body's thermal plume, or on the body/clothing surface.

1.1.1 Personal Ventilation

The transport of the harmful reaction products to the breathing zone is assisted by the rising thermal plume around the human body in typical ventilation systems. Conventional mixing ventilation systems are often designed to create a uniform environment where fresh air is mixed with indoor air pollutants prior to inhalation. Laboratory measurements and CFD simulations have shown that displacement ventilation can provide better air quality; however, a study found that nearly *50 %* of occupants were dissatisfied with the indoor air quality with displacement ventilation (Naydenov et al., 2002; Melikov et al., 2004). One method often studied to improve indoor air quality in the BZ of individuals is

PV. PV delivers fresh air directly to the BZ with enough momentum to penetrate the rising thermal plume and decrease the amount of harmful contaminants inhaled. It is common to use large fresh air flow rates, sometimes as high as the total fresh air flow rate for the space, through the PV system to achieve better air quality in the BZ (Cermak and Melikov, 2006; Faulkner et al., 2003; Faulkner et al., 2002; Faulkner et al., 2000, Faulkner et al., 1999; Melikov and Kaczmarczyk, 2006). However, to ensure adequate air quality in the entire space, it is typical for PV systems to be used in conjunction with general ventilation systems limiting the fresh air flow rate through the nozzle to a fraction of the total amount of fresh air for the space as indicated by ASHRAE 62 (2004). A comprehensive review of PV systems has shown that the PV jet velocity at the face must be no less than *0.3 m/s* to obtain the highest quality of inhaled air (Bolashikov et al., 2003). This can be accomplished by using a large circular jet with a long potential core to minimize the entrainment of environmental pollutants. However, with a limitation to the fresh air flow rate, a large diameter jet will decrease the velocity of the potential core which could lead to an insufficient velocity at the face. To accommodate both limitations, Khalifa and Glauser (2006) invented a novel low-mixing Co-flow PV nozzle that can greatly lengthen the fresh air core while maintaining a low PV fresh air flow rate.

With PV, occupants can control their environment, including their thermal environment, at their workspace with the opportunity for energy savings. However, fundamental issues exist with PV and must be investigated further. Researcher have studied PV for a wide range of scenarios including single round nozzles, multiple nozzles, headphone devices, different nozzle shape and various proximities to occupants (Bolashikov et al. 2003;

Faulkner et al. 1995, 1999, 2000, 2002; Fisk et al. 1990; Cermak et al. 2003, 2006; Kaczmarczyk et al. 2002; Melikov et al. 2001, 2004, 2006; Nielsen et al. 2005; Khalifa et al. 2008, 2009). The amount of air quality improvement for PV systems has been shown to depend on the design of the PV system, its relative position to occupants, PV air flow rate and direction and the temperature difference between the PV air jet and the room air (Faulkner et al., 1999, Melikov et al., 2002). It has been estimated that the optimal performances of most PV systems deliver air between *50 %* and *60 %* of the clean air quality (Melikov 2004 and authors therein). For this work, the use of a single jet PV system and a Co-flow nozzle (Khalifa and Glauser, 2006) are investigated to determine the increase air quality benefits that can be achieved through the use of the novel PV design by Khalifa and Glauser (2006).

1.1.2 Chemistry

Ozone initiated chemistry and inhaled exposure to its associated harmful products has increased in the indoor environment in recent years for two main reasons (Weschler et al. 2006): 1) there has been an increase in the outdoor Ozone levels and 2) there has been an increase in the use of cleaning products. To expand on reason two, in the indoor environment the concentration levels are higher than the levels that exist outdoors. These compounds are mostly made up of Terpenes and their concentrations exist 5-7 times higher indoors than outdoors (Saarela et al. 2000). Indoor sources of Terpenes include: consumer products, cleaning products, building materials, and air fresheners. On average, people spend 20-30 minutes a day cleaning (Wiley et al. 1991) and it has been predicted that a person inhales an average of 10mg/day of organic compound from cleaning products (Nazaroff and Weschler, 2004). Ozone reactions with Terpenes are a multi-step, multi-path process that produces many products including: radical products such as OH, HO_2 and NO_2 (Calogirou et al., 1999), volatile organic compounds (VOCs), semi-volatile organic compounds (SVOCs) and ultrafine particles (Sidheswaran & Tavlarides, 2008; Chen & Hopke, 2010), which can all be harmful to one's health (Pope & Dockery, 1996; Gao, 2010). The higher molecular weight products that are formed from Ozone/Terpene reactions are generally present in the condensed phase and are usually associated with sub-micron particles (Weschler and Shields, 1997). The distribution between gas and condensed phase depends on the vapor pressure of the compound and the surface area of the existing airborne particles and low vapor pressure products contribute to the growth of secondary orgainic aerosols (Rohr et al., 2003; Sarwar et al., 2003; Wainman et al., 2000; Weschler and Shields, 1999). The formation of secondary particles has been shown to increase when Ozone and Terpenes are present and the potential exists for the accumulation of fine particles in excess of *20 µg/m3* in indoor air when the presence Ozone is elevated in outdoor air (Wainman et al., 2000). It has been estimated that the Ozone/Limonene reaction results in *~22 %* aerosols (Grosjean et al., 1993), however, nucleation was not considered for this work.

1.2 Existing Work

Prior to the start of this work, there have been many authors that have studied different aspects of the subjects of this dissertation. To cover all the different facets of this work, reviews of existing work have been incorporated in five main areas: computational modeling of the indoor environment, PV, exposure, indoor chemical reactions and jets.

1.2.1 Computational Modeling

In recent history, computing ability has increased with the use of parallel processors making the use of computational fluid dynamics (CFD) a valuable tool for modeling the indoor environment. Modeling the indoor environment introduces a unique set of challenges which can have a momentous affect on the accuracy of the solution. To expand on this, the next section is devoted to existing work focused on computationally modeling the indoor environment, specifically the turbulence model, grid development and geometry and breathing modeling methods.

1.2.1.1 CFD modeling (Turbulence model, grid development and geometry)

Chen and Srebric (2002) developed a procedure for the verification, validation and reporting of indoor environmental CFD analysis. This manual describes the identification of the relevant physical phenomena for an indoor environmental analysis and whether or not a particular CFD code has the capability of accounting for those physical phenomena for verification. Validation involves demonstrating the coupled ability of a user and a CFD code to accurately conduct a simulation of the indoor environment. Reporting the results involves summarizing the CFD analysis so that others can make informed assessments of the value and quality of the work. The set of instructions include verifying basic flow and heat transfer features, turbulence models, auxiliary heat transfer and flow models, numerical methods and assessing CFD predictions. Validation was applied for confirming the abilities of the turbulence model and other auxiliary models at predicting physical phenomena in a particular environment, confirming the discretization method, grid resolution and numerical algorithm and confirming the user's ability to use the CFD code to perform an indoor environmental analysis. Reports should include all the aspects of verification and validation for technical readers.

Topp et al. (2002) investigated the influence of geometry on local and global airflow when using a CSP in CFD. A low Reynolds number k-ε turbulence model was used. The grids used ranged from ~*180,000* cells for the block manikin geometry to ~*300,000* cells for the detailed manikin geometry. The y plus (y^+) values in both cases were less than one across most of the surfaces. A convective heat flow rate of *38 W* was given at the surface of each manikin. The results show that a simple geometry can be used when concerned with the global airflow in the room, however, when concerned with the local airflow a simple geometry is not sufficient and a detailed manikin must be used.

Sorensen and Voigt (2003) modeled flow and heat transfer around a seated thermal manikin using CFD. The manikin used for this work was in the seated position with its arms down to the side. The manikin was unclothed and had no hair. The CFD model was almost an exact replica of an actual thermal manikin used in many experiments. The grid used for this work consisted of *1* million cells and was a mixture of structured and unstructured cells. Around the manikin there were 20 layers of extruded triangular prisms to resolve the boundary layer near the manikin's surface. STAR-CD was used to calculate the flow and heat transfer around the body. This study included surface to surface radiation. The surface temperature of the manikin was *31˚C*. Measurements of the natural convection flow around the thermal manikin were compared to experimental data. It was found that the agreement was excellent and the PIV measurements above the head were well predicted.

Sorensen and Nielsen (2003) studied the quality control of CFD in indoor environments. Modeling aspects of turbulence, BCs, numerical errors, differencing scheme and computational grid were discussed. Examples are given to stress the main points related to numerical errors. When using CFD the authors recommend that the influence of grid-dependency should be assessed, differencing schemes of first order should be avoided, the range of y^+ should be in accordance with the specifications from the code developers, the solution should be sufficiently converged, and double precision representation of real numbers should be used. When publishing CFD the authors recommend that the description of the CFD code, boundary and initial conditions, and turbulence model should be detailed enough so that the calculations can be reproduced by another investigator. Existing CFD codes should be cited fully. Topology and size of grid should be described. The influence from grid-dependency should be addressed and a qualitative estimate of the expected deviations from the exact solution to the governing equations must be given. The choice of differencing scheme should be described. The range of y^+ should be stated. Finally, if possible the authors recommend that the calculations should be validated against measurements or standard test cases of a similar problem if possible.

Nielsen (2004) studied different aspects of modeling air movement in the indoor environment using CFD including the accuracy of numerical schemes, BCs at the supply opening, accounting for obstacles in the room, and the accuracy of turbulence models for a 3D wall jet. A comparison of a first order upwind scheme, second order upwind scheme and a third order QUICK scheme was made and it was found that a second order scheme should be used whenever possible to achieve accurate solutions. Three different modeling methods were given for modeling the supply opening to a room which includes: the simplified BCs, the box method and the prescribed velocity method. It was found that all methods can be accurate, but special care must be taken if the simplified BC method is used. This paper concluded that it is important to model furniture such as desks in the indoor environment. And finally, it was found that the k-ε model is an acceptable model in many situations, but that the RSM can achieve higher accuracy when modeling a 3D wall jet because of the use of wall reflection terms. The v^2-f model did not show any improvement for the prediction of the 3D wall jet.

Gao and Niu (2005) give a review of the thermal environment around the human body. This paper reviews CFD studies using computational thermal manikins. This paper reviews the different geometries used and who uses them, the different turbulence models used, the differences in grid resolution for these complicated geometries, BCs, radiative heat transfer, convective heat transfer and contaminant distribution.

Deevy et al. (2008) used CFD to model a human in a displacement ventilation system and compared the results to experimental data. The experiments were carried out by Kato and Yang (2005) and were not detailed. The experimental conditions were designed to correspond to the benchmark CFD displacement ventilation case with a few differences.

A comparison of unsteady Shear Stress Transport with Detached Eddy Simulation turbulence models were made to consider the influence of turbulence modeling. Velocity and temperature fields were calculated in the domain and time averaged to compare with experimental data. A detailed CSP geometry was used for the simulations along with the modeling of thermal radiation through the discrete ordinates radiation model. The grid consisted of *~200,000* cells with an average y^+ of *4* and a maximum y^+ of *8*. URANS and DES gave similar results with DES matching experimental fields slightly better; however, it was recommended that improvements be made in the CFD modeling.

Sideroff and Dang (2008) conducted a detailed computational study of the flow around a computer simulated person (CSP) in an empty displacement ventilated room. Results from Reynolds Averaged Navier-Stokes (RANS) and Large Eddy Simulation (LES) methods were compared to the benchmark test for evaluating CFD in the indoor environment of Nielsen et al. (2003). This study identified certain requirements of different computational aspects to achieve accurate CFD simulations of the personal micro-environment. These included grid refinement, convergence monitoring, turbulence modeling and radiation modeling. It was found that achieving grid independent solutions while maintaining an acceptable cell count (100,000 surface elements) using tetrahedral topology was necessary. For grid convergences it was shown that other quantities needed to be monitored to determine actual convergence of the solution. The results showed that neglecting radiation modeling when heat-flux boundary conditions were used was erroneous and that if the actual surface temperatures were known, then the effects of radiation could be included without actually including a radiation model. The v^2-f model did not yield improvement over the standard k-□ model. With the use of these computational aspects, very good agreement between CFD results and test data was obtained.

Dygert et al. (2009) studied the modeling of the human body to examine the personal micro-environment. The air quality in the personal micro-environment of a person, depends strongly on both the ventilation system, and the strength and location of pollutant sources. This study focused on the general requirements to accurately simulate the air quality in the breathing zone of a person using CFD when steep gradients of velocity, temperature, and contaminants are present near the person. Two configurations were discussed in the paper: a person sitting in an infinite domain with no nearby ventilation system (buoyancy-driven flow alone), and the case of a person sitting in a room with a combined displacement and personal ventilation system. The latter case compares the computational results with test data for validation purposes. It was found that for grid considerations for a seated CSP with human-like features the body surface resolution on the order of at least 30,000 elements with grid clustered in the head region should be used for a full CSP. More elements should be used for a standing CSP to take care of the back torso and the thighs. To resolve the thermal boundary layer around the CSP, at least five layers of prismatic cells around the CSP should be used to achieve y^+ values less than three (when using FLUENT's enhanced wall treatment) and a maximum growth rate of 1.2. It was found that the k-□ family of turbulence models with a near-wall treatment should be used. It was shown that with the enhanced wall treatment option enabled, the commercial software FLUENT did a very good job at matching test data on the mean flow quantities. Using this model, the average y+ value on the CSP should be 3 or less. When modeling a CSP with rectangular blocks it was found to be not adequate. The sudden change in cross-sectional features of the neck and the head is important. In addition, the curvatures of the head/neck/shoulders can also affect the prediction of air quality in the PμE.

1.2.1.2 Modeling Breathing

Murakami (2004) described the analysis results of flow and temperature fields around the human body and examines the quality of inhaled and exhaled air. This paper also studies dry eye syndrome. The low Reynolds number *k*-□ model, LES model and experiments were used in a displacement ventilation setup to analyze the flow and temperature fields. The inhalation velocity was set as *1.18 m/s*. It was found that both LES and experiment showed that the high power of fluctuations of velocity and temperature around the body exists between *0.1* and *1.0 HZ*. From other CFD results, the author was able to determine that approximately *17 %* of exhaled air was re-inhaled. It was also stated that when the protective boundary layer around the eyes is broken by outside air movement eyes can become dry.

Melikov (2004) experimentally evaluated the different characteristics that represent a breathing thermal manikin such as: body size and shape, the number of the body segments and their size, posture and positioning, clothing, control mode, surface temperature, response time, sweating, breathing simulation, and air quality evaluation and assessment. It is recommended that a realistic sized and shaped manikin is used, that the area of the segments in contact with the chair be as close as possible to the contact area of the chair surface, the manikin should allow for posture changes to simulate different office work, it is recommended to use a thermal manikin dressed with fitted clothing in order to decrease the uncertainty of the measurements, it is recommended that the comfort mode is used when specifying the control mode at the manikins surface, exhalation through the nose should generate two jets symmetrical to a vertical plane with a *30*° angle between them, and these should be inclined toward the chest at *45*° from a horizontal plane through the tip of the nose, exhalation from the mouth should generate a horizontal jet, and the size of each nostril should be $50\ mm^2$ and the mouth opening should be $100\ mm^2$.

Zhu et al. (2005) used a steady state low Reynolds number model and an unsteady low Reynolds number model to examine the inhalation region of a human in a stagnant environment. Inhalation was modeled as steady inhalation at *6 lpm* or unsteady inhalation at *6 lpm*. The manikin's surface temperature was kept or modeled as *32.9 °C*. The velocity fields, influence of exhalation on inhalation, and the inhalation region were examined. These results were compared to experimental data of the inhalation region of a thermal manikin found by using tracer gas with steady inhalation only. The simulation and experimental data agreed well. It was found that humans inhale air from the lower areas which is pulled by the rising thermal plume. It was also found that when using CFD a simple representation of a human body is not sufficient when examining the BZ. More specifically, the jaw cannot be ignored because it diverts airflow around the face.

Gao and Niu (2006) studied the person to person spread of infectious diseases and how this relates to human exhaled air in the indoor environments. This paper used CFD to model the exhaled air when breathing, sneezing, and coughing and how the exhaled air can be transported to another person. Two detailed CSP's are used for this work. The ventilation system in the room is displacement ventilation. The RNG k-ε model was used to process a *2.5* million cell grid with a y^+ less than *1*. The breathing curve was approximated as a sinusoidal curve with a breathing rate of *8.4 lpm*. Sneezing and coughing were modeled as a 1s exhalation at *250 lpm*. The area of the nose and mouth is *1.5* and $2.5m^2$, respectively. Exhaled air is directed from the nose at *30* ° and from the mouth horizontally. The temperature of the exhaled air is *34 °C* and the density is *1.15* kg/m^3. The results show that inter-person contamination during the regular breathing process is very low and exposure to pollution cause by sneezing or coughing is highly directional.

Melikov and Kaczmarczyk (2007) experimentally analyzed a breathing thermal manikin during realistic simulations of respiration. The importance of breathing simulation, breathing cycle, breathing mode, treatment of exhaled air, natural convection around the body, nose and mouth geometry, body geometry, body posture and clothing design were tested. It was found that the air quality above the lip (<*0.01 m* away) with a non-breathing manikin is almost the same as the inhaled air of a breathing manikin; however, measurements taken further away may lead to incorrect assessment. It was found that simulating a pause during the breathing cycle did not change air quality; however, it did affect the amount of air re-inhaled during respiration. Also, it was found that more exhaled air is re-inhaled when the exhalation is from the mouth than from the nose. The temperature and humidity of exhaled air did not have a significant impact on the inhaled air temperature, relative humidity, or concentration measurements; however, it did increase the amount of exhaled air re-inhaled. A recommendation is made to standardize the nose and mouth geometry because the size and shape will affect the momentum and direction of exhaled air and therefore affect the transport of exhaled air between occupants. It is important to accurately model the geometry of a human body with details to capture the correct flow field in the BZ. Body posture can also affect the air distribution in the BZ and it was found that a manikin seated upright will receive better air quality than a manikin leaning over the desk when horizontal PV is used. Finally, clothing design will affect the space between the body and the clothing and will have an effect on the measurements.

Chao et al. (2009) characterized the expiration air jets and droplet size distribution immediately at the mouth opening. Healthy volunteers were used to measure the velocity and droplet size during coughing and speaking. Interferometric Mie imaging was used to measure the droplet size and particle image velocimetry was used for measuring air velocities. When measuring the volunteers during speaking people were asked to count from *1-100*. It was found that the average expiration air velocity was *11.7 m/s* for coughing and *3.9 m/s* for speaking. The geometric mean diameter of droplets from coughing was found to be *13.5 µm* and *16.0 µm* from speaking. The estimated total number of droplets expelled ranged from *947* to *2085* per cough and *112-6720* for speaking. The estimated droplet concentration ranged from *2.4* to $5.2\ 1/cm^3$ per cough and $0.004\text{-}0.223\ cm^{-3}$ for speaking.

1.2.2 Personal Ventilation

In the indoor environment, ventilation requirements are defined by ASHRAE 62.1 (2004) and are based on the size of a space and the occupancy within the space, however, there are no requirements about the distribution of ventilation air in space. In most existing buildings today, air is delivered by either a mixing or displacement ventilation system, where the fresh air is delivered far from the occupant and can become polluted and uncomfortable by the time it reaches a dwellers BZ. To overcome these shortcomings of conventional ventilations systems, PV has been introduced. To summarize previous work based on PV, the following section provides an extensive review of computational and experimental studies.

Bauman et al. (1993) studied the localized comfort control with a desktop task conditioning system using laboratory and field measurements. It was shown that the local thermal conditions could be controlled over a wide range by adjusting the air trajectory and supply volume. The results noted that large nozzles with low velocity jets were preferred for their ability to limit draft discomfort for occupants. Occupants tended to adjust their systems when the conditions are perceived to be warm and it was suggested that low velocity air at a cool temperature should be used through the PV system.

Tzuzuki et al. (1999) experimentally studied individual thermal comfort control with desk-mounted and floor-mounted task/ambient conditioning. Three PV systems were studied including a desk mounted Personal Environment Module (PEM) and ClimaDesk (CDesk) and a floor mounted Task Air Module (TAM). The results showed that the PEM provided whole body cooling to the user more effectively than the other two units and was superior in pollutant removal efficiency. Improved air quality was achieved locally with both desktop devices when 100% fresh air was used through the PV systems.

Melikov (2001) developed and evaluated air terminal devices for personalized ventilation and studied their abilities. The systems included the PEM, a Computer Monitor Panel (CMP) that is attached to the top of the computer monitor and delivers air toward the manikin horizontally, a Movable Panel that is positioned in front of the manikin above the head and directs air downward toward the manikins face, a Vertical Desk Grill (VDG) that is attached to the front of the desk and delivers air upward toward the manikin and a Horizontal Desk Grill (HDG) that is attached to the front of the desk and delivers air horizontally to the manikins body. For this study, flow rates through the PV systems were as high as *23 l/s* and it was found that the CMP provided the highest air quality. When considering thermal comfort, it was concluded that the VDG was superior over the other designs studied.

Melikov et al. (2002) studied the benefits of personalized ventilation through experimental investigations using a breathing thermal manikin. The experimental setup was a typical office space with a desk and a computer. The breathing thermal manikin had a breathing cycle of *6 lpm* with an exhalation temperature of *34 °C* and a relative humidity of *95 %.* 5 different air terminal devices were tested including a movable panel, computer monitor panel, vertical desk grill, horizontal desk grill and personal environments module. It was found that the ventilation effectiveness increased with flow rate (up to *23 l/s*) and none of the air terminal devices were able to deliver *100 %* fresh air under the parameters used in this study. The CMP delivered the highest amount of personalized air in the inhalation air. The VGD achieved the maximum personal exposure effectiveness. The MP and VGD performed best under non-isothermal conditions. Also, a rather small amount of exhaled air (< *1 %)* was re-inhaled with the use of PV and that the temperature of the inhaled air generally decreased with an increase in the flow rate from the air terminal devices.

Kaczmarczyk et al. (2002) studied the effects of a personalized ventilation system on perceived air quality and sick building syndrome symptoms (SBS) by conducting a study of 30 human subjects when using an occupant controlled PV system in an office environment. The study showed that using fresh, outdoor air at ~20°C through the PV system significantly increases perceived air quality and the occupant's ability to concentrate and reduce the occurrence of headaches. The study suggests that PV could improve occupant productivity.

Bolashikov et al. (2003) experimentally studied new air terminal devices with high efficiency for PV applications. The two devices examined were a Round Moveable Panel (RMP) that was like a large shower head and an innovative headset device. In this study, the flow rate through the RMP from *5-15 l/s* and the flow rate through the headset device ranged from *0.18-0.5 l/s*. The results showed that 100 % PV air could be inhaled with the RMP and up to 80 % for the headset device. When considering thermal comfort, the RMP was able to adequately cool the whole body, while the headset device was not due to the low flow rates through this device. With the range of flow rates studied, it was found that the velocity of the PV jet needed to be at least *0.3 m/s* at the target zone to penetrate the thermal plume.

Faulkner et al. (2003) experimentally studied the ventilation efficiencies and thermal comfort of a desk-edge-mounted task ventilation system. The desk-edge-mounted task ventilation system was attached to the bottom of the front edge of the desk. The results showed that this device achieved a 50% increase in the effective ventilation rate in the BZ of the manikin while maintaining comfortable draft conditions.

Melikov (2004) reviews existing information on performance of personalized ventilation and human responses to it. Indoor air quality and thermal comfort are assessed by analyzing the airflow interaction near the human body. It is recommended that PV nozzles have low initial turbulence, large diameters, a minimum target velocity of *0.3 m/s* and a maximum of *1.5 m/s*, allow for adjustments of flow and direction and use air at temperatures of *3-4 ˚C* cooler than room air.

Gao and Niu (2004) used experiment and CFD simulations of a detailed thermal manikin to study the micro-environment around the manikin with and without PV. The experimental details were reported as earlier experiments and were not given in this paper. Two new indices for calculating air quality in the BZ are introduced. For the CFD simulation the standard k-ε model was used with standard wall functions. The grid consisted of ~*2* million cells and resulted in a y^+ that ranged from *10-29*. The breathing process was modeled as a steady inhale at *8.4 lpm* which correlates to light physical work. The PV system delivered airflow at *3* rates (*0.0* to *3.0 l/s*) and it was found that the best inhaled air quality was achieved at the airflow rate of *0.8 l/s* in the CFD; however, the experimental results show that the best air quality was achieved at a flow rate of *3.0 l/s*. The heat transfer coefficient was found to be $4.95\ v/m^2\,°C$, which is higher than accepted values. The grid was coarsened to have a y^+ that ranged to *15-29* and the results compared better with the experimental data. This paper recommends that improvements be made in the CFD modeling.

Nielsen et al. (2005) studied personal exposure between people in a room ventilated by textile terminals with and without the use of PV. The textile terminals consist of a half cylinder diffuser with a fabric covering that projects air from the ceiling with air flow rates that ranged from 6-8 l/s. The study showed that this PV system was able to improve air quality while simultaneously improving the protection of an occupant from cross contamination.

Niu and Gao (2007) experimentally studied a chair based PV system where the PV supply nozzle was directly below the chin. Two different air terminal devices were studied for this work with different geometries. One nozzle has a square geometry where as the other is circular. Eight different combinations of lengths and diameters of the nozzle were used for comparison. All air terminal devices had a fresh air supply flow rate of less than *3.0 l/s*. The air terminal devices were placed directly in the BZ of the manikin or person. Tracer gas was used to characterize the ventilation efficiency. It was found that supplying fresh air directly to the BZ reduced the level of pollutants in the inhaled air by up to *80 %* with the different air terminal devices. It was found that the quality of inhaled air increased with an increase in the supply air flow rate. Personalized supplied air lowered inhaled air temperatures and improved perceived air quality with temperatures ranging from *15-22 ˚C*. From the experiments with people it was found that people were more sensitive to the flow rate rather than the supply temperature. Finally, better inhaled air quality and thermal comfort could consequently be achieved by personalized ventilation with a proper design.

Halvonova and Melikov (2009) studied the performance of “ductless” personalized ventilation in conjunction with displacement ventilation. This paper compared “ductless” personalized ventilation in conjunction with displacement ventilation with the performance of displacement ventilation alone in an office room test chamber. Two thermal manikins were used with realistic geometries. In this setup there were two sources of pollutants, the exhaled air of one manikin and a point source on one of the desks. A walking person caused mixing of clean air near the floor with the polluted warmer air and the effects of this were measured for the two cases. It was found that for the displacement only case there was a decrease in the inhaled air quality. The performance of the “ductless” PV system was better, but it was found that the results were very sensitive to the location of the walking person.

Khalifa et al. (2009) experimentally studied two PV systems in a full size, *2.0 x 2.6 x 2.5 m*, plexiglass chamber with a seated, real-size thermal manikin. The thermal manikin used for the experiment represents a *1.8 m* tall average male. This manikin has 20 independently controlled segments that can be set to a desired skin temperature or heat flux. The manikin was not clothed for the experiment and was seated upright for testing with a constant surface temperature of *~32 ˚C*. The diameter of the primary nozzle was *50.8 mm* and the diameter of the secondary nozzle was *105.6 mm*. The PV nozzle was placed *0.41 m* from the manikin’s nose, along the vertical symmetry plane of the manikin. A mixing box, located in the room, was used to deliver fresh air to the primary nozzle and recirculated air to the secondary nozzle and both nozzles were fitted with flow strengtheners and a set of two screens. General ventilation was also supplied to the chamber through a floor-mounted *0.23 x 0.24 m* four-way directional grill diffuser fed by a variable-air volume box in the under-floor plenum. The air supplied through the floor diffuser and secondary nozzle was seeded with SF_6. The exhaust of the chamber is through a *0.58 x 1.17 m* perforated ceiling outlet. Tracer gas measurements were taken within the BZ of the manikin at *10 mm* and *25 mm* from the tip of the nose for the single jet PV system and the Co-flow nozzle as shown in Figure 4.4 and 4.5. The primary nozzle delivered *2.4 l/s* of clean air, while a total of *18.9 l/s* were delivered to the room. When the secondary nozzle was active, *6.7 l/s* of seeded air were delivered through it, resulting in approximately the same exit velocity for the primary and secondary nozzles, and the floor diffuser flow was lowered by this amount. Concentration measurements were taken in the manikin's nose and mouth, in the primary nozzle, the secondary nozzle, in the under-floor plenum, and in the chamber exhaust. To measure the concentration of tracer gas in the BZ, six sampling probes were mounted on a vertical rake and were transversed vertically while recording tracer gas concentrations using a multi-gas monitor based on the photo-acoustic infrared detection method.

Nagano et al. (2009) studied the free convection flow within the BZ when using confluent jets to improve performance of personalized ventilation. This work used upward confluent plane jets to deliver fresh air to the BZ. The inner jet always supplied clean air while the outer jet delivered recirculated air to assist the inner jet which minimized the mixing between the two jets. This paper particularly looked at the thermal effects of this PV system. It was found that using this system slightly cooled the back of the manikin's neck.

Bolashikov et al. (2009) studied the control of the free convection flow within the BZ when using confluent jets. This work used upward confluent plane jets to deliver fresh air to the BZ. The inner jet always supplied clean air while the outer jet delivered recirculated air to assist the inner jet which minimized the mixing between the two jets. This paper focused on the inhaled air quality of the manikin with PV. Experiments were performed under isothermal conditions in a full scale test room representing a typical office space. The thermal manikin had a realistic human body shape. Tracer gas measurements were conducted to study the benefit of the PV system. It was found that this PV system resulted in improved air quality in the BZ, but the benefit was limited by the separation of the flow around the manikins head due to the shoulder and neck region.

Nielsen (2009) experimentally studied the control of airborne infectious diseases in ventilated spaces. The experiments were conducted with motion and without in the presence of two life-size manikins to represent patients in a hospital ward and tested the use of PV. One patient was the source of airborne infections and the other was the target. A system suitable for a bed is a PV system which uses pillows, mattresses, etc. as supply openings of fresh air by using fabric as a diffuser. The results showed that the transport process of particles and tracer gases at high flow rates is reduced. It was found that stratification of exhalation air is possible in displacement ventilation systems which can increase cross-infection. The results showed that PV built into hospital beds, which is a new possibility, can be used to reduce cross-infection without having separate rooms for each patient. PV can also be used to reduce the emissions from the source patient and protect other individuals in the space.

1.2.3 Exposure assessment with CFD

To determine the direct impact air quality has on occupants, the effects of pollutants in the BZ needs to be conducted. This section provides a review of different studies that were conducted to determine exposure assessment with CFD.

Murakami et al. (1998) modeled a human body using CFD in a displacement ventilation system. Flow and temperature fields around the manikin were analyzed and the age of supply air and residual lifetime of air in the room were also calculated using a low Reynolds number turbulence model. The grid consisted of *~125,000* cells for the half space and the y^+ values were reported to be less than 5. The heat transfer at the manikin's surface was set to $20\ W/m^2$ and resulted in a mean surface temperature of *31 °C*. Concentration distributions were found for three different contaminant sources and the quality of the breathing air was examined. It was found that concentration stratification appears similar to the temperature stratification in a displacement ventilation system. If the rising stream around the body surface is not broken by the surrounding airflow, whether it enhances or decreased air quality of the BZ depends on the location of the contaminant generation. Positive influence on air quality in BZ when contaminants are generated in the upper part of the room and a negative effect when contaminant is generated near the floor. The CFD results were compared to previous experimental data and a good agreement was found.

Lai et al. (2000) developed expressions for an inhalation transfer factor (ITF) and a population inhalation transfer factor (PITF). The ITF is the pollutant mass inhaled by an exposed individual per unit pollutant mass emitted from an air pollution source, where PITF is for the total fraction of an emitted pollutant inhaled by all members of the exposed population. ITFs and PITFs were calculated for outdoor releases from area, point, and line sources and for indoor releases in single zone and multi-zone indoor environments and in motor vehicles. PITFs for outdoor emissions were on the order of 10^{-6} to 10^{-3} where as indoor PITFs were much higher $\sim 10^{-3}$ to 10^{-1}. It was also found that for a conserved species released within a single, well-mixed compartment, the ITF is inversely proportional to the outdoor air ventilation rate.

Hayashi et al. (2002) used CFD to analyze the rising stream around a human body and its effect on inhalation air quality. This paper proposes new indices for evaluating the inhaled air region: Index showing the effectiveness of contaminant ventilation and index showing the effectiveness of contaminant inhalation. This paper studied three different postures, 1) standing, 2) sitting and 3) laying. The standard k-e model was used for this computation. The grid for the standing posture was *~160,000* cells, for sitting *~190,000* cells and for laying *~140,000* cells. It was found that when a human body is standing, it inhales the air of the lower part of the room because of the rising stream that is generated by heat. And inhaled air volume of *14.4 lpm* was used. When sitting, the inhaled air region is similar to the standing posture. Finally, when laying, the inhaled air region is distributed over the horizontal direction of the mouth near the floor.

Hayashi et al. (2002) used the standard k-e model, steady inhalation at *14.4 lpm* and specified heat flux at the manikin's surface to examine the characteristics of indoor ventilation and its effects on contaminant inhalation. This paper also introduces a new index to show the effectiveness of contaminant ventilation. The grid used for this study had about *150-200,000* cells. The inhaled air region was examined for three different postures: standing, sitting and laying down. The velocity of *0.22 m/s* was calculated above the head for the standing posture, *0.17 m/s* for the sitting posture and *0.16* for the sleeping posture. It was found that when a person is standing or sitting the person inhales air from the lower part of the room because the thermal plume carries the air from the floor to the BZ. While sleeping, the inhaled air is distributed over the horizontal direction of the mouth near the floor. It was also found that the residual lifetime for air to be inhaled is relatively low when in the sleeping posture than when standing.

Nielsen et al. (2002) used CFD to calculate contaminant flow and personal exposure. An artificial lung was used to simulate breathing. It was found that when flow comes from behind a person, the BL can entrain and transport contamination to the BZ from relatively large distances (*1.5 ft*) Also; exhaled air is carried some distance from the body, while inhaled air is taken from the immediate surroundings. Exhaled air is carried away by the thermal plume during the short pause between inhalation and exhalation and air exhaled horizontally through the mouth results in much larger exposure levels than does air exhaled through the nose. Air exhaled through the mouth can be locked in a thermally stratified layer where concentrations several times greater than the return concentration may occur, while, air exhaled through the nose has been observed to follow the boundary-layer flow and thermal plume to the upper part of the room. The general flow field is re-established after a few minutes, while the thermal plume is re-established after a few seconds after disruption from movements; therefore, local effects of movement and exhalation are not problematic in most situations

Bennett et al. (2002) developed a metric to determine the incremental intake of a pollutant released from a source or source category and summed it over all exposed individuals during a given exposure time, per unit of emitted pollutant. This metric is called an iF and it was developed to bring cohesiveness to the field of pollutant transport. iF is one step in determining air pollution health risk assessment. Health risk assessment can be determined by multiplying the iF by a usage factor, emission factor and the toxicity of each pollutant considered.

Bjorn and Nielsen (2002) studied the influence of the human exhalation on flow fields, contaminant distribution, and personal exposure in displacement ventilation rooms using experimental setups and CFD. Experiments were carried out in a test room at *20 °C*. Two thermal breathing manikins were used in various configurations including both standing and the breathing contaminant released through the nose, both standing and the breathing contaminant released through the mouth, one standing behind the other and the breathing contaminant released through the nose and one standing and one sitting with the breathing contaminant released through the mouth. A nostril with a diameter of *12 mm* is used ($1.32\ cm^2$) and an exhale temperature of *33-34 ˚C* through the mouth and *32-33˚C* through the nose. For the CFD calculations the k-ε model was used with logarithmic wall functions. The manikins were represented as heated boxes in the simulation. No details on the grid were given. It was found that personal exposure depends on the BZ height in relation to the stratification height. It was also found that the exhalation jet is able to penetrate the BZ of a person standing nearby and that exposures in the order of magnitude of ten times the return concentration can occur and that air exhaled horizontally through the mouth results in much larger exposure than air exhaled through the nose (exhalation through the nose is not an acute problem in most ventilation systems). The authors also stated that the stratification of exhaled air will break down immediately as soon as the physical movements begin and that the protective effect of the thermal plume will disappear at speeds of *0.2 m/s* and a moving person creates a strong wake behind them that can destroy the thermal boundary layer of a seated person which causes larger exposures to contaminants.

Gadgil et al. (2003) used CFD predictions of mixing time of a pollutant in an unventilated, mechanically mixed, isothermal room to study the accuracy of the standard k-e model for predicting the mixing time and the extent that the mixing time depends on the room airflow, rather than the source location within the room. A Sc of *0.9* was used for simulation. The CFD simulations modeled 12 mixing experiments performed by Drescher et al. (1995) and the CFD predictions of mixing time were found to be in good agreement with the experimental measurements. The results show that there is a large dependence of the mixing time on the velocity and turbulence intensity at the source location.

Zhao et al. (2005) studied the transport of particles during periodic breathing and pulsed coughing or sneezing. A zero equation turbulence model and the drift flux model were used to calculate flow fields and particle distributing in an indoor environment. The results show that the transport of particles from breathing is limited and may only transport a short distance. However, sneezing and coughing with an outlet velocity of *20 m/s* could cause particles to transport distances greater than *3 m* even at high air change per hour. From this, it is important for humans to practice good personal habits (covering mouth) to defend against transport of disease.

Khalifa et al. (2006) computationally studied occupant exposure in an office cubicle. A simplified occupant was modeled with blocks representing the torso, thighs and legs. The grid used consisted of ~100,000 structured cells. The modeled cubicle had many emitting surfaces as well as various occupant positions. The simplified model was compared to a more refined model and predicted very similar concentration trends to within ± 10 % in the BZ. The manikin representation, supply diffuser location, occupant position and orientation were analyzed. The results showed that the spatial non-uniformities could result in as much as 45 % differences in exposure compared to simplified models based on the well mixed assumption.

Zhu et al. (2006) studied the transport characteristics of saliva droplets in a calm indoor environment. 3 healthy male subjects were used to study the transport characteristics of saliva. It was found that more than *6.7 mg* (varied from *6-8 mg*) of saliva is expelled at a velocity of up to *22 m/s* (ranged from *6 -22 m/s* with *10 m/s* most prominent) during a single cough. This leads to saliva droplets traveling more than *2 m*. Then 4 simulations were carried out to investigate how the size of the droplets effected the transport: Both occupants sitting with supply air near the cougher, both sitting with air supply away from cougher, one laying and one standing with supply air above bed and one laying and one standing with the supply air opposite the standing manikin. Steady breathing and coughing were assumed. The standard k-e model was used with first order upwind accuracy and log-law wall functions. There were a total of *4,620* elements on the sitting manikin's surface and *13,520* elements on the standing manikin surface grid and *2,860* on the laying surface manikin grid. The grids varied from *~450-575,000* total cells. The BC applied to the manikins surface was *33.8 W*. The cough was modeled as *22 m/s* constant flow at *32 °C* with random droplets. The results showed that droplets *30 µm* or less in diameter are not affected by gravity or inertia and their transport was mostly due to the indoor flow fields, droplets of *50-200 µm* were significantly affected by gravity and fell as the flow field weakened and droplets of greater than *500 µm* traveled almost straight and impacted on the first opposite object. Other results show that there is a high risk of droplet infection within short distances and when lying down the location of the supply air has a significant effect on the transport of saliva droplets.

Gao and Niu (2006) studied the transient process of respiration and inter-person exposure assessment using CFD. This paper studies the human respiration process and the transport of exhaled air by breathing, sneezing and coughing. A detailed manikin was used for this work. The total number of cells used for this work was *2.5* million and were clustered near the manikin. The low Reynolds number RNG k-ε model was used with the enhanced wall treatment. A sinusoidal breathing curve was used to simulate breathing at a rate of *8.4 l/m*. A concentration of *1000 ppm* of a tracer gas was added to the exhaled air. It was found that personal exposure to the exhaled air from the normal respiration process of other persons is very low in an office space with displacement ventilation. This finding is consistent with the steady state findings of the same setup. It was found that re-inhalation of exhaled air was *10 %* for nasal breathing and *0 %* for oral breathing. Finally, when two people are facing each other cross-infection may occur due to the long transport distance of the sneezed air, however, sneezing is highly directional.

Brohus et al. (2008) studied the influence of persons' movements on ventilation effectiveness. This work includes results from a systematic investigation of the movements' influence on the ventilation effectiveness using human subjects combined with tracer gas measurements. Several typical human movements are tested including: moving your arms upward and downward, moving your arms randomly, moving your arms horizontally and walking. It was found that mixing ventilation is more robust when comparing ventilation effectiveness than displacement ventilation, however, when movement stops displacement ventilation is found to be more effective. Finally, it was found that the change in ventilation effectiveness is very dependent of the type of movement.

Nazaroff (2008) used mathematical models and empirical data to explore how iF varies with governing parameters for episodic indoor pollutant releases. iF is defined as the attributable pollutant mass taken in by an exposed population per unit mass emitted from a source. It is found that the iF depends on building-related factors, occupant factors, and pollutant dynamic factors. In a simple case of a nonreactive pollutant in a well-mixed indoor space with steady occupancy and constant ventilation and breathing rates, the iF is the ratio of the occupants' volumetric breathing rate to the buildings ventilation flow rate. Typical indoor iF range from *0.001- 0.1* or *1,000-100,000* per million. Some fraction of the pollutant intake may be retained in the body with the remainder exhaled. And finally, for each pollutant of concern, the partial health risk would be estimated as the product of the four terms: usage factor, emission factor, iF, and toxicity.

1.2.4 Chemical Reactions

Constituents of indoor air vary throughout the day, but always contain an assortment of chemicals at different concentrations. With the existence of several different chemicals, reactions in the indoor environment occur frequently and decrease the concentration levels of reactants while increase the concentration levels of products. The following section is focused on typical indoor reactions and computational work dealing with modeling these reactions.

1.2.4.1 General Chemical Reaction Papers

Atkinson et al. (1990) determined the rate constants for reactions between Ozone and several different Terpenes using a combination of absolute and relative rate techniques. For the absolute rate constant measurement the first and second order rate constants were found by plotting the Ozone decay rate against the Terpene concentration. The slope of this plot would be the second order rate constant and the y-intercept would give the first order rate constant. For the relative rate constant measurement, multiple reactions were monitored at one time where one reaction has a known reaction rate. In this case the natural log of the initial Terpene concentration over the decayed Terpene concentration is plotted against the natural log of the initial reference Terpene concentration over the decayed reference Terpene concentration. The resultant plot is a straight line with a slope of the second order rate constant of the unknown Terpene over the second order rate constant of the known Terpene with a zero intercept. The paper found good agreement for the second order rate constants for the Terpenes measured using the two methods.

Cano-Ruiz et al. (1993) studied the removal of reactive gases at indoor surfaces by looking at combining mass transport and surface kinetics. A computational model was used for predicting indoor deposition velocities and an approximate analysis based on this model was used to obtain algebraic expressions for the deposition velocity of reactive gases. Three airflow conditions were used for this work, 1) forced laminar convection parallel to a flat plate, 2) laminar natural convection flow along an isothermal vertical plate and 3) homogeneous turbulence in an enclosure. The gas-surface kinetics are modeled by using a reaction probability (fraction of pollutant molecular collisions with a surface that results in irreversible removal). Reaction probabilities for this work were obtained from published experimental data. It was found that Ozone deposition occurs at the transport limited rate when the reaction probability is $\sim 3x10^{-4}$ for typical indoor airflow conditions and that Ozone deposition can be predicted by surface kinetics alone if the reaction probability is $\sim 5x10^{-7}$.

Reiss et al. (1994) modeled Ozone deposition onto indoor residential surfaces. This included the transport of the pollutant to the surface and the uptake of the pollutant onto the surface (boundary layer resistance and surface uptake resistance). The reaction probability (mass accommodation coefficient) is required for this work. This work presents an experimental method in order to determine the reaction probability. It was found that the reaction probabilities ranged from 10^{-5}-10^{-7} for Ozone deposition onto glass, latex paint and vinyl and paper wall paper. For these cases it was found that the reaction probability was either surface uptake limiting, boundary layer transport limiting or both.

Weschler and Shields (1997) studied potential reactions among indoor pollutants. This paper reviews the chemistry for indoor pollutants and potential reactions. In indoor settings a chemical reaction must occur within a time interval shorter than the residence time for a packet of indoor air. At typical ventilation rates, these reactions include Ozone with nitric oxide, nitrogen dioxide and selected unsaturated hydrocarbons; thermal decomposition of peroxyacyl nitrates; numerous free radical reactions; and selected heterogeneous processes. The products that can be produced include: aldehydes, ketones, carboxylic acid and various organic nitrates. It has been shown that some of these products can be more irritating than the reactants themselves. It was also stated that certain species may photalyze under indoor illumination, especially fluorescent lights. The reactions on indoor surfaces become more significant in the indoor environment because the surface-to-volume ratio increase.

Fruekilde et al. (1997) studied the ozonolysis at vegetation surfaces to investigate if it was a source of acetone, 4-oxopentanal, 6-methyl-5-hepten-2-one, and geranyl acetone in the troposphere. Laboratory experiments were conducted to measure the reaction products of Ozone with foliage of common vegetation. It was found that squalene was a strong precursor for geranyl acetone. It was also found that human skin lipids which contain Squalene as a major component is a strong precursor for the four compounds plus nonanal and decanal. Reaction rates for 6-methyl-5-hepten-2-one and 4-oxopentanal with Ozone are given in this work.

Weschler and Shields (1999) studied the indoor Ozone/Terpene reactions, specifically the formation of indoor particles due to these reactions. This paper uses adjoining offices to study the particulate growth when Ozone reacts with Terpenes. It finds that particles were formed from the reaction of limonene with Ozone. This results in yields of *10-15 %*. The greatest production of particles was for particles of size *0.1-0.2 µm* diameter sized particles.

Wainman et al. (2000) gave results for a series of experiments aimed to investigate the reaction of Ozone and D-limonene. It was stated that Terpenes are commonly found in indoor air at higher concentrations than the ambient (outdoor) air and that the addition of Ozone to an office building could lead to high concentrations of fine particles when Terpenes were present. For the experiments *60-100 ppb* of Ozone was introduced. The results show a clear potential for significant particle concentrations to be produced in the indoor environments from these reactions. An increase in the *0.1-0.2 µm* particle concentrations began in all of the experiments as soon as the Ozone was introduced. The results showed that *99.5-99.9 %* of all particles measured were between *0.1-0.3 µm*. This shows that the potential exists for the accumulation of PM2.5 in excess of *20 µg/m3* in the indoor air as a result of using Terpene-based products in the presence of elevated outdoor-generated Ozone concentrations. The paper also showed evidence that relative humidity may play a role in the formation of particles via the Ozone-limonene reaction, but this point was not examined further.

Weschler (2000) looked at the concentration and chemistry of Ozone in the indoor environment. The indoor level of Ozone is based on many factors including outdoor Ozone levels, air exchange rates, indoor emission rates, surface removal rates, and chemical reactions indoors. The levels of Ozone indoors can vary on an hour to hour basis and a season to season basis. Under normal conditions the half life of Ozone is between *7* and *10* minutes indoors. Only a small fraction of indoor reactions with Ozone occur fast enough to compete with the air exchange rate. This paper summarizes rate constants for Ozone and commonly identified indoor pollutants.

Morrison et al. (2003) studied the rapid measurement of indoor mass-transfer coefficients. Two methods for rapidly and directly measuring species fluxes at indoor surfaces are introduced, which allows one to evaluate the transport-limited deposition velocity (mass-transfer coefficient). The two methods give results that are in order-of-magnitude agreement with predicted indoor mass-transfer coefficients.

Sarwar et al. (2003) Studied the significance of secondary organic aerosol formation in buildings. This paper studies the formation of particles and gas-to-particle partitioning of the products from a Ozone/a-pinene reaction. Initially most particles ranged from *0.1-0.2 μm* but this range decreased as steady state was obtained.

Weschler (2004) studied Ozone initiated reaction products in the indoor environment. This paper found that for each molecule of Ozone consumed by a reaction that roughly a molecule of hydroxyl radicals is produced. It is thought that hydroxyl radicals can be more harmful to an individual than Ozone itself. A human study was conducted to see the effects of oxidation products on the indoor environment air quality. When examining the Ozone/limonene chemical reaction it was found that after a *20* minute exposure to the products of this reaction at realistic indoor concentrations there is an increase in the blinking rate in the human subjects tested.

Thornberry and Abbatt (2004) studied the heterogeneous reactions of Ozone with liquid unsaturated fatty acids. This study included detailed kinetics and gas-phase product studies. Three fatty acids were considered for this work including: oleic acid, linoleic acid and linolenic acid. A coated wall flow tube and chemical ionization mass spectrometry was used to determine the kinetics. It was found that the gas surface reaction probabilities for Ozone loss was $8x10^{-4}$ for oleic acid, $1.3x10^{-3}$ for linoleic acid and $1.8x10^{-3}$ for linolenic acid. It was found that the temperature dependence of the surface uptake of Ozone was small and positive. For linoleic acid the reaction probability was found to be independent of relative humidity.

Nazaroff and Weschler (2004) analyzed air pollutant exposures from the use of cleaning products. Based on typical iFs (10^{-2}) in the indoor environment and the emission of *1 g/day/person* of organic compound from cleaning product, the authors predict that a person inhales an average of *10mg/day/person*. The authors also give direct evidence of health hazards from inhaling cleaning products including accidental poisoning from inappropriate use and asthma, allergy and respiratory irritation.

Morrison et al. (2006) studied the spatial distribution of pollutant transport to and from indoor surfaces. The average transport limited deposition velocity over a *12 h* period was found for Ozone. It was observed that a tighter distribution of flux core filters placed near one-another than for filters separated by greater than one meter, higher fluxes near sources of air movement such as supply vents and computers and there were consistent results in a single location over 5 days. It was found that the mass-transfer coefficient in a room sized laboratory chamber to be proportional to the device diameter raised to the power of *-0.45*.

Morrison and Wiseman (2006) studied the temporal considerations in the measurement of indoor mass transfer coefficients. The studied a broad range of indoor conditions, all of which were realistic. It was found that the time averaged, transport limited deposition velocity measurement could be in error by as much as *40 %*. Higher reactive species produced the highest measurement error. For moderately surface reactive compounds (such as Ozone) the error incurred varied depending on the type of surface for deposition. It was determined that for continuous flux measurements from field experiments in apartments, labs and offices suggest that the time averaged deposition velocity was in error by about *5-15 %.*

Tamas et al. (2006) studied the short-term assessments of PAQ for Ozone and limonene, separately and together were conducted and the impact of filtration and influence of the Ozone generation method were examined through experimental trials. The concentration of Ozone, total VOC and size-fractioned particles were continuously monitored in four identical *40* m^3 low-polluting test offices ventilated at *1.4* h^{-1}. When limonene was added to the office, *50 %* of the sensory panel was able to recognize a fruit odor when the limonene concentration exceeded *85 ppb*, while only *16 %* could at *40 ppb*. The results showed that the TVOC concentrations that were detected increased when limonene was added to the room. It was also shown that the PAQ was the worst in all experiments when Ozone and limonene were present together; in fact, more that *50 %* were dissatisfied with the PAQ when Ozone and limonene were present together.

Weschler (2006) looked at Ozone's impact on public health, specifically, the contributions from indoor exposures to Ozone and products of Ozone initiated chemistry. This paper related measured outdoor Ozone concentrations to morbidity and mortality. The authors looked at how indoor levels of Ozone and Ozone initiated oxidation produces could be the cause of this relation. It was found that between *25-60 %* of the total daily intake of Ozone is inhaled indoors. It was also found that the average daily indoor intakes of Ozone oxidation products are roughly one-third to twice the indoor inhalation of Ozone itself. It is concluded that indoor exposures to Ozone and oxidation products can be reduced by the use of filters in the ventilation air and minimizing the use of products and materials that have emissions that react with Ozone.

Weschler et al. (2006) studied indoor chemistry and health. This paper found that oxidative chemistry has increased indoors over the recent years because of the increase in the Ozone levels outdoors, the increased use in cleaning products and tighter buildings. It was also found that the inhalation of Ozone and oxidation products activates macrophages which are the second most potent secretory cells in the body and mediate inflammatory responses. Over activation of these cells can lead to tissue injury and poor perception of indoor air quality.

Colemann et al. (2008) studied the Ozone consumption and volatile byproduct formation from surface reactions with aircraft cabin materials and clothing fabrics. In this work, two small-chamber experiments were conducted at low relative humidity and high air exchange rates for new and used cabin materials and laundered and worn clothing. Ozone depositions, Ozone uptake and primary and secondary emissions of VOC's were measured. It was found that the deposition velocities ranged from *0.06* to *0.54 cm/s*. It was found that the presence of Ozone increased the emissions of VOC's from the different materials. The results showed that Ozone reactions with surfaces reduce the Ozone concentration in the cabin but generate volatile byproducts of greater concern for health reasons.

Sidheswaran and Tavlarides (2008) studied the gas and particle phase chemistry of linalool and ozone reactions in two stainless steel chambers. Fluorescence techniques were employed in identifying and quantifying these species in the sub-micron particles. A preliminary analysis of the products show a number of identified intermediates including 2-ethenyl-2-methyl-5-hydroxytetrahydrofuran, 2(3H)-furanone-5-ethenyldihydro-5-methyl-, tetrahydro-1-methyl-5-oxo2-furancarboxylic acid and 2-hydroxy-2,3-dimethylsuccinic. The reaction rate constant for the oxidation of linalool by ozone was found to be 3.49×10^{-16} cm^3/molecules-sec. The paper concluded that the concentration of linalool and the concentration of ozone play a vital role in the formation and growth of particles and the yield of the products in the particle phase was obtained.

Venkatachari and Hopke (2008) studied the characterization of products formed in the reaction of ozone with alpa-pinene to understand the formation mechanisms and the potential health effects of particle-bound oxidative species. The alpha-pinene/ozone reaction was studied using liquid chromatography-multiple stage mass spectrometry. It was found that oxidant species were clearly stable for at least 1-3 hours making it possible for these species to bind onto particles which would form fine particulate organic peroxides.

Morrison (2008) summarized the interfacial chemistry in indoor environments based on a workshop sponsored by the National Science Foundation. This paper provides an overview of indoor surface chemistry and how people might reduce occupant exposure to air pollution.

Pandrangi and Morrison (2008) studied Ozone interactions with human hair. Specifically they studied Ozone uptake rates and product formation. Hair samples from before and after washing were used. The hair samples were exposed to Ozone for 24 hours and the

Ozone consumption rates and product emission rates were quantified. Unwashed hair near the scalp exhibited the greatest Ozone uptake and reaction probability, otherwise there was no measureable difference between washed and unwashed hair. Emitted compounds included geranyl acetone, 6MHO and decanal. It was found that the uptake of Ozone was nearly transport limited.

Corsi and Morrison (2009) give results for decreased ventilation rates used for energy conservation that result in increased production of formaldehyde and secondary organic aerosols. A well-mixed model of a typical home is used and the increase in products is measured with the decrease in air exchange rate. The chemical reaction modeled was linalool and Ozone. It was found that indoor Ozone levels are half the outdoor levels even at an air exchange rate of *1*. Surface reactions were found to dominate the removal of Ozone in this case. It was found that linalool and the two by-products increased with lower air exchange rate, which is consistent with the literature. The paper makes arguments about the effect of temperature and humidity on the reaction rate of Ozone and Terpenes, but no evidence is given.

Wisthaler and Weschler (2009) studied the reactions of Ozone with human skin lipids. In this paper proton transfer reaction-mass spectrometry was used to analyze air, specifically looking for volatile products resulting from Ozone/human skin lipid reactions. In vivo and human subject experiments were conducted. The results of the spectrometry give detected products that include: acetone, 6-MHO, geranyl acetone, OH-6MHO, 4-OPA, 4-MON, 4-MOD, succinic dialdehyde, 5-hydroxy-4-oxopentanal, levulinic acid and oxobutanoic acid. These results are consistent with other squalene/Ozone reaction products. Squalene is the single most abundant unsaturated constituent of skin lipids. Further studies in this paper show that Squalene is the major scavenger of Ozone between room air and the skin surface. These surface reactions reduce the mixing ratios of Ozone indoors, but increase the mixing rations of volatile products and these products can be airway and skin irritants.

1.2.4.2 Chemical Reactions with CFD

Weschler and Shields (2000) used a one compartment mass balance model to simulate unimolecular and bimolecular reactions in the indoor environment and studies the influence of ventilation on chemical reactions. This work first studies steady state scenarios, but at low air exchange rates steady state may not be achieved. So, dynamic model and experimental observations were also examined. It was shown that products from indoor pollutants increase as the ventilation rate decrease because there is more time for the reaction to take place; therefore, adequate ventilation is necessary not only to remove pollutants with indoor sources, but also to limit reactions among indoor pollutants. The experimental reactions examined were between Ozone and limonene and results were obtained for low and high ventilation rates. The concentrations of monitored products in the simulation were much larger at the lower ventilation rates, which is consistent with experiment. The potential for reactions is another reason to maintain adequate ventilation in indoor environments.

Sorensen and Weschler (2002) modeled a *13.6 x 40.6 m* 2D room with CFD and examine the concentrations of two gaseous compounds that react in an indoor setting to produce a hypothetical product at two different air exchange rates. The low Reynolds number *k-*□ model was used with a species $Sc_t = 0.9$. Only surface deposition of Ozone was included in this model. *80 ppb* of Ozone entered the room through the supply air and D-limonene was modeled as a floor source with a source strength of $1.89\ mg/m^2h$ and was constant in time. The diffusion coefficient of Ozone in air was given as $18.2 \times 10^{-6}\ m^2/s$, for D-limonene it was $6.2 \times 10^{-6}\ m^2/s$ and the hypothetical product it was $6.0 \times 10^{-6}\ m^2/s$. A reaction rate of $k = 1.0184\ 1/ppb{\cdot}h$ was used for the second order reaction rate between Ozone and D-limonene. It was determined that if the CFD calculation can predict the momentum transport correctly, it is reasonable to assume that the transport of species is reliable as well. The results show that there is a large concentration gradient in the room for both reactants and product. This shows that reactions occur at different rates across the room and that the time available for these reactions to occur varies across the room. These results were compared to a one-compartment mass-balanced model assuming perfect mixing and differed significantly. This implies that the well mixed assumption can be an invalid assumption in the indoor environment when chemical reactions occur.

Ito et al. (2003) used a chemical reaction model was for gas phase reactions in the CFD analysis for a 2D room simulation. The CFD cases that were run include modeling Ozone alone, D-limonene alone, and the reaction of Ozone and D-limonene. VOC concentration distributions were found for the three cases and shown for comparison. The surface deposition of Ozone was analyzed in all analytical cases. It was found that the room averaged concentration of Ozone and D-limonene are decreased by about *20 %* when chemical reactions are included. CFD and experimental results were very consistent and it was confirmed that they analyze the flow fields with sufficient accuracy.

Ito et al (2004) created a 2D CFD simulation to analyze the distribution of Ozone in indoor air. The turbulence model that was used was a low Reynolds number k-e model and the grid had y^+ values of less than *1*. The wall surface deposition flux of Ozone was modeled as a heterogeneous wall surface reaction, and values for Ozone entering the room through the supply air were *0.65 ppm* and *2.44 ppm*. The CFD results were compared to a 3D experimental setup with a 2D flow field where the concentration distributions were measured. The distribution of Ozone was not uniform and was in good agreement with the room model experiment.

Ito (2007) conducted experiments and carried out computational simulations to analyze Ozone distribution in model rooms with laminar and turbulent flow fields. A flat plate test chamber was used to obtain mass accommodation coefficients (reaction probability) for Ozone when it is adsorbed by different materials. A second experiment was conducted in a full size test chamber where different materials lined the walls. Ozone was introduced through the ventilation system and the adsorption of Ozone was monitored. Along with the second experiment, a computational study was conducted using a 2D grid to represent the 3D chamber with similar BCs. The walls of the 2D grid were set to have the same reaction probability as found in the flat plate test chamber experiments. Decent agreement was found between the CFD and experimental cases (~*10%* different).

Rim et al. (2009) studied the influence of chemical interactions at the human surface on BZ levels of reactants and products. In this paper, validated CFD was used to simulate an occupant in a ventilated room where the BZ levels of Ozone were measured. To validate the CFD model a cylindrical human simulator was used in an environmental stainless steel chamber. Different ventilation rates were studied that ranged from *0.7* and *0.9* ACH and the Ozone concentration was determined. For the experimental setup the Ozone decay rate, air exchange rate, Ozone removal rate and deposition velocity of Ozone was determined. The deposition velocity was found for the same CFD setup for three different grids (the size of the first cell height varied) and the difference between the CFD and experiments were found. For the CFD calculations the heated cylinder is assumed to be a perfect sink of Ozone. The percent difference varied from *15-38 %*. It was found that the cell size distribution moderately affects the velocity and concentration profiles when Neumann thermal BCs are used. It is noted that the differences between the experimental and CFD are greater than the experimental error but are determined sufficiently accurate to give insight into Ozone mass transfer in the vicinity of an occupant. With the results of the validation setup a more detailed manikin was used to determine the BZ Ozone and product concentrations. It was found that large concentration gradients occur between BZ and bulk air with a ceiling supply. It was concluded that micro-environment measurements alone should not be used to assess the intake of Ozone.

1.2.5 Fluid Jets

Jet flow characteristics are widely studied for a variety of applications. For this work, the PV system consists of a nozzle that produces a low Reynolds number (Re) jet aimed toward an occupants BZ. For this type of PV, a fluid jet is responsible for delivering fresh air to the BZ. The potential core length of a jet determines the distance that 100% fresh air can reach and the elongation of the potential core is important for the performance of these systems. The critical Re for transition to turbulence in jet flow is ~2,300; however, Re dependence and nature of dependence for turbulent, transitional and laminar jets are still debated. Ricou and Spalding (1961) reported that beyond a Re of *20,000* the jet entrainment becomes constant or independent of Re. Above a Re of *20,000* it is found that the potential core length is 4-5 nozzle diameters (4-5D) in length (Bogey & Bailly, 2006; Lee et al., 1997). However, there are authors that have found Re dependence for high Re. For lower Re the published data is even less consistent. Kwon & Seo (2005) reported that the length of the potential core decreased as the Re increased for Re of *177-5,142*. Bogey & Bailly (2006) also showed a decrease in potential core length with increasing Re for Re of *1,700* to *400,000*. This trend was also shown by Todde et al. (2009) for Re of *850* to *6,750* and by Fellouah et al. (2009) for Re of *6,000* to *30,000* and Xia & Lam (2009) for Re of *1000* to *5000.* An opposite trend was found by Abdel-Rahman et al. (1996) where they found the potential core length got longer with increasing Re from *1,430* to *19,400.* An opposite trend was also shown for Re of *11,000* to *50,000* by Lee et al. (1997) and Symons & Labus (1971) found no dependence for Re of *255* to *1839.* Nottage showed an increasing potential core length for a Re of *6,000* to *30,000* and a constant potential core length for Re above *30,000* (Awbi, 2007). The discrepancy of the Re dependence of potential core lengths in jets could be due to the varying transition point of laminar to turbulent jets. For laminar and transitional jets, the potential core length increases with decreasing Re (Todde et al., 2009; Xia & Lam, 2009; Kwon & Seo, 2005; Bogey & Bailly, 2006) and for turbulent jets, the potential core length decreases with decreasing Re (Lee et al., 1997; Awbi, 2007). Kuethe & Schetzer (1959) reported laminar flows at Re of up to *40,000*, however this is very unlikely in uncontrolled situations and can turn turbulent with the slightest disturbance. They showed that the transition to turbulence usually occurs around *2,000*.

Abdel-Rahman et al. (1996) studied the near-field characteristics of circular jets at low Reynolds numbers. This paper uses experiments to investigate the effect of Reynolds number on the near-field region of circular, turbulent jets. It was found that the Reynolds number had a strong effect on the jet flow behavior in the near-field region, in fact, the centerline velocity decays faster and the potential core is sorter for lower Reynolds numbers.

Malmstrom et al. (1997) studied the centerline velocity decay measurements in low-velocity axisymmetric jets. Low-velocity, isothermal, axisymmetric jets from different diameter nozzles were used to measure velocity profiles and examine the dependence of the diffusion of the jet on the outlet conditions. It was found that when the velocity decreased the centerline velocity decay coefficient also decreased when the velocities were less than *6 m/s*.

Papodopoulos et al. (1999) studded a generic centerline velocity decay curve for initially turbulent axisymmetric jets. This paper gives normalized centerline velocity decay and normalized centerline turbulent intensity for different Reynolds numbers, and calculates the virtual origin for a constant density axisymmetric jet with a non-uniform velocity distribution from experimental data.

Mi et al. (2001) studied the influence of jet exit conditions on the passive scalar field of an axisymmetric free jet. This paper investigates the influence of initial flow conditions on the passive scalar fields of a turbulent free jet from a round nozzle. Two sets of initial conditions were compared and significant differences were found between the flows from the two nozzles. This paper gives different centerline velocity decay coefficients and jet speed coefficients for different Reynolds numbers.

Xu et al. (2002) studied the effect of different initial conditions on a turbulent round free jet. This paper studied the difference of a jet exiting from a smooth contraction nozzle and from a long pipe with fully developed flow with the same Reynolds number. The exit mean velocities are given and are shown to be different. Centerline velocity decay, development of turbulent intensities and mean velocity radial profiles are given.

Other initial conditions have also been shown to have an effect on the properties of turbulent jets. Burattini et al. (2004) showed a lengthening of the potential core from 4D to 6D by the use of a screen in the nozzle exit to reduce turbulence for a Re of *47,000*. Mi et al. (2001) showed a dependence upon initial conditions, specifically the jet exit velocity profile. The results showed that the entire flow field was influenced by the initial conditions for a Re of *16,000*. Xu & Antonia (2002) also showed an effect of the jet nozzle exit type for a Re of *86,000*. Ball & Pollard (2008) gives a comprehensive review of the studies performed on a turbulent round jet.

1.3 Necessary Research

The review of the existing work shows the need for new research, while showing the level of detail required to achieve reliable computational results:

1. While many studies cover a broad range of PV concepts, there is a need for a detailed analysis of an energy neutral PV system that can penetrate the rising thermal plume in realistic configurational setups.
2. The research has shown a complex airflow patterns within the indoor environment, specifically in the BZ, characterized by the interaction of forced and natural convection, geometry and breathing. To study inhalation exposure under typical indoor scenarios, the research has shown that attention must be paid to these details for simulation purposes.
3. Although the use of a block CSP was found acceptable for large scale modeling, research has shown that specific details of a CSP (legs, shoulders and head) must be included for simulations. Further, accounting for the correct surface heat transfer of CSPs are necessary, while a better understanding of simplified thermal modeling methods needs to be pursued.
4. While many experimental/computational studies have been undertaken to better understand indoor chemical reactions, most studies do not include a

detailed occupant or the presence of an occupant at all. Of the limited computational studies, most do not include a CSP. The computational studies that do include an occupant often simulate hypothetical reactions or use a simplified BC to represent indoor reactions. This, along with the above statements, furthers necessitates the need for a validated computational model to assess inhalation exposure in the indoor environment to avoid expensive experimental modeling.

1.4 Objectives and Scopes

In order to reach the final goal described previously, there were two main objectives of this work:

1. Develop and validate a CFD Model of the Syracuse University's personal environmental laboratory (PEL).
2. Assess the performance of PV for a range of exposure scenarios.

Through the validation process, many intermediate studies needed to be conducted to determine the importance of certain computational modeling parameters, including:

1.a. Grid sensitivity, topology and geometry considerations and Turbulent Schmidt number.

1.b. The effect of nozzle exit BC's such as turbulence intensity and length scale, flow rate and temperature.

1.c. The effect of CSP BC's such as temperature and moisture.

1.d. The effect of different breathing simulation methods, including steady state no breathing, steady state inhalation, unsteady sinusoidal breathing and an unsteady realistic profile.

1.e. Radiation modeling method.

1.f. The accuracy of modeled reaction probabilities, 1st order reaction constants and 2nd order reaction constants.

To assess PV, a wide range of indoor scenarios were modeled including:

2.a. Occupant exposure to non-reacting sources in a typical office configuration.

2.b. Occupant exposure to non-reacting sources for different cubicle configurations to determine exposure away from the PV system and cross contamination.

2.c. Occupant exposure to non-reacting sources for different PV configurations.

2.d. Occupant exposure to reacting sources involving 1st- and/or 2nd-order reactions (Hill, 1977) of VOCs emitted from the human body, clothing or from nearby emitting surfaces, and Ozone present in the room.

1.5 Diagram of Work

This thesis is divided into seven chapters, with each chapter describing a different aspect of this work. Chapter 1 gives the background information describing the problem along with the objectives of this thesis. Chapter 1 also gives a summary of existing studies relating to this thesis as well as the necessary research that still needs to be addressed. Chapter 2 goes on to describe the modeling considerations for the indoor environment. A brief description of the governing equations is given followed by more details describing the turbulence model, radiation, mass transport and post processing parameters.

Chapter 3 begins the computational validation for this thesis. First, the existing experimental work is described followed by the computational domain and setup used to match the experiment. In-depth details are given for grid development and the refinement needed in particular regions of the domain. Next, results are given describing the flow structures of the jet and thermal plume interaction region to show the complex nature of the problem being simulated and, finally, validation is shown for a series of modeling parameters and boundary conditions.

Chapter 4 continues the computational investigation with an in-depth analysis of the effect of different computational boundary conditions on the indoor air quality and model accuracy. The simulated boundary conditions include: 1) nozzle exit temperature, 2) nozzle exit turbulence, 3) nozzle flow rate, 4) CSP surface temperature, 5) CSP skin wittedness, 6) breathing simulation method and 7) radiation.

The thesis continues with Chapter 5 to assess indoor exposure to non-reacting sources. This chapter begins by introducing a novel method to model a species flux in Fluent. Next, iF is determined for indoor sources in a typical office setup and is further examined for multiple cubicles with and without the use of PV. This chapter closes by examining alternate placements of PV nozzles and the potential gain in air quality.

Chapter 6 proceeds with model validation with the validation of the Ozone/D-limonene reaction and Ozone/Squalene reaction. Existing experimental data is given and compared to simulated CFD results. The validated model is then used to examine inhalation exposure for a typical office space. This thesis then closes with conclusions in Chapter 7.

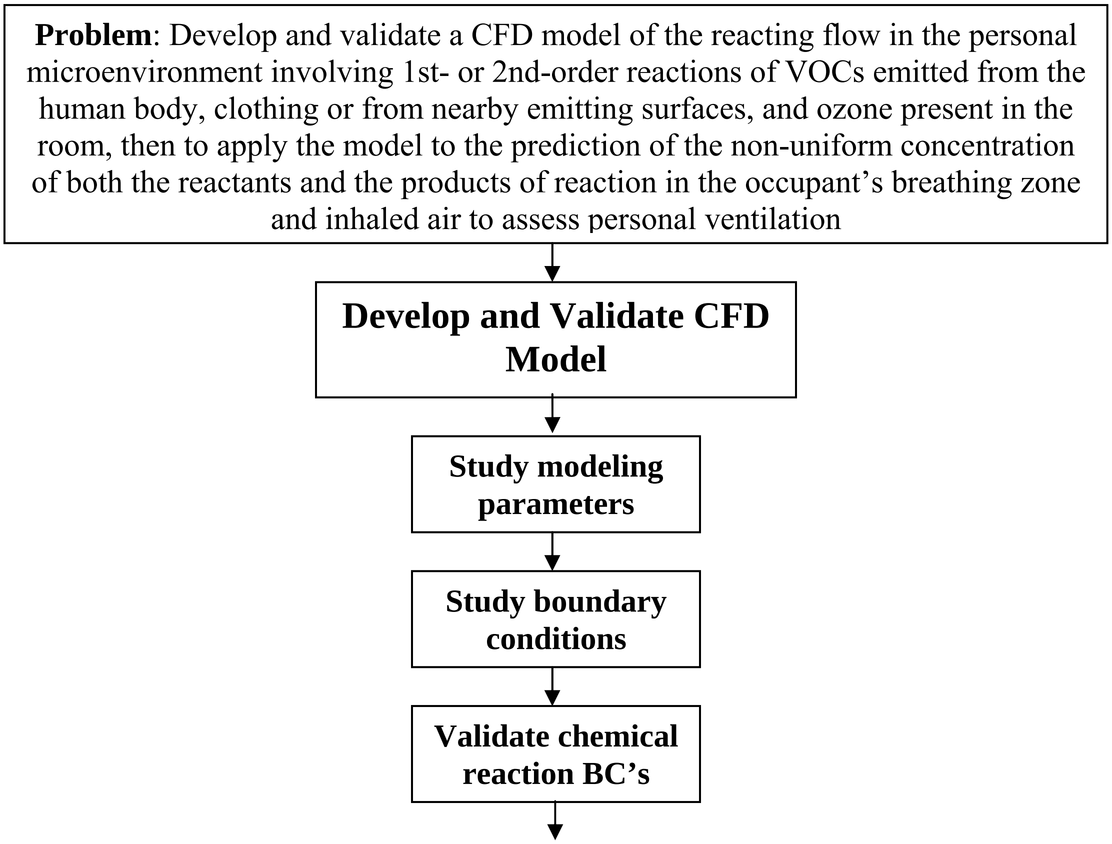

Problem: Develop and validate a CFD model of the reacting flow in the personal microenvironment involving 1st- or 2nd-order reactions of VOCs emitted from the human body, clothing or from nearby emitting surfaces, and ozone present in the room, then to apply the model to the prediction of the non-uniform concentration of both the reactants and the products of reaction in the occupant's breathing zone and inhaled air to assess personal ventilation

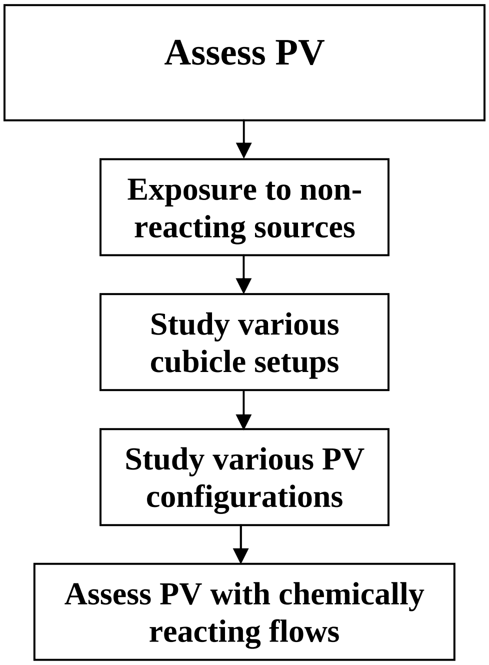

1.6 *Importance of Work*

With the majority of the time of the average American spent indoors, the quality of indoor air is a major concern. The two PV nozzles studied for this work increase indoor air quality in the BZ without increase energy consumption, with the novel Co-flow nozzle exhibiting superior performance. Recent work has linked Ozone reaction products in the indoor environment to multiple health hazards. With this in mind, a detailed computational study is proposed to investigate inhalation exposure from indoor chemical reactions and to assess the benefit of PV systems to reduce this inhalation exposure. This research produced significant results such as the development of a validated CFD model that can accurately predict the trajectories of PV jets in conjunction with the rising thermal plume and accurately capture the transport of 1st and 2nd order reaction products in the BZ of a CSP.

2 Modeling Considerations for the Indoor Environment

In the indoor environment, complex flows emerge with the existence of air movement from two main sources; forced convection (ventilation systems) and natural convection (buoyancy driven flows from temperature gradients, i.e. human body, computer etc.) Further, the addition of chemical reactions to these flows adds another order to the difficulty of the problem. The influence of these factors on inhalation exposure needs to be understood to a further degree to make qualified conclusions about the indoor environment. To do this, proper physics and chemistry needs to be applied.

To describe turbulent reacting flows, the basic equations that are used are the Navier-Stokes equations with the inclusion of chemical reactions and species conservation. In the indoor environment the concentrations of reactants and products is very low (ppm-ppb). This implies that the frequency time of molecular collisions is low. Because of this, there have been challenges to the applicability of the Navier-Stokes equations to hightly dilute mixtures, but for this work we adopt the Navier-Stokes equations as the underlying equations for turbulent reacting flows. With turbulent reacting gases, buoyant convection due to density differences is important. Density changes can be significant with the heat release from chemically reacting gases and leads to full interaction between turbulence and chemistry. This means that the turbulence influences the chemical behavior and the heat released with the exothermic chemical reactions alters the turbulence. However, for this work the concentrations of the reacting gases is on the order of ppb and it is assumed that these reactions do not affect the flow field (heat release from chemical reactions is not modeled).

The conservation equations for mass, momentum and energy for a multi-component, weakly reacting, gas mixture are the first step to describing these flows. In the indoor environment, simplifications can be made to these equations.

Conservation of Mass

For Mass conservation, incompressibility (constant density) can be assumed in the indoor environment where there are low velocities and air is at standard temperature and pressure. To assume incompressible flow, the Mach number (u/c where c is the speed of sound in the fluid) needs to be less than *0.3*. In the indoor environment, typical velocities range from *0-1 m/s* and the speed of sound in air is *346 m/s*, which results in a Mach number of *0.0029*. Mass conservation has two meanings when dealing with chemical reactions. First, overall mass conservation for the gas mixture leads to the continuity equation; second, conservation of individual species includes accumulation, convection, diffusion and creation or destruction by chemical reactions. Conservation of mass is given as:

$$\frac{\partial \rho}{\partial t} + \frac{\partial}{\partial x_k}(\rho u_k) = 0 \qquad (2.1)$$

where ρ is the mixture density and u is the velocity.

The RANS conservation equations for chemical species is given as,

$$\frac{\partial}{\partial t}(\rho Y_i)+\frac{\partial}{\partial x_k}(\rho u_k Y_i)=\frac{\partial}{\partial x_k}\left(\rho D_i+\frac{\mu_t}{Sc_t}\right)\frac{\partial Y_i}{\partial x_k}+R_i+S_i \tag{2.2}$$

where Y_i is the local mass fraction of species i, $\mathrm{R_i}$ is the net rate of volumetric production of species i by chemical reactions and S_i is an additional volumetric source terms for species i. For a total of N species, only N-1 specie equations will be solved since the mass fraction of the species must sum to unity, resulting in the mass fraction of the Nth specie to be determined by one minus the sum of the N-1 solved mass fractions.

Conservation of Momentum

Conservation of momentum is given as:

$$\frac{\partial}{\partial t}(\rho u_j)+\frac{\partial}{\partial x_k}(\rho u_k u_j)=-\frac{\partial p}{\partial x_j}+g_j+\frac{\partial}{\partial x_k}\left(\mu_{eff}\frac{\partial u_j}{\partial x_k}+\mu_{eff}\frac{\partial u_k}{\partial u_j}-\frac{2}{3}\left(\mu_{eff}\delta_{kj}\frac{\partial u_l}{\partial x_l}\right)\right) \tag{2.3}$$

where μ_{eff} is the effective viscosity (includes both molecular and turbulent viscosity) of the mixture, p is the hydrostatic pressure, g_i is the body force in direction i and Kronecker delta: $\delta_{ij}=1$ if $i=j$ and $=0$ if $i\neq j$. The subscript k and j indicate quantities associated with the coordinate directions. For incompressible flow, $\partial u_k/\partial u_k = 0$ therefore this term drops out of Equation (2.3). Although density changes are important for buoyancy calculations, the assumption of incompressibility can also be applied here. In the indoor environment, natural convection is very important because of to density differences from the presence of temperature differences between the room air and the human body or any other warm and cold objects. To determine if the flow from natural convection is important, Archimedes number is considered. Archimedes number, which is the ratio of the buoyancy to inertia forces (Grashoff number (Gr) and the square of the Reynolds number (Re)), is given as:

$$Ar = \frac{Gr}{\mathrm{Re}^2} = \frac{g\beta \Delta TL}{u^2} \tag{2.4}$$

where g is the acceleration due to gravity, β is the volumetric thermal expansion coefficient, $\triangle T$ is the temperature difference between the human body and surrounding air and L is a typical length scale (e.g. person's height). Archimedes numbers close to or greater than *1* show that thermal buoyancy is as important as inertia forces. Typical indoor values of Ar are around *10* or higher, which shows a strong influence of natural convection on the flow in the room and therefore it must not be ignored.

To model density differences, while still assuming incompressibility, density is modeled using the so called Incompressible Ideal Gas Law. In Fluent, the incompressible ideal gas law can be used when pressure variations are small enough that the flow is fully incompressible and the ideal gas law is used to illustrate the relationship between density and temperature. With density being modeled this way the solver will compute density as:

$$\rho = \frac{p_{op}}{\frac{R}{M_w}T} \tag{2.5}$$

where p_{op} is the operating pressure, R is the universal gas constant and M_w is the molecular weight of the gas. This allows density to only be dependent on the operating pressure and not the local relative pressure field, i.e., density is expressed as a function of temperature only. With the application of incompressibility, constant properties, gravity as the only body force and the use of the incompressible ideal gas law, the conservation of momentum equation can be simplified as:

$$\frac{\partial}{\partial t}(u_j) + \frac{\partial}{\partial x_k}(u_k u_j) = -\frac{1}{\rho}\frac{\partial p}{\partial x_j} + \frac{\mu_{eff}}{\rho}\frac{\partial^2 u_j}{\partial x_k^2} - \frac{p_{op}}{\frac{R}{M_w}T} g_j \tag{2.6}$$

Another common way to include buoyancy in the incompressible flow simulation is through the Boussinesq approximation. The Boussinesq approximation assumes changes in density only in the body force term of the momentum equation where the change is a function of temperature given by,

$$\rho \approx \rho_0 (1 - \beta \Delta T) \tag{2.7}$$

The original intention of the Boussinesq approximation was for the use of buoyancy driven flows in an infinite domain where the operating temperature can be defined by the bulk fluid temperature. This approximation works acceptably well in wall bounded flows where there is minimal gradients in the bulk flow, but the Boussinesq approximation can lead to convergence difficulties in CFD simulations and was not considered for this work (Dygert, 2010).

Conservation of Energy

Conservation of energy can be written in many forms with static temperature, static enthalpy, stagnation enthalpy or internal energy as the principal variable. The energy equation solved by Fluent is given as:

$$\frac{\partial}{\partial t}(\rho E)+\nabla\cdot(\vec{u}(\rho E+p))=\nabla\cdot\left(k_{eff}\nabla T-\sum_{j}h_{j}\overrightarrow{J_{j}}+(\bar{\bar{\tau}}_{eff}\cdot\vec{u})\right)+S_{h} \tag{2.8}$$

where k_{eff} is the effective thermal conductivity of the gas mixture, J_j is the diffusion flux of species *j*, $\left(\mathrm{J}_{\mathrm{j}}=-\rho D_{j}\frac{\partial Y_{i}}{\partial x_{j}}\right)$ where Y_j is the mass fraction of species *j* and S_h is the heat from any chemical reactions or any other defined heat sources, which is not included in this work. The first term on the RHS of the equation is the energy transfer due to conduction, the second term on the RHS of the equation is the energy transfer due to species diffusion and the third term on the RHS of the equation is the viscous dissipation term. And,

$$E = h - \frac{p}{\rho} + \frac{v^2}{2} \tag{2.9}$$

where sensible enthalpy h is defined for ideal gases as,

$$h = \sum_j Y_j e_j + \frac{p}{\rho} \tag{2.10}$$

for incompressible flows, where

$$e_j = c_p (T - T_{ref}) \tag{2.11}$$

where T_{ref} is *298.15 K*.

The heat conduction term can be shown to equal:

$$k_{eff} \frac{\partial T}{\partial x_k} = \frac{\mu_{eff}}{\Pr_{eff}} \frac{\partial h}{\partial x_k} - \frac{\mu_{eff}}{\Pr_{eff}} \sum_i h_i \frac{\partial Y_i}{\partial x_k} \tag{2.12}$$

where $\Pr_{eff}$ is the effective Prandtl number ($\Pr_{eff}=\mu_{eff}c_p/k_{eff}$, where c_p is the specific heat at constant pressure).

Viscous dissipation is neglected because it is small in low speed flow. Also when using the pressure based solver the pressure work and kinetic energy are neglected based on the assumption of incompressible flow. With these simplifications and since we are dealing with low-speed flows, the conservation of energy equation, in terms of static enthalpy, is given as:

$$\frac{\partial}{\partial t}(\rho h)+\frac{\partial}{\partial x_k}(\rho u_k h)=\frac{\partial}{\partial x_k}\left[\frac{\mu_{eff}}{\Pr}\frac{\partial h}{\partial x_k}+\mu_{eff}\left(\frac{1}{Sc}-\frac{1}{\Pr}\right)\sum_{i=1}^{N}h_i\frac{\partial Y_i}{\partial x_k}\right] \qquad (2.13)$$

where, *Sc* is the Schmidt number ($Sc=\nu/D$, which is the measure of the relative importance of viscous and diffusional properties of a gas, *D* is the diffusion coefficient), and. It is often the case where $Sc \approx \Pr$ so that $(1/Sc-1/\Pr)=1$, which simplifies this equation. It should also be noted that viscous dissipation is neglected since it is negligible in low speed flows. This equation also omits the $\partial p/\partial t$ term based on the assumption of low Mach number.

2.1 Turbulence Model

Turbulence is characterized by chaotic, stochastic property changes in fluid flows where fluid particles rapidly mix due to random three-dimensional velocity fluctuations. The velocity fluctuations mix transported properties like momentum, energy and species concentration which causes the transported quantities to fluctuate as well. Since the mixing and the fluctuations can be of small scales simulating turbulence can become very computationally expensive. To get around this, the exact governing equations are time-averaged, ensemble-averaged or manipulated to remove the small scales. With the modified equations there are more variables and therefore there is a need for turbulence models to determining the additional variables in terms of known quantities known as closure. Turbulence models are simpler mathematical models used to physically model the full Navier-Stokes Equations to predict turbulence. In this approach, it is assumed that the stochastic motions average to zero over a sufficiently long period of time which results in the mean value. The turbulent model used for this work is a Reynolds Averaged Navier-Stokes (RANS) models. When considering turbulence and natural convection, one must analyse the non-dimensional Rayleigh number to estimate the onset of turbulence. Transition from laminar to turbulent flow is known to occur at Rayleigh numbers of order 10^9-10^{10}. Absent of forced convection, the Rayleigh number is given as,

$$Ra = \frac{g\beta\Delta TL^3}{\nu\alpha} \tag{2.14}$$

where α is the thermal diffusivity and ν is the kinematic viscosity of air at the desired temperature (2.4×10^{-5} and 1.6×10^{-5} m^2/s, respectively). Using typical indoor values as done for the calculation of Archimedes number, a Rayleigh number of 2×10^9 is found, indicating the flow may be transitional. The majority of available turbulent models are not equipped to handle both transitional and turbulent flow, therefore, fully turbulent flow is used for this work, specifically RANS models.

For modeling a computer simulated person (CSP) in the indoor environment, researchers have used a wide range of turbulence models including the standard *k-ε* model (Gao and Niu, 2004; Hayashi et al. 2002; Sideroff and Dang, 2008), the RNG *k-ε* model, (Gao and Niu, 2006; Khalifa et al., 2006), the realizable *k-ε* model (Russo et al., 2009) and the SST *k-ω* model (Deevy et al., 2008). Zhai et al. (2007) and Zhang et al. (2007) studied CFD validation using benchmark cases to represent the indoor environment with mean velocity, temperature and turbulent quantities. The results of this work concluded that the *k-ε* turbulence models performed reasonable well when predicting the mean flow quantities, but the results were problem dependent. Since this research also includes jet flow, the recommendation of Shih et al. (1995) was followed and the Realizable *k-ε* turbulence model was used along with the enhanced wall treatment option. The Realizable *k-ε* model provides superior prediction of the spread of both planar and round jets. The modeled transport equation for *k* in the *k-ε* turbulence model is given as,

$$\frac{\partial}{\partial x_j}(\rho k u_j) = \frac{\partial}{\partial x_j}\left[\left(\mu + \frac{\mu_t}{\sigma_k}\right)\frac{\partial k}{\partial x_j}\right] - \rho\overline{u_i' u_j'}\frac{\partial u_j}{\partial x_i} + \beta g_i \frac{\mu_t}{\mathrm{Pr}_t}\frac{\partial T}{\partial x_i} - \rho\varepsilon \qquad (2.15)$$

where ρ is the fluid density, k is the turbulent kinetic energy, ε is trubulent dissipation, u_j are the mean velocity components, μ is the molecular dynamic viscosity, μ_t is the turbulent viscosity, β is the coefficient of thermal expansion, g_i is gravitational acceleration in direction i, T is temperature, Pr_t is the turbulent Prandtl number for energy, and σ_k and σ_ε are the turbulent Prandtl numbers for k and ε, respectively. The left hand side (LHS) represents the advection terms, the first term on the right-hand-side (RHS) represents the diffusion of k by both molecular and turbulent viscosities, the 2nd term on the RHS is the production of *k* by the mean flow shear, the 3^{rd} term is the production of *k* by buoyancy effects, and the last term is the *k* dissipation by turbulence.

It is noted that this equation is the same equation solved for both the Standard k-ε turbulence model and RNG k-ε turbulence model. The improvement over these other two models comes through the model constants and the development of a new ε equation. The term “realizable” from the Realizable k-ε model means that the model mathematically satisfies the physics of turbulent flows. Specifically, the normal Reynolds stress term must always be positive and this was achieved by changing the standard eddy viscosity model constant (C_μ) from a constant to one that is related to the mean strain rate (Shih et al., 1995). To understand this, the expression for the normal Reynolds stress in an incompressible strained mean flow is given as,

$$\overline{u^2} = \frac{2}{3}k - 2\frac{\mu_t}{\rho}\frac{\partial u}{\partial x} \tag{2.16}$$

and by definition is a positive quantity.

The turbulent viscosity, μ_t, is computed by combining *k* and □ as,

$$\mu_t = \rho C_\mu \frac{k^2}{\varepsilon} \tag{2.17}$$

Equation 2.4 could become negative or “non-realizable” when the strain is large enough or when the second term on the RHS (includes the standard eddy viscosity model constant, C_μ) of the Reynolds stress equation is larger than the first term on the RHS. To overcome this, the Realizable *k-ε* model models C_μ, as variable to the mean flow and turbulence. The standard eddy viscosity model constant, C_μ, is defined as,

$$C_\mu = \frac{1}{A_0 + A_s \dfrac{ku^*}{\varepsilon}} \tag{2.18}$$

where, A_0 and A_s are model constants and,

$$u^* \equiv \sqrt{S_{ij}S_{ij} + \overline{\Omega}_{ij}\overline{\Omega}_{ij}} \quad , \overline{\Omega}_{ij} = \overline{\Omega_{ij}} - 3\varepsilon_{ijk}\omega_k \text{ and } S_{ij} = \frac{1}{2}(u_{i,j} - u_{j,i}) \tag{2.19}$$

where, $\overline{\Omega_{ij}}$ is the mean rate-of-rotation tensor viewed in a rotating reference frame with angular velocity ω_k.

Further improvement of the Realizable *k-ε* model is through the modeling of the □ equation which, for standard models, does not always give the appropriate length scale for turbulence. A specific flaw of other turbulence models in regard to this research is the anomaly of the spreading rate of planar jets versus a round jet. This anomaly is mainly due to the model dissipation rate equation and was improved to predict complex turbulent flows (Shih et al., 1995). The transport equation for □ for the Realizable *k*-*ε* model given as,

$$\frac{\partial}{\partial x_j}(\rho \varepsilon u_j) = \frac{\partial}{\partial x_j}\left[\left(\mu + \frac{\mu_t}{\sigma_\varepsilon}\right)\frac{\partial \varepsilon}{\partial x_j}\right] - \rho C_1 S_\varepsilon + \rho C_2 \frac{\varepsilon^2}{k + \sqrt{\nu \varepsilon}} + C_{1\varepsilon}\frac{\varepsilon}{k} C_{3\varepsilon} \beta g_i \frac{\mu_t}{\Pr_t}\frac{\partial T}{\partial x_i} \qquad (2.20)$$

where $C_1 = \max\left[0.43, \frac{\eta}{\eta + 5}\right]$, $\eta = S\frac{k}{\varepsilon}$, $S = \sqrt{2S_{ij}S_{ij}}$ and C_2, $C_{1\varepsilon}$ and $C_{3\varepsilon}$ are model constants.

The LHS of the ε equation represents the advection terms, the first term on the right-hand-side (RHS) represents the diffusion of *ε* by both molecular and turbulent viscosities, the 2nd term on the RHS is the production of *ε*, and the 3rd term is the destruction of *ε* by buoyancy effects. The first major difference with this equation compared to other models is that the Reynolds stresses do not appear in the dissipation equation which makes this model more robust than the standard model when used with second-order closure schemes, since the means strain rate, S, normally behaves better than the Reynolds stresses in numerical calculations. This allows for better prediction of the spread of both planar and round jets. A second improvement is that the production term (second term on the RHS) does not involve the production of *k*, which is based on the concept of spectral energy transfer. Also, this equation does not have any singularities in the destruction term, that is, even if *k* vanishes or becomes smaller than zero there will be no singularities with the elimination of *k* in the denominator.

When modeling in Fluent, the enhanced wall treatment option was used in conjunction with the Realizable *k-ε* model. This is a near-wall modeling approach that combines a two-layer model with enhanced wall functions. If the height of the first cell height is fine enough ($y^+ \sim 1$) the two layer model is used and the enhanced wall treatment allows the realizable *k-ε* model to resolve the laminar sublayer without the need for a wall function. However, in regions where the viscous sublayer is not fully resolved ($3 < y^+ < 10$) an enhanced wall function is used, which blends the turbulent law of the wall with the viscous sublayer law to model the boundary layer near the wall.

2.2 *Radiation*

It is common practice to neglect radiative heat transfer and only include ~half the heat transfer from the human body through convective heat transfer in the indoor environment to avoid perceived difficulties associated with radiation calculations. With small temperature differences and strong forced convection, the heat transfer into and out of a space is dominated by convection and neglecting radiation may be warranted; however, this may not be the case for the indoor environment and radiation may play a significant roll. Simply neglecting half the heat loss can be in error due to the non-linear coupling of radiant and convective surface heat transfer. In its simplest form, Convective heat transfer is given as,

$$q_{conv} = h(T_{wall} - T_{ref}) \tag{2.21}$$

where h is the heat transfer coefficient, T_{wall} is a typical skin temperature and T_{ref} is the supply air temperature entering the domain. Radiative heat transfer in its simplest form,

$$q_{rad} = \sigma(T_{wall}^4 - T_{ref}^4) \tag{2.22}$$

where σ is the Stefan-Boltzmann constant.

For this work, radiative heat-absorption in air is ignored and we view radiation as a surface phenomenon. To compute the balance of incoming and outgoing radiation at a surface, certain radiative properties are required which include surface emissivity, absorptivity and reflectivity for an opaque surface. Emissivity, ϵ, may be defined as the ratio of radiation emitted by the surface to the radiation emitted by a blackbody at the same temperature . Absorptivity, α, is a property that determines the fraction of the irradiation absorbed by a surface. Reflectivity, κ, determines the fraction of the incident radiation reflected by a surface. Determinations of these properties are difficult because they are characterized by directional and spectral dependence and assumptions must be made. The first is to assume that a surface is diffuse, which means the properties independent of direction. Also, the modeled surfaces are assumed to be gray surfaces which are defined as surfaces for which ϵ and α are independent of wavelength over the spectral regions of the irradiation and the surface emission. With these assumptions, Kirchoff's Law can be obtained where ϵ = α, or the total emissivity of the surface is equal to its total absorptivity (Incropera, 2007).

The net radiation at a surface is described by,

$$q_{rad,i} = A_i(J_i - G_i) \tag{2.23}$$

where A_i is area of surface i, J_i is radiosity defined by $J_i \equiv E_i + \kappa_i G_i$, where E_i is the emissive power and G_i is the irradiation. To analyze radiative exchange between two or more surfaces geometrical features of the radiation exchange are first established by developing the notion of a view factor, F_{ij}. F_{ij} is defined as the fraction of the radiation leaving surface i that is intercepted by surface j. The radiosity of all the surfaces examined are used to evaluate the irradiation of surface i, given as,

$$A_i G_i = \sum_{j=1}^{N} F_{ji} A_j J_j \tag{2.24}$$

and using the reciprocity relation where $A_iF_{ij}=A_jF_{ji}$, this can be rewritten as

$$A_i G_i = \sum_{j=1}^{N} F_{ij} A_i J_j \tag{2.25}$$

with the cancelation of A_i and substituting into the equation for the net radiation,

$$q_{rad,i} = A_i\left(J_i - \sum_{j=1}^{N} F_{ij} J_j\right) \tag{2.26}$$

and using the summation rule it can be shown that the net radiation is given by (Incropera and DeWitt, 2002),

$$q_{rad,i} = \sum_{j=1}^{N} A_i F_{ij} (J_i - J_j) \tag{2.27}$$

which equates the net rate of radiation transfer from surface i, q_i, to the sum of components q_{ij} related to radiative exchange with other surfaces.

In Fluent, radiation was simulated using the Surface to Surface model where the energy flux leaving a given surface is composed of directly emitted and reflected energy and the amount of incident energy on a surface from another surface is a direct function of the surface-to-surface view factor (described previously). Fluent computes the surface-to-surface radiant energy flux from a system of N x N equations (N is the number of participating surface elements, which was the number of triangles on the interior surface mesh). To solve this system of equations, N^2 view factors (depend on geometry) are needed and are computed prior to the simulation.

2.3 Mass Transport

2.3.1 Species Transport

The conservation equation for chemical species is given by equation 2.2. The turbulent diffusivity for species transport is derived from the eddy diffusivity using the turbulent

Schmidt number (Sc_t), which is has been previously defined. It has been shown that using a Sc_t of 0.9 to 1.0 produces better agreement of the computational results with experimental data (Sorensen and Weschler, 2002; Gadgil et al., 2003; Yang et al., 1998; and Yang et al, 2001).

When solving the conservation of chemical species in Fluent, R_i of equation 2.2 is determined by Arrhenius expression,

$$R_i = M_{w,i} \sum_{r=1}^{N_R} \hat{R}_{i,r} \tag{2.28}$$

where $M_{w,i}$ is the molecular weight of species i and $\hat{R}_{i,r}$ is the Arrhenius molar rate of creation/destruction of species in reaction r.

For a forward reaction the molar rate of creation/destruction of species i in reaction r is given as,

$$\hat{R}_{i,r} = \Gamma(v''_{i,r} - v'_{i,r}) \left(k_{f,r} \prod_{j=1}^{N} (C_{j,r})^{(\eta'_{j,r} + \eta''_{j,r})} \right) \tag{2.29}$$

where Γ is the net effect of third bodies, v_{ir}' is the stoichiometric coefficient of reactant i, v_{ir}'' is the stoichiometric coefficient of product i, $k_{f,r}$ is the forward rate constant of the reaction, $C_{j,r}$ is the molar concentration (kgmol/m^3) of species j in the reaction r, $\eta_{j,r}'$ is the rate exponent for the reactant specie j in reaction r and $\eta_{j,r}''$ is the rate exponent for the product species j in the reaction r.

The Arrhenius expression is given by,

$$k_{f,r} = A_r T^{\beta_r} e^{-E_r/RT} \tag{2.30}$$

where A_r is the pre-exponential factor, β_r is the temperature exponent, E_r is the activation energy for the reaction and R is the universal gas constant.

For bimolecular chemical reactions the second order reaction rate constant relates to the rate of change of reactants and products as,

$$\frac{d(C_P)}{dt} = -\frac{d[(C_A)}{dt} = -\frac{d(C_B)}{dt} = k_{f,r}(C_A)(C_B) \tag{2.31}$$

which describes the reaction of $A + B = P$. These relationships are included in the transport equations for species in Fluent.

The surface deposition of species in the indoor environment depends on the local concentration close to surfaces and the flux at the surface is given by (Cano-Ruiz et al. 1993),

$$J_s = -\gamma \frac{\langle v \rangle}{4} C(\Delta y) \tag{2.32}$$

where γ is the mass accommodation coefficient or reaction probability, $\langle v \rangle$ is the Boltzmann velocity for the chemical species, and $C(\Delta y)$ is the concentration at a distance from the surface equal to 2/3 of the mean molecular free path. The mean molecular free path ($6.5 \times 10^{-8}\ m$) is small compared to the grid size ($1 \times 10^{-3}\ m$) typically used in the indoor environment to resolve flow fields. To overcome the need to use such small scales an expression for the flux based on the first cell height was developed by Cano-Ruiz et al. (1993) and is given as,

$$J_s = \frac{-\gamma\langle v \rangle / 4}{1 + \left(\gamma\langle v \rangle / 4 / D_m\right)\Delta y_1} C\left(\Delta y_1\right) \tag{2.33}$$

This expression was used to determine the flux boundary condition to set on walls based on a reaction probability to predict wall adsorption.

To examine the relationship of reaction probability and mass transfer, overall resistance was examined. The overall resistance to mass transfer is given as,

$$\frac{1}{v_d} = \frac{1}{v_t} + \frac{4}{\langle v \rangle \gamma} \tag{2.34}$$

where v_d is the deposition velocity and v_t is the transport limited deposition velocity.

2.4 Post Processing

There are many parameters and indices that have been developed to quantify the quality of indoor air. For this work, two were chosen; one index to describe the quality of room air spatially and another to quantify inhaled air quality.

2.4.1 Air Quality Index

Air quality was examined using an Air Quality Index (AQI). Results of the species concentration were normalized to give AQI, defined as,

$$AQI = \frac{C_b - C_e}{C_p - C_e}, \tag{2.35}$$

where C_p is the species concentration at the clean air (primary) nozzle exit, C_e is species concentration in the exhaust, and C_b is the species concentration at a point in the BZ.

When $AQI = 1.0$, clean air is present at point b, and when $AQI = 0.0$, the air at point b is perfectly mixed (as it would be in an ideal mixing-ventilation system). AQI is related to ventilation effectiveness for contaminant removal (Awbi, 2003) by:

$$\varepsilon_v = \frac{C_p - C_e}{C_p - C_b} = \frac{1}{1 - AQI} . \tag{2.36}$$

We note that ε_v approaches infinity when fresh air is delivered to the BZ; which makes the use of this parameter awkward in cases where a PV system can deliver clean, fresh air to the BZ. Therefore, we used AQI in this thesis.

2.4.2 Intake Fraction

Air pollution is a serious concern in the indoor environment and many pollutants, some toxic, can be traced to indoor sources. Studying the transport of these pollutants and their effect on inhalation exposure in the indoor environment is useful when determining air pollution health risk assessment. Exposure to pollutants through inhalation can be expressed as an intake fraction (iF), which is defined as the integrated incremental intake of a pollutant released from a source or source category and summed over all exposed individuals during a given exposure time, per unit of emitted pollutant. iF is given by (Bennet et al., 2002):

$$iF = \frac{\sum Intake-of-pollution-by-an-individual-(mass)}{Rate-of-pollution-released-in-the-environment-(mass)} . \tag{2.37}$$

The rate of pollution released in the environment was calculated as $\dot{m}_{enters} \pm \dot{m}_{created}$. iF is one step in determining air pollution health risk assessment. Health risk assessment can be determined by multiplying the *iF* by a usage factor, emission factor and the toxicity of each pollutant considered (Nazaroff, 2008).

3 Development and Validation of the a CFD the Model

Validated CFD simulations can be employed to determine the effectiveness of a PV system more efficiently and cost effectively than through detailed experimental investigations of the flow, temperature, humidity and concentration fields in the occupied space. CFD-based tools can then be utilized to optimize the design of PV systems and their placement within the work space, especially the design and placement of novel energy-efficient PV systems that are aimed at achieving high BZ air quality with only a small fraction of the fresh air indicated by ASHRAE Standard 62.1-2004 (2004).

The quality of the air in the BZ of a person receiving fresh air through a directed PV jet is strongly affected by turbulent entrainment of the surrounding contaminated air in the jet's mixing region, as well as by the interaction of the PV jet with the human thermal plume and the room currents created by mixing or displacement general ventilation. The degree of entrainment is in turn affected by the design and exit conditions of the PV nozzle and general ventilation diffuser, and by the location of the PV nozzle and general ventilation diffuser relative to the person. While numerous experimental investigations of these factors have been carried out and yielded invaluable insights into the performance of a variety of PV configurations under a wide range of scenarios (Bolashikov et al. 2003; Faulkner et al. 1995, 1999, 2000, 2002; Fisk et al. 1990; Cermak et al. 2003, 2006; Kaczmarczyk et al. 2002; Melikov et al. 2001, 2004, 2006; Nielsen et al. 2005; Khalifa et al. 2008, 2009), the design of an effective PV system can be considerably advanced by employing validated, high-fidelity CFD techniques.

A detailed CFD model of a PV setup comprising of a PV nozzle, seated CSP and floor diffuser was developed. Then experimental tracer gas concentration data for the same setup was used to validate the CFD model. Specifically, we compared CFD results with the experimental results obtained with both a conventional round nozzle and a novel low-mixing Co-flow nozzle (Khalifa and Glauser, 2006) directing a PV fresh air jet toward the BZ of a seated thermal manikin in a thermally controlled chamber ventilated also by a floor diffuser behind the manikin. For validation we examined grid refinement, geometry and thermal BC's, turbulent Schmidt number and turbulence model.

3.1 Existing Experimental Configuration

The experimental set-up conditions and results from Khalifa et al. (2009) were used for validation of a CFD model. In the experiment, investigations of the design and performance characteristics of PV systems were studied. The PV systems satisfied acceptable ergonomic and aesthetic considerations and were studied in combination with general ventilation while delivering a fraction of fresh air (~*2.4 l/s*) indicated by ANSI/ASHRAE 62.1-2004. Two PV systems were compared for this study; a single jet PV system and a novel Co-flow nozzle design shown in Figure 3.1 and 3.2. The single jet PV system aims clean air at a person's BZ while a turbulent shear layer develops at the boundary of the jet, entraining polluted surrounding air. This causes mixing of polluted and clean air and a rapid erosion of the clean air potential core. For fresh air to be delivered directly to the BZ of a person with this system, the PV system would have to be in close proximity (≤ *4-5D*; *D* is the diameter of the nozzle) to the BZ, which is not always practical. The second PV system studied was invented by Khalifa and Glauser (2006) to overcome these challenges. The Co-flow nozzle was introduced as a novel low-mixing PV nozzle that can greatly lengthen the clean air potential core of a PV jet at low clean air flow rates. This nozzle consists of a primary nozzle surrounded by a concentric annular secondary nozzle. The concept of this nozzle is to deliver fresh air from the primary nozzle while delivering recirculated air from the secondary nozzle at nearly the same velocity as the primary clean air. By matching the exit velocities of the primary and secondary nozzles the shear stress at the primary jets boundary is greatly diminished. This reduces turbulent mixing at the interface between the primary and secondary which extends the primary jet's core much farther as shown in Figure 3.3.

In Khalifa et al. (2009), the two PV systems were tested in a full size, *2.0 x 2.6 x 2.5 m*, plexiglass chamber with a seated, real-size thermal manikin as shown in Figure 3.4 and 3.5. The thermal manikin used for the experiment represents a *1.8 m* tall average male. This manikin has 20 independently controlled segments that can be set to a desired skin temperature or heat flux. The manikin was not clothed for the experiment and was seated upright for testing with a constant surface temperature of *~32 ˚C*. The diameter of the primary nozzle was *50.8 mm* and the diameter of the secondary nozzle was *105.6 mm*. The PV nozzle was placed *0.41 m* from the manikin's nose, along the vertical symmetry plane of the manikin. A mixing box, located in the room, was used to deliver fresh air to the primary nozzle and recirculated air to the secondary nozzle and both nozzles were fitted with flow strengtheners and a set of two screens. General ventilation was also supplied to the chamber through a floor-mounted *0.23 x 0.24 m* four-way directional grill diffuser fed by a variable-air volume box in the under-floor plenum. The air supplied through the floor diffuser and secondary nozzle was seeded with SF_6. The exhaust of the chamber is through a *0.58 x 1.17 m* perforated ceiling outlet.

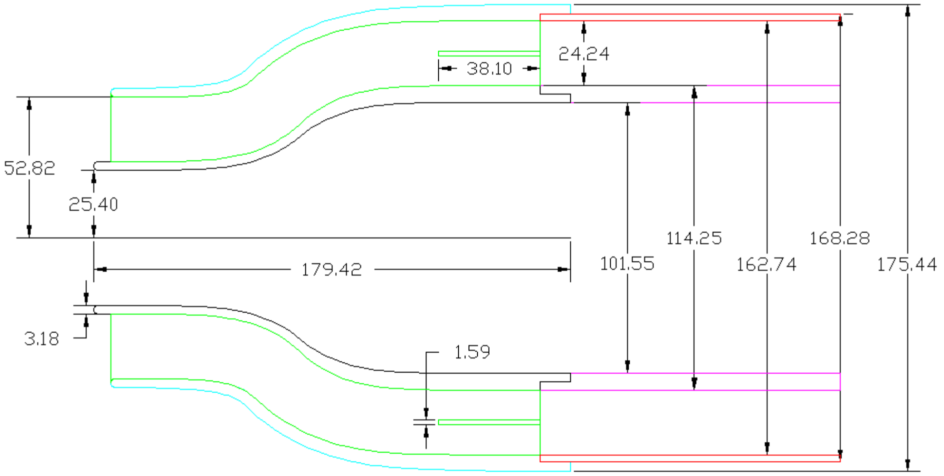

Figure 3.1: Low mixing co-flow nozzle design with dimensions (mm).

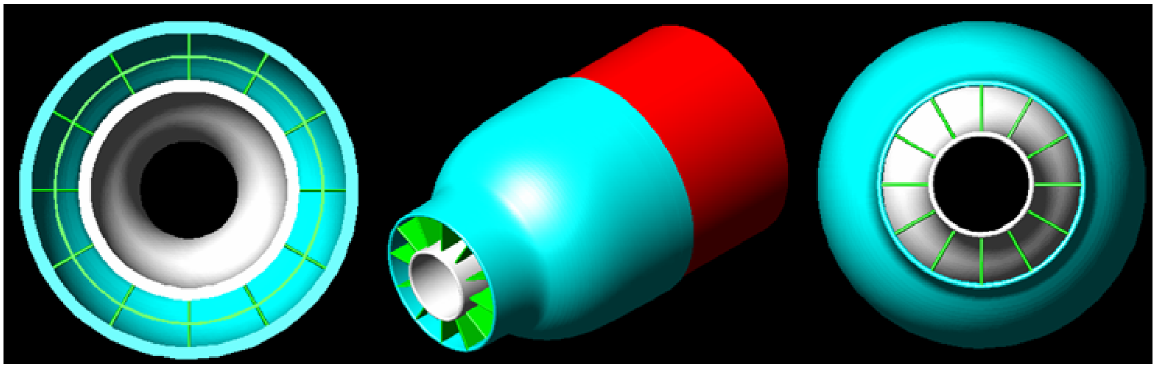

Figure 3.2: Three dimensional co-flow nozzle design.

Tracer gas measurements were taken within the BZ of the manikin at *10 mm* and *25 mm* from the tip of the nose for the single jet PV system and the Co-flow nozzle as shown in Figure 3.4 and 3.5. The primary nozzle delivered *2.4 l/s* of clean air, while a total of *18.9 l/s* were delivered to the room. When the secondary nozzle was active, *6.7 l/s* of seeded air were delivered through it, resulting in approximately the same exit velocity for the primary and secondary nozzles, and the floor diffuser flow was lowered by this amount. Concentration measurements were taken in the manikin's nose and mouth, in the primary nozzle, the secondary nozzle, in the under-floor plenum, and in the chamber exhaust. To measure the concentration of tracer gas in the BZ, six sampling probes were mounted on a vertical rake and were transversed vertically while recording tracer gas concentrations using a multi-gas monitor based on the photo-acoustic infrared detection method.

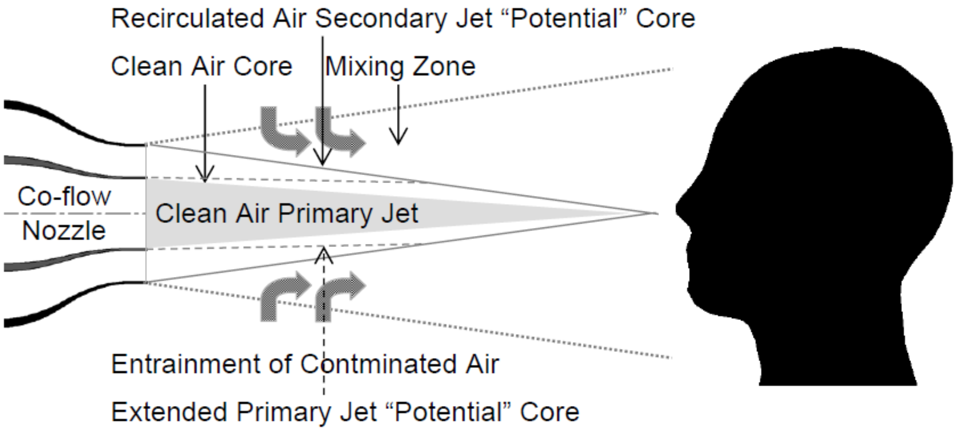

Figure 3.3: Novel Co-flow PV Nozzle and its Entrainment Process.

Figure 3.4: Manikin, BZR, and PV Nozzle Configuration.

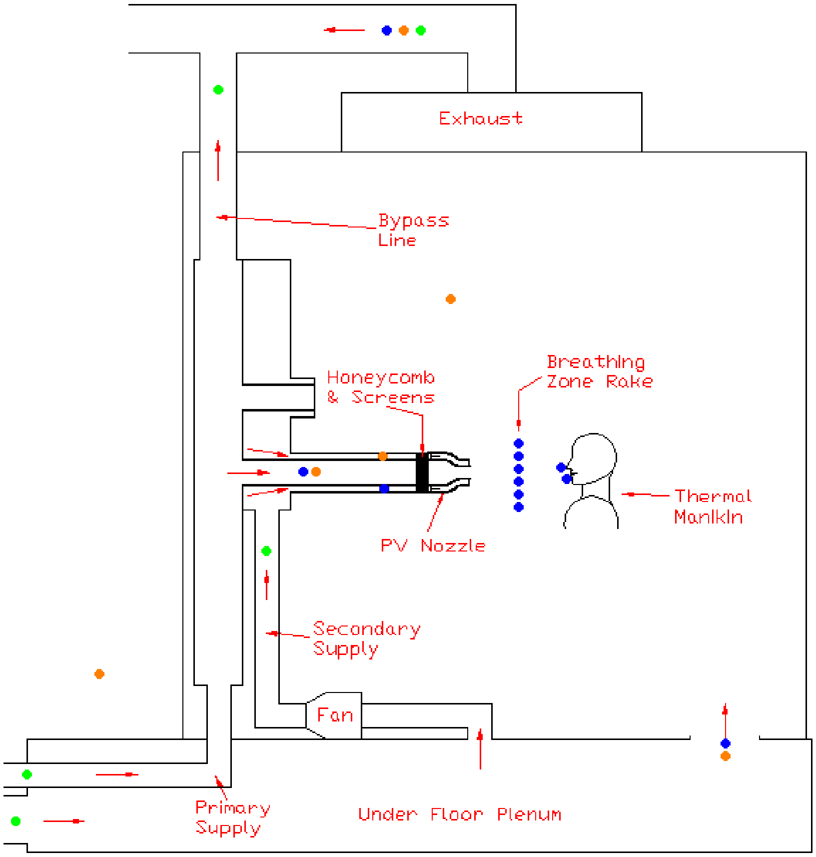

Figure 3.5: Experimental Setup with Measurement Locations.

The error of the experimental results were due to the accuracy of the concentration measurements, sampling rake traversing position uncertainty, and flow unsteadiness between point measurements. The concentration measurement errors were negligible and much of the AQI uncertainty is attributed to flow fluctuations, and results in an AQI uncertainty of </= *5 %.* The error of the positioning of the sampling rake was estimated to be ± *0.5 mm* (~ *2 %* of the nozzle radius) in the vertical traversing direction.

3.2 *Computational Domain and Setup*

The computational domain that was used for validation is shown in Figure 3.6. It represents a chamber measuring *2.0* x *2.6 x 2.5 m*, in which there is a CSP, a mixing box, a Co-flow nozzle (Khalifa and Glauser, 2006), a floor diffuser and a ceiling exhaust vent, similar to the experimental set-up described in detail in Section 3.1, Khalifa et al. (2008) and Khalifa et al. (2009). A symmetry BC was applied through the center plane of the CSP, floor diffuser and Co-flow nozzle; therefore, only half of the room was modeled in the CFD analysis. This is a slight deviation from the modestly unsymmetrical placement of the floor diffuser and ceiling exhaust in the experimental set-up, which we judged to have a negligible effect on the jet mixing zone and the jet/thermal plume interaction dynamics.

The Navier-Stokes equations were solved using a commercial software package, Fluent. The Realizable *k-ε* turbulence model was used along with the enhanced wall treatment option as discussed in Section 2.2. Second-order accurate upwind schemes were employed to solve the momentum and energy equations, and a second-order accurate scheme was used for the pressure interpolation.

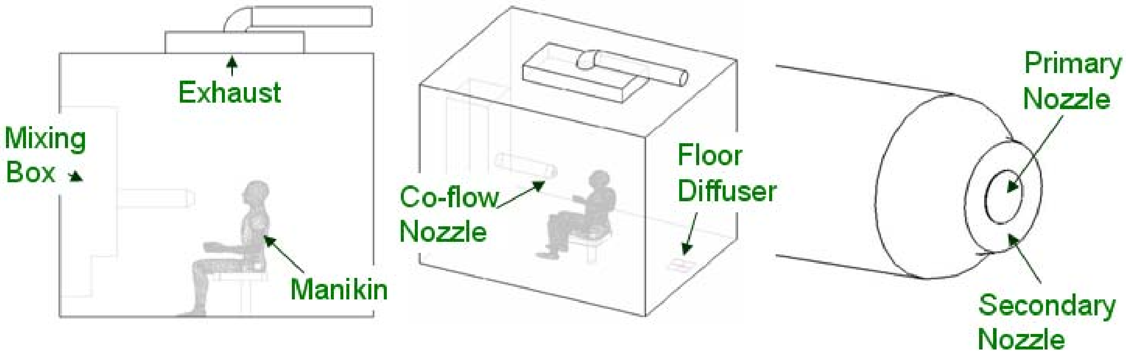

Figure 3.6: Computational domain and PV nozzle.

BCs that were employed in the validation CFD model were similar to the conditions in the experimental setup. For the Co-flow case, a velocity profile shown in Figure 3.7 was used for the primary and secondary jets with a velocity magnitude of *~1.2 m/s* for both that closely matched the experiential profile. For the conventional round nozzle (referred to as the 'Primary' case) a velocity profile was used that is similar to the primary profile of the Co-flow nozzle, with a velocity magnitude of *~1.2 m/s* and the secondary jet was turned-off. A pressure outlet was used at the exhaust with a value of *0* gage pressure in both cases. To maintain the same air supply to the chamber in both the Co-flow and Primary cases, the air supply through the floor diffuser in the Primary case was increased to compensate for turning-off the secondary jet as shown in Table 3.1. The CSP surface temperature, the primary and secondary jet temperatures, the floor diffuser air supply temperature, the average chamber wall temperature, and the average floor temperature was set to match those of the corresponding experimental cases (Khalifa et al., 2009) as shown in Table 3.1. The floor temperature was not measured experimentally and the variation of floor temperatures was examined to achieve better agreement with the CFD and experimental results. The inclusion of seat geometry was tested to determine its need.

The turbulent intensity for the primary and secondary jets was set in the computational model to match the experimental set up. Values for the turbulent intensity for the primary and secondary nozzles varied in the experiments from *1.5 %* to *2.0 %* (Khalifa et al., 2009)*;* and a value of *1.7 %* was used for the CFD validation representing the most often measured turbulent intensity.

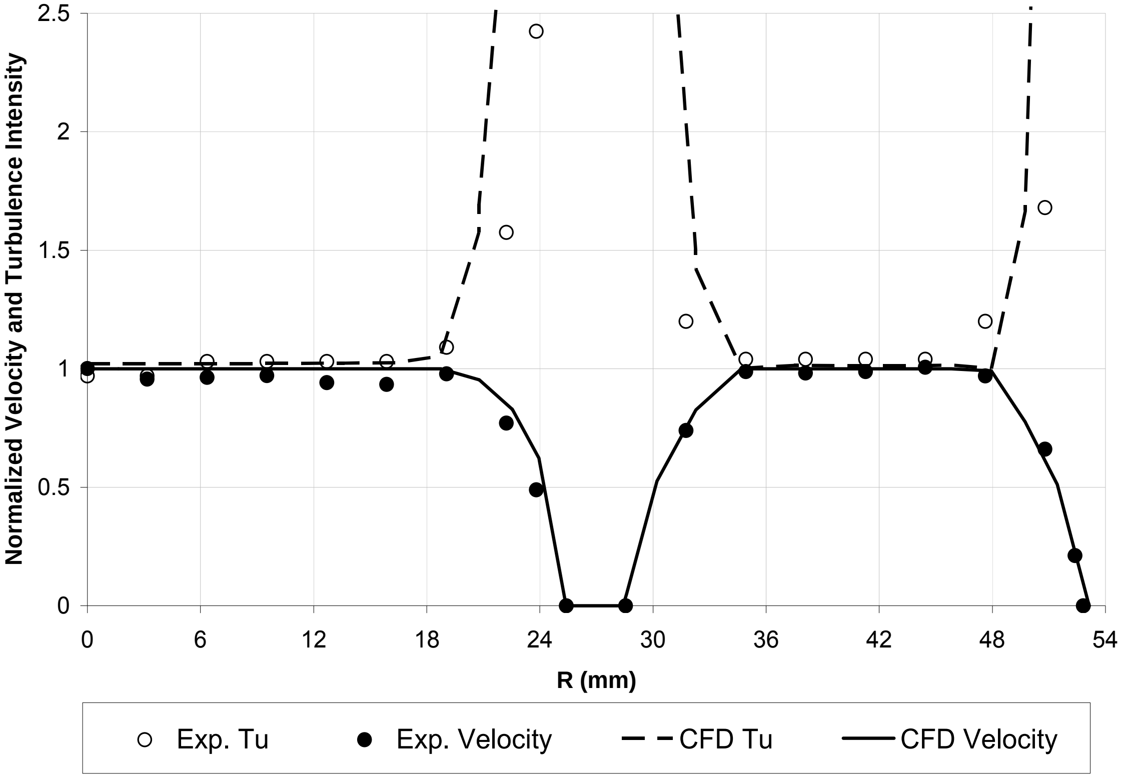

Figure 3.7: Normalized turbulent intensity and velocity profiles at the nozzle exit.

For species transport, an SF_6 concentration was supplied through the floor diffuser and the secondary nozzle, while the primary air was kept free of SF_6. Results of the SF_6 concentration were normalized to give a profile of AQI at *10* and *25 mm* from the CSP's nose on the symmetry plane were generated and compared against test data from Section 3.1. The Schmidt number for the computational model is investigated and compared with experimental data to determine the optimal value for validation.

Table 3.1: Computational BC's for validation cases. 'S' refers to the single (Primary) jet PV system and 'C' refers to the Co-flow PV system.

Test Series	**1S**	**1C**	**2S**	**2C**	**3S**	**3C**	**4S**	**4C**	**5S**	**5C**
Profile Distance from Nose, mm	10.0	10.0	25.0	25.0	10.0	10.0	10.0	10.0	10.0	10.0
Primary Jet Temperature, °C	23.5	23.5	23.5	23.5	20.0	20.0	26.0	26.0	23.5	23.5
Primary Nozzle Air Flow, l/s	2.4	2.4	2.4	2.4	2.4	2.4	2.4	2.4	2.4	4.7
Secondary Jet Temperature, °C	--	22.2	--	22.2	--	21.2	--	22.9	--	22.4
Secondary Nozzle Air Flow, l/s	0.0	6.7	0.0	6.7	0.0	6.7	0.0	6.7	0.0	13.4
Floor Diffuser Air Temperature, °C	20.5	20.2	20.3	20.3	20.4	20.0	20.6	20.3	21.3	21.4
Floor Diffuser Air Flow, l/s	16.5	9.7	9.7	9.7	16.1	9.7	16.3	10.0	14.1	0.8
Chamber Exhaust Temperature, °C	24.2	24.5	24.6	24.6	24.2	23.5	24.4	24.4	25.6	25.9
Nose Distance from Nozzle, m	0.41	0.4	0.41	0.41	0.41	0.41	0.41	0.41	0.41	0.41

3.3 *Grid Development*

For this work it is critical that the CFD tool can accurately predict the entrainment/mixing of the surrounding polluted room air and the clean air from the PV nozzle, and it is equally important that the CFD tool can accurately capture the interaction between the PV jet and the thermal boundary layer in the BZ. To this end, in addition to proper modeling of flow-physics (e.g. topology, turbulence mixing, buoyancy effects, and fluid/thermal BCs), one must select the necessary grid resolution in several critical areas; namely, (1) number of cells in the radial direction of the nozzle to accurately capture the shear-layer entrainment process, (2) the grid distribution in the mixing region between the PV jet and the CSP's head, (3) the grid resolution in the BZ to handle the flow interaction between the PV jet and the CSP's thermal boundary layer, and (4) the development of the rising thermal plume around the CSP. Dygert et al. (2009) has shown that the proper prediction of the thermal plume strength is greatly dependent on sufficient resolution of the near-wall flow. Alkandry et al. (2008) recommended using a surface resolution on the order of 30,000 triangular elements or more to define the entire CSP, or 15,000 when symmetry is used. Clustering is also suggested for the mouth and nose region to enhance details in the BZ. For the wall treatment chosen for this work, a proper y^+ must be maintained around the CSP which has been found to be achieved by using a first cell height of 0.5mm and a growth rate of 1.1 (Topp et al., 2002; Sorensen and Voigt, 2003, Sideroff and Dang, 2008; Russo et al., 2008, 2009) For this work, two grids, one fine and one coarse, were developed to show grid importance.

3.3.1 Fine Grid

To start the grid-generation process, the geometry of a seated thermal CSP was imported into the grid generation software and CAD-cleanup was preformed. For ease of creating a grid and for alignment with a desk, the hands were removed from the CSP. Also, the grid for the CSP was created in a Z-man block for ease of moving from one grid to another as shown in Figure 3.8 and ensures that the grid around the CSP was the same for every case studied. The Z-man block represents a volume close to the CSP that resulted in a 'Z' shape.

In order to resolve the boundary layer, the surface mesh was created based on the guidelines given in Sideroff and Dang (2008) where grid independence was shown and validated for a CSP in an otherwise empty room while being ventilated using displacement ventilation. The surface grid was created and the total number of elements on the half surface of the CSP was approximately *20,000*. These elements are clustered around the mouth and nose of the CSP as seen in Figure 3.9. The surface grid was further refined to resolve the thermal boundary layer around the heated CSP. The grid size and total number of cells on the CSP surface is shown in Figure 3.10. The cell boundary layer has a start size of *0.5 mm*, a growth rate of *1.1* and a total of five layers. This grid resolution results in an average y^+ of *1.5* with a maximum value of less than *3* on the CSP surface.

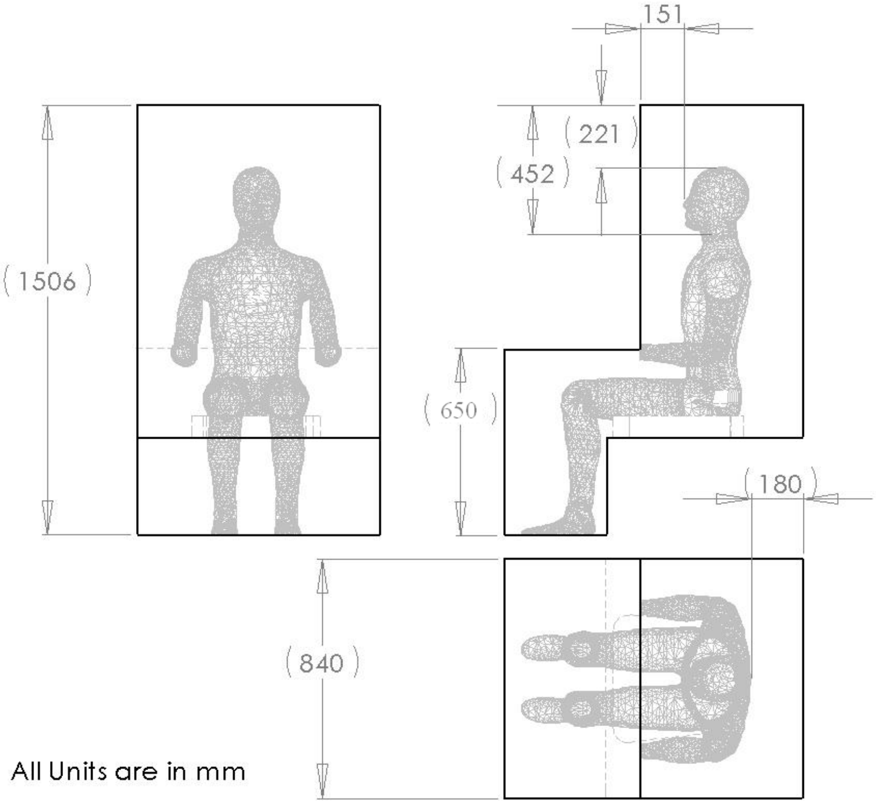

Figure 3.8: Z-man block for CSP grid creation.

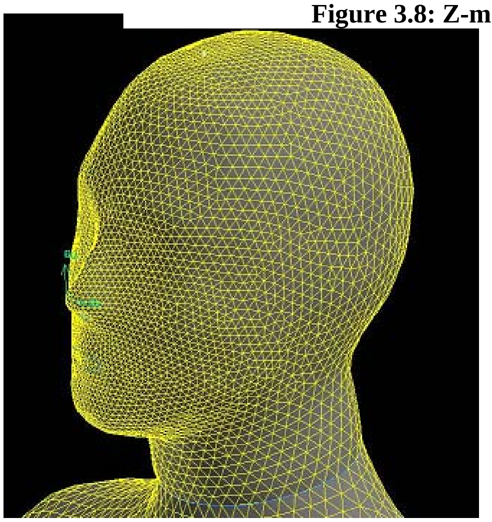

Figure 3.9: Surface face mesh.

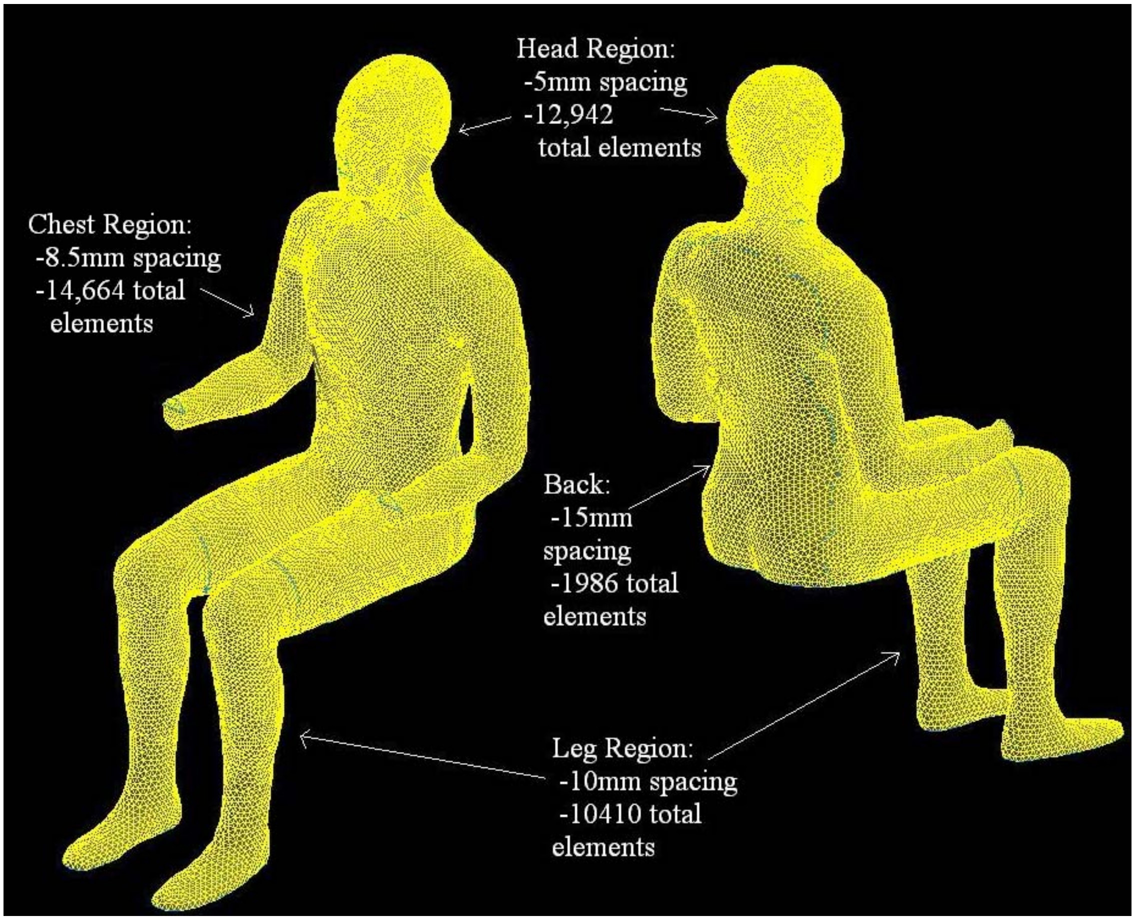

Figure 3.10: Grid size and total number of cells for each region of the body.

In order to establish the grid resolution appropriate for computing the entrainment process between the clean air jet and the polluted surrounding air, axisymmetric free jet CFD studies were performed and the results compared with abundant experimental data available in the literature (e.g., Mi et al., 2001; Malstrom et al., 1997). The results from this study are shown in Appendix A and it was found that an unstructured grid with 10 cells across the radius of the nozzle was sufficient to capture the jet characteristics.

As shown in Figure 3.11 a relatively uniform unstructured mesh was applied in the mixing region between the CSP and the PV jet. Ten cells should be used across the radius of the nozzle and clustering near the shear layer that would result in cells with length scale on the order of *2 mm* as shown in Figure 3.11. This is smaller than the length scale of the CSP's surface grid, which is on the order of *3 mm* on the CSP surface at the mouth and nose and as large as *12 mm* on the CSP's back. A structured grid was used in the outer domain to reduce the total number of cells. The final grid consists of about *4.2 million* cells and is shown in Figure 3.11. It should be noted that the total number of cells is controlled by the grid size in the mixing region, and not by the CSP's surface grid.

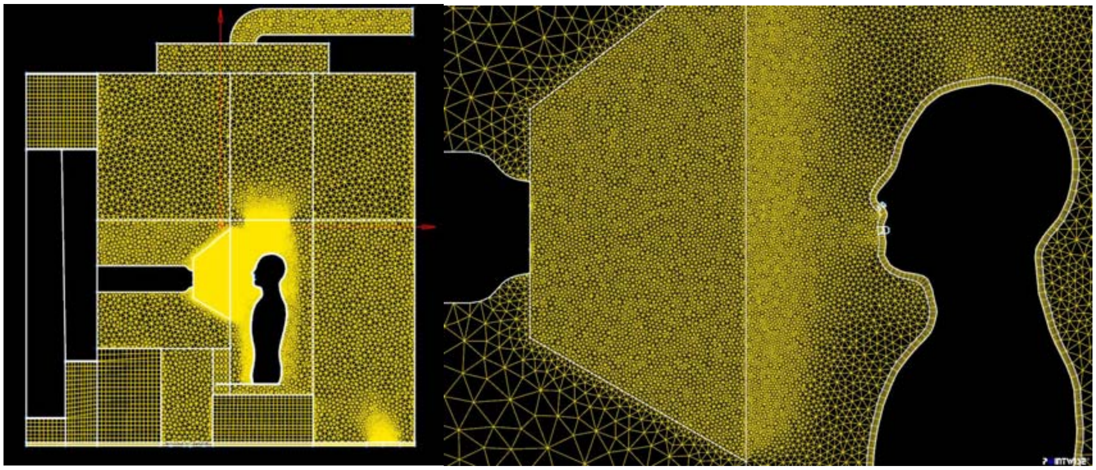

Figure 3.11: Room grid created in GRIDGEN.

3.3.2 Coarse Grid

A coarse grid was also created for comparison to show the necessity of such a fine grid described in Section 3.3.1. To illustrate the importance of resolving the mixing region between the PV jet and the thermal plume, a coarser mesh of *800,000* cells with cell size on the order of *4* to *5 mm* in the jet mixing region (*5* cells were chosen across the radius of the jet), and the number of elements defining the CSP geometry was reduced from *20,000* to *4,500* on half the CSP surface. The size of the computational cell next to the CSP surface was increased from *0.5 mm* to *10 mm*, resulting in an average y^+ value of *4.5*. A comparison of the two grids can be found in Table 3.2.

Table 3.2: Grid details of mixed-convection flow cases, representing half of the CSP w/symmetry.

CSP Case	Surface elements	Surface grid type	Volume grid type	Prism B.L.	1st cell height	Avg. y+	Max y+
Baseline	19000	tri	tetrahedral	Yes, 5 layer	0.5mm	1.5	3
Coarse Grid	4500	tri	tetrahedral	No	10.0mm	4.5	6

3.4 *Flow Structure in the Jet/Thermal Plume Interaction Region*

The CFD-generated flow field shows that, depending on the momentum of the PV jet relative to the thermal plume, the jet trajectory between the PV nozzle and the CSP's BZ could be strongly influenced by the cross-interaction between the PV jet and the CSP's thermal plume. This flow interaction is important with respect to AQI in the CSP's BZ because it can enhance the mixing between the clean air in the PV jet and the warm and polluted air in the thermal plume, and the extent of the jet deflection also has an impact on AQI. In the present study, we note that the momentum of the jet in the Co-flow case is four times higher than in the Primary case, and therefore, the interaction of the thermal plume and the Co-flowing jets is less significant than for the case of the Primary jet alone.

Figure 3.12a shows contours of the vertical velocity component (or *y*-component) in a vertical plane perpendicular to the nozzle axis *250 mm* from the nose, and *50 mm* from the nose for the Primary case. It is evident that in the seating position, the thermal plume extends from the knee to the CSP's upper body (Sideroff & Dang, 2008). At *250 mm* from the nose, the thermal plume consists of two separate pockets of *y*-component velocity with magnitude on the order of *0.13 m/s* above the legs. At *50 mm* from the nose, the thermal plume is much larger and stronger, with *y*-component velocity magnitude on the order of *0.2 m/s* in the vicinity of the PV jet. The contour plot at the plane *50 mm* from the nose clearly shows the thermal plume interacting with the PV jet; in particular, the flow in the thermal plume below the PV jet decelerates as it approaches the PV jet, and then accelerates around it. A close look at the shape of the PV jet, shown in Figure 3.12b, presented as AQI contours, reveals that its circular shape is mostly preserved until it approaches the CSP, where it becomes highly distorted. On the other hand, the circular shape of the jet in the Co-flow case is preserved much farther (not shown here), as its momentum is *4* times higher than that of the Primary case.

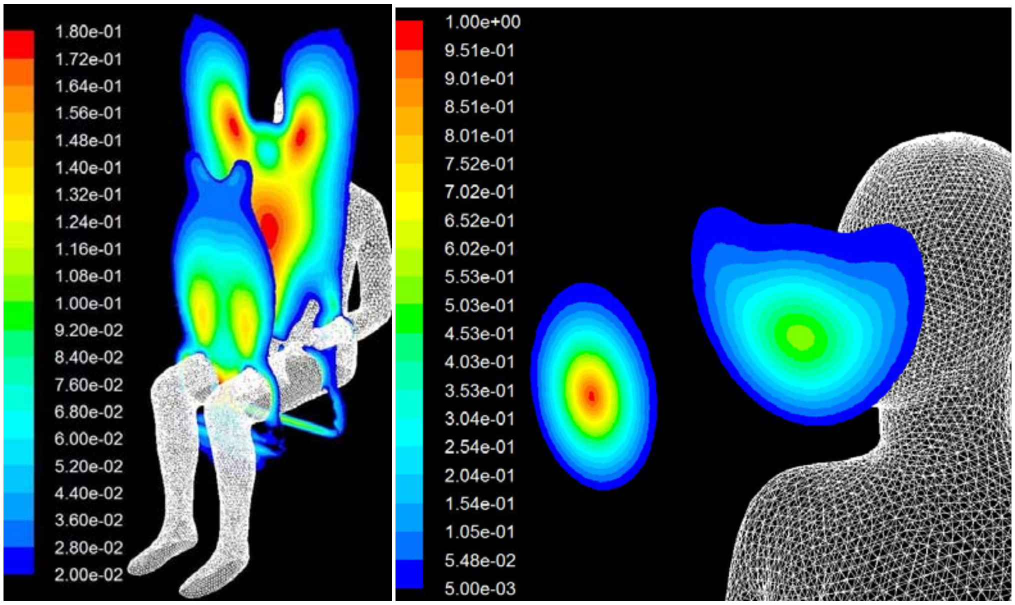

Figure 3.12: a) Vertical velocity (m/s) contours 50 and 250 mm from the nose for the Primary case, b) Shape of the jet in terms of AQI 50 and 250 mm from the nose for the Primary case.

3.5 CFD Validation

Validation comparisons were performed for different computational and experimental strategies. First the Coarse grid was compared to the experimental results. Second, using the Fine grid, the effects of far field BC's and geometry were determined for validation. Next, the turbulent Schmidt number effect was determined to find the optimal value. Then, a comparison was made for five turbulence models. The Fine grid was then set the same computational setup as the Coarse grid and compared as the baseline validation case. Finally, the experimental parameters were altered to test different jet temperatures and flow rates and compared to the computational results with the same modifications.

3.5.1 Coarse Grid

A simulation was conducted using the Coarse mesh of *800,000* cells with cell size on the order of *4 to 5 mm* in the jet mixing region (about a factor of 2 larger than the fine mesh). Figure 3.13 includes the CFD results using the coarse mesh for Cases 1S/C. The y-axis is the vertical distance normalized with respect of the primary nozzle radius, *R*. The CFD results show that the peak AQI value was under-predicted while the jet spread is over-predicted when the Coarse mesh is used, indicating that numerical diffusion is excessive with the Coarse mesh. For the conventional nozzle case, the maximum AQI at *10 mm* from the nose was *0.38* for the Coarse mesh compared to *~0.46* for the experimental results. For the Co-flow nozzle case, the maximum AQI at *10 mm* from the nose was *0.68* for the Coarse mesh compared to *~0.9* for the experimental results. Although the general trend of AQI improvement was captured with the Coarse mesh, the magnitude of the improvement was significantly under-predicted by the Coarse mesh. In particular, the predicted improvement in AQI between the Co-flow nozzle and the conventional nozzle was *0.44* for the experimental results, while it was only *0.3* for the Coarse mesh. Thus, if the Coarse mesh was used to evaluate the advantage of the Co-flow nozzle over the conventional nozzle, one would have under-predict the improvement in AQI by *50 %.*

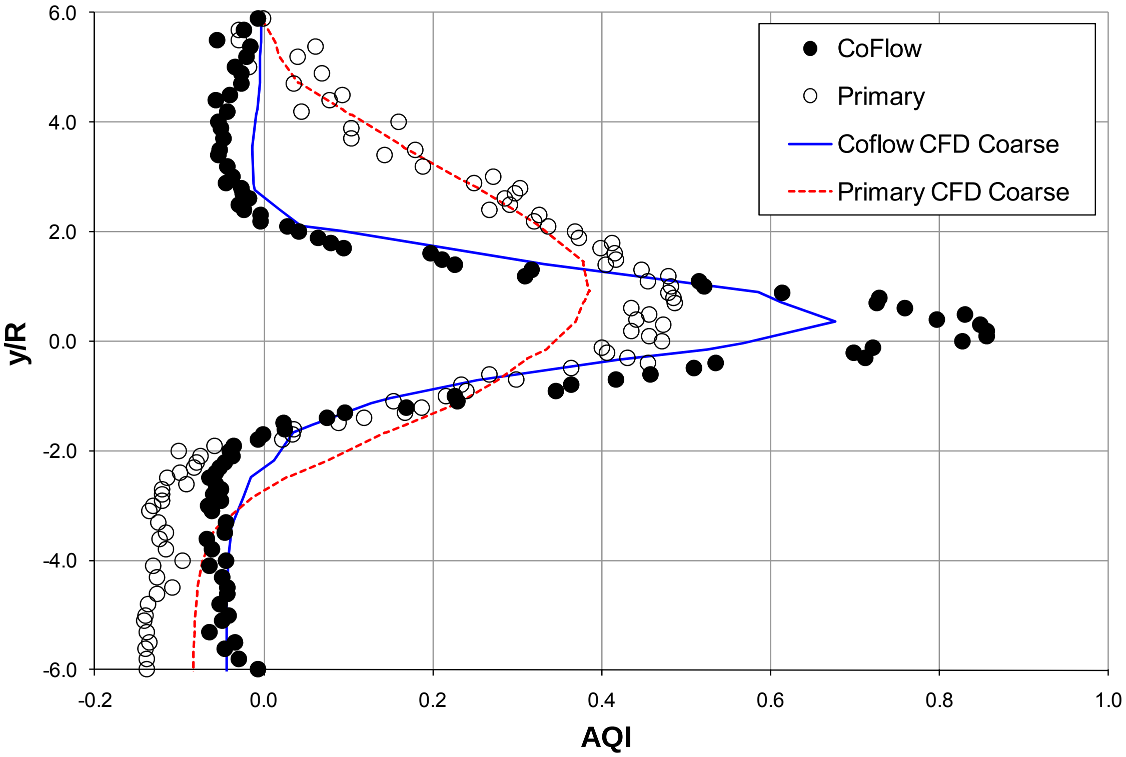

Figure 3.13: Effect of grid resolution on AQI for Case 1S/C.

3.5.2 Effect of Geometry and Far Field Boundary Conditions

Over the course of this CFD validation study, we learned that care must be taken in setting up the CFD calculation to obtain good agreement with test data for the Primary case because of the strong interaction between the thermal plume and the PV jet. In particular, accurate predictions of the jet deflection and jet spreading rate in the Primary case was not possible unless the correct thermal BC is imposed on the floor, and the inclusion of the seat as a solid surface, as both had a large impact on the strength of the thermal plume. The Co-flow case was less sensitive to these effects because its momentum is much larger.

Figure 3.14 shows the sensitivity of the AQI profile for Case 1S to several parameters. In Case A, the CSP seat was not included in the simulation (many researchers may neglect a seat for ease of modeling) and the floor temperature was set to the room temperature $23.5\ ^oC$ (an assumption made due to a lack in the experimental data for this value). The result shows that the jet deflection is over-predicted, indicating that the thermal plume is too strong. Next, in Case B, the seat bottom was included in the simulation while the floor temperature is kept at $23.5\ ^oC$. The result shows that the jet deflection is reduced, but it is still higher than the experimental value. Finally, in case C (used in Section 3.5.3, 3.5.4 and 3.5.5), with the seat included and the floor temperature set to a value of $22\ ^oC$ (determined from the under-floor air temperature and the room air temperature), the CFD results match very well with the test data.

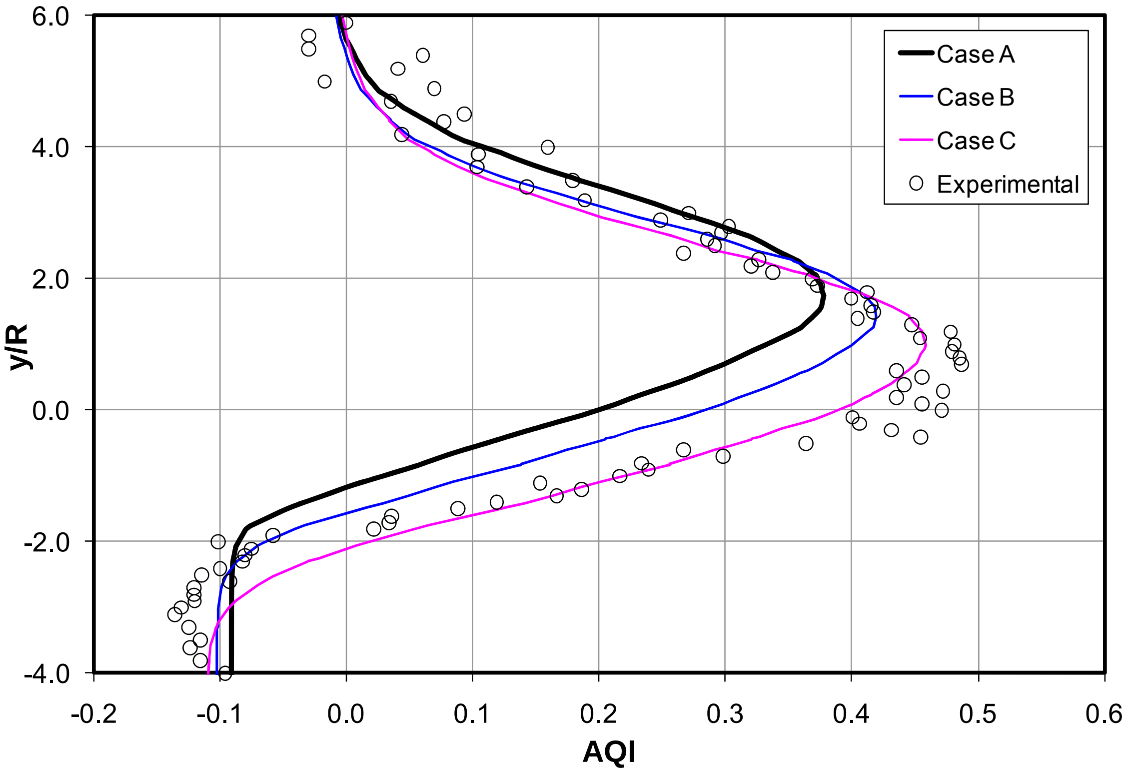

Figure 3.14: Sensitivity of AQI prediction to BCs.

The same excellent agreement between CFD and test results was also obtained when the seat bottom was deleted but the correct floor temperature was specified, indicating that the latter is the more important factor when the floor temperature is lower than room temperature. This exercise demonstrates that it is important to handle BCs with care in order to properly simulate cases involving strong interactions between PV jets and the thermal plume. Figure 3.15 shows velocity contours for Case A, B and C. It is clearly shown that the deflection of the Primary jet was sensitive to different BCs.

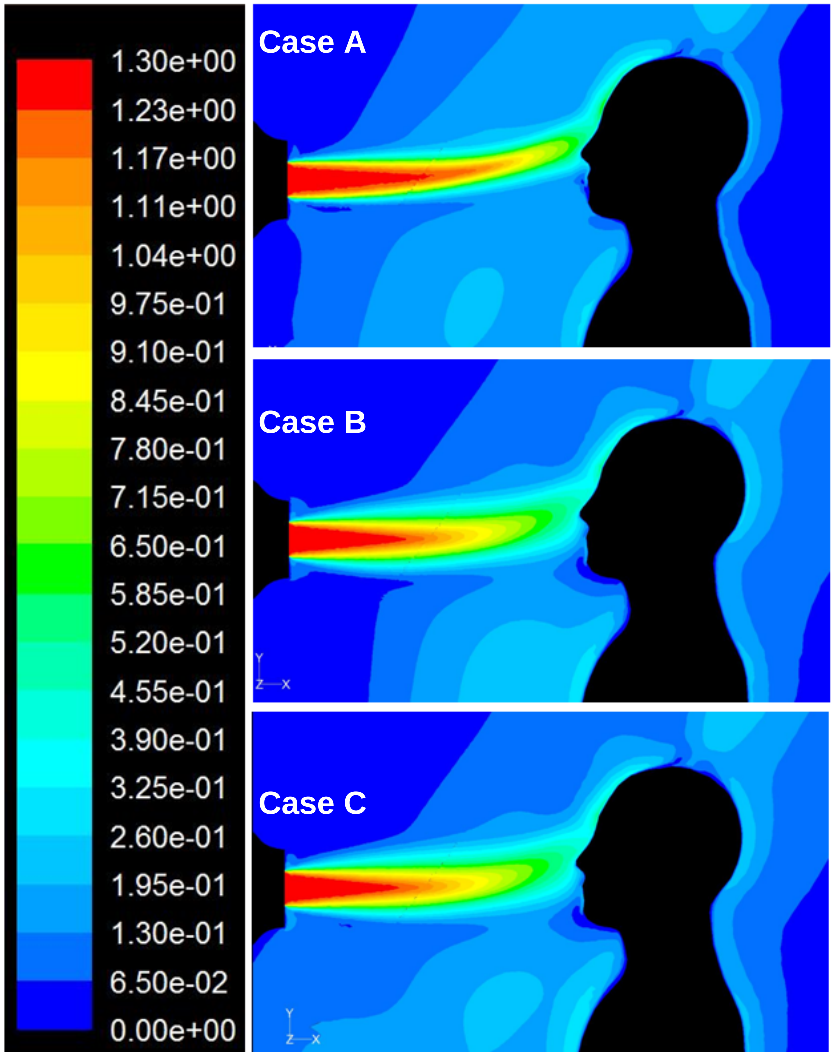

Figure 3.15: Velocity contours for Case A, B and C to show sensitivity to BCs.

3.5.3 Optimal Turbulent Schmidt Number

A PV jet approaching a person's face will decelerate as the stagnation point is approached. The flow-field in the vicinity of the stagnation point, which is often located in the BZ for a PV set-up, depends on surface curvature. Therefore, a block-head with a flat face would result in a different flow-field near the stagnation point from that of a curved egg-shaped head. However, turbulent fluctuations and turbulent thermal and mass diffusivities in the vicinity of the stagnation point have been shown to be considerably higher than those in the far field (Galloway, 1973; Hargrave et al., 1986). Therefore, the temperature and species concentration parameters in an approaching PV jet tend to project closer to the face while the velocity continues to decelerate (Khalifa et al., 2009). Therefore, it is important that the correct values of the turbulent mass and thermal diffusivities (or, alternatively, the turbulent Schmidt and Prandtl numbers) be used in CFD calculations in which details of the flow near the stagnation point (BZ) are important.

Experimental data was utilized to determine the optimal Sc_t to be used in the CFD model to predict the species transport in the indoor space accurately. Figures 3.16 and 3.17 show the effect of the Sc_t on the AQI profiles *10* and *25 mm* from the CSP's nose compared to experimental data, respectively. Varying agreements from reasonable to excellent were obtained for both PV systems with all Sc_t tested.

The plots show that Sc_t has the greatest impact on the peak of the AQI profiles. The Figure shows the lowest computational peak AQI value for a Sc_t of 0.7 for both PV cases with the computational peak AQI values increasing with increasing Sc_t. The varying Sc_t capture different points in the scatter of the experimental data, and therefore, no determination of the most accurate Sc_t that should be used for the computational studies can be made from these figures alone.

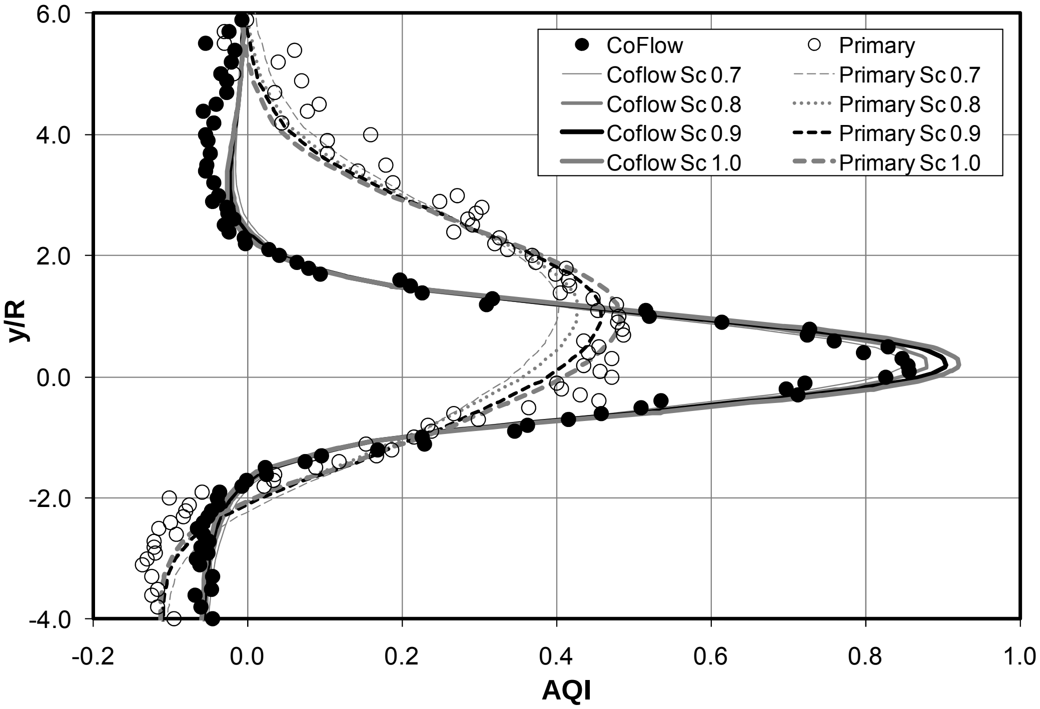

Figure 3.16: Shows the effect of the computational Schmidt number on the AQI profile 10 mm from the CSP's nose against experimental data.

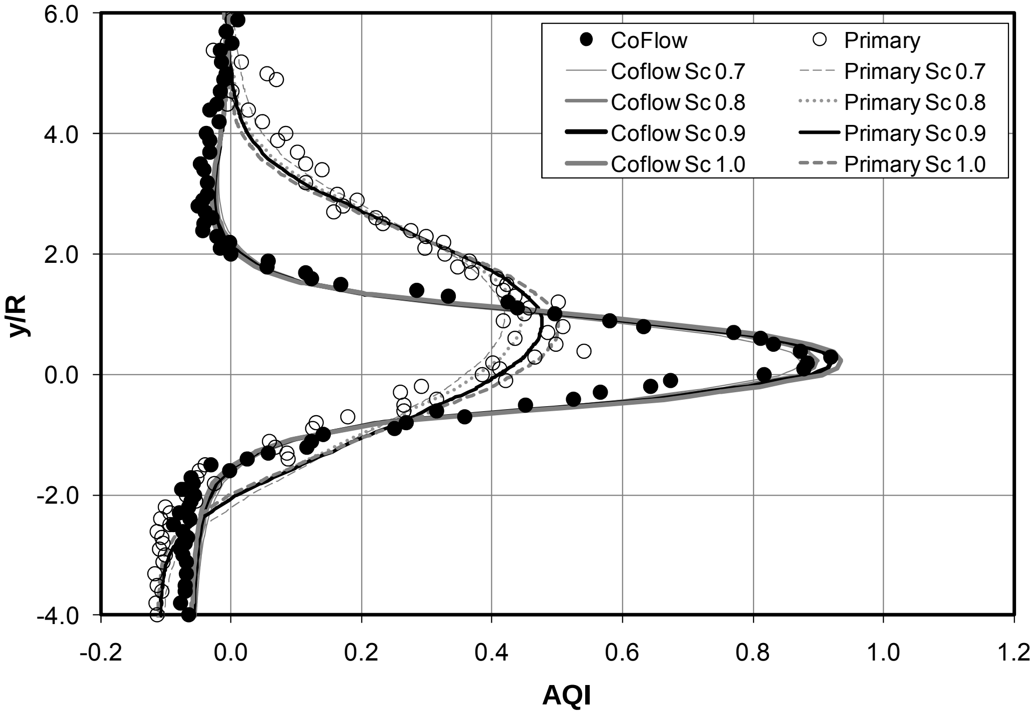

Figure 3.17: Shows the effect of the computational Schmidt number on the AQI profile 25mm from the CSP's nose against experimental data.

To select the optimal value of Sc_t, the RMS difference (error) between the experimental and computational results was calculated for each Sc_t. The computational results for the Primary and Co-flow nozzles at *10 mm* and *25 mm* were combined for each Sc_t and a single RMS deviation for each Sc_t was found. This was done for 2 data sets: a) the entire range of experimental values and b) data within ±1 nozzle diameter of the peak the AQI profiles. The results are shown in Figure 3.18, which indicates that the optimal Sc_t is close to *0.9*. Therefore, a Sc_t of *0.9* was chosen for the rest of this work. It is noteworthy that this value is also consistent with the recommendations of other researchers (Gadgil et al., 2003; Sorensen & Weschler, 2002; Yang et al., 1998; Yang et al., 2001).

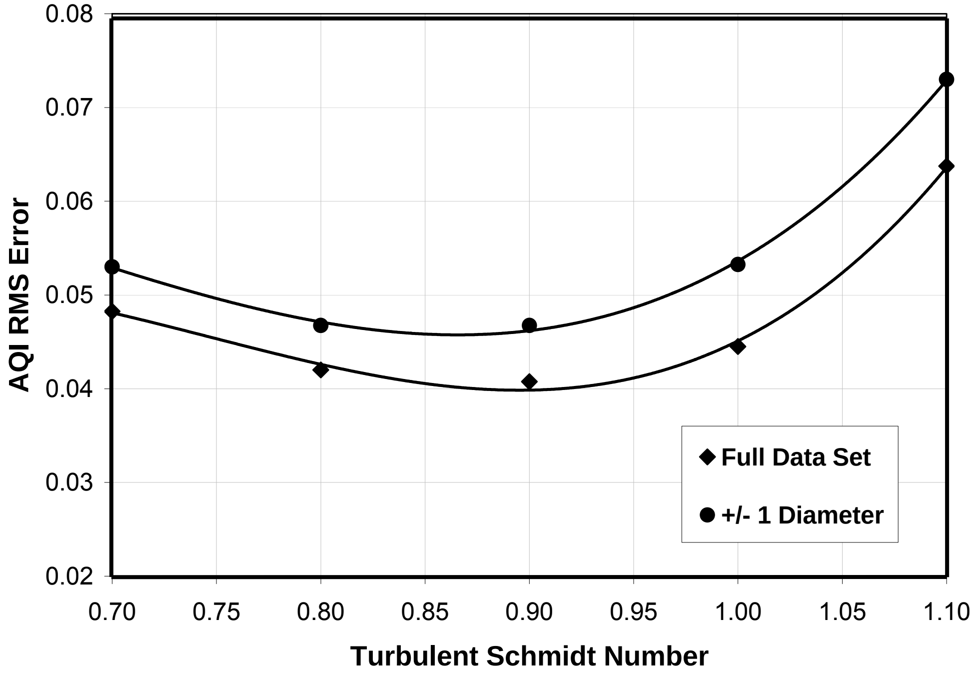

Figure 3.18: AQI RMS errors for different Sc_t.

3.5.4 Turbulence Model

Using the Fine grid, the CFD predictions of AQI in the personal micro-environment with five turbulence models available in the commercial software Fluent are compared for the conventional nozzle, as this case is more sensitive to the strength of the thermal plume discussed earlier. The turbulence models include the k-ε family of turbulence models (standard, realizable, and RNG) and the k-ω family of turbulence models (standard and shear stress transport (SST)).

Figure 3.19 shows comparisons of the AQI between the test data and the CFD results along a vertical line in the symmetry plane located *10 mm* from the CSP's nose, along with the experimental data. The results show that the k-ε family of turbulence models are very similar and compare well with the test data, while both the standard and SST k-ω

turbulence models did a poor job at predicting both the jet deflection/distortion and jet spreading. 2D jet studies of the *k-ω* turbulence models showed an over prediction in the jet potential core length with lower jet spread. When comparing average convective heat flux, the *k-ε* family of turbulence models differ from the baseline case by less than *1 %,* while the *k-ω* family of turbulence models is ~*4 %* higher than the baseline case. The use of the Realizable *k-ε* turbulence model was continued for the rest of this work.

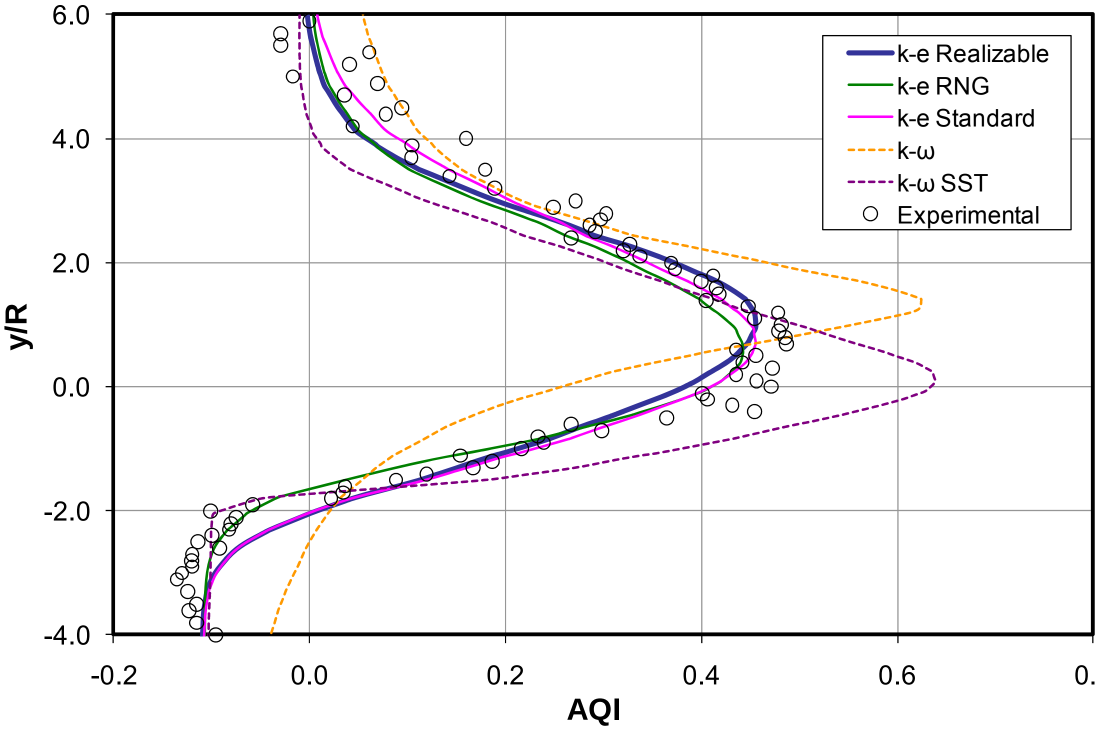

Figure 3.19: Comparison of different turbulence models for Case 1S/C.

3.5.5 Fine Grid Validation

With the inclusion of the seat, correct floor BC, optimal turbulent Schmidt number and the use of the Realizable *k-ε* turbulence model combined with the Fine grid, validation of this model was achieved. Figures 3.20 and 3.21 show comparisons of AQI between the test data and the CFD series 1S/C and 2S/C in Table 3.1 along vertical lines in the symmetry plane and located *10* and *25 mm* from the CSP's nose, respectively. The experimental error was included for three representative points: 1) at the peak of the profile, 2) along the steep gradient and 3) at the base of the profile. Error in AQI varies along the profile given since an error in the transverse location can have a larger impact on AQI for the steep portion of the profile compared to the base. Excellent agreements were obtained for both the Co-flow case and the Primary (single jet) case. These results show that, at *10 mm* from the nose, there is little deflection in the jet trajectory of the Co-flow case, while the jet trajectory of the Primary case is deflected upward by about one nozzle radius. Another observation is that, as required by mass conservation, the Co-flow case is capable of delivering cleaner air but in a narrower region than the Primary case. This is clearly the goal of PV systems, which is to deliver clean air only where it is needed and for the nozzle angle would be adjustable when implemented to aim the nozzle to deliver the freshest air to the BZ. The resulting velocities *2 cm* from the face from the Co-flow nozzle and Primary nozzle are *0.94* and *0.55 m/s* respectively. Finally, we note that the results shown in Figures 3.20 and 3.21 are taken along the symmetry plane (where the experimental traverses were obtained) and should not be interpreted as being the same on other planes in all cases. For example, a plot of the AQI profile in a horizontal plane cutting through the location of maximum AQI value would show a profile nearly similar to that in the vertical plane for the Co-flow case, but because of the distortion and deflection of the PV jet by the thermal plume in the Primary case, the horizontal core erosion would appear to be larger for the Primary case.

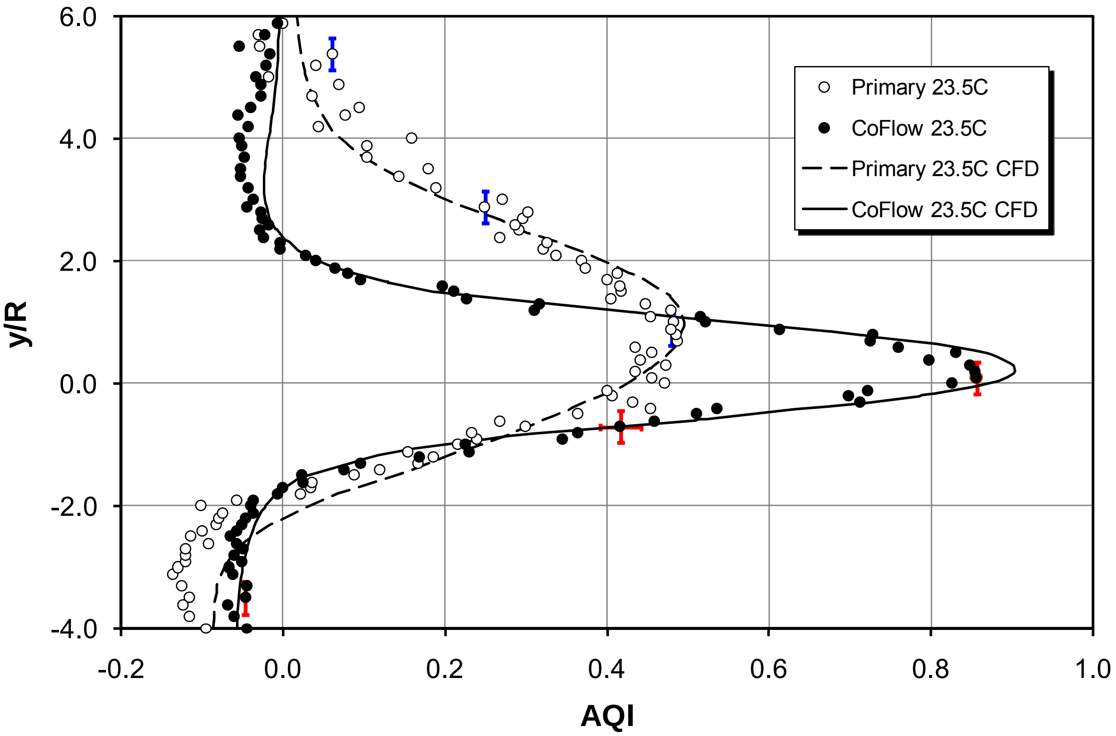

Figure 3.20: AQI 10 mm from the nose for Case 1S/C.

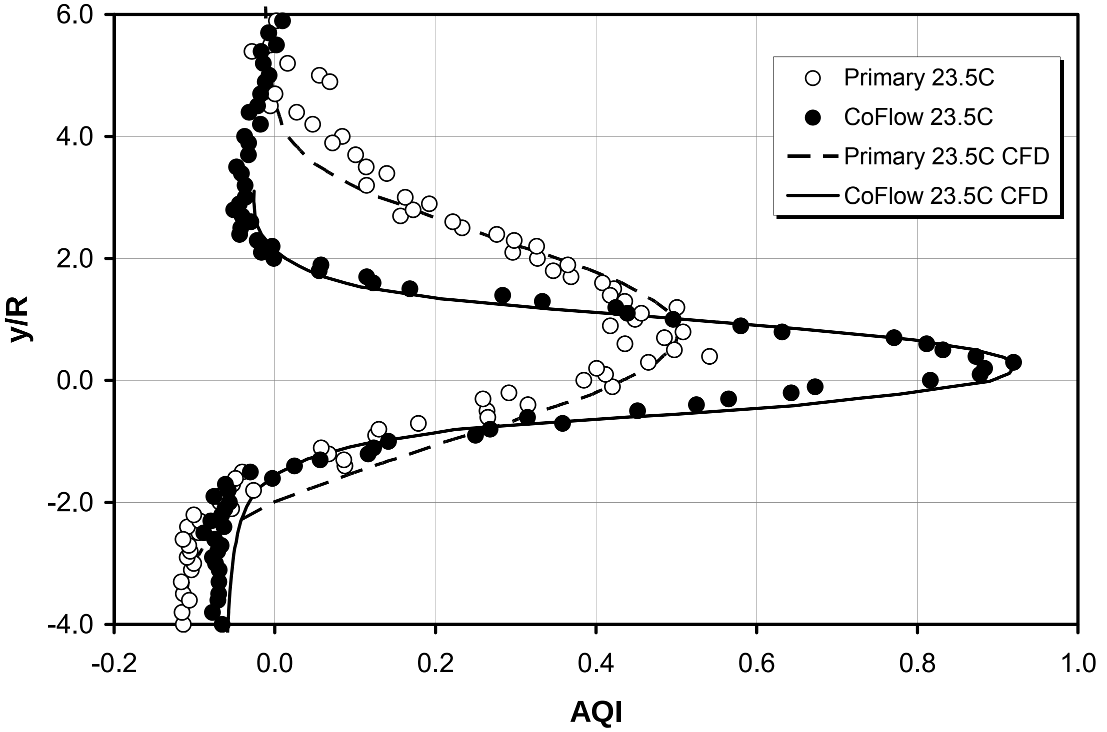

Figure 3.21: AQI 25 mm from the nose for Case 2S/C.

Figure 3.22 shows comparison of the AQI on the CSP's face between these two cases. The figure clearly shows that the Co-flow is much more effective in delivering clean air to the occupant than the single jet Primary case, as indicated by the much larger region of high values of AQI. This is true even if the primary nozzle in Primary case is re-aligned so that the PV jet impinges directly at the target BZ of the occupant.

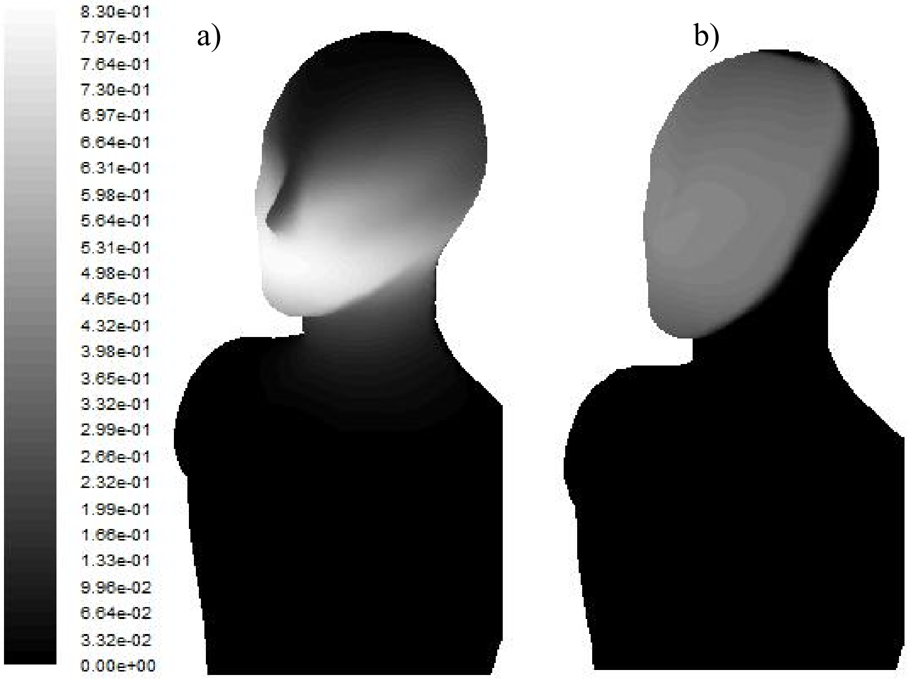

Figure 3.22: AQI contours for 1S/C a) Co-flow case and b) Primary case.

To quantify the effects of the PV primary jet's exit temperature on the air quality in the BZ, additional test cases were carried out. The temperature of the primary jet was changed from *23.5 °C* to *20.0 °C* (cool case) and *26.0 °C* (warm case) while keeping the secondary jet temperature *~23 °C* (see Table 3.1). Figure 3.23 shows the AQI profiles for different nozzle temperatures for the cases 1S/C, 3S/C and 4S/C (Table 3.1) along a vertical line *10 mm* from the CSP's nose. The *y*-axis is the vertical distance, where *y* is measured from the nozzle centerline and normalized with respect to the primary nozzle radius *R*. Good agreements were obtained for the Co-flow and Primary cases. The results show that the Primary case is more sensitive to temperature changes than the Co-flow case, but neither the Co-flow nor Primary case is highly sensitive to these modest temperature changes.

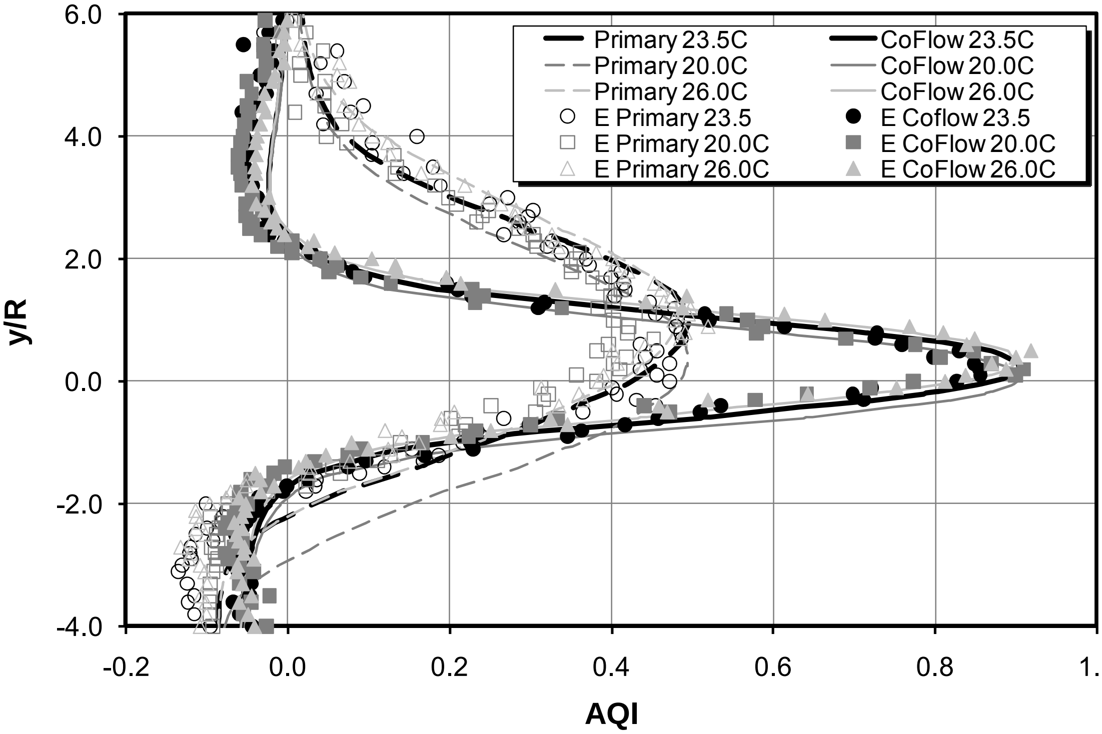

Figure 3.23: Comparison of experimental and computational AQI profiles along a vertical line 10 mm from the CSPs nose for an increase and decrease of the Primary temperature of *3 °C* compared to the Baseline (Cases 1S/C, 3S/C and 4S/C).

To validate the data for different flow rates, Figure 3.24 shows the comparison of AQI between the test data and the CFD results along a vertical line located *10 mm* from the

CSP's nose for Cases 5S and 5C. Excellent agreements were obtained for the Co-flow and Primary cases. These results show that, at *10 mm* from the nose, there is little deflection in the jet trajectory of both the Co-flow and Primary cases.

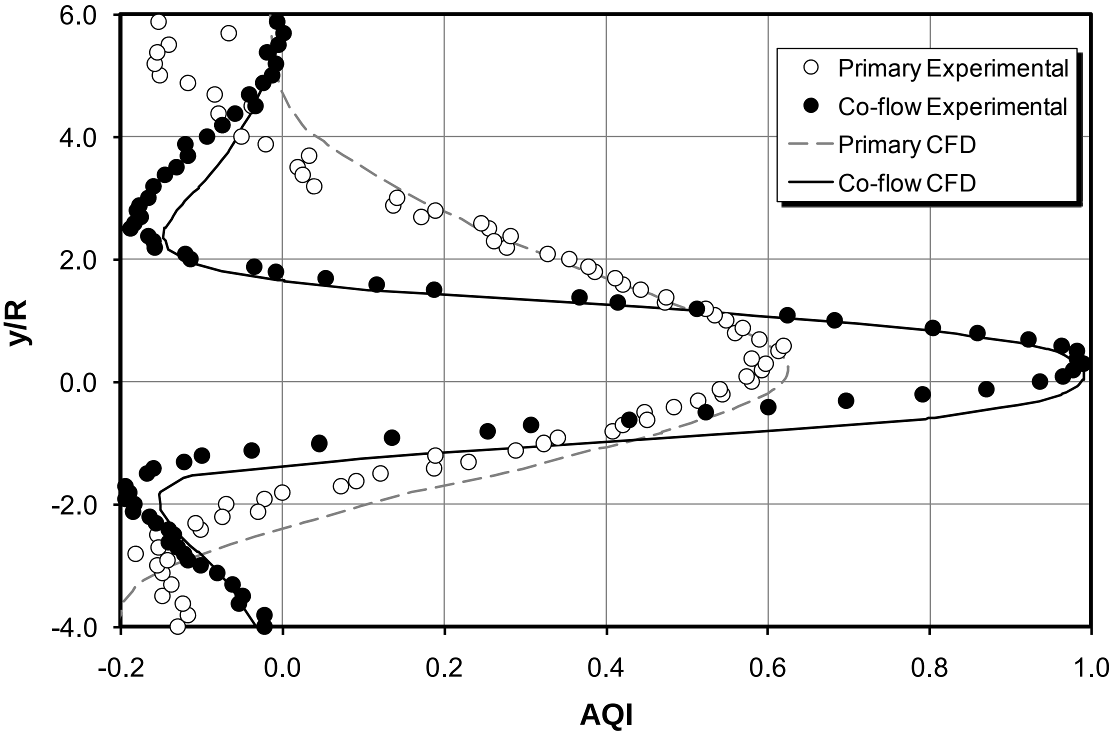

Figure 3.24: Comparison of experimental and computational AQI profiles along a vertical line *10 mm* from the CSP's nose for a flow rate of *4.8 l/s* (Cases 5S/C).

3.6 *Chapter Conclusions*

Overall, the CFD model presented in this work exhibits excellent agreement with the experimental results. The CFD results show similar jet spreading as the experimental results for both the Co-flow and Primary cases, as well as a higher jet deflection and distortion for the Primary nozzle than the Co-flow nozzle. The Co-flow nozzle shows little or no deflection of the jet in the experimental results or CFD results. The deflection and distortion of the Primary-only jet can be attributed to the effect of the thermal plume around the CSP and the low momentum of the single jet at the prescribed low "clean" air supply of only ~*2.4 l/s*, compared with the Co-flow nozzle which provides additional momentum (~*4 times*) with the recirculated secondary flow (*2.4 l/s* of fresh, primary air plus *6.7 l/s* of recirculated, secondary air).

In this work, a high-fidelity CFD model based on the use of Fluent has been created to simulate the effectiveness of PV systems. When an adequate grid size is used along with proper implementation of BCs, turbulent Schmidt number, the realizable k-ε turbulence model coupled with the enhanced wall function was able to predict the air quality in the BZ accurately. The pollutant transport CFD model shows excellent agreement with the experimental results. With the use of the optimally determined value of the turbulent Schmidt number, Sc_t, the CFD model was able to capture the peak AQI values in the different profiles in front of the CSP's nose better than using the default values assumed in commercial CFD codes. A Sc_t of *0.9* was found to give the best agreement with experimental data. Excellent agreement between CFD results and test data was obtained for the AQI in the BZ for two different PV nozzles: a simple single nozzle and a novel Co-flow nozzle (Khalifa & Glauser, 2006). The validated CFD model can be used as a reliable tool to optimize the design and placement of PV systems, and to investigate the flow, temperature, humidity and concentration in the BZ more cost-effectively and faster than laboratory testing.

In addition to the importance of properly modeling ambient thermal BCs, it is noted that factors such as clothing, which alter the surface temperature of the CSP, should also be considered. In general, the thermal resistance of clothing serves to decrease the surface temperature which should be modeled on the CSP and is dependent on the type of clothing. Heavy clothing may also change the shape of the CSP. This effect was not considered in this study.

4 Boundary condition investigation

Validated CFD simulations can be employed to determine the effectiveness of a PV system more efficiently and cost effectively than through detailed experimental investigations of the flow, temperature, humidity and concentration fields in the person's BZ. Computational modeling can become time consuming and computationally expensive very easily when modeling the indoor environment. With the complexity of the problem that we are trying to model, it is important to determine what simplifications, if any, can be made during computational modeling. With the depth of involvement of this problem, nozzle and CSP BC's were examined individually with the validated model to determine their importance.

Table 4.1 (a, b) presents additional cases that were analyzed using the validated CFD model where jet and CSP BC's were varied. For these cases, one parameter was changed at a time and the total air flow into the domain was also kept at *18.9 l/s* (*~5 ACH*). In addition to these test cases skin wittedness, breathing simulation method and the effects of modeling radiation were determined and conclusions were made for the simplified modeling of the indoor environment.

Table 4.1: Cases Simulated

(a)

Test Series	1S	1C	1Sa	1Ca	1Sb	1Cb	1Sc	1Cc	1Sd	1Cd
Primary Jet Temperature, °C	23.5	23.5	23.5	23.5	23.5	23.5	23.5	23.5	23.5	23.5
Primary Nozzle Air Flow, l/s	2.4	2.4	2.4	2.4	2.4	2.4	4.8	4.8	3.6	3.6
Primary Turbulent Intensity, %	1.7	1.7	5.0	5.0	10.0	10.0	1.7	1.7	1.7	1.7
Primary Length Scale, mm	3.0	3.0	3.0	3.0	3.0	3.0	3.0	3.0	3.0	3.0
Secondary Jet Temperature, °C		22.2		22.2		22.2		22.2		22.2
Secondary Nozzle Air Flow, l/s		6.7		6.7		6.7		13.4		10.1
Secondary Turbulent Intensity		1.7		5.0		10.0		1.7		1.7
Secondary Length Scale, mm		3.5		3.5		3.5		3.5		3.5
Body Temperature °C	32.0	32.0	32.0	32.0	32.0	32.0	32.0	32.0	32.0	32.0
Nose Distance from Nozzle, m	0.4	0.4	0.4	0.4	0.4	0.4	0.4	0.4	0.4	0.4

(b)

Test Series	1Se	1Ce	1Sf	1Cf	1Sg	1Cg	1Sh	1Ch	1Si	1Ci
Primary Jet Temperature, °C	23.5	23.5	23.5	23.5	23.5	23.5	23.5	23.5	23.5	23.5
Primary Nozzle Air Flow, l/s	1.8	1.8	1.2	1.2	0.6	0.6	2.4	2.4	2.4	2.4
Primary Turbulent Intensity, %	1.7	1.7	1.7	1.7	1.7	1.7	1.7	1.7	1.7	1.7
Primary Length Scale, mm	3.0	3.0	3.0	3.0	3.0	3.0	3.0	3.0	3.0	3.0
Secondary Jet Temperature, °C		22.2		22.2		22.2		22.2		26.0
Secondary Nozzle Air Flow, l/s		5.1		3.4		1.7		6.7		6.7
Secondary Turbulent Intensity		1.7		1.7		1.7		1.7		1.7
Secondary Length Scale, mm		3.5		3.5		3.5		3.5		3.5
Body Temperature °C	32.0	32.0	32.0	32.0	32.0	32.0	28.0	28.0	25.0	25.0
Nose Distance from Nozzle, m	0.4	0.4	0.4	0.4	0.4	0.4	0.4	0.4	0.4	0.4

4.1 *Domain and Setup*

The domain and setup used for this section of work is the same as the validation domain and setup, See section 3.1 except for the radiation cases which is described in Section 4.8.

4.2 *Effect of Temperature Conditions at Nozzle Exit*

To quantify the effects of the PV primary jet's exit temperature on the air quality in the BZ, additional CFD test cases were carried out, emulating the experimental procedure.

The temperature of the primary jet was changed from *23.5 °C* to *20.0 °C* (cool case) and *26.0 °C* (warm case). Figure 4.1 shows the AQI profiles for different temperature values for the CFD cases 1S/C, 3S/C and 4S/C (Table 3.1) along a vertical line *10-mm* from the CSP's nose. The results show that the Primary case is more sensitive, in terms of jet deflection, to temperature changes than the Co-flow case, but neither the Co-flow nor Primary case is highly sensitive to these modest temperature changes. The same trend was shown for the experimental results (Khalifa et al., 2009). This result shows that the benefits of the Co-flow PV systems are not sensitive to typical indoor temperature variations showing the robustness of the designs.

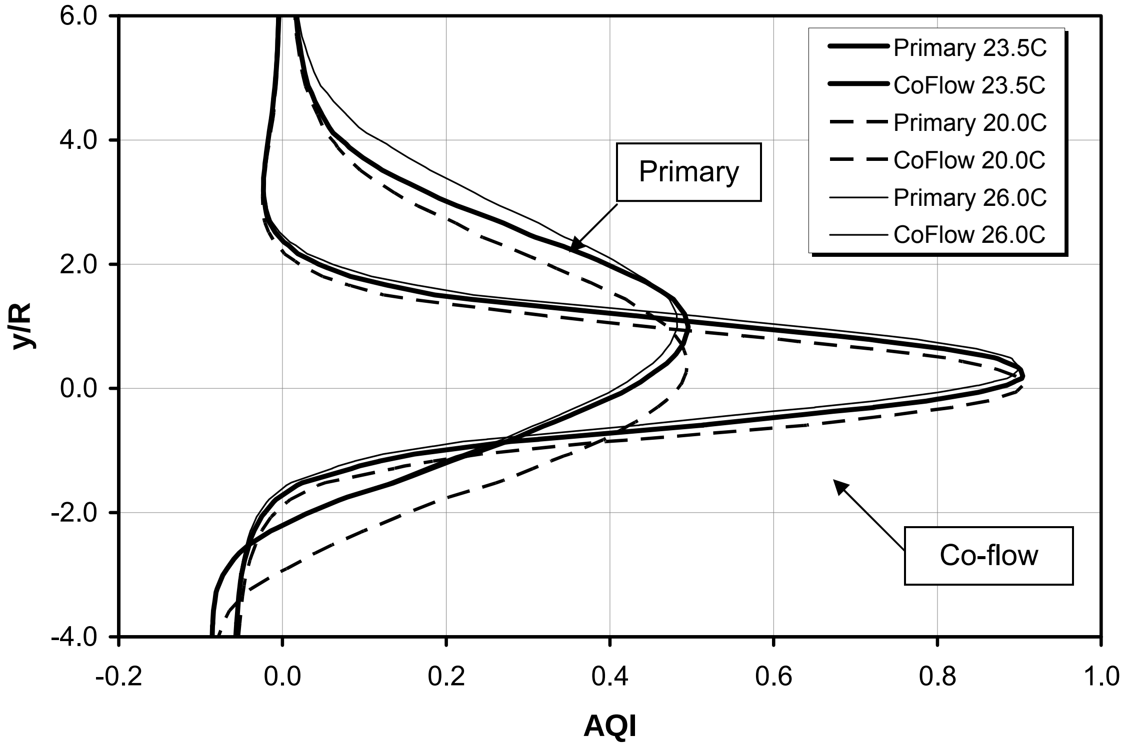

Figure 4.1: Temperature effect on AQI 10 mm from the nose.

4.3 *Effect of Turbulence Conditions at the Nozzle Exit*

To quantify the effects of nozzle exit turbulence characteristics of the PV jet on the air quality in the BZ, two additional CFD test cases were carried out. The average turbulent intensity (*Tu*) at the nozzle exit was changed from *1.7 %* to *5.0 %* and then to *10.0 %.* Figure 4.2 shows the AQI profile for different *Tu* values for the CFD cases 1S/C, 1S/Ca and 1S/Cb (Table 2) along a vertical line *10-mm* from the CSP's nose. The results show that the Co-flow case is highly sensitive to *Tu*, while the Primary case is not (The same trend was found when using other turbulence models in the k-ε family). For example, at *10.0 %* turbulent intensity, the benefit from the Co-flow case is not much higher than that of the Primary case. This can be explained by examining the turbulent kinetic energy equation given for the Realizable *k-ε* model (Shih et al., 1995) (or other *k-ε* models) as:

$$\frac{\partial}{\partial x_j}(\rho k u_j) = \frac{\partial}{\partial x_j}\left[(\mu + \frac{\mu_t}{\sigma_k})\frac{\partial k}{\partial x_j}\right] - \rho\overline{u_i^{'}u_j^{'}}\frac{\partial u_j}{\partial x_i} + \beta g_i \frac{\mu_t}{\mathrm{Pr}_t}\frac{\partial T}{\partial x_i} - \rho\varepsilon , \qquad (4.1)$$

where ρ is the fluid density, k is the turbulent kinetic energy, ε is its dissipation, u_j are the mean velocity components, μ is the molecular dynamic viscosity, μ_t is the turbulent viscosity, β is the coefficient of thermal expansion, g_i is gravitational acceleration in direction i, T is temperature, Pr_t is the turbulent Prandtl number for energy, and σ_k and σ_ε are the turbulent Prandtl numbers for k and ε, respectively. The left hand side (LHS) represents the advection terms, the first term on the right-hand-side (RHS) represents the diffusion of k by both molecular and turbulent viscosities, the 2nd term on the RHS is the production of k by the mean flow shear, the 3rd term is the production of k by buoyancy effects, and the last term is the k dissipation term described by the ε differential equation (omitted).

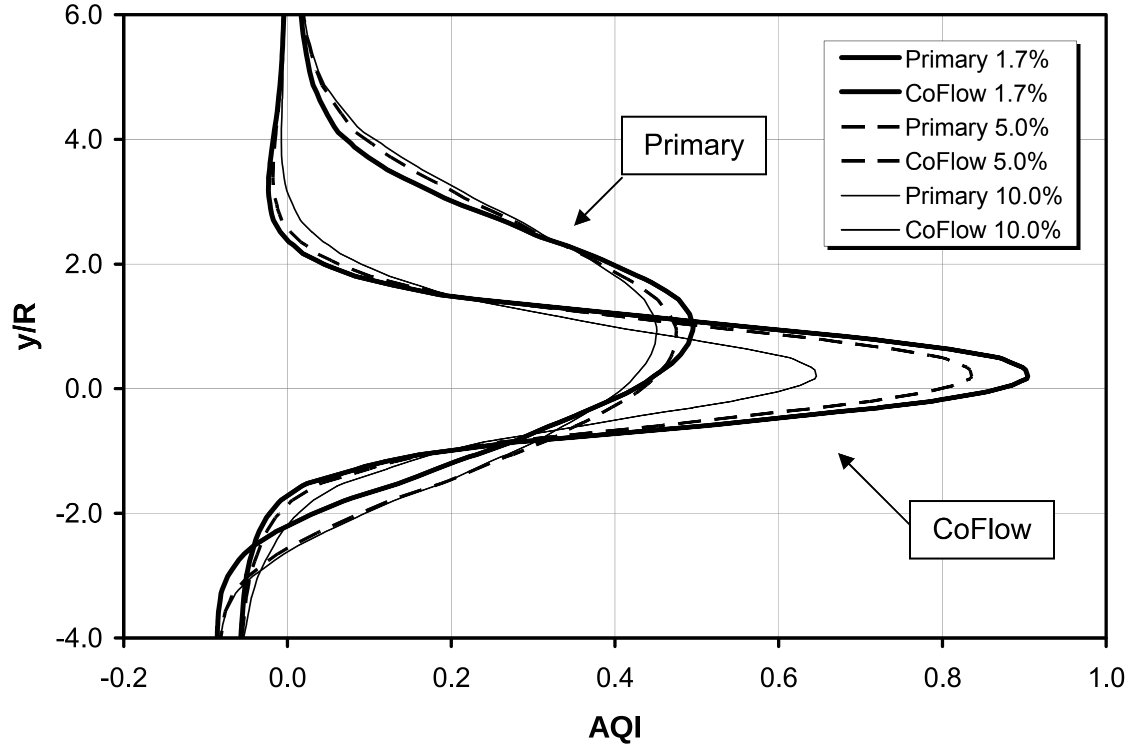

Figure 4.2: Turbulent intensity effect on AQI 10 mm from the nose.

With the addition of the secondary nozzle to the primary nozzle, the shear layer around the primary is reduced, which significantly diminishes the mean velocity gradient in the primary/secondary shear layer (as intended by the design of the Co-flow nozzle (Khalifa & Glauser, 2006), the velocity of the secondary Co-flowing jet is nearly equal to that of the primary). As a result, the shear generated turbulence (second term on the RHS of Eq. 4.1) is also greatly diminished. If k emanating from the nozzles and advected into the mixing region is also low, k in the mixing region will remain low, and along with it, the turbulent viscosity, given in the k-ε model as:

$$\mu_t = \rho C_\mu \frac{k^2}{\varepsilon}. \tag{4.2}$$

This is the fundamental advantage of the Co-flow nozzle. As *Tu* increases at the primary and secondary nozzle exits, k advected into the mixing region also increases (LHS of Eq. 4.2) and, even in the absence of the shear production term (2nd term on the RHS of Eq. 4.1) advected turbulence will diffuse across the mixing region by molecular and turbulent viscosity, and the turbulent viscosity will increase, enhancing mixing and entrainment. In a single jet surrounded by an essentially quiescent air, the production term dominates, therefore an increase in the turbulent diffusivity due to turbulence advected into the mixing region from the nozzle exit impacts the results less, whereas for the Co-flow case advection and associated diffusion are dominant and significantly impacts the flow making it more sensitive to increased *Tu* at the nozzle exit.

The sensitivity of the air quality in the BZ to the turbulent length scale was also evaluated, with the length scale at nozzle exit increased from *3 mm* to *8 mm* (*~12 % to ~32 %* of primary nozzle radius). The CFD results show that both the Co-flow and the Primary cases were insensitive to the turbulence length scale parameter in this range.

4.4 *Effect of Nozzle Flow Rate*

It is relatively easy to achieve a high AQI in the BZ by supplying a large amount of clean air from a nozzle that is close to the BZ, especially if the nozzle is large (large potential core). PV systems will almost always be used in conjunction with other ventilation systems that will provide recirculated air diluted with some clean air. If PV systems used in conjunction with general ventilation systems are to remain energy neutral (i.e., use no more energy for conditioning the outdoor, clean air than a conventional mixing ventilation system designed in accordance with ASHRAE 62 (ANSI/ASHRAE Standard 62.1-2004), the total amount of fresh air delivered from the PV system and any other ventilation system must not exceed the amount indicated by ASHRAE 62. However, it is possible to apportion the total amount of fresh air indicated by ASHRAE 62 differently between the PV and general ventilation (all the results presented so far were for providing only about one-third, i.e., *2.4 l/s*, of the ASHRAE 62 recommended amount through the PV primary nozzle). Figure 6.3 shows the effect of varying the PV flow rate on AQI in the BZ while maintaining *~5 ACH* total flow into the chamber and a total of ~ *7.5 l/s* of fresh air. The AQI shown in Figure 4.3 is the peak profile value on a vertical line *10 mm* from the nose. As the flow rate increases, the Co-flow case approaches an AQI of *1.0* (*100 %* fresh air), while the Primary case approaches an AQI of *0.7*. Figure 6.3 also shows that the Co-flow nozzle is beneficial over the Primary nozzle for all flow rates, with the largest improvement being at around *2.4 l/s*.

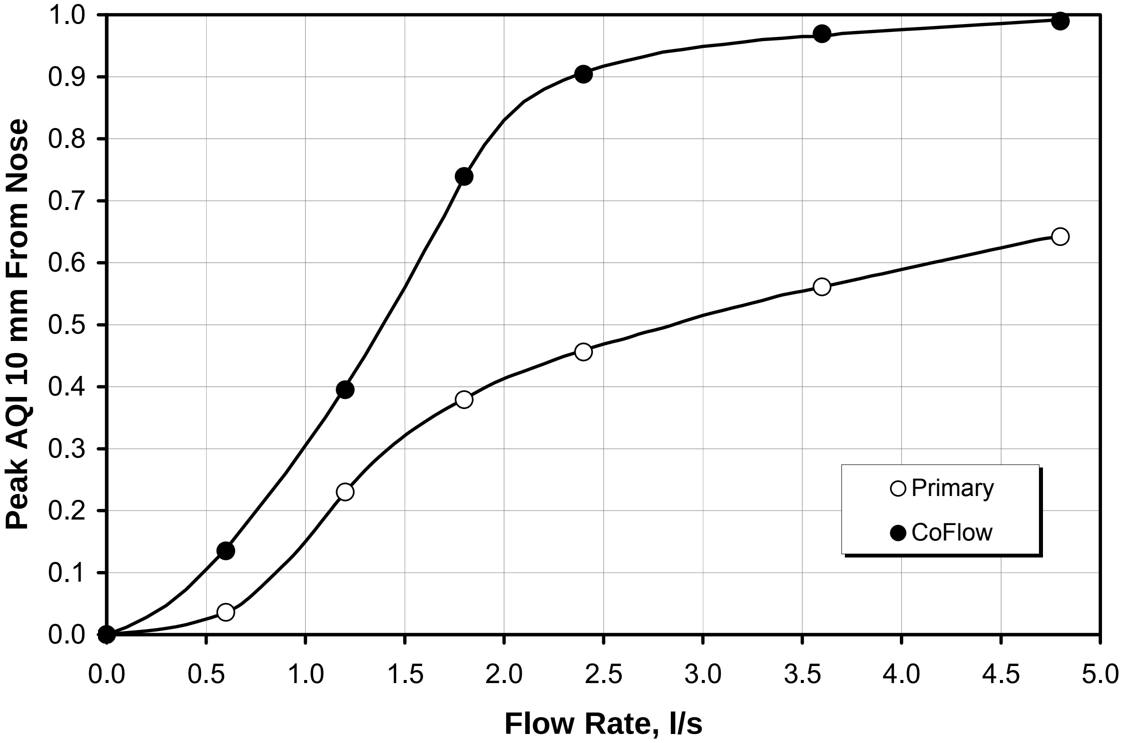

Figure 4.3: Effect of nozzle flow rate on AQI. All cases at 5 ACH total air supply.

For circular jets, as in the one used for PV in this work, the Navier-Stokes equation for the flow in the x direction can be described as,

$$u\frac{\partial u}{\partial x}+v\frac{\partial u}{\partial r}=-\frac{1}{\rho}\frac{\partial P}{\partial x}+\nu\left(\frac{\partial^2 u}{\partial x^2}+\frac{1}{r}\frac{\partial u}{\partial r}+\frac{\partial^2 u}{\partial r^2}\right)-\left[\frac{\partial}{\partial x}(\overline{u'^2})+\frac{\partial}{\partial r}(\overline{u'v'})+\frac{\overline{u'v'}}{r}\right] \tag{4.3}$$

in cylindrical coordinates where *x* and *r* are the directions of *u* and *v* and the superscript (′) indicates the fluctuating components. For high Re flow (Re>3 x 10^4), that is, the inertial forces are much larger than the viscous forces, the viscous stresses in the developed region are much smaller than the corresponding turbulent stresses and can be neglected. With this assumption and other manipulations of this equation a universal expression for the centerline velocity decay can be developed (Appendix A). However, for low and transitional Re jets, the viscous terms are of more importance and there is a clear dependence of centerline velocity, specifically the potential core length, on Re, which has been shown by many authors (Lee et al., 1997; Awbi, 2007; Todde et al., 2009; Xia & Lam, 2009; Kwon & Seo, 2005; Bogey & Bailly, 2006). For this work, the effect of Re on potential core length of a PV nozzle is investigated for low Re flows.

Fully turbulent jets occur when Reynolds Numbers (Re) are greater than *30,000* (Awbi, 2007) and are independent of initial conditions (exit Re). The Re shown in Figure 4.3 range from *2,053* to *8,512* and do not fall within the Re independent region. In this range, the characteristics of flow development are found to be Re dependent. The results in Figure 4.3 and results from Lee et al. (2007) were used to predict peak AQI values for a range of Re from *0* to *25,000* and are shown in Figure 4.4. The 'Calculated' values are those resulting from CFD simulations and the 'Predicted' values are those given by a line to fit the data. For a single jet, this figure shows a clear AQI dependence on Re for low Re flow and becomes independent of Re for Re >*20,000*. When looking at the Co-flow prediction, the potential core length is only a function of Re for Re < *10,000* (less than half the region in which the Primary nozzle is affected). This is an important characteristic of the Co-flow nozzle. Since AQI is less dependent on Re, the performance of the Co-flow nozzle can be maximized at much lower flow rates, therefore reducing draught for the individual. For the Primary nozzle to deliver its maximum AQI (0.78) to the BZ the Re has to be >*18,000* (> *10 l/s* fresh air flow rate), whereas the Co-flow nozzle could produce the same AQI at a Re of *3,080* (*1.8 l/s* fresh air flow rate). To this point, it is clear that an AQI value of *1.0* (*100 %* fresh air) could never be reached by the Primary nozzle at this distance (*41 cm*) regardless of how much the flow rate was increased due to its limitations of a circular jet becoming Re independent in the fully turbulent region.

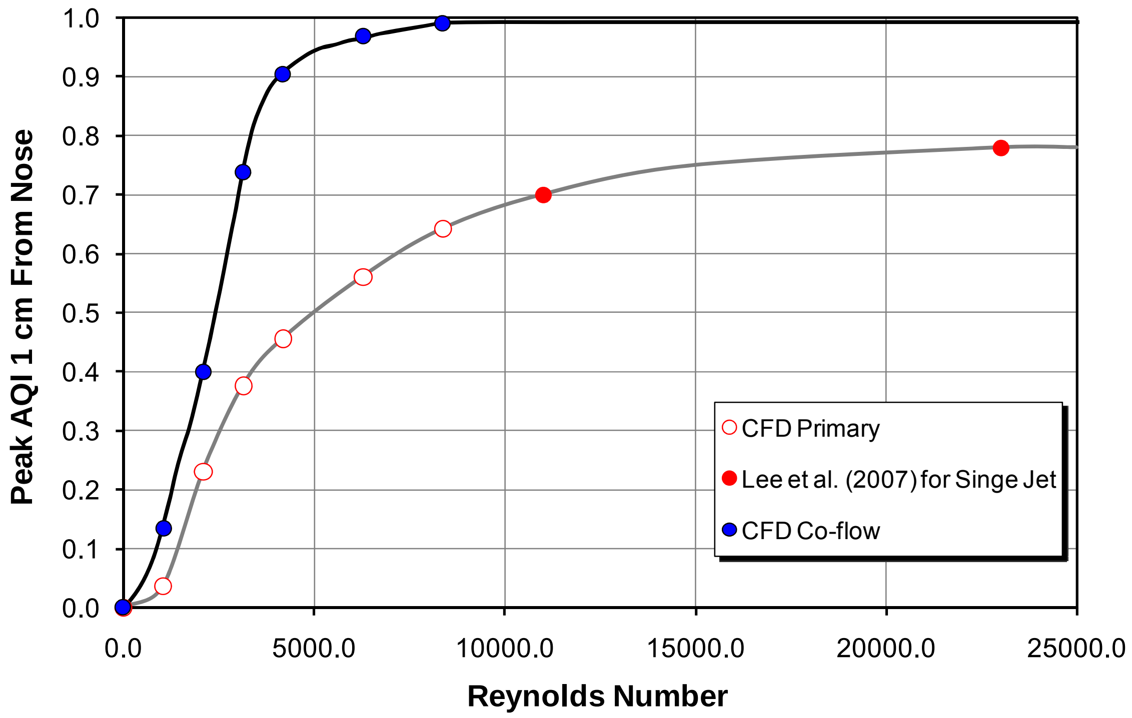

Figure 4.4: Prediction of AQI as a function of Re.

To examine the flow development dependency on Re further, the potential core length was plotted as a function of x/D for various Re as shown in Figure 4.5 for centerline velocity and Figure 4.6 for centerline AQI values. Both are compared to experimental results given by Lee et al. (2007) for low Re free jets. These figures clearly show the change in potential core length with a change in Re. For the lowest Re tested (*2,053*) the potential core length is *1.5D* and increases for the highest Re tested (*8,215*) to *~4.5D*. This is in quantitative agreement with the results given for turbulent jets, where the potential core length decreases with decreasing Re (Lee et al., 1997; Awbi, 2007). Lee et al. (2007) shows that the potential core length of a jet with an exit Re of *11,000* is *~4D* and increases for a jet with exit Re of 50,000 to *5D*. Table 4.2 shows a summary of potential core lengths from this work as well as laminar, transitional and turbulent jets from the literature. Table 4.2 shows that longer potential core lengths (which could lead to higher AQI values in the BZ) for laminar and transitional jets. Laminar jets can produce longer potential core lengths, but it is unpractical to assume that PV nozzles are able to deliver laminar jets for typical PV jet Re in realistic setups and conditions. Laminar jets were found to exist at Re of up to 40,000 in completely controlled experimental environments, but would become turbulent with the slightest disturbance (Kuethe & Schetzer, 1959). In the indoor environment, people move around and there is cross flow between ventilation systems that would produce significant disturbances near the PV jet which would make the possibility of laminar jets unlikely. Kuethe & Schetzer (1959) also showed that jets transitioned to turbulence at a Re of 2,000 for realistic environments.

Figure 4.5 shows the velocity tends to zero as the jet approaches the CSPs head, whereas Figure 4.6 does not show this trend for concentration profiles. Another difference between the two plots is that the mean concentration at the jet centerline starts to drop slightly earlier for the concentration profiles than for the velocity profiles. This result is consistent with findings of Xia & Lam (2009), Papantoniou & List (1989) and Davidson & Pun (1999). Xi & Lam (2009) also reported that the shortening of the concentration potential core lengths compared to velocity potential core lengths does not occur. This is because the Sc_t used for this case is less than *1.0*, indicating that the momentum diffusivity is lower than the species diffusivity.

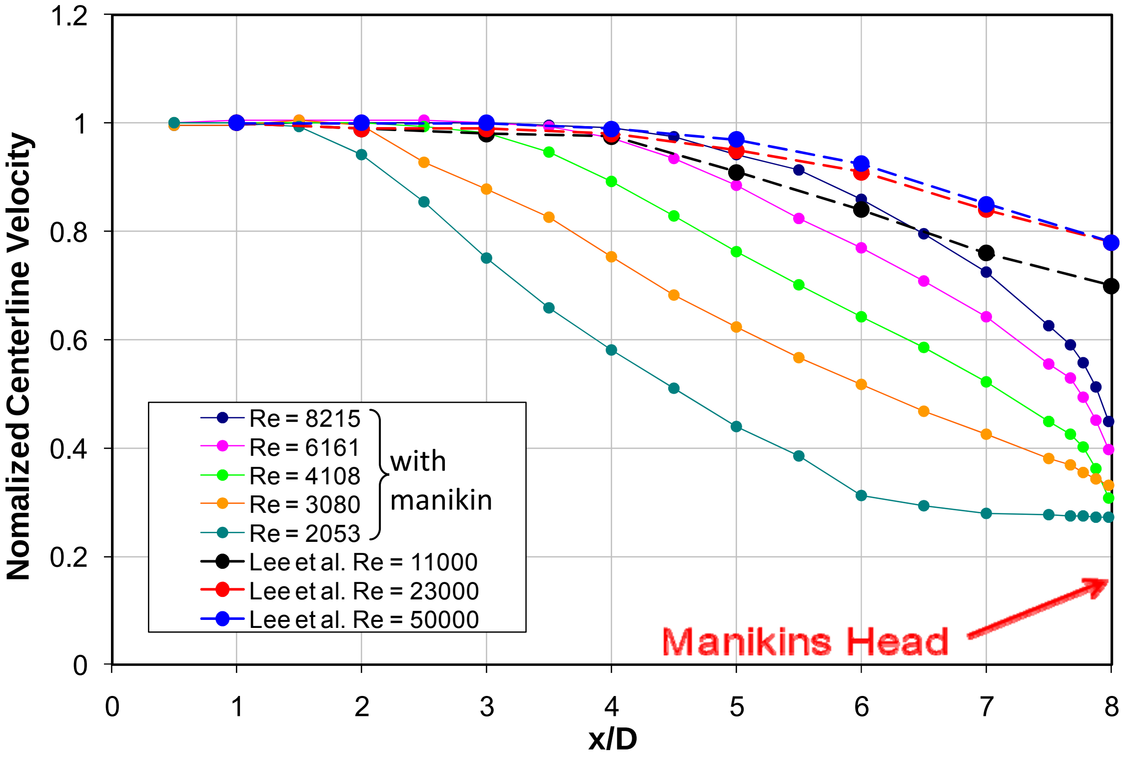

Figure 4.5: Centerline Velocity of the Primary PV jet as it approaches the CSPs head for various Re compared to low Re jet studies by Lee et al. (2007).

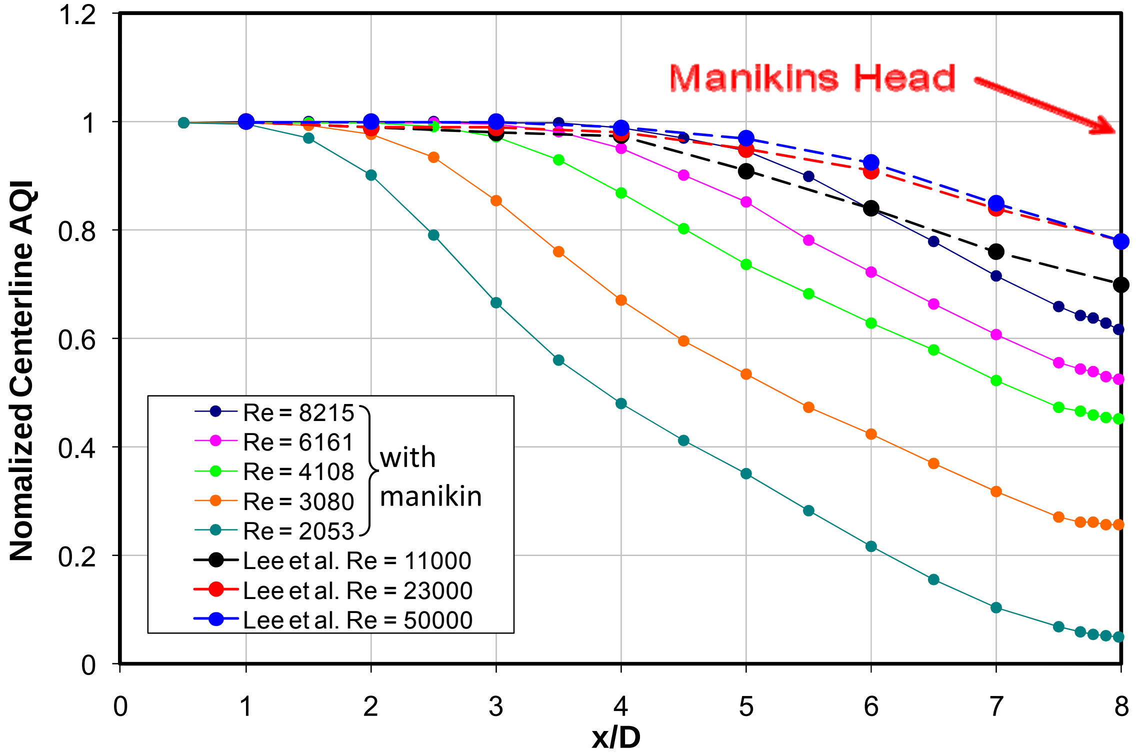

Figure 4.6: Centerline AQI of the Primary PV jet as it approaches the CSPs head for various Re compared to low Re jet studies by Lee et al. (2007).

To determine the optimal nozzle design, the results in Figure 6.5 are reconfigured and shown in Figure 4.7. Figure 4.7 shows the potential core length as a function of Re for low Re flows. These results were used to find the optimal nozzle diameter for different flow rates. The curve fit shown in Figure 4.7 was used to calculate the potential core length for a fixed flow rate as a function of Re by varying the nozzle diameter. This was done for three reasonable indoor fresh air flow rates of *2.4 l/s*, *3.6 l/s* and *4.8 l/s* and the results are shown in Figure 4.8. The optimal diameter of a PV nozzle at a fresh air flow rate of *2.4 l/s* is *~3-4 in*, for *3.6 l/s* it is *~ 4-5 in* and for *4.8 l/s* it is *~6-7 in*. The *2 in* diameter nozzle that is used for this work is very close to optimal at a fresh air flow rate of *2.4 l/s* and was chosen based on limitations of the stereo lithography system used for making the nozzle, not optimal design.

Table 4.2: Summary of potential core lengths (PCL) for turbulent (red), transitional (purple) and laminar jets (blue).

Author	Year	Re	PCL
Russo & Khalifa (CFD)		2053	1
		3080	2
		4108	3
		6161	3.5
		8215	4.5
Todde et al. 2009	2009	850	9.5
		1050	7.5
		1350	6
		1620	6
		2175	5.5
		2700	5.5
		4050	5
		5400	5
		6750	5
Xia & Lam	2009	~1000	9.5
		~2000	5.5
		3000-5000	4.5
Bogey & Bailly	2006	1700	8
		2500	6.5
		5000	5.7
		10000	5.4
		400000	5.1
Lee et al. 1997	1997	11000	4.5
		23000	5
		50000	5
Symons & Labus	1971	255	<3
		437	<3
		925	<3
		1255	<3
		1839	<3

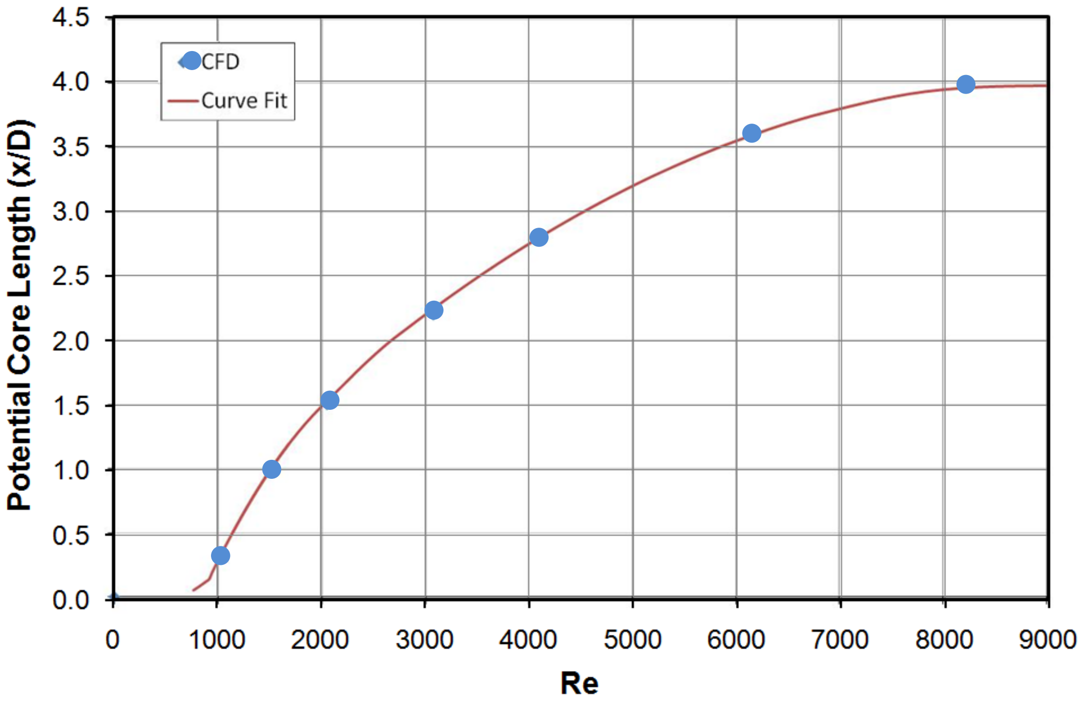

Figure 4.7: Potential core length as a function of Re for low Re flow.

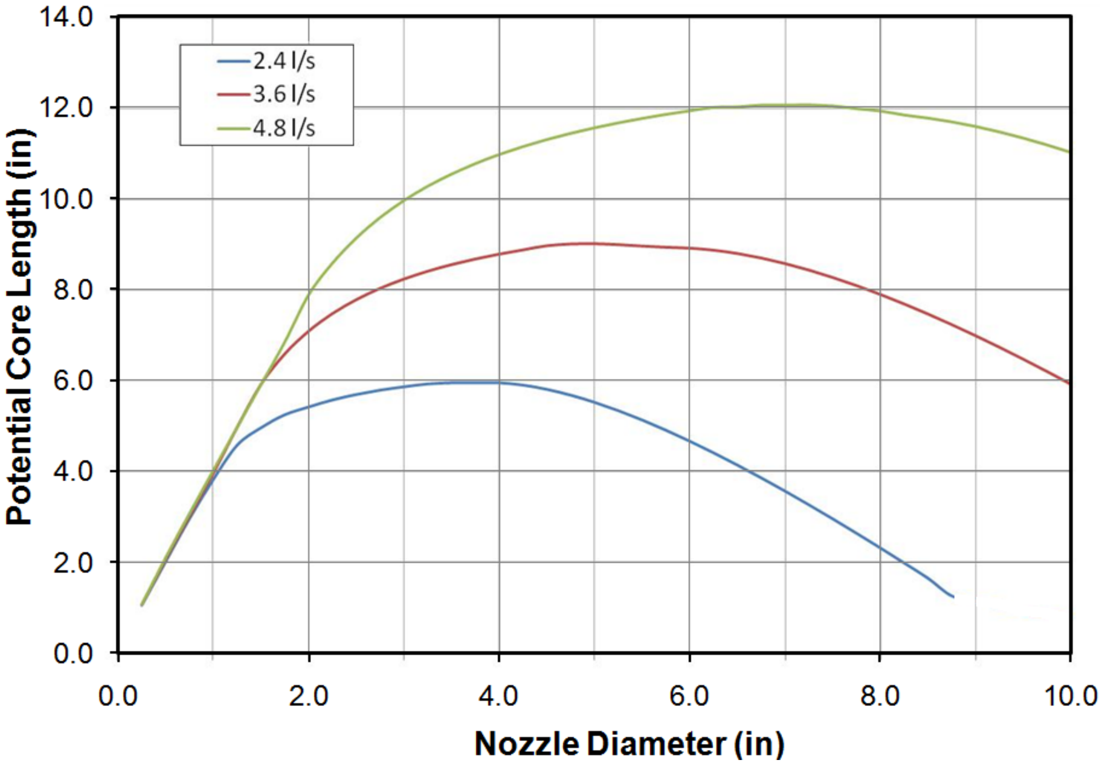

Figure 4.8: Potential core length predictions as a function of nozzle diameter for various flow rates.

4.5 *Effect of Strength of Thermal Plume (CSP surface temperature)*

The insulation that clothing provides determines the exterior surface temperature in contact with room air and therefore the strength of the thermal plume. To study this effect, two additional CFD simulations were run with the CSP temperature at *28.0* and *25.0 ºC* (cases 1Sh/Ch and 1Si/1Ci in Table 6.1, respectively). Figure 4.9 shows that, when the CSP surface temperature is decreased, the AQI profile deflection is decreased for the Primary case (the deflection in the Co-flow case was small in all cases). This can be explained by the fact that with the lower body temperature, the thermal plume is weaker and hence its influence on the PV jet is less pronounced. For decreased CSP surface temperature the profiles appears to show that the jet cross section is less deformed; the cross section of the jet maintains its roundness longer as the body temperature is decreased. With the higher CSP temperature, the jet cross section is noticeably more deformed (stretched in the horizontal direction), as discussed earlier in Figure 4.1. It has already been shown that the interaction of the thermal plume and the Co-flow jet was insignificant due to the higher total momentum of the co-flowing jets, so increasing the *clo* value (clothing insulation), which weakens the thermal plume, shows little or no effect on the concentration profile for the Co-flow case. For both cases the magnitude of peak AQI was relatively unaffected by changing the strength of the thermal plume. This is in contrast to Melikov & Kaczmarczyk (2007), who have shown that the clothing insulation can significantly affect the air quality in the BZ. This discrepancy can be explained by how the measurement of air quality was taken in the experiment conducted by Melikov & Kaczmarczyk, who recorded the air quality only at a single fixed point and made no adjustment to the nozzle angle, which could miss the peak value.

In this work, the air quality was examined along a vertical line that shows the change in the peak AQI position, which can be adjusted relative to the CSP's BZ by realigning the nozzle slightly up or down.

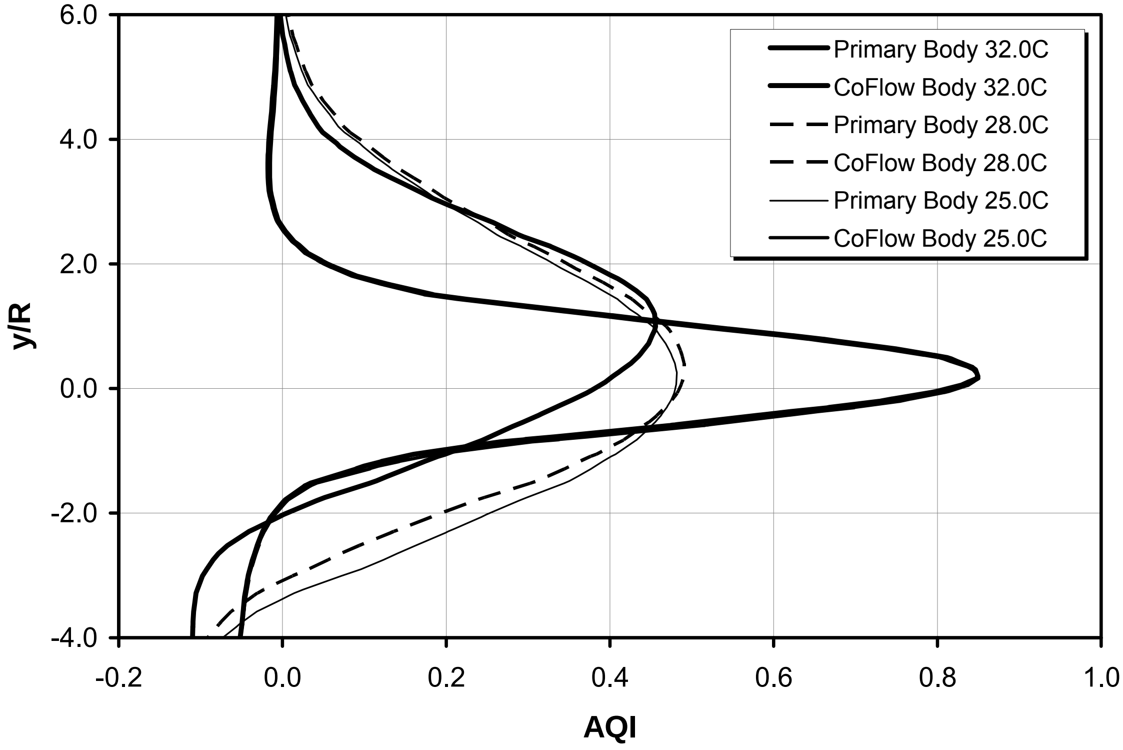

Figure 4.9: Effect of clothing insulation on AQI. All other conditions were identical (Co-flow lines all fall on top of one another).

4.6 *Effect of skin wettedness*

Humans excrete sweat (mostly water) through sweat glands in the skin as a means of thermoregulation. The evaporation of sweat from the skin is a mechanism that the body uses to cool itself through the latent heat of evaporation of water. The evaporation of sweat changes the moisture content in the air around the body and decreases the density of the surrounding air, which increases the strength of the rising thermal plume. At *32 ˚C* (body temperature) there is *3.3 %* water vapor in the air. When computationally modeling the details of a CSP and the BZ with PV, the simulation becomes very complex and computationally expensive. Other aspects, such as sweating, can add another order to the degree of difficulty of the problem and are often neglected because of their complexity. To determine if sweating can be ignored in a typical office setup, a case was studied to determine the effect of skin moisture on AQI. For this, water vapor was modeled at the CSP surface to covering either 0%, 6% or 50% of the body.

AQI was used to monitor the effect of skin moisture (sweating) of the CSP. Different skin wettedness' (w), which is the percentage of the skin that releases moisture, were applied as BCs to the CSP's surface. Three cases were run for comparison: *0 %* wettedness (no moisture), *6 %* wettedness (typical value with none/light activity) and *50 %* wettedness (when sweat would begin to drip from the body).

Figure 4.10 shows the AQI profiles along a vertical line *1 cm* from the CSP's nose for the Primary and Co-flow PV systems compared to experimental data for a case with no skin moisture. There is less than a *1 %* change in the AQI profiles for the three different skin wettedness cases for both the Primary and Co-flow PV systems. The results show that skin moisture has no effect on the air quality in the BZ when using PV.

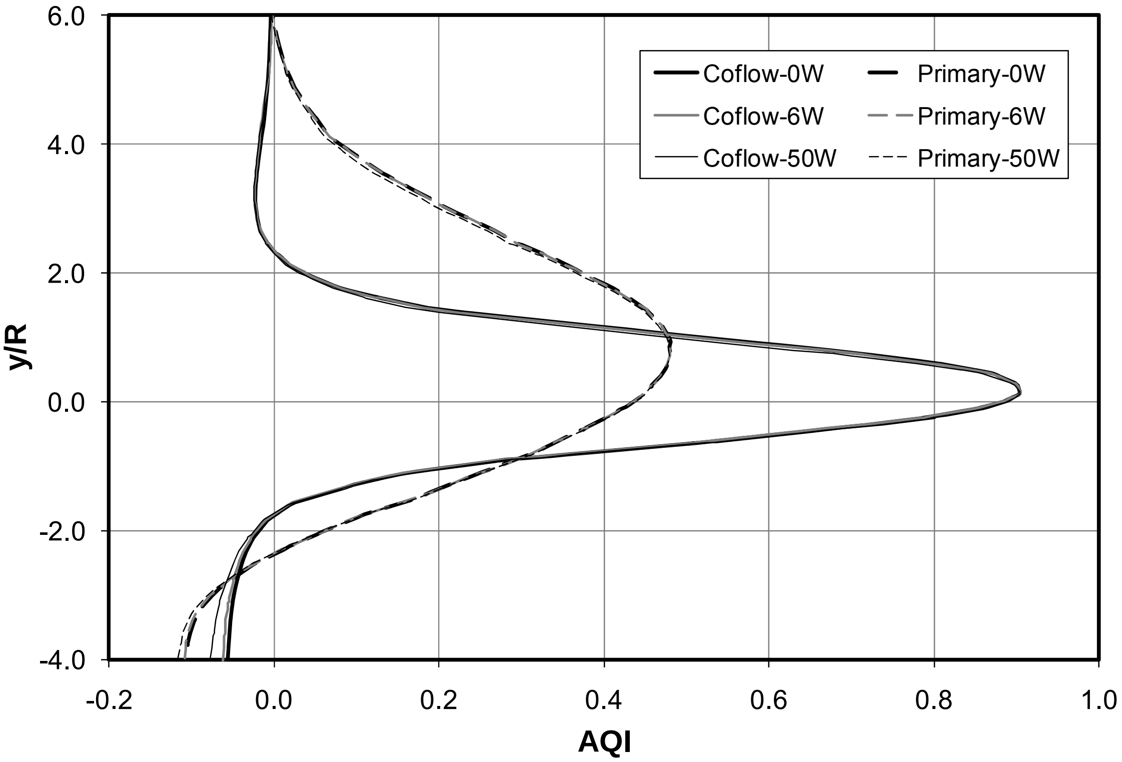

Figure 4.10: AQI profile 1 cm from CSP's nose for *0 %* skin wettedness, *6 %* skin wettedness and *50 %* skin wittedness.

Figure 4.11 looks into the effects of skin moisture further. Figure 4.11 shows the velocity of the thermal plume around a CSP for the three skin wittedness BCs without PV. Compared to *0 %* skin wettedness, increasing the skin wettedness to *50 %* only resulted in a *9 %* increase in momentum. This increase in momentum is not expected in typical office situations since it is rare that a person would be sweating to the point of water dripping from the skin in these types of settings. Table 4.3 shows how these results compare to a change in body temperature for *0 %* relative humidity and *50 %* relative humidity. It is shown that the effect of the change in surface temperatures (up to *47 %* momentum difference) is much greater than that from a change in skin wittedness (at most *9 %* momentum difference). A few degree variation in skin temperature from day to day is typical depending on clothing and other thermal factors, where as *50 %* skin wittedness is not expected. The results also show that modeling 50% RH in the room decreases the momentum of the thermal plume by ~3%, which is still small compared to a change in skin surface temperature, and reduces the effect of skin wittedness and can be ignored.

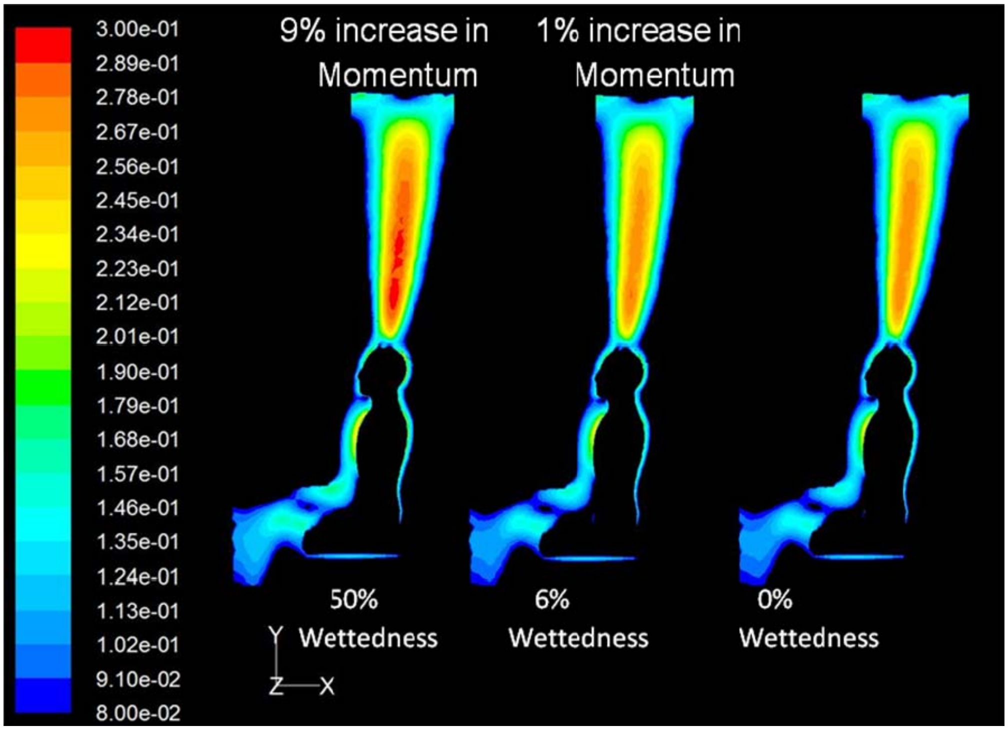

Figure 4.11: Velocity magnitude contours for different skin wittedness and the resulting increase in the momentum.

From these results it was determined that adding complex, realistic features, such as sweating, to a CFD model of the BZ of a CSP does not improve the results of the solution. The results show that sweating can be ignored when studying the BZ using PV.

Table 4.3: How the effect of skin wettedness compares to changes in other BCs that affect the strength of the thermal plume.

	Skin Wettedness	Body Temperature	Relative Humidity	Momentum Difference
Case 1	0%	32°C	0%	Base Line
Case 2	6%	32°C	0%	1%
Case 3	50%	32°C	0%	9%
Case 4	0%	28°C	0%	-47%
Case 5	0%	32°C	50%	3%
Case 6	6%	32°C	50%	<1%
Case 7	50%	32°C	50%	6%
Case 8	0%	28°C	50%	-47%

4.7 Effect of breathing simulation

The indoor environment has many pollutant sources including: building materials, furnishings, cleaning products, air cleaning devices, solvents, flame retardant, adhesives, paint, plasticizer, UV lighting, photocopiers and laser printers (Uhde & Salthammer, 2007). These sources can emit species that are harmful themselves or that could react with other emitted species to create harmful products when inhaled. These factors make the proper modeling of inhalation exposure highly significant.

To properly model inhalation exposure, it is important to capture realistic details in the BZ when conducting experiments or carrying out computational simulations. When using a computation model, modeling realistic details of CSP's in the indoor environment have been shown to have little effect on the overall airflow in a room, but have been shown to significantly affect the local results in the thermal plume and the BZ. Important features that need to be simulated or are needed for the simulation have been outlined in detail in

Dygert et al. (2009) and authors therein. Some important details include: detailed CSP geometry, high resolution grid, turbulence model, surrounding furniture and thermal BCs. When computationally modeling the details of a CSP and the BZ, the simulation is very complex and computationally expensive. With the addition of a PV system the complexity of the simulation increases due to the need to accurately capture the interaction of the rising thermal plume around the CSP with the PV jet aimed toward the BZ. To determine inhalation exposure, a breathing model must also be simulated in the model. The addition of unsteady breathing can add another order to the degree of difficulty of the problem which makes the understanding of different breathing simulation methods important.

Breathing CSP's have been used for many experimental and computational applications including room air distribution (Cermak and Melikov 2006), for studying PV systems (Melikov et al. 2002; Melikov, 2004), inter-person exposure (Gao and Niu, 2006; Cermak and Melikov, 2003, 2006) and studying inhalation contaminants (Hayashi et al., 2002; Zhu et al., 2005; Murakami, 2004). The method of simulating breathing ranges from no breathing with an assumed volume of air for inhalation, no breathing with a point used for the assumed inhaled air concentration, steady state inhalation, simplified unsteady breathing profiles (step or sinusoidal curve) and realistic breathing profiles. In this paper we compare different simulation methods for a thermal, breathing CSP with and without PV to see if some complex aspects of the simulation can be ignored. First we study the effect of four breathing simulation methods and their effect on iF with and without PV and the effect of the condition of the exhaled air. Then, we look at the effect of a source location on the iF with different breathing method without PV.

4.7.1 Detailed considerations of the BZ

Further validation is given here for the inhalation region. Computational air quality at the mouth and nose were compared to experimental points within the nostril and mouth, respectively. An additional comparison is given to determine the effect of different breathing simulation methods on the BZ air quality by comparing air quality profiles in the BZ with experimental data using the same setup. The breathing simulation methods compared are steady state no breathing, steady state inhalation and unsteady sinusoidal breathing. Details of the experimental setup and results are given in Khalifa et al. (2009). For this simulation and experiment, SF_6 was supplied through the floor diffuser and the secondary nozzle, while the primary air was kept free of any species. Results were normalized to give a profile of AQI. Computational AQI values were found for the nostril and mouth of the CSP and compared with experimentally measured AQI values. AQI profiles located *10 mm* from the CSP's nose on the symmetry plane were also generated and compared against test data.

Next, inhalation exposure variation due to different breathing simulation methods was determined. This was done for a case without PV (Case 1), a single jet PV system (Case 2) and the Co-flow jet PV system (Case 3) (Khalifa & Glauser, 2006). In these cases, a contaminant entered the room through the ventilation system and the amount inhaled by the CSP was monitored. The breathing methods that are studied for these cases are: 1) steady state, no breathing using the Brohus (1997) hemisphere method, 2) steady state inhalation (*6 lpm*), 3) unsteady, sinusoidal breathing (*6 lpm*) and 4) unsteady, realistic breathing (*6 lpm*). 6 lpm represents the inhalation rate for the full space (3 lpm through each nostril). For the hemisphere method the average concentration of a hemisphere representing the inhaled air was used to determine the inhalation concentration. A *1.2 cm* sphere radius located in the BZ adjacent to the nostril was used to determine the inhalation concentration. During unsteady breathing the exhaled air was set to *34 °C* and the profiles are given in Figure 4.12.

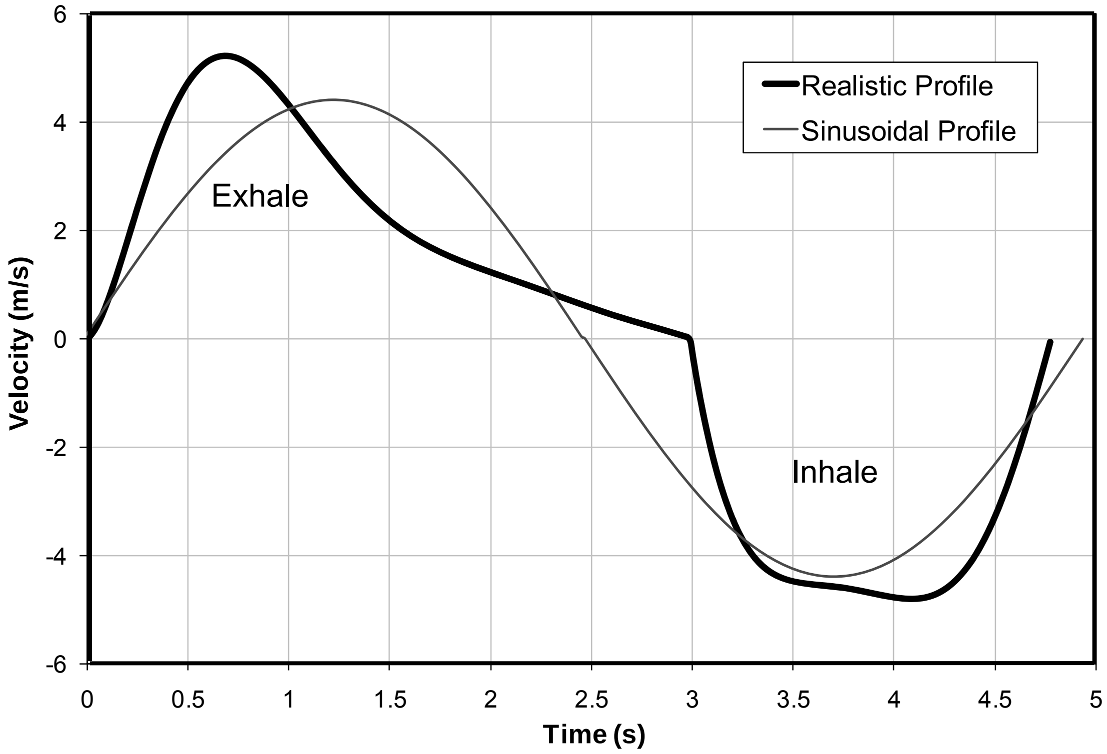

Figure 4.12: Sinusoidal and realistic breathing profiles.

In this work, nostrils are approximated as circular holes with opening area of *38.5 mm*^{2}(each) and was based on the nostril size of the manikin described in the CFD validation experimental study, and air exits the nostrils at *30°* from the sagittal plane and *45°* from the coronal plane. This nostril size is smaller than the *113 mm*^{2} used by Bjorn and Nielsen (2002), and smaller than *75 mm*^{2} used by Gao and Niu (2006), it is the same as that used by Melikov and Kaczmarcyzk (2007) and slightly smaller than the *50.2 mm*^{2} recommended by Melikov (2004). The angles at which the nostril is oriented are the same as those used by Bjorn and Nielsen (2002) and Melikov (2004) and are slightly different from the 30˚ from the sagittal and coronal plane used by Gao and Nui (2006). Due to variations from person to person these values are considered acceptable.

For the previously described unsteady cases the exhaled air concentration was equal to the inhaled air concentration, however, this is not always the case. When breathing, the concentration of CO_2 in exhaled air is *100* times higher than the CO_2 in inhaled air. Based on this, the effect of the exhaled air concentration was examined for the unsteady breathing cycles. To give insight into re-inhalation and the importance of modeling exhaled air, a case that uses the same exhaled air concentration as inhaled was simulated and compared to a case where the exhaled air concentration was *100* times that of the inhaled air.

Next, inhalation through the mouth for the steady state, no breathing hemisphere case, steady state inhalation case and unsteady, sinusoidal breathing case were simulated and compared to the nasal breathing methods at *6 lpm* with and without PV. For oral breathing air was exhaled horizontally from the CSP's mouth through a semi-ellipsoid opening of $241.5\ mm^2$. This value is very similar to the $250\ mm^2$ used by Gao and Nui (2006), smaller than the $340\ mm^2$ used by Hayashi et al. (2002), larger than the $158\ mm^2$ used by Melikov and Kaczmarczyk (2007) and larger than the $100.4\ mm^2$ recommended by Melikov (2004). Due to variations from person to person these values are considered acceptable. Finally, exhaled air concentrations of *100* times the inhaled concentration was used for oral and nasal breathing and compared to a case that used the inhaled air concentration as the exhaled air concentration.

4.7.2 Experimental Comparison

Figure 4.13 shows the comparison of experimental and CFD results of AQI values in the nose and mouth for the Co-flow and Primary PV system. Table 4.4 summarizes the values for the experimental and computational cases and produces the percent difference between them for the Co-flow and Primary PV systems. There is less than a *7.5 %* difference for all cases. Better agreement is achieved for nasal values for both the Co-flow and Primary PV system than for oral values. The experimental results are only measured at a single point whereas the computational results are averaged over the center of each opening and could be the reason for any disagreement between CFD and experiment. There is a much larger opening for the mouth than nostril, which could be the reason for the greater difference in oral comparisons. Also, and probably more importantly, a slight difference in the alignment of the PV jets between the experimental and the CFD could explain the difference. With this, the air quality in the BZ is shown to have good agreement with experimental data and is the basis of using steady experimental local concentration results for further validation of this work.

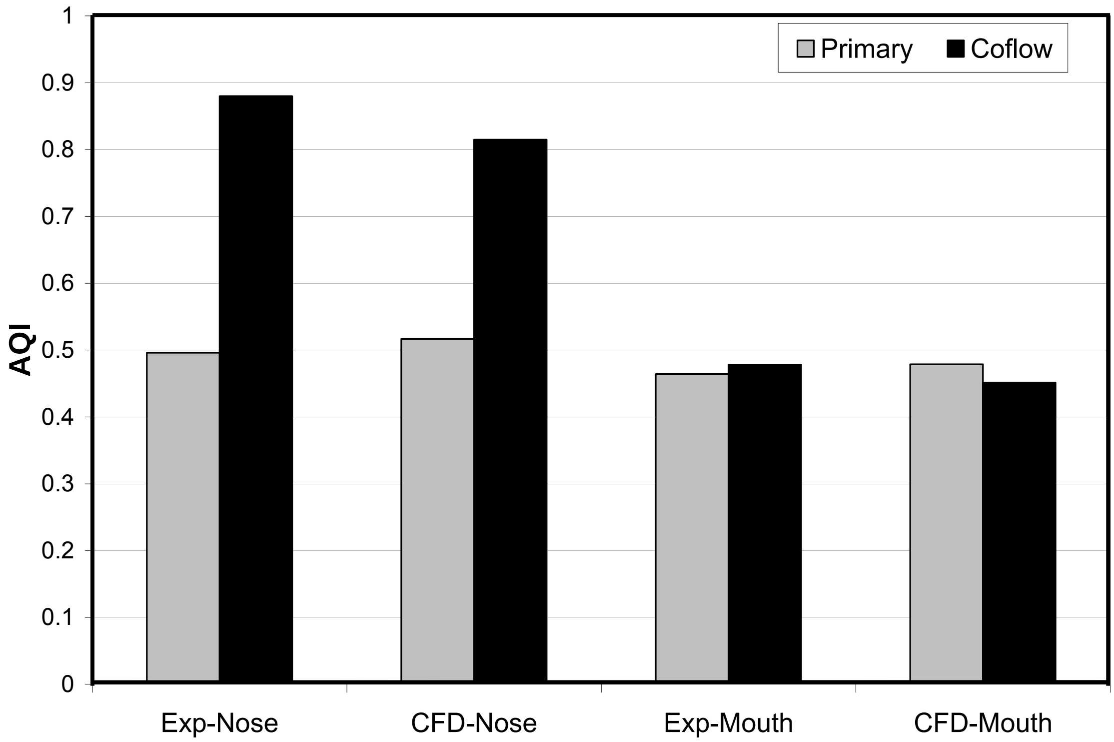

Figure 4.13: Bar chart showing the differences between experimental and computational values at the nose and mouth of a CSP for the Co-flow and Primary PV systems.

Table 4.4: Summary of experimental and computational values with the percentage differences for the Co-flow and Primary PV systems.

	Coflow AQI			Primary AQI		
	Exp	CFD	% diff	Exp	CFD	% diff
Nose	0.4961	0.5166	4.13223	0.4642	0.4789	3.16674
Mouth	0.88	0.8147	-7.4205	0.4783	0.4516	-5.5823

Figure 4.14 shows the comparison of AQI profiles *1 cm* from the CSPs nose for three breathing methods and experimental results with no breathing. The computational data is

for different breathing simulation methods including: steady state no breathing, steady state inhalation, and unsteady sinusoidal breathing. For the unsteady breathing method a profile is given for three different positions in the breathing cycle; peak inhalation, peak exhalation and the position between the two where there is zero inhalation or exhalation. Only slight changes can be seen in the AQI profiles with the variation of breathing simulation method for the peak exhalation profile during unsteady sinusoidal breathing. This difference can be attributed to the disturbance of air from the exhalation jet. On inhalation, however, this disturbance has disappeared and reverts back to the steady state results. This proves that the breathing method has little to no effect on the concentration profile *10 mm* from the nose and confirms Brohus's (1997) hemisphere assumption. Further, the differences caused by unsteady breathing are small and give little additional meaning to the results.

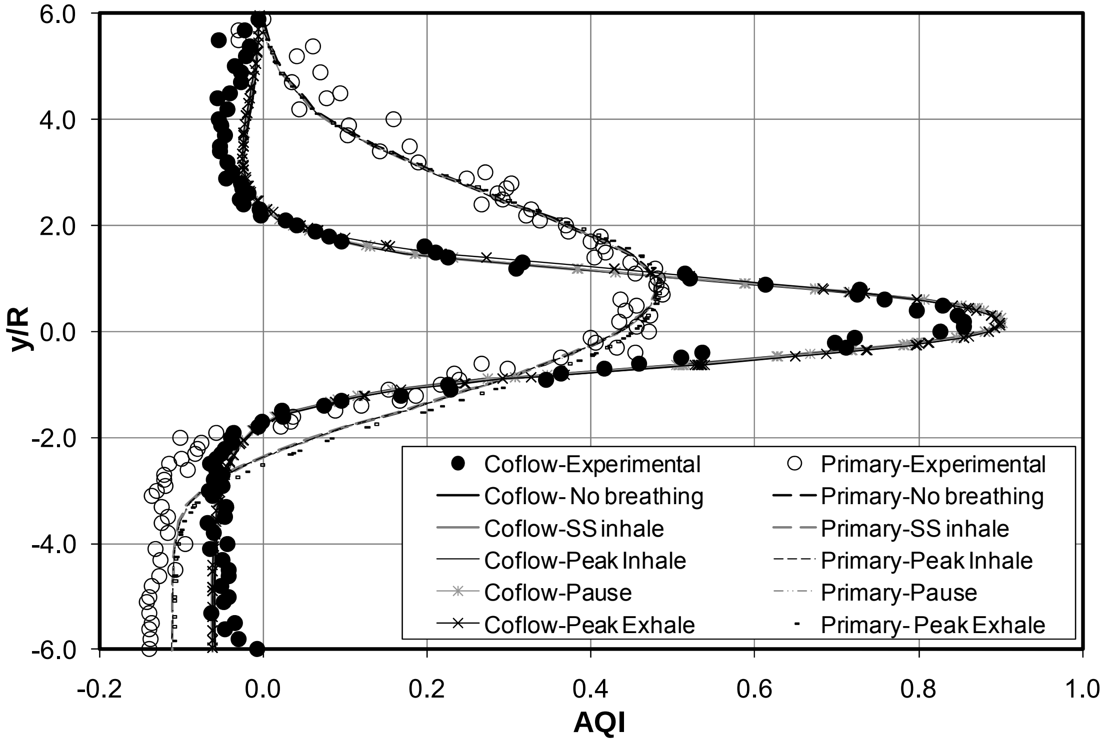

Figure 4.14: Experimental and computational AQI profiles 1cm from the CSPs nose.

4.7.3 Breathing Method with Contaminated Recirculated Air

Figure 4.15 shows the calculated iF for the four breathing methods for Case 1, 2 and 3. The iF for Case 1 varies between *5230* and *5290* per million (~*1 %* change). For case 2 and 3 the iF vary ~*5 %* from *2700* to *2850* and *2320* to *2200* per million, respectively. The results from Case 1, 2 and 3 show that there are negligible differences between the four breathing simulation methods used when examining the quality of air through nasal inhalation with or without PV.

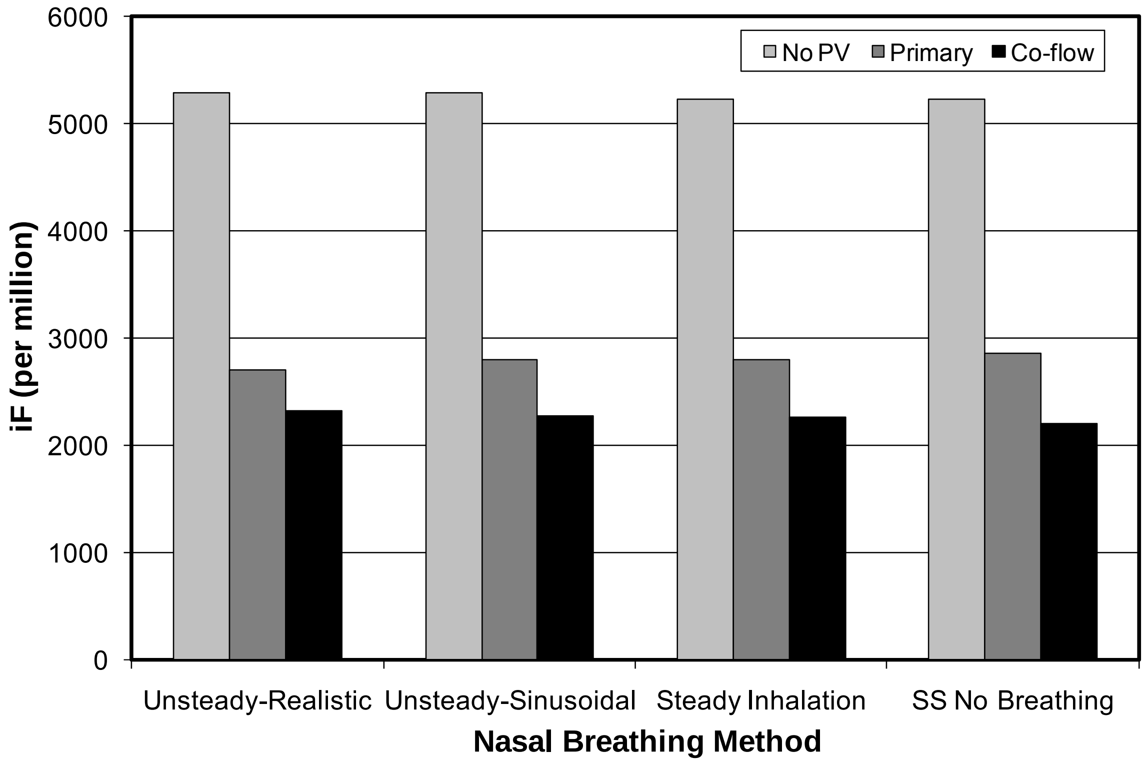

Figure 4.15: iF for different breathing methods.

Simulating a pause in the realistic profile did not impact the iF for any case. Further, the results show that the air quality in the BZ of a non-breathing CSP is the same as the inhalation air quality of a breathing CSP. This is consistent with the results of Melikov (2007) where it was found that the air quality above the lip (<*0.01 m* away) with a non-breathing manikin is the same as the inhaled air of a breathing manikin and that it is not important to simulate breathing when examining the quality of the inhaled air.

Figure 4.16 shows the comparison for the steady state inhalation breathing simulation method with a body surface temperature of *32 °C* and *28 °C*. There is a *2 %* change or less when comparing iF with different body temperatures with steady inhalation. This shows that when using contaminated recirculated air as the inhalation component there is a negligible effect due to body temperature.

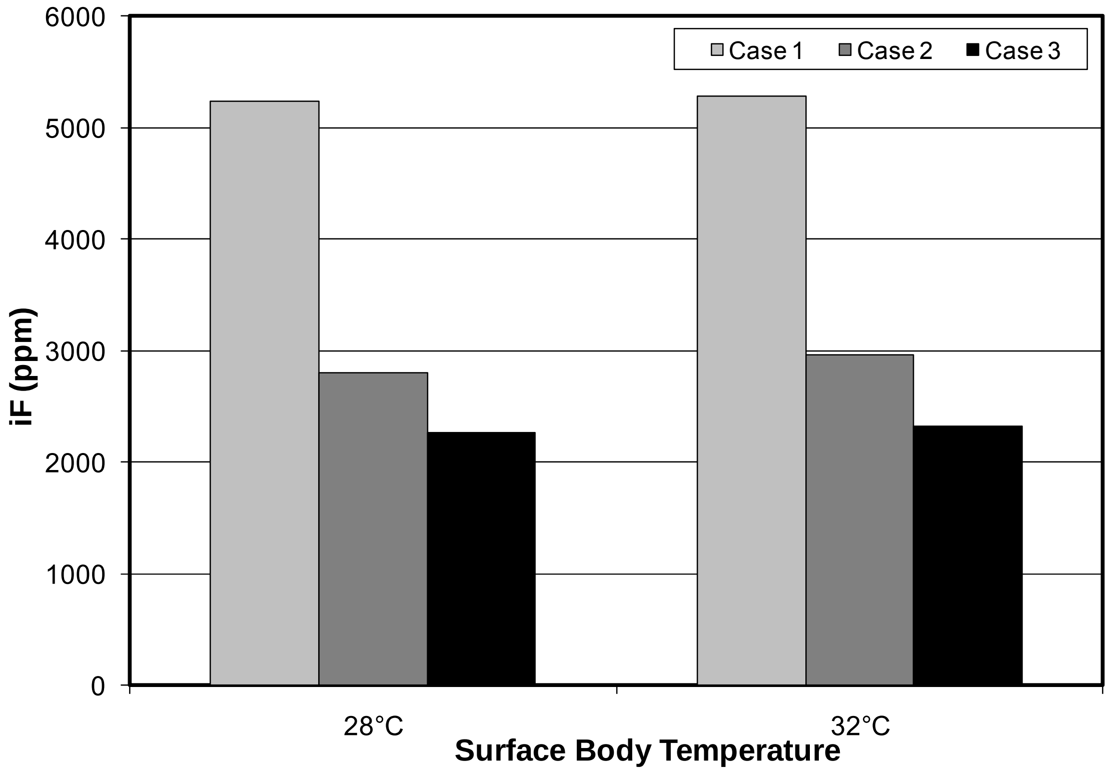

Figure 4.16: The effect of body surface temperature on iF with contaminated recirculated air.

The body temperature was not expected to be a factor in determining the iF with the recirculation air as the contaminant during inhalation. Without a PV system, the concentration in the recirculated air would become the concentration of the entire room for a steady state calculation; therefore, changing the strength of the thermal plume would not affect the local concentration in the BZ (this would only change the momentum of the thermal plume and not the path from which air is inhaled).

4.7.4 Effect of Exhaled Air Concentration

Figure 4.17 shows the calculated iF for Case 1, 2 and 3 for the two unsteady simulations with the same exhaled air concentration as inhaled and with the exhaled air at *100* times the concentration of the inhaled air. For Case 1 there is *~0-2 %* change in iF with a change in exhaled air concentration, and there is less than a *1 %* change in iF for Case 2 and 3 when using different exhaled air concentrations. From this it can be concluded that, when comparing inhalation from contaminated recirculated air, the concentration of exhalation has negligible effects on iF.

To show this point further, Figures 4.18, 4.19 and 4.20 show species concentration contours at 4 points during the sinusoidal breathing cycle for Case 1, 2 and 3, respectively, when the exhaled air concentration is 100 times the inhaled air concentration. Concentration contours at 4 points during the realistic breathing cycle for Case 1, 2 and 3 give similar results when the exhaled air concentration is 100 times the inhaled air concentration. 'A' corresponds to the peak exhalation, 'B' is at the transition from exhalation to inhalation, 'C' is at peak inhalation and 'D' is at the transition from inhalation to exhalation as denoted by the breathing profile in each figure. When comparing the results from the simulations run with different exhalation concentrations, it was found that the exhalation air concentration had little effect on the re-inhaled air concentration for Case 1, 2 and 3.

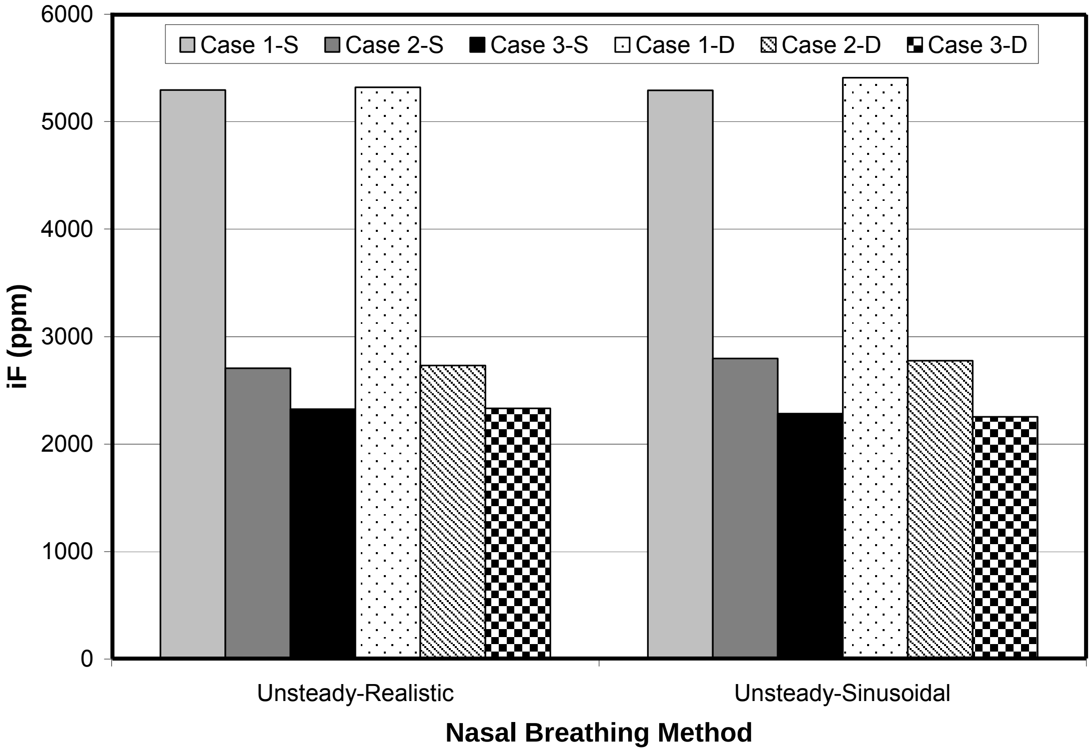

Figure 4.17: iF for unsteady, realistic and sinusoidal breathing methods with different exhaled air concentration values. An 'S' corresponds to an exhaled air concentration equal to the inhaled air and a 'D' corresponds to an exhaled air concentration of 100 times the inhaled air concentration.

For Case 1, Figure 4.18 shows air is exhaled through the nose in a pocket in front of the face. The exhaled air is quickly swept upward by the thermal plume and the air in the BZ during inhalation has again reached the well mixed concentration in the BZ without exhalation. In this case the upward moving thermal plume has enough momentum to remove the contaminated exhaled air away from the BZ before inhalation begins. For Case 2, Figure 4.19 shows air is exhaled through the nose in a small pocket in front of the face. The exhaled air is quickly swept behind the CSP as it is exhaled by the PV system. The PV system removes the exhaled air from the BZ faster than the thermal plume; therefore, the air in the BZ has reached the well mixed concentration before the inhalation portion of the cycle. For Case 3, Figure 4.20 shows air is exhaled through the nose in a small pocket in front of the face and almost immediately swept behind the CSPs head. The momentum of the Co-flow PV system is 4 times higher than the single jet PV system so the removal of exhaled air happens more rapidly and the air in the BZ has reached the well mixed concentration by the end of the exhalation cycle. From these figures it is apparent that the exhalation air has little to no effect on the inhalation air quality. For Cases 2 and 3, the removal of contaminated exhaled air by the thermal plume is aided by the PV system which forces air away from the BZ. For Case 2 and 3, this is consistent with the findings of Melikov et al. (2002) and Melikov & Kaczmarczyk (2007) where it was shown that a very small amount of exhaled air (<*1 %*) was re-inhaled when using PV systems. Figures 4.21, 4.22 and 4.23 shows concentration contours at 4 points during the realistic breathing cycle for Case 1, 2 and 3. These figures show the same trend as the sinusoidal breathing simulation results.

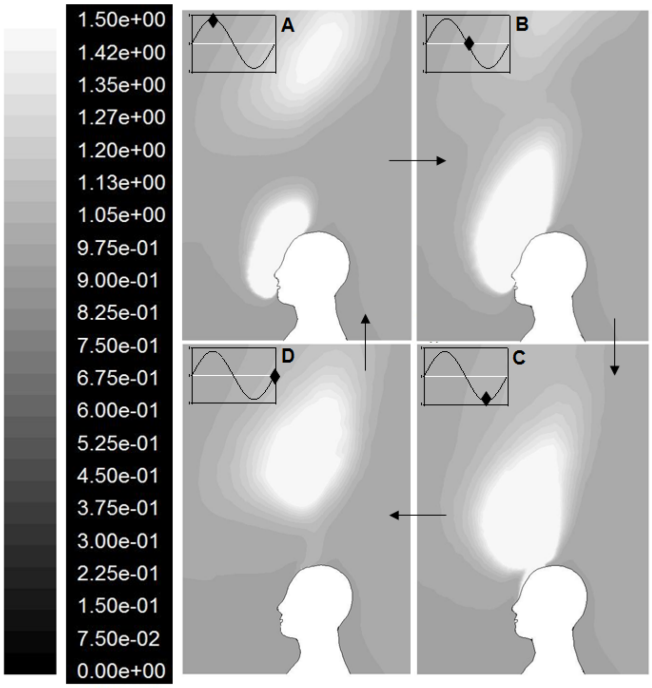

Figure 4.18: Concentration contours at 4 points during the sinusoidal breathing cycle with no PV.

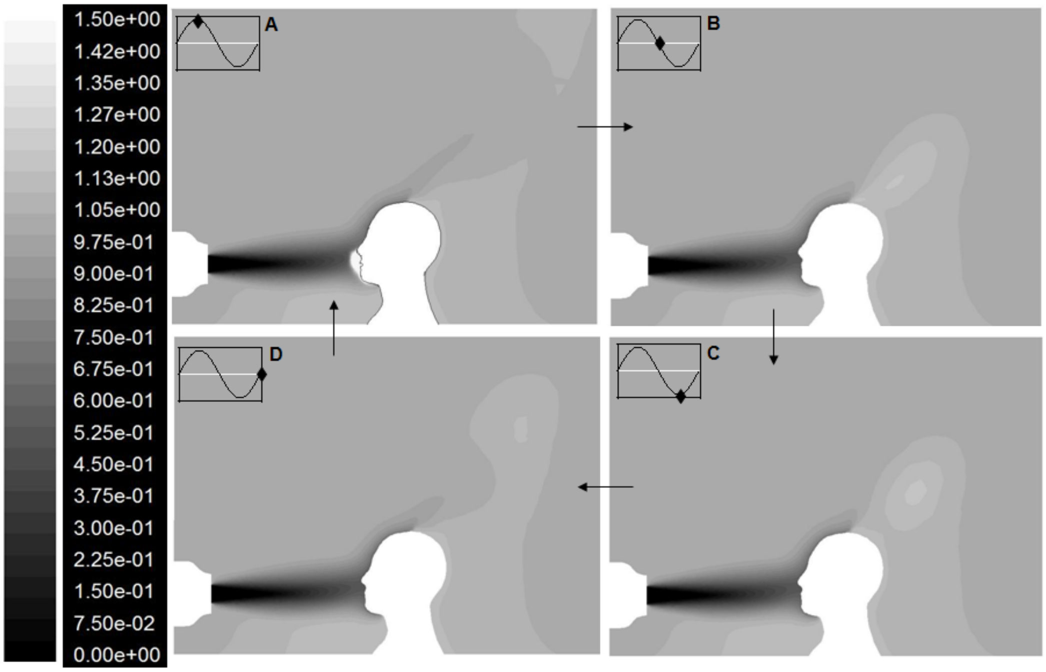

Figure 4.19: Concentration contours at 4 points during the sinusoidal breathing cycle with Primary PV.

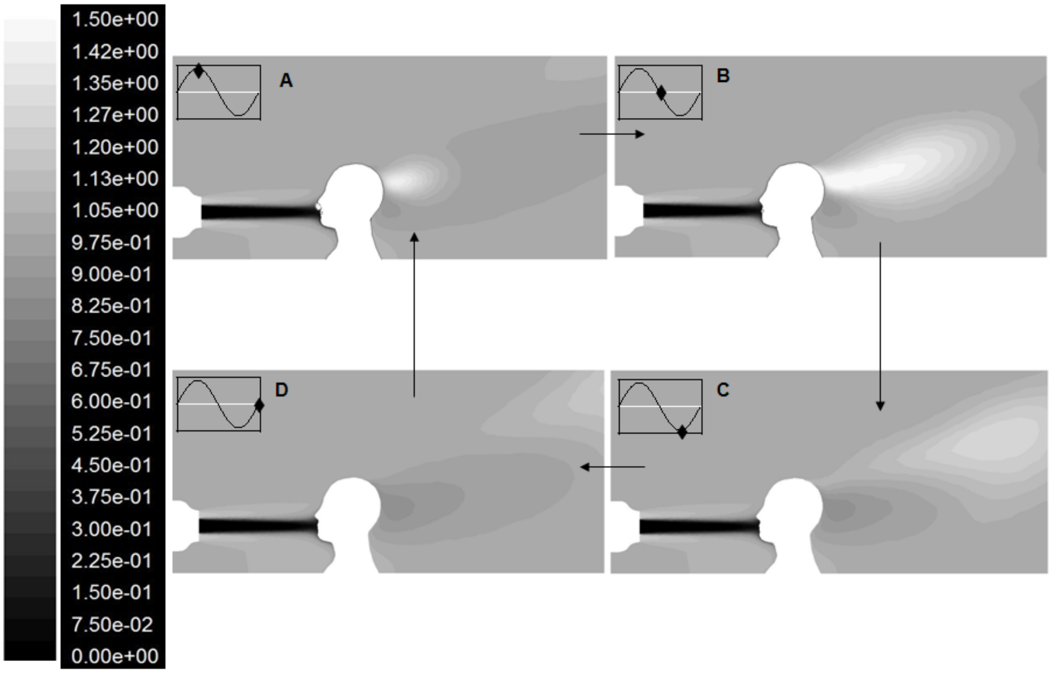

Figure 4.20: Concentration contours at 4 points during the sinusoidal breathing cycle with Co-flow PV.

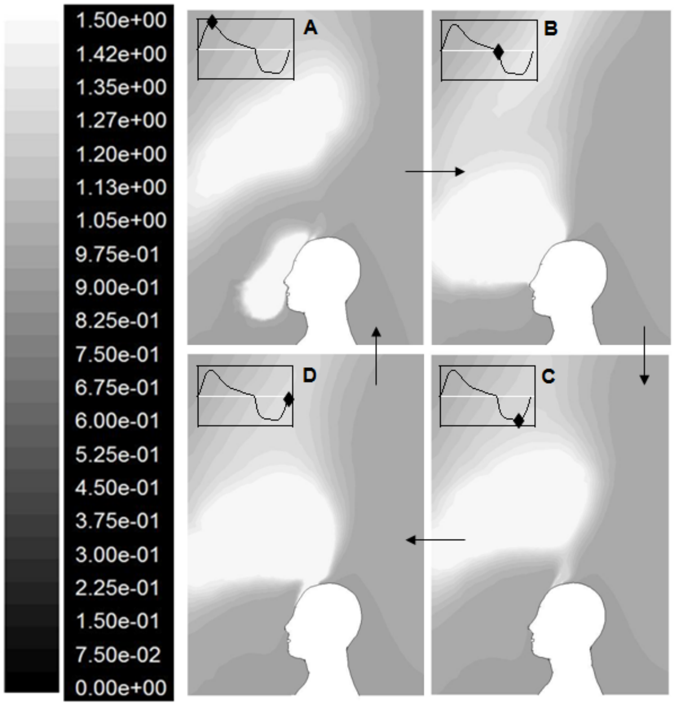

Figure 4.21: Concentration contours at 4 points during the realistic breathing cycle with no PV.

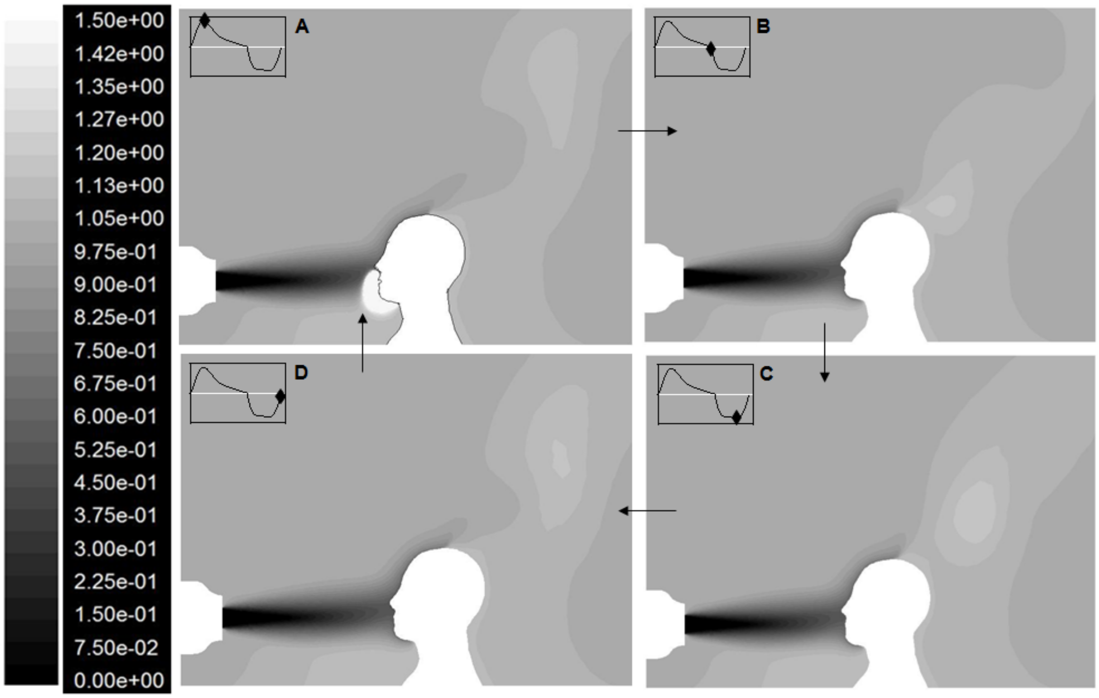

Figure 4.22: Concentration contours at 4 points during the realistic breathing cycle with Primary PV.

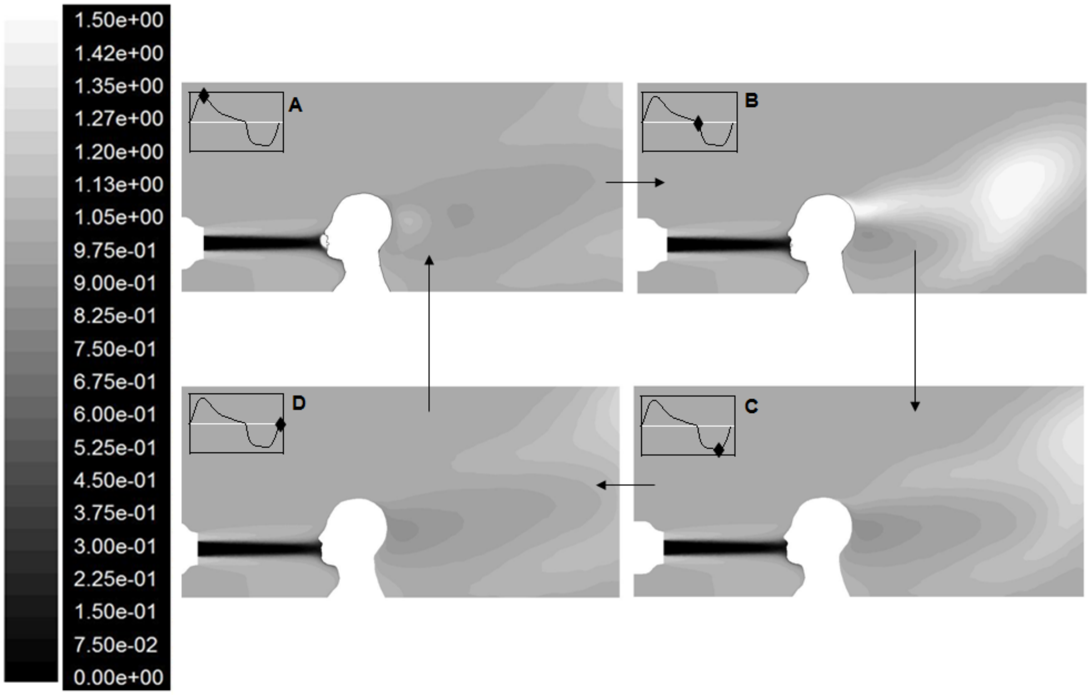

Figure 4.23: Concentration contours at 4 points during the realistic breathing cycle with Co-flow PV.

4.7.5 Nasal vs. Oral Breathing

Figure 4.24 shows the iF for Case 1, 2 and 3 for nasal and oral breathing when simulating breathing using unsteady sinusoidal breathing, steady state inhalation and steady state no breathing. For Case 1, differences in iF between nasal and oral breathing was *~1 %* for all breathing methods. This is expected for the case without PV due to the nearly well mixed condition in the room. For Case 2, differences in iF between nasal and oral breathing ranged from *10-15 %* for the different breathing simulation methods. For Case 3, differences in iF between nasal and oral breathing were *~60 %* for all breathing simulation methods. For Cases 2 and 3 there are significant differences in iF between nasal and oral breathing methods which are due to the alignment of the PV nozzle. For Cases 2 and 3, the center of the PV system is aligned *~40 mm* below the CSP's nose. For Case 2, the jet from the PV system is deflected by the rising thermal plume, delivering fresher air to the nose than to the mouth. For Case 3, the Co-flow jet is not deflected by the thermal plume due to its high momentum and, therefore, delivers fresher air to the mouth than to the nose. Although the iF for Case 3 during nasal breathing is higher than the iF during oral breathing it is still lower, indicating fresher air, than all other cases tested. A slight realignment of the PV jets could change these difference between nasal and oral iF quite significantly.

Figure 4.25 shows the calculated iF for Case 1, 2 and 3 for unsteady sinusoidal breathing with the same exhaled air concentration as inhaled and where the exhaled air concentration was 100 times that of the inhaled air. For nasal breathing, Case 1 has *~0-2 %* change in iF with a change in exhaled air concentration, and there is less than a *1 %*

change in iF for Case 2 and 3 when using different exhaled air concentrations. For oral breathing, Case 1, 2 and 3 change ~*2 %* with different exhaled air concentrations. From this figure it is apparent that the exhalation air has little to no effect on the inhalation air quality.

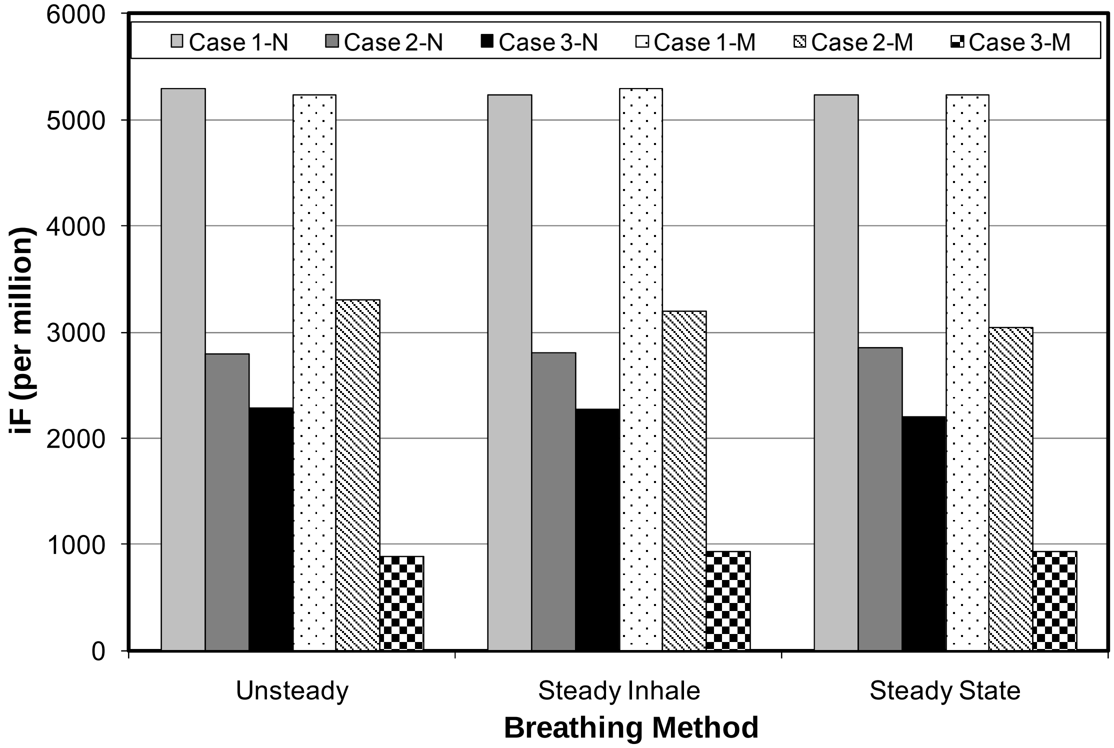

Figure 4.24: iF for Case 1, 2 and 3 for nasal and oral breathing for 3 different breathing simulation methods. 'N' is for nasal breathing and 'M' is for oral breathing.

Figures 4.26, 4.27 and 4.28 show species concentration contours at 4 points during the oral sinusoidal breathing cycle for Case 1, 2 and 3, respectively, when the exhaled air concentration is *100* times the inhaled air concentration. These figures show the same trend as the nasal breathing results show in Section 4.7.3.

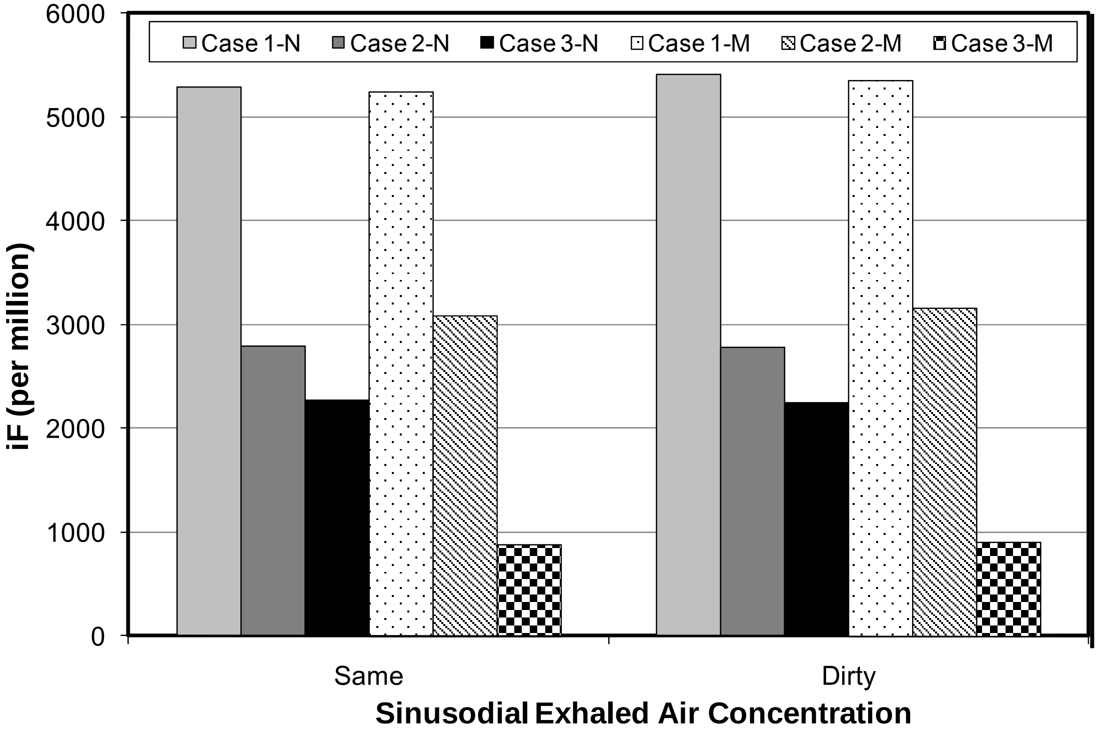

Figure 4.25: iF for nasal (N) and oral (O) breathing methods. 'Same': exhalation air was the same as the inhalation air and 'Dirty': exhalation air was 100 times the inhalation concentration.

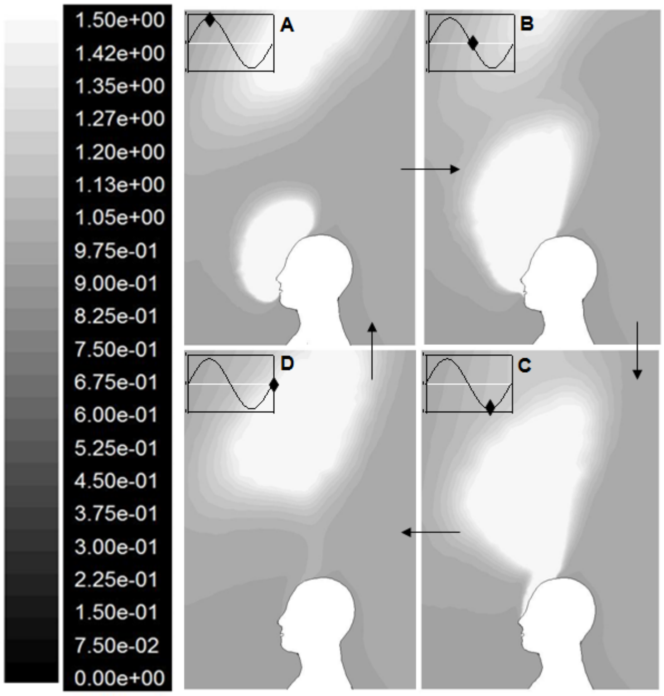

Figure 4.26: Concentration contours during the oral sinusoidal breathing cycle with no PV.

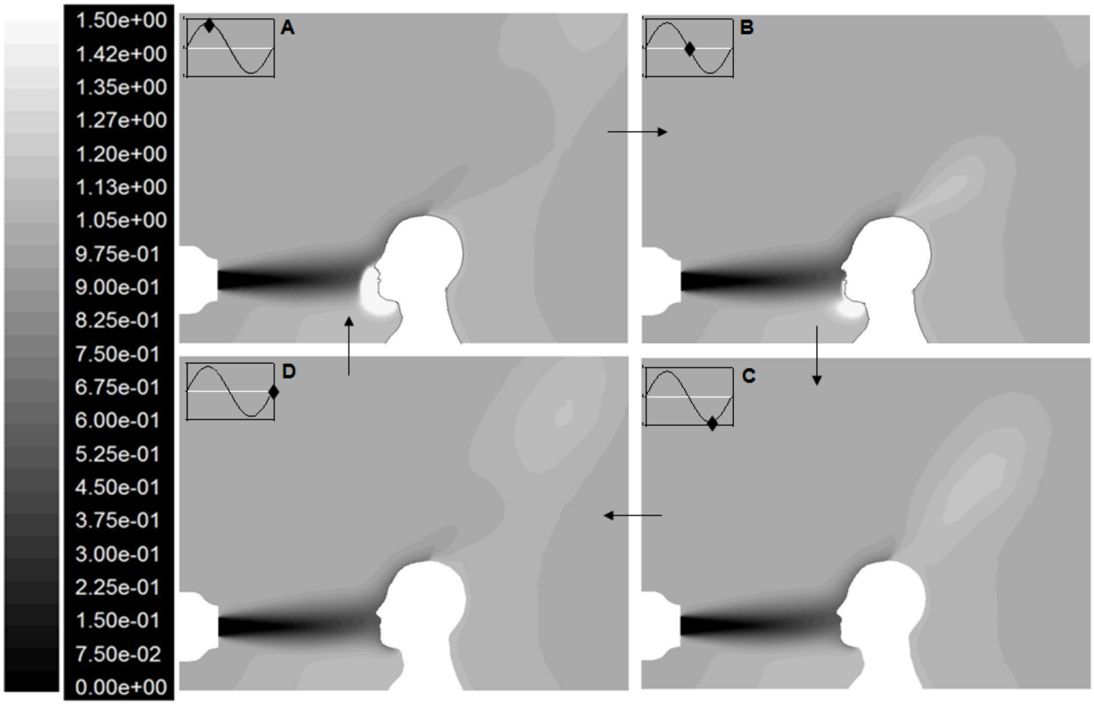

Figure 4.27: Concentration contours at 4 points during the oral sinusoidal breathing cycle for the Primary PV system.

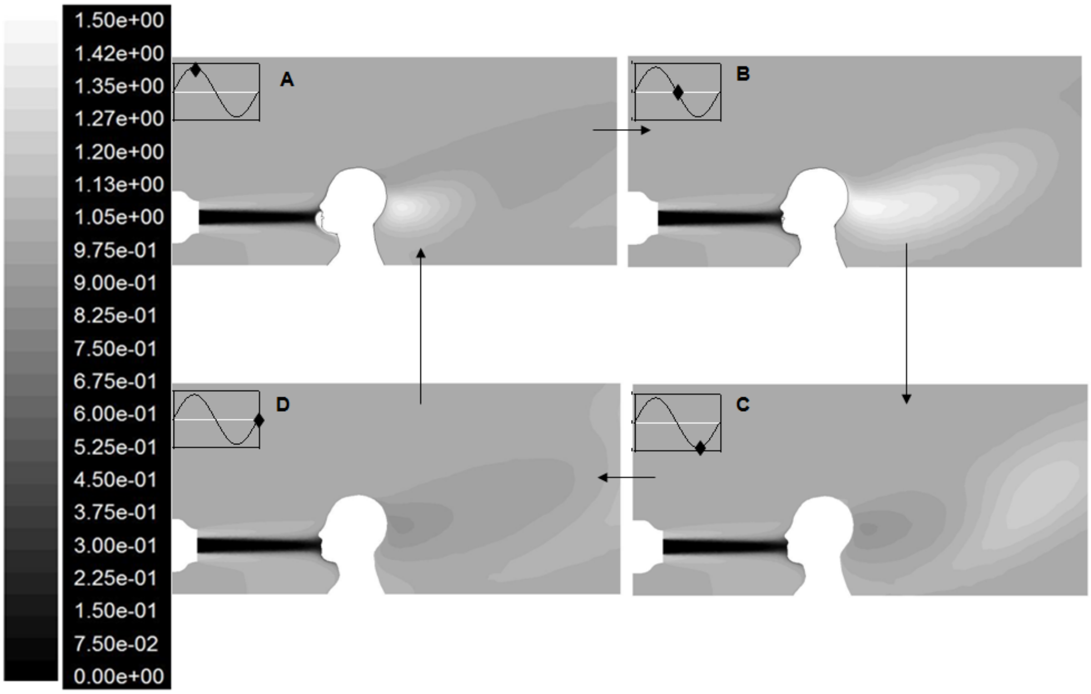

Figure 4.28: Concentration contours at 4 points during the oral sinusoidal breathing cycle for the Co-flow PV system.

4.7.6 Section Conclusions

The CFD model used for this investigation is a good representation of the experimental case. Although previously validated for profiles in front of the seated manikin, this paper offers further validation specific to inhalation exposure. There was less than a *7.5 %* difference between the air quality in the CFD compared to the air quality of the experiment for the nostril and mouth region. Better agreement was found for nasal values for both the Co-flow and Primary PV system than for oral values.

When modelling inhalation exposure in a typical office setup, it was found that adding complex, realistic features, such as unsteady breathing, to a CFD model of the BZ of a CSP does not improve the results of the solution. The results show that breathing can be ignored when studying the BZ with or without PV. However, the recommendations of this work are that steady state inhalation should be used as the breathing method because it does not increase the complexity of the simulation compared to unsteady methods and makes post processing easier compared to using a presumed volume of air method. However, modeling breathing is necessary when studying re-inhaled air and the transport of exhaled contaminants between people.

It was also found that the concentration of the exhaled air had little to no effect on the inhalation exposure. It was shown that the strength of the thermal plume and/or the momentum of the PV jet carried contaminants away from the BZ before re-inhalation.

When comparing nasal to oral breathing, inhalation exposure was found to vary due to their location relative to the PV jet. For the case without PV, no difference was found between nasal and oral breathing. A PV jet can create high concentration gradients in the BZ which can result in different inhalation exposure when breathing through the mouth compared to through the nose.

It was that using a nostril area average gives poor results when comparing inhalation exposure to indoor sources. High gradient of species in the boundary layer around the CSP were present when the source is emitted from the body, which results in an increased exposure when using a nostril area average. It is concluded that using a surface nostril average should be used with great caution or not at all when modelling inhalation exposure.

4.8 Radiation

Energy exchange at the CSP surface is the driving source for the thermal plume strength. Accurately capturing this effect has been shown to be necessary for the correctness of the results. Neglecting radiation when heat-flux boundary conditions were used showed to produce erroneous results (Sideroff and Dang, 2008). Thermal radiation alters surface and air temperatures in a space, which can alter room air flow patterns. For this thesis, the work of Sideroff (2009) was expanded to better understand simplified modeling techniques (variations of thermal BC's) that can be used to simulate the effects of radiation in the indoor environment. Sideroff (2009) conducted a detailed computational study of the flow around a CSP in an empty domain that was being ventilated by a displacement ventilation system. Benchmark tests for evaluating CFD in the indoor environment of Nielsen et al. (2003) were used for evaluating simplified radiation models to accurately predict the radiative exchange between indoor surfaces. The grid and computational setup that was used is outlined in detail by Sideroff (2009) and boundary conditions were set to match Nielsen et al. (2003). The domain used for that study consisted of a standing CSP in an otherwise empty room shown in Figure 4.29.

First, Sideroff (2009) examined the impact of radiation using a surface-to-surface radiation model. With the inclusion of radiation, Sideroff was able to achieve satisfactory results when comparing vertical velocity profiles above the head of the CSP to experimental results from Nieslen et al. (2003) using the full flux emitted by the CSP. To avoid some of the complexities with radiative modeling and the determination of radiative material properties, the study also analyzed the results where different thermal BC's were employed. For one case, only the convective heat flux from the CSP was used with adiabatic wall BC's (only modeled ~38% of body heat into the room) and for a third comparison average temperatures for the CSP body and walls were used. From these results it was concluded that neglecting radiation modeling when heat-flux BC's are used is erroneous and that if surface temperatures are known, the effects of radiation could be reasonably accounted for without actually including a radiation model.

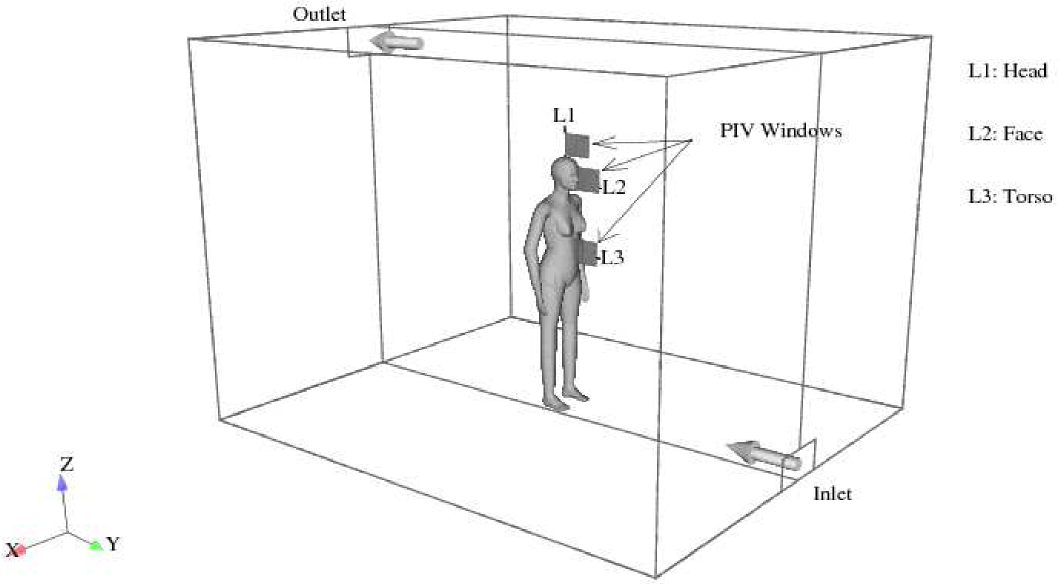

Figure 4.29: Displacement ventilation room configuration (Sideroff, 2009).

To understand the influence of thermal BC's on the results further, this study was extended to include three additional thermal BC scenarios. In all, the six cases investigated include 1) modeling radiatiative heat flux and convective heat flux from the

CSP with adiabatic walls (Sideroff, 2009), 2) modeling an average convective heat flux from the CSP with adiabatic walls (Sideroff, 2009), 3) modeling an average surface temperature on the CSP and an average surface temperature for each wall computed from Case 1 (Sideroff, 2009), 4) modeling an average surface temperature on the CSP and an average surface temperature for all the walls, 5) modeling an average convective heat flux from the CSP and an average convective heat flux for each wall computed from Case 1 and 6) modeling an average convective heat flux from the CSP and average convective heat flux for all the walls. A summary of these cases is given in Table 4.5. All thermal BC's from Case 2, 3, 4, 5, and 6 were determined from Case 1. For Case 3 and 5 the average BC's were found for each wall surface, whereas, for Case 4 and 6 a single average was found for all other surface except for the CSP surface and applied to all the walls (including the ceiling and floor).

Table 4.5: Thermal BC's studied.

	Boundary Conditions	
	CSP	Walls
Case 1	Rad. And Conv. Flux	Adiabatic
Case 2	Conv. Flux Only	Adiabatic
Case 3	Temperature	Temperature
Case 4	Temperature	Uniform Temperature
Case 5	Conv. Flux Only	Conv. Flux
Case 6	Conv. Flux Only	Uniform Conv. Flux

To understand the effect of these BC's on the thermal plume strength and room air flow, we first examine the differences in surface temperature and convective heat flux from the CSP for each case. Figure 4.30 shows the body temperature distribution over the CSP for

Cases 1-6. Case 1 is used as the baseline case for comparison and it is clear that defining a convective heat flux BC (Case 2, 5 and 6) creates a more non-uniform distribution of temperatures over the body surface. When radiation is modeled, there is heat exchange between surfaces on the CSP, resulting in temperature distributions that are not significantly different than uniform temperatures. This affect is not modeled when modeling convective heat flux only and results in decreased temperatures for the extremities of the CSP and higher temperatures at the CSP core. This figure also shows that there is a difference in surface temperature and surface temperature distribution between Case 2, 5 and 6 where the same convective heat flux was defined at the CSP surface in each case. This implies that, not only is the CSP thermal BC's important, but the thermal BC applied to the rest of the surfaces in the domain have an impact on the resulting CSP surface temperature. This point is investigated further later in this section.

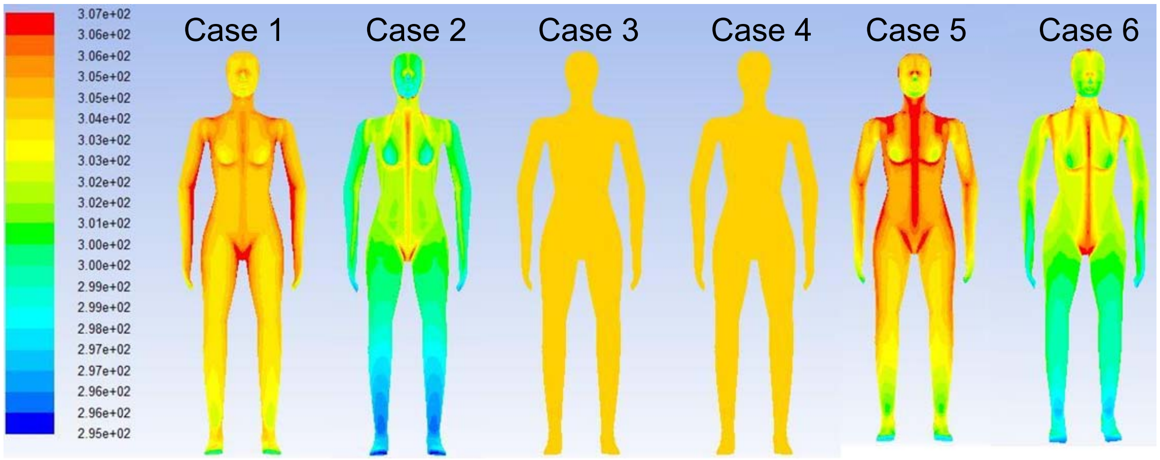

Figure 4.30: CSP surface temperatures for Cases 1-6.

Figure 4.31 shows the convective heat flux over the CSP surface for Cases 1-6. Case 1 is used as the baseline case for comparison and it is clear that defining an average temperature BC (Case 3 and 4) on the CSP creates a more non-uniform distribution of convective heat flux over the CSP surface. Unlike the temperature distribution for defined convective heat flux BC's, specifying a temperature BC on the CSP appears to result in the same convective heat flux distribution even when wall BC's are modeled differently.

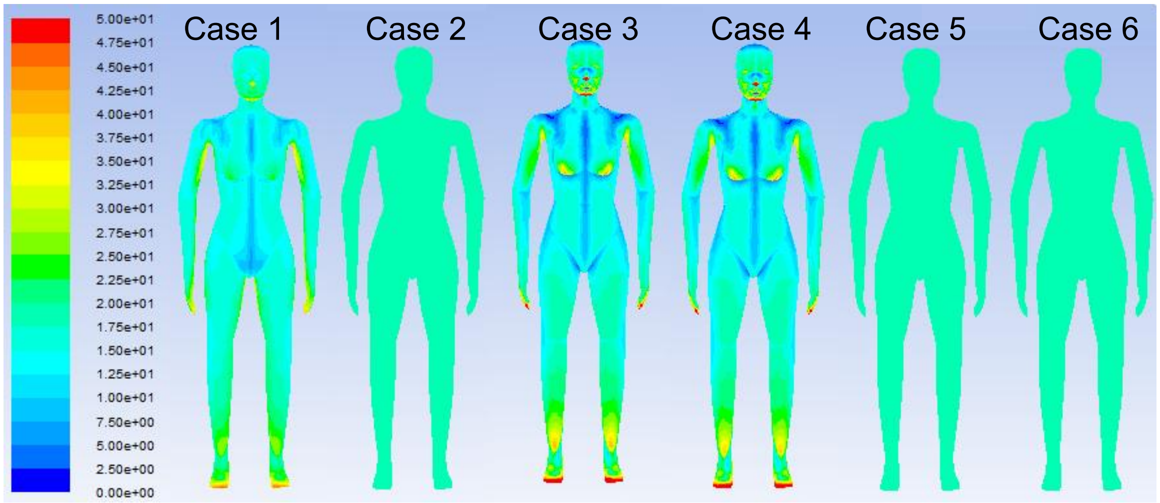

Figure 4.31: Convective heat flux distribution for Cases 1-6.

Table 4.6 gives a summary of the average temperature and convective heat flux for the CSP and averaged for all walls for each case. Compared to Case 1, Case 3, and 4 give the same average temperatures for the CSP and Walls (this is expected since the temperature BC's for Case 3 and 4 are based on the averages of Case 1). Case 5 also results in the same average surface temperature for the CSP with slightly lower average surface temperatures on the wall. Case 5 slightly under predicts the CSP and wall temperatures and Case 2 (widely used in simple CFD work) under predicts both temperatures by *4-5 ˚C*. When looking at the resulting average convective heat flux, Case 4 and 5 give the same averages for the CSP and Walls (this is expected since the convective heat flux BC's for Case 5 and 6 are based on the averages of Case 1). Case 2 shows the same convective heat flux from the CSP, but, since adiabatic walls are modeled, produce no convective flux from the walls. Case 4 and 5 slightly under predict the convective heat flux from the CSP and walls.

Table 4.6: Summary of surface temperatures and heat fluxes for Cases 1-6.

	Temperature (˚C)		Heat Flux (W/m^2)	
	CSP	Walls	CSP	Walls
Case 1	31.39	25.15	17.84	0.89
Case 2	27.85	20.35	17.84	0.00
Case 3	31.39	25.15	17.46	0.82
Case 4	31.39	25.15	17.36	0.82
Case 5	31.39	25.06	17.84	0.89
Case 6	29.98	24.41	17.84	0.89

To explore these differences on a quantitative level, the verticle velocity *5 cm* above the CSP was plotted and compared to experimental resutls of Nielson et al. (2003) in Figure 4.32. From this figure, we can see that Case 1, 3 and 4 achieve the best agreement with the experimental results and result in a profile with similar shape. Case 2 results in a significant over prediction (up to *~32 %*) in the vertical velocity compared to the experimental results with an over prediction of vertical velocity close to the head. Although valuable details are learned from this plot, using a single profile for comparison could be misleading and a qualitative comparison was made.

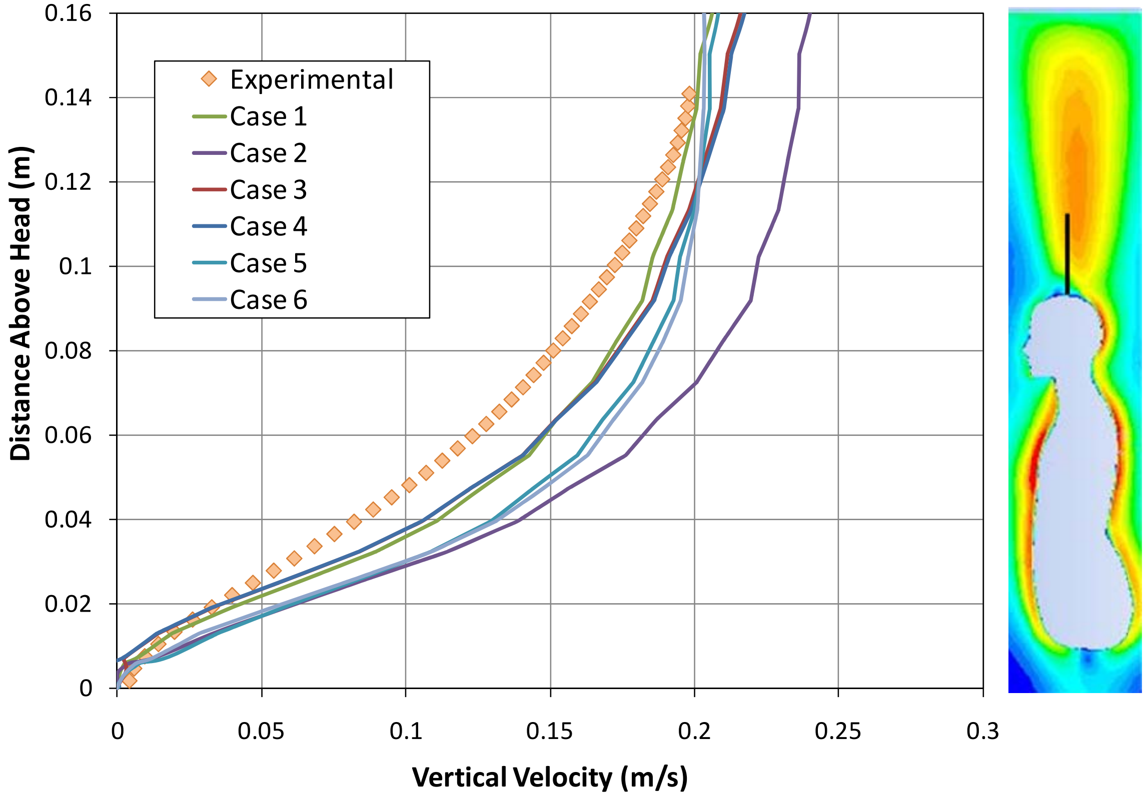

Figure 4.32: Vertical velocity about the CSP head.

To further examine the impact of the thermal BC's on capturing the correct heat transfer between the CSP and surrounding environment, velocity contours were examined to show the resulting thermal plume for each case (Figure 4.33). Compared to the baseline case (Case 1) it is clear that the thermal BC's have a considerable impact on the resulthing thermal plume. Case 3, 4 and 5 most closely resembles the thermal plume shown for Case 1, however, Case 2 and 6 show an increase and decrease in velocity above the head, respectively. The differences between Case 1 and 2 can be explained by the very non uniform temperature distribution on the body in Case 2 which leads to an overprediction of the velocity along the symmetry plane of the CSP. Although Case 5 and 6 have the same CSP thermal BC they show differences in the thermal plume strength and shape. Since this cannot be due to a difference in CSP thermal BC, it must be a reslut of the wall thermal BC's. This implies that averaging the convective heat flux from all the walls, as in Case 6, leads to an underpredction of the strength of the thermal plume which changes the overall room flow patterns.

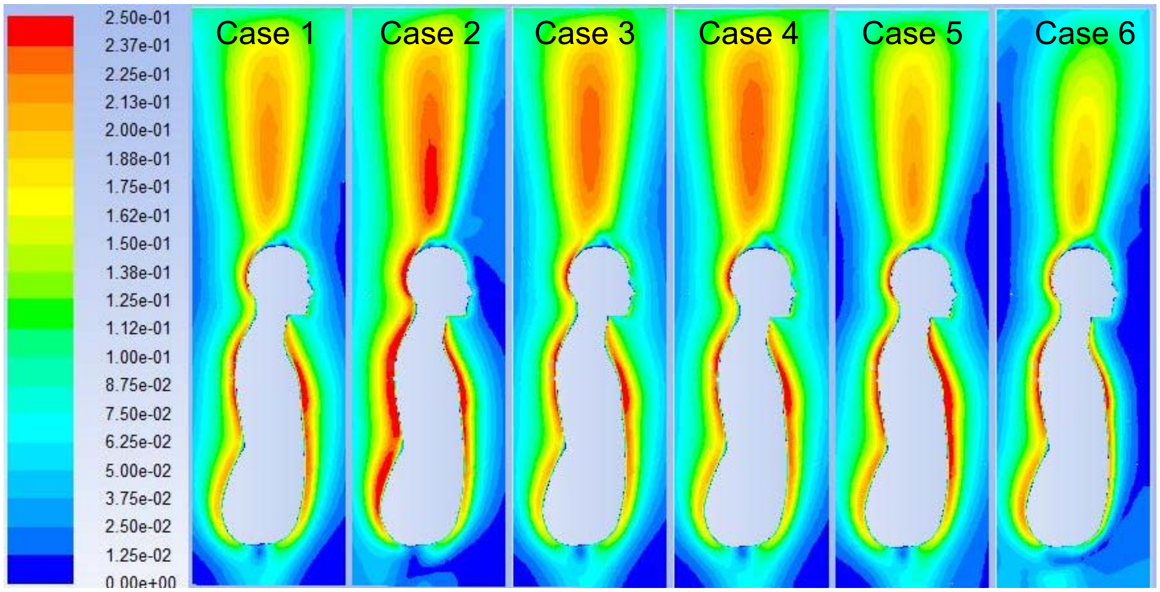

Figure 4.33: Velocity magnitude contours along the CSP symmetry plane.

The velocity magnitude was also examined along a plane *5 cm* above the CSP head for Cases 1-6 and the velocity magnitude contours are shown in Figure 4.34. Here, similar trends are shown. Case 3, 4 and 5 most closely represent the thermal plume shape shown for Case 1, however, Case 2 and 6 show an increase and decrease in velocity above the head, respectively.

Speculation has been made concerning the importance of the wall thermal BC's along with the CSP BC's on the overall patterns in the room and resulting heat transfer. Figure 4.35 shows the temperature contours along the CSP bisecting plane for Cases 1-6.

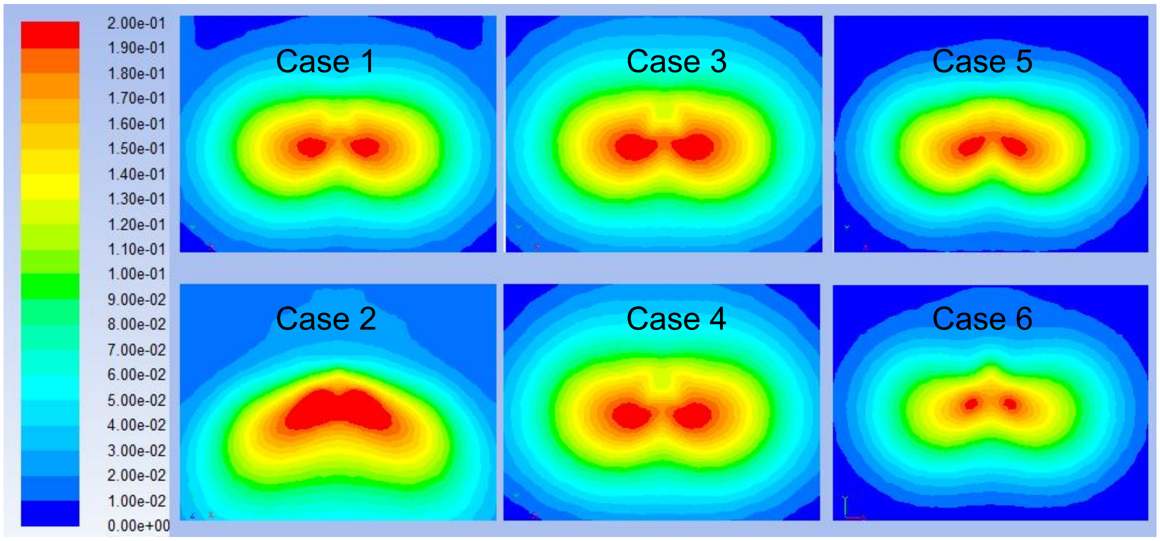

Figure 4.34: Velocity magnitude contours 5 cm above the CSP.

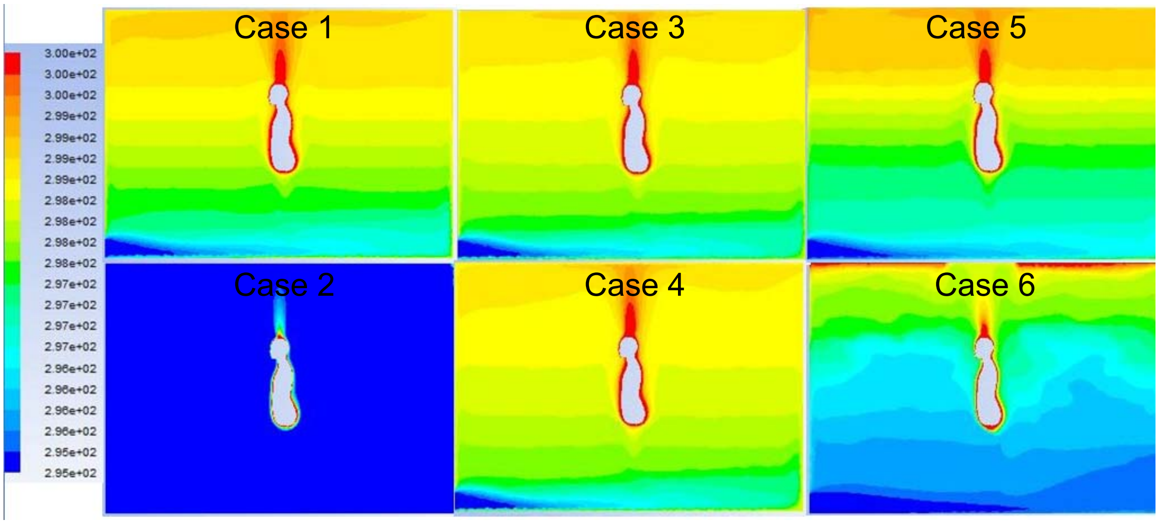

Figure 4.35: Temperature Stratification along the CSP bisecting plane.

Temperature stratification exists in the room, which is a characteristic of a displacement ventilation system and is shown in Case 1. Simplifications in the thermal BC modeling using temperature BC’s (Case 3 and 4) are shown to closely depict the stratifications of Case 1, while Case 5 shows the same characteristics. Simplified BC’s in Case 2 and 6 show unsatisfactory results due to interactions with wall BC's and do not resemble characteristics of Case 1.

The results so far have indicated that using temperature BC's capture the effects of radiation without having to model any of the associated complexities of radiation, while specifying convective heat flux only is very sensitive to the treatment of the thermal BC's on the wall. Case 3 and 4 model individual wall average and whole room wall average temperature BC's, respectively. Likewise, Case 5 and 6 model individual wall average and whole room wall average convective flux BC's, respectively. However, Case 3 and 4 produce nearly the same results, whereas, there are significant differences between Case 5 and 6. To examine this more closely, the average temperate and convective heat flux are given for each wall surface for Case 3 and 4 in Table 4.7 and for Case 5 and 6 in Table 4.8. Here we can see that the range of temperatures of the wall surfaces do not very significantly and using an average temperature is a good representation of the temperature of each wall. However, the convective heat flux from each wall surface varies widely and even changes direction. When averaging these values it does not result in a value that is a good representation of the convective heat flux for each wall (model a negative heat flux at the ceiling with a positive one) as shown in the results for Case 6 where incorrect temperatures and velocity predictions were made.

The results show that simplified modeling of thermal BC's can account for radiation effects (Case 3, 4 and 5), but that there is a significant dependence on the wall thermal BC's and determining the correct thermal BC on the body is not enough when dealing with radiation. In situations where modeling radiation is difficult, modeling surface temperatures is shown to be easily implemented and gives very similar results compared to modeling radiation. Modeling convective heat flux has also been shown to produce reasonable results, however, it is more sensitive to BC treatment and determining proper BC is this case would be difficult. If setting up an experiment to be used for CFD validation, controlling surface temperatures for the ease and accuracy when defining BC's in the CFD model is recommended.

Table 4.7: Temperatures modeled for each wall surface for Case 3 and 4 with the resulting convective heat flux.

	Temperature (˚C)		Heat Flux (W/m^2)	
	Case 3	Case 4	Case 3	Case 4
Ceiling	25.34	25.12	-0.50	-0.77
Floor	24.81	25.12	2.94	3.36
F_wall	25.14	25.12	0.53	0.46
R_wall	25.19	25.12	0.69	0.49
S_wall	25.15	25.12	0.61	0.52

Table 4.8: Convective heat flux modeled for each wall surface for Case 5 and 6 with the resulting temperature.

	Temperature (˚C)		Heat Flux (W/m^2)	
	Case 5	Case 6	Case 5	Case 6
Ceiling	25.63	27.34	-0.56	0.89
Floor	24.48	22.83	2.96	0.89
F_wall	25.05	24.01	0.65	0.89
R_wall	25.08	23.89	0.80	0.89
S_wall	25.07	24.00	0.70	0.89

4.9 *Chapter Conclusions*

This chapter addressed the modeling and effect of seven boundary conditions. Supplementary cases were run to evaluate the effect of changing the primary jet temperature from *20.0* to *26.0 °C*, the PV nozzle exit turbulence intensity (*Tu*) from *1.7* to *10.0 %,* the turbulence length scale from *3 mm* to *8 mm*, the flow rate from *0.6* to *4.8 l/s*, CSP surface temperature from *25.0 to 32.0 ºC,* skin wettedness from *0 %* to *50 % w*, varying the breathing simulation method from no breathing to realistic breathing methods and modeling radiation.

1) The nozzle exit temperature variations over the range used was shown to have little effect on the concentration profile.
2) It was shown that the inlet *Tu* level is very important when using a Co-flow nozzle. With low *Tu*, such as that produced by convergent nozzle designs employed in the companion experimental investigation (Khalifa et al., 2009), the gain from using a Co-flow nozzle versus a single jet is significant. However, as the turbulent intensity increases, particularly of the secondary jet, the benefit of a Co-flow nozzle diminishes. This highlights the importance of using convergent nozzles with clean inlets to realize the advantages of the Co-flow design. It was found that changing the turbulent length scale from *3 mm* to *8 mm* had no measurable effect on air quality in the BZ, therefore a simple screen or honeycomb in the nozzle would be sufficient. It also was shown that the shape and the deflection of the jet in the Primary case were sensitive to a change in the CSP's surface temperature (i.e., clo value) and the Co-flow case was not.

3) The performance of the Co-flow nozzle can be maximized at much lower flow rates, therefore reducing draught for the individual, since this nozzle is less dependent on Re. To this point, it is clear that an AQI value of 1.0 (100 % fresh air) could never be reached by the Primary nozzle at this distance (41 cm) regardless of how much the flow rate was increased due to its limitations of a circular jet becoming Re independent in the fully turbulent region. It was found that the optimal diameter of a PV nozzle at a fresh air flow rate of 2.4 l/s is ~3-4 in, for 3.6 l/s it is ~ 4-5 in and for 4.8 l/s it is ~6-7 in.
4) It was shown that adding complex, realistic features, such as sweating, to a CFD model of the BZ of a CSP does not improve the results of the solution. The results show that sweating can be ignored when studying the BZ using PV.
5) It was found that adding complex, realistic features, such as unsteady breathing, to a CFD model of the BZ of a CSP does not improve the results and the recommendations of this work are that steady state inhalation should be used as the breathing method because it does not increase the complexity of the simulation compared to unsteady methods and makes post processing easier compared to using a presumed volume of air method.
6) It was found that adding complex, realistic features, such as unsteady breathing, to a CFD model of the BZ of a CSP does not improve the results. The results show that breathing can be ignored when studying iF with or without PV. Insignificant differences were found for iF for all breathing methods simulated. However, the recommendations of this work are that steady state inhalation should be used as the breathing method because it does not increase the

complexity of the simulation compared to unsteady methods and makes post processing easier compared to using a presumed volume of air method. Modeling breathing is necessary when studying re-inhaled air and the transport of exhaled contaminants between people.

7) The results show that simplified modeling of thermal BC's can account for radiation effects, but that there is a significant dependence on the wall thermal BC's and determining the correct thermal BC on the body is not enough when dealing with radiation and the use of temperature BC's on the CSP and walls is used for the remainder of this work.

The results shown reaffirm the advantages of a Co-flow nozzle when compared to a conventional single nozzle. In fact, the computational results show that the peak AQI for the Co-flow nozzle is more than twice the Primary nozzle's. It is clear that the Co-flow nozzle is able to deliver clean air a much longer distance. In addition, the study shows that the AQI in the BZ delivered by the conventional single nozzle is a strong function of the thermal conditions of the air around the body, e.g., effect of clothing on the strength of the person's thermal plume, and the difference in temperature between the surrounding air and the fresh PV air. This is largely due to the deflection of the jet as it interacts with the thermal plume, rather than the deterioration in the AQI peak value. Hence, for conventional single nozzles, especially at low PV flow, the position and/or angle of the nozzle will have to be adjusted based on the aforementioned thermal conditions in order to deliver the highest air quality in the BZ. On the other hand, the performance of the Co-flow nozzle is insensitive to the same thermal conditions, and hence no adjustment of the nozzle position and/or angle is needed to compensate for these inevitable variations.

These observations also highlight the importance of evaluating the performance of PV systems, and other ventilation systems that produce steep gradients in the BZ, based on a profile of air quality in the BZ, rather than single point measurements, which could lead to an under estimation of the potential advantage of PV systems that can be realized with a modest adjustment of the PV nozzle position and/or angle.

5 Exposure to non-reaction sources

The concept of PV is not new; however, the call for it is growing. Although more people are seeing a positive use for PV, there are still several that would dispute its need. The main augments against PV include decreasing the air quality away from the device, creating greater cross contamination and poor ergonomic and aesthetic implementation. To combat these ideas, this chapter is focused on showing the usefulness of PV for the removal of non-reacting indoor sources in spaces with a single occupant and multiple cubicle settings.

5.1 Modeling Species Flux

In order to specify a pollutant mass flux at the wall within the capabilities of Fluent, two alternative methods can be employed. Currently Fluent does not allow the specification of a specie flux BC at the wall. One approach utilizes a scalar transport equation for a *fictitious* species to be defined by the user – a so-called *User Defined Scalar Method* (UDSM) (Fluent). The other is a novel method developed for this work whereby a fictitious chemical reaction is applied at the wall to produce the desired pollutant flux. We labeled this the *Fictitious Surface Reaction Method* (FSRM).

A UDS can be used to model emissions from a surface in CFD. Both, the UDS transport equation and the species transport equation in the FSRM follow the same form, namely:

$$\frac{\partial \rho\phi_k}{\partial t} + \frac{\partial}{\partial x_i}\left(\rho u_i \phi_k - \mathit{\Gamma}_k \frac{\partial \phi_k}{\partial x_i}\right) = S_k \tag{5.1}$$

Where ϕ_k is a scalar, $\mathit{\Gamma}_k$ is the transport coefficient and S_k is a ϕ_k source term. Since ϕ is a fictitious scalar, care must be taken in simulating buoyancy effects when the changes in fluid density produced by either a temperature difference or a concentration difference are too large to be described by the simplified Boussinesq approximation (Kay & Crawford, 1980), or when simulating indoor chemical reactions. However, for low concentrations (ppb or ppm) such as those found in the indoor environment, and absent indoor chemical reactions, the UDSM is quite adequate.

As an alternative, in the FSRM a pollutant mass flux at the surface can be created by introducing a *fictitious* surface reaction that converts “air” into a pollutant at the wall. On a reacting surface whose outward normal is *n*, the incoming diffusion mass flux and the rate of production (or destruction) of species *i* are related by a mass balance equation of the form (Russo & Khalifa, 2009):

$$J_{i,w} = -\rho D_i \left(\frac{\partial Y_i}{\partial n}\right)_w = M_i R_{i,w} \tag{5.2}$$

where $J_{i,w}$ is the diffusive mass flux of species i at the wall, ρ is the density of air, D_i is the diffusion coefficient of species i in air, Y_i is the mass fraction of species i in the air, M_i is the molecular weight of species i, and $R_{i,w}$ is the molar surface reaction rate per unit area at the wall (*positive when i is produced at the wall*). We will assume a fictitious chemical reaction at the wall of the form:

$$\text{air} + \text{surface (catalyst)} \rightarrow \text{product (pollutant)} \tag{5.3}$$

The stoichiometric coefficients of the reactant and product species were assumed to be equal to *1*. Since we are dealing with low species concentrations on the order of ppm and ppb, it was assumed that the mass fraction of air will always be *1* and the reaction is first order. With these assumptions, the normal flux from a surface can be expressed as (Incropera et al., 2007):

$$J_{i,w} = \rho k_{i,r} Y_{i,w}, \tag{5.4}$$

in which $k_{i,r}$ is a reaction rate constant (per unit area) for the production of species i at the wall. This flux can be implemented by specifying an appropriate value of the reaction rate. Figures 2.1 and 2.2 present a comparison of the species concentration along a horizontal and vertical line in the center of a two-dimensional room computed by the two methods. It can be seen that the two methods lead to identical results.

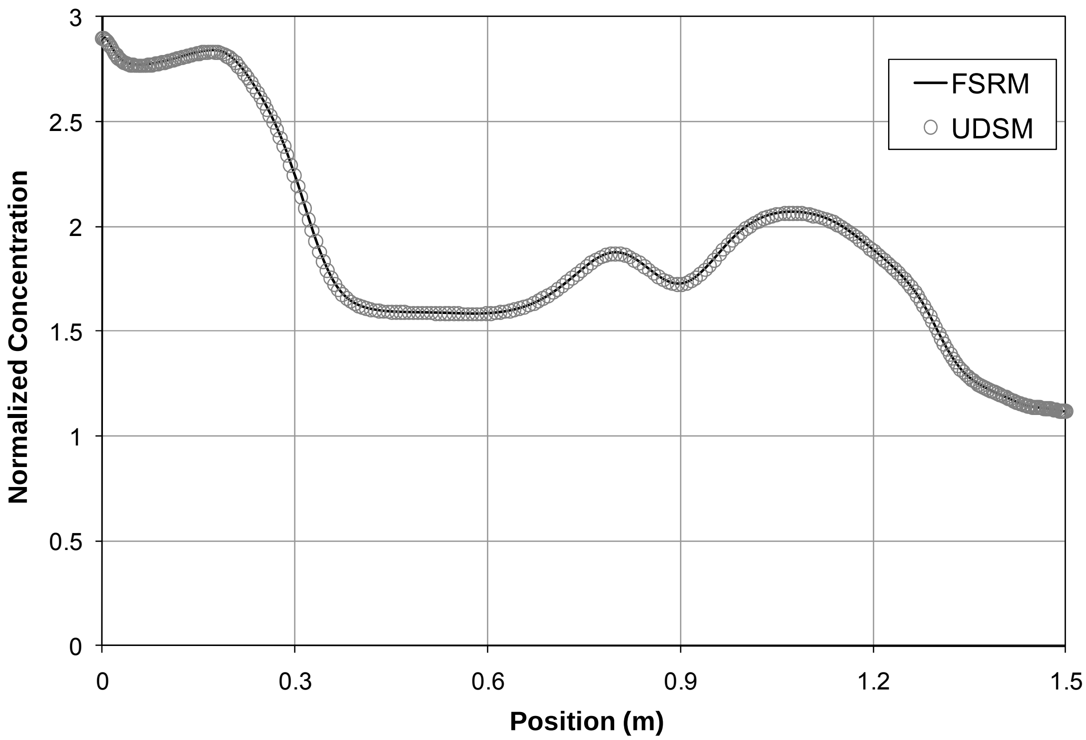

Figure 5.1: Specie concentration comparison of using a FSRM and a UDSM along a horizontal centerline in a 2D case.

Nevertheless, using the FSRM in place of the UDSM offers certain advantages. First, it allows the user to specify the thermo-physical properties of the emitted species, not just the diffusion coefficient as required in the UDSM. This enables the user to solve the species transport equations as a coupled (or an uncoupled) set, along with the continuity, momentum and energy equations. The FSRM also allows the inclusion of the full density effect when buoyancy is present, and not resort to the simplified Boussinesq approximation and its well known pitfalls. In addition, the FSRM allows the straightforward inclusion of surface or volume chemical reactions of the pollutants with other species such as Ozone (Sorensen & Weschler, 2002). This cannot be done in the UDSM without additional coding through user-defined functions and similar commercial CFD code work-around add-ons. From this, we concluded that the FSRM is a valid, simple approach for specifying the mass flux of a pollutant emitted from a surface. Therefore, we decided to use the FSRM throughout this work.

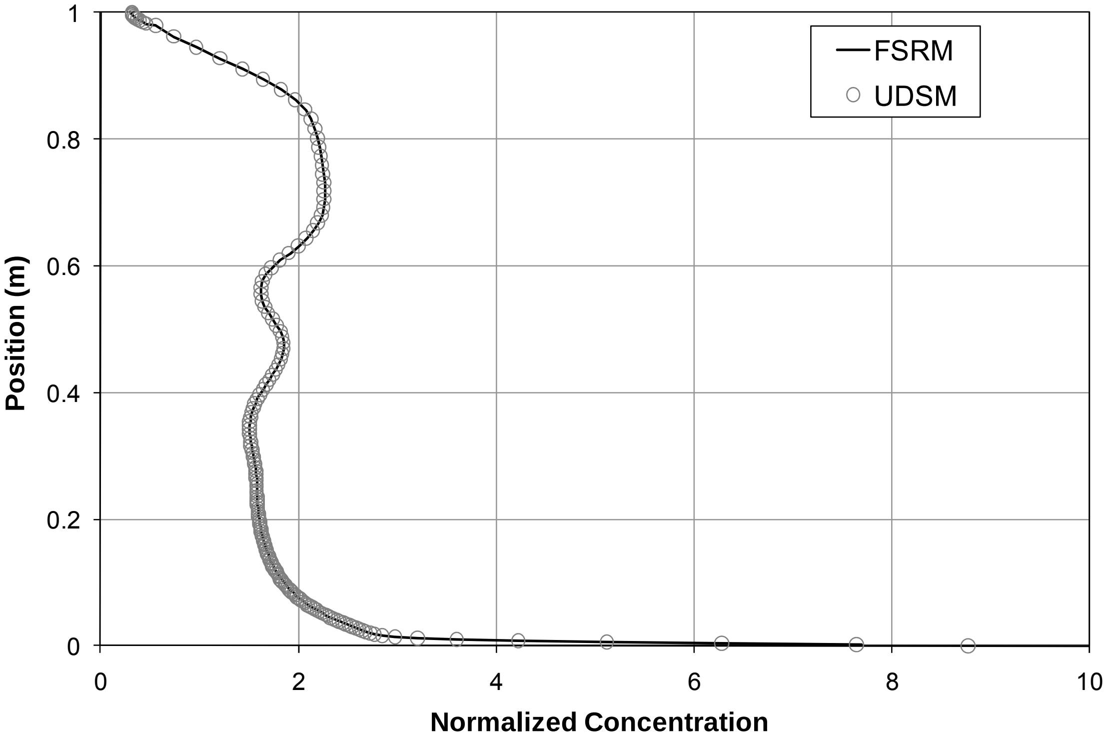

Figure 5.2: Specie concentration comparison of using a FSRM and a UDSM along a vertical centerline in a 2D case.

5.2 Intake Fraction for indoor sources

In many cases inhaled air is assumed to have a pollutant concentration value equal to a well mixed condition. However, this may be in serious error when there is a pollutant source located in the room, especially in the vicinity of the occupant. In fact, the air quality in the BZ and, therefore, the exposure due to inhalation can be strongly affected by the ventilation system and proximity to the source. In displacement ventilation systems it was found that there is a positive influence on air quality in the BZ when contaminants are generated in the upper part of the room and a negative effect when contaminants are generated near the floor (Nazaroff, 2008). It has also been shown that the use of a PV system can result in a much higher BZ air quality (Bolashikov et al. 2003; Faulkner et al. 1995, 1999, 2000, 2002; Fisk et al. 1990; Cermak et al. 2003, 2006; Kaczmarczyk et al. 2002; Melikov et al. 2001, 2004, 2006; Nielsen et al. 2005; Khalifa et al. 2008).

Many authors have employed CFD to study exposure in the personal microenvironment (PμE) (Brohous, 1997; Dygert et al., 2009; Nazaroff, 2008; Russo et al., 2009; Topp et al., 2002; Zhu et al., 2005). In these studies the representation of the CSP ranged from simple block geometry to more realistic, anatomically-correct shapes. It was shown that the use of block-type CSPs to represent the human body results in a significantly different flow field around the head (Topp et al., 2002; Khalifa et al., 2006; Dygert et al., 2009) where it was found that the gap between the legs, shoulders, and chin should be included in the model. The effect of different CSP shapes could significantly impact the estimation of *iF* by CFD, especially in the presence of PV jets and their interaction with the body's thermal plume and was investigated.

The study to determine the effect of breathing simulation method on inhalation air quality was extended to include exposure to non-reacting sources. A comparison was made using 4 different breathing methods. This is done to see if the location of the source is significant when simplifying a breathing method. The four breathing methods studied here include 1) averaging the area concentration of the CSP's nostril during steady state, no breathing, 2) using the hemisphere volume method proposed by Brohus (1997) during steady state, no breathing, 3) steady state inhalation and 4) unsteady sinusoidal breathing. Modeling breathing by averaging the concentration of the area was added for this setup to test how gradients near the BZ would affect the inhaled air concentration. In all cases pollutants with the same material properties are released from the floor, walls, desk and body with the same source strength.

5.2.1 Domain and Setup

The domain and setup used for experimental comparisons is the same as the validation domain and setup; See section 3.1. The computational domain was then expanded with the addition of a desk and is shown in Figure 7.1. The domain represents a typical office space that is *2.6 m* x *2.5 m* x *1.7 m*. In every case there was a seated thermal CSP, desk, floor diffuser and exhaust. For ease of computation, a symmetry plane is applied through the center of each component of the room so that only half of the domain was modeled. Figure 7.1a and 7.1b show the Block CSP and Detailed CSP geometry used for the evaluation of the effect of geometry on *iF*. The Block CSP includes features that have been found to be important such as the gap between the legs, shoulders, and chin (Brohus, 1997; Khalifa et a., 2006; Dygert et al., 2009). The block and detailed CSP followed the same guidelines for grid generation as detailed in Section 3.1. Both CSP geometries had ~20,000 cells on half the CSP with clustering around the CSP mouth and nose. The boundary layer around the CSP and total number of cells in the domain were also kept consistent for comparison. The Detailed CSP was also adopted to study the effect of PV on iF, using the aforementioned single and the Co-flow nozzles (Figure

5.1c); both were compared with the no-PV set-up in Figure 5.1b. The domain in Figures 5.1b and 5.1c were then used again to study the effect of changing the CSP body surface temperature from *32°C* to *28°C*.

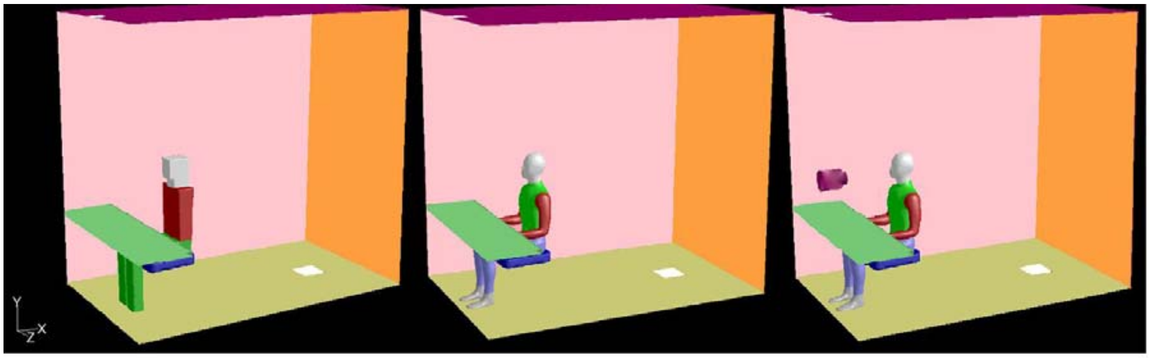

Figure 5.3: Computational domains: a) domain with Block CSP, b) domain with Detailed CSP and c) domain with Detailed CSP and PV nozzle.

In all cases pollutants with the same material properties are released from the floor, walls, desk and body with the same pollutant mass flux. This should not affect the relative iF, which is normalized with the value corresponding to perfect mixing. The CSP was set to have a constant surface temperature of *32 °C* (or *28 °C*), the walls and ceiling were set to have a constant temperature of *23 °C*, the floor was set at a constant temperature of *22 °C* and the supply air was set to *21 °C*. A total of *18.9 l/s* were supplied to the room through the floor diffuser or through the floor diffuser and PV system combined, equivalent to ~*5* total air changes per hour (ACH). BCs that varied for each case are shown in Table 5.1. The *iF* was computed for a steady (continuous) inhalation process at *6 lpm* (*0.1 l/s)*. This simple inhalation method was found to yield results that are indistinguishable from realistic cyclic inhalation (Russo & Khalifa, 2009) and is discussed in Chapter 3.7.5.

The grid development used and CFD strategy for this work follows the same method described for the CFD validation and is shown in Figure 5.2.

Table 5.1: Cases analyzed and air supply rates for each case.

Test Series	No PV	Primary	Co-flow
Floor Diffuser Air Flow, l/s	18.9	16.5	9.7
Primary Nozzle Air Flow, l/s	0	2.4	2.4
Secondary Nozzle Air Flow, l/s	0	0	6.7

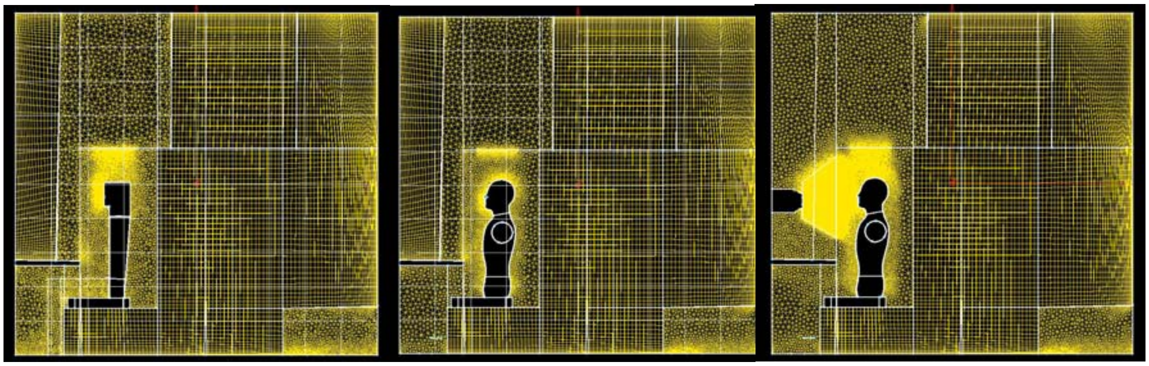

Figure 5.4: a) Grid with block CSP, b) grid with detailed CSP and c) grid with detailed CSP and PV.

5.2.2 CSP Geometry

Figure 5.5 shows comparisons of species contours for the block CSP geometry and the detailed CSP geometry along the symmetry plane. The dark blue region indicates cleaner than well mixed air and the red regions indicate dirtier air. This figure shows the difference in the pollutant distribution due to the geometry of the CSP. For the block CSP there is a much higher velocity near the face (*~0.25 m/s*) than for the detailed CSP (*~0.1 m/s*) which would affect the transport of the pollutant from the source to the BZ. For the sources released in the vicinity of the ventilation air (floor and body), the block CSP exhibits a wider column of polluted air flowing upward into the BZ than the detailed CSP. For the sources released away from the floor air diffuser (wall and desk), the opposite trend is exhibited. The thermal plume seems to act as a buffer between the CSP and the pollutant sources released away from the floor diffuser. Clearly, the CSP morphology has a significant effect on *iF* estimation and the use of a block geometry could lead to large errors as result of the unrealistic air flow field it produces around the head, neck and shoulders. However, this should not be taken to imply that *iF* estimations of acceptable accuracy cannot be obtained unless all the minute details of the human body are captured in the CFD simulations. It is important that the CSP representation avoids sharp edges and bluff shapes, and must include such generic human body details as *rounded* shoulders, neck, chin and head. Inclusion of small details, such as the nose, the ears, etc, has not been shown to be as important as the overall shape of the CSP.

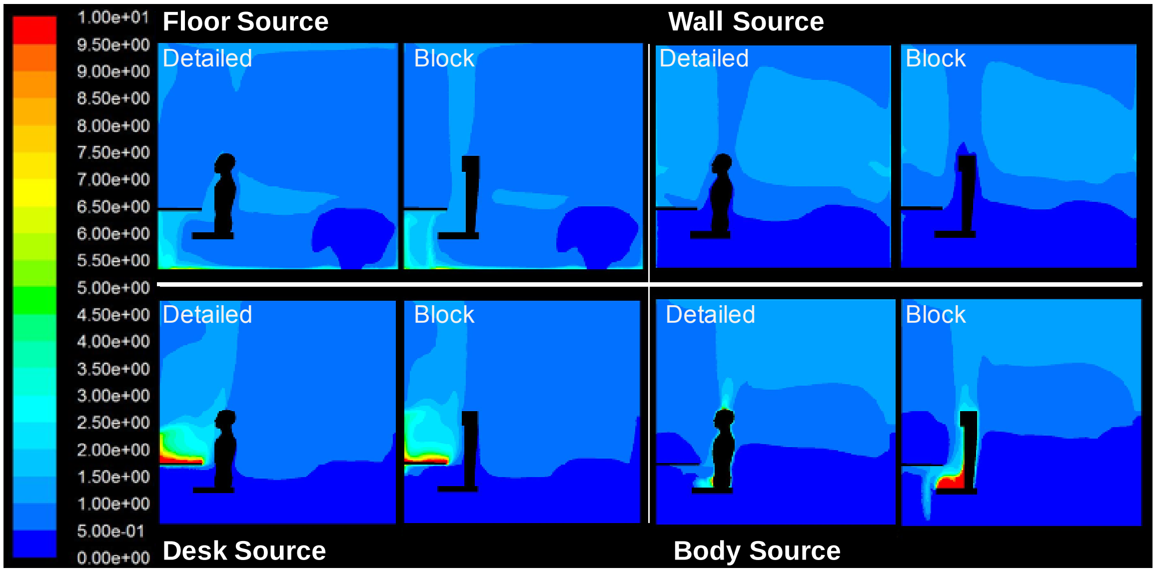

Figure 5.5: Normalized concentration for Block and Detailed CSPs. A value = 1.0 corresponds to well-mixed air. A value >1.0/<1.0 corresponds to more/less polluted air.

Figure 5.6 compares the corresponding *iF* normalized with the well-mixed condition for each pollutants source for the two representations of the CSP. With the exception of the floor source, it is evident that the rooms are not well mixed for both the detailed and block CSP. The results show that pollutants released from a source within the room do not exhibit well mixed behavior, and further support the idea that the well mixed assumption should not be used when there are indoor sources. The Block CSP case shows that the largest *iF* corresponds to the body source, whereas the results from the Detailed CSP case show that the largest *iF* corresponds to the desk source. Figure 5.4 also shows an increase in *iF* for the floor and body sources and a decrease in *iF* for the desk and wall sources.

It can be surmised from these results that the thermal plume transports pollutants generated near the supply air diffuser (floor and body in this study) to the BZ, while it acts as a buffer against pollutants that are generated away from the supply air diffuser (wall and desk in this study). Further, the results from the CSP geometry comparison show that using a Block CSP can result in more than double the *iF* values predicted with a Detailed CSP for some sources, and less than half those predicted with a Detailed CSP for other sources, depending on the source location in relation to the supply air diffuser and the CSP. This is attributed to the fact that the thermal plume, particularly in the vicinity of the head, is strongly affected by the shape of the CSP (Dygert et al., 2009). We note that the findings that Block CSP geometry is not as accurate when studying the details of the flow and concentration fields in the BZ or the quality of the inhaled air are consistent with the conclusions of Topp et al. (2002) and Melikov & Kaczmarczyk (2007).

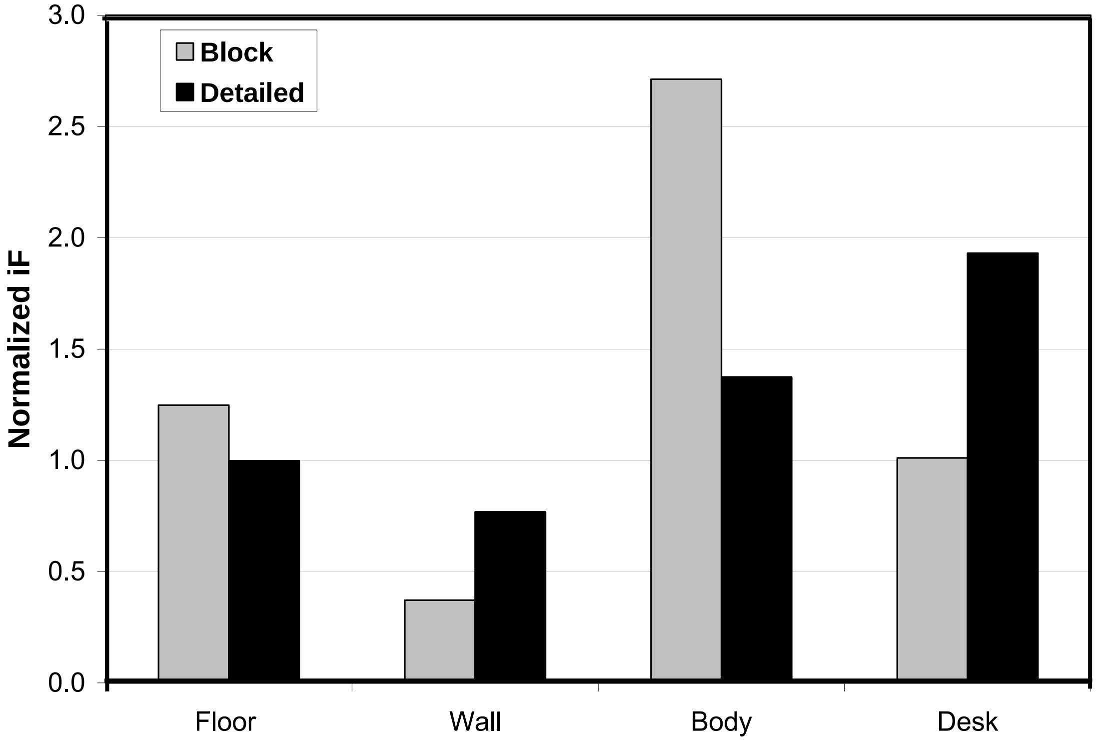

Figure 5.6: Normalized iF for Block and Detailed CSPs. A value = 1.0 corresponds to well-mixed air. A value >1.0/<1.0 corresponds to more/less polluted air.

5.2.3 Benefit of Personal Ventilation

When using the guidelines determined from the geometry comparison, the improvement in inhaled air quality was determined for two PV systems. Figure 5.7 shows comparisons of species contours for the two PV nozzle types along the symmetry plane. The concentration values have been normalized with the well mixed condition. The dark blue region indicates cleaner than well mixed air and the red regions indicate dirtier air. This figure shows the change in the distribution of the species due to the addition of a PV system. When compared with Figure 5.7, it is clearly shown that the PV systems deliver fresh air to the BZ which does not allow the transport of species to the BZ. With the effects of the Co-flow PV system more pronounced.

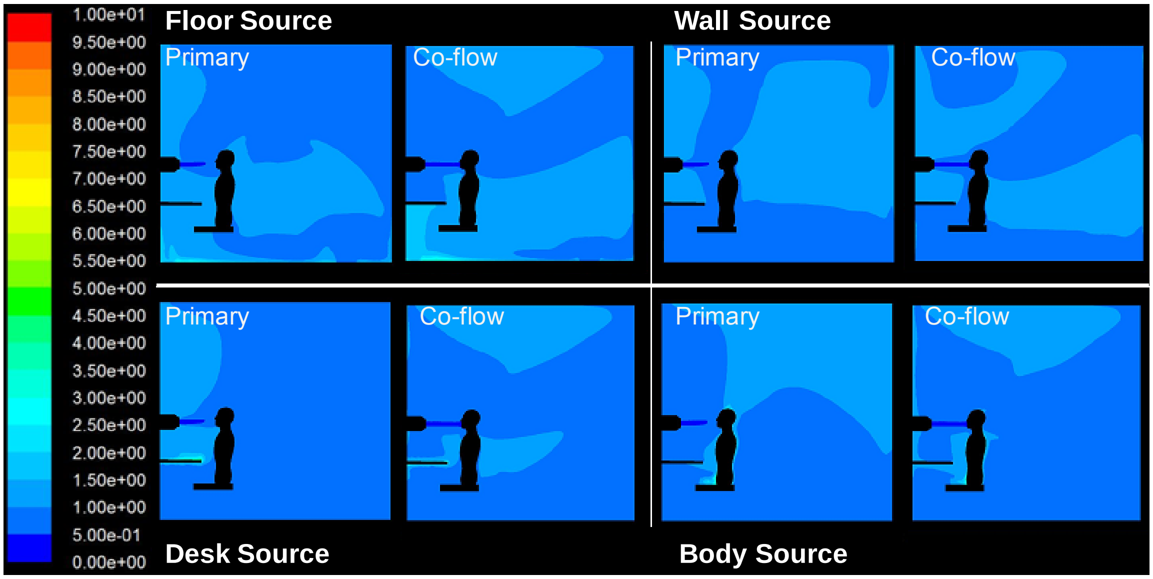

Figure 5.7: Normalized concentration for Primary and Co-flow PV nozzles. A value = 1.0 corresponds to well-mixed air; a value >1.0/<1.0 corresponds to more/less polluted air.

Figure 5.8 shows a comparison of normalized *iF* of each source for the Detailed CSP case without PV and with the two types of PV nozzles. The figure shows a decrease in *iF* for both PV systems, with a greater decrease for the Co-flow case. It is clear that the Co-flow PV system is much more effective in removing pollutants from the occupants BZ than the single jet Primary case. It was shown that both PV systems were able to decrease the *iF* and, therefore, increase the inhaled air quality. As found in Khalifa et al. (2009) and Russo et al. (2009), the results also show that the Co-flow nozzle design is superior to the single primary jet when delivering fresh air to the BZ. Another important trend that should be noted is that, with the use of PV systems, the effect of the location of the source becomes less significant and the *iF* values are nearly equal for all sources.

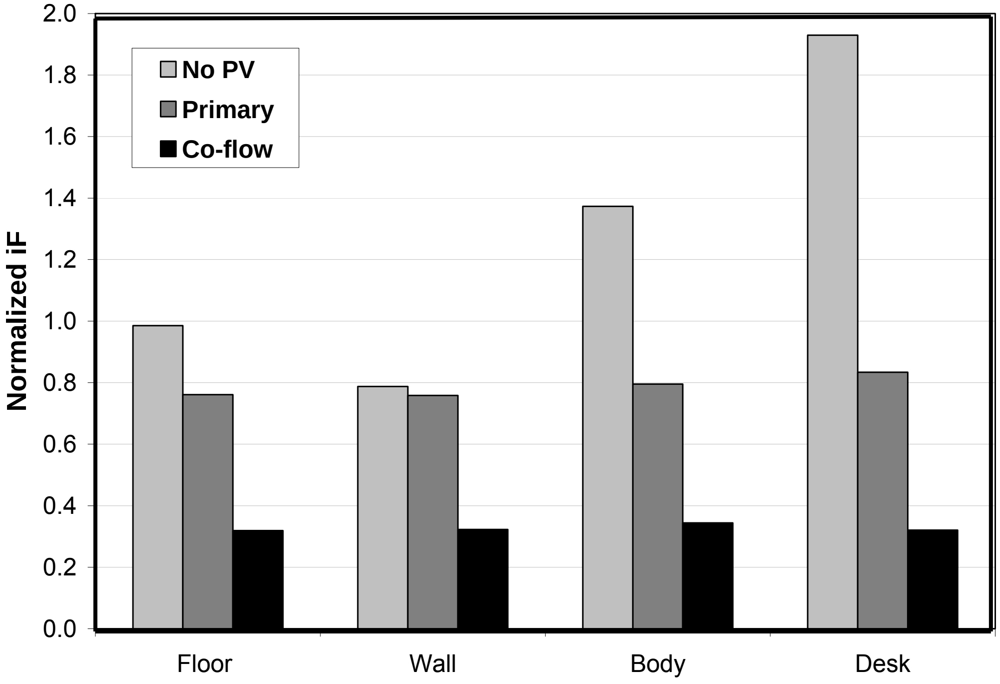

Figure 5.8: Normalized iF for No PV, Primary and Co-flow PV nozzles. A value = 1.0 corresponds to well-mixed air. A value >1.0/<1.0 correspond to more/less polluted air, respectively.

5.2.4 Effect of Body Surface Temperature

The results presented so far were computed for a CSP surface temperature of *32 °C*, corresponding to a naked or scantly clothed body. This is the case where the thermal plume is expected to be strong, which constitutes a challenge for PV jets penetrating into the BZ (Melikov, 2004; Russo et al., 2009; Dygert et al., 2009). To assess the effect of CSP surface temperature on *iF*, we analyzed the no-PV case and the two PV systems when the body surface temperature was reduced to *28 °C*, which is a more appropriate value for a clothed person. Figure 5.9 shows that the CSP surface temperature has a relatively small or negligible effect on *iF* values for all pollutant sources.

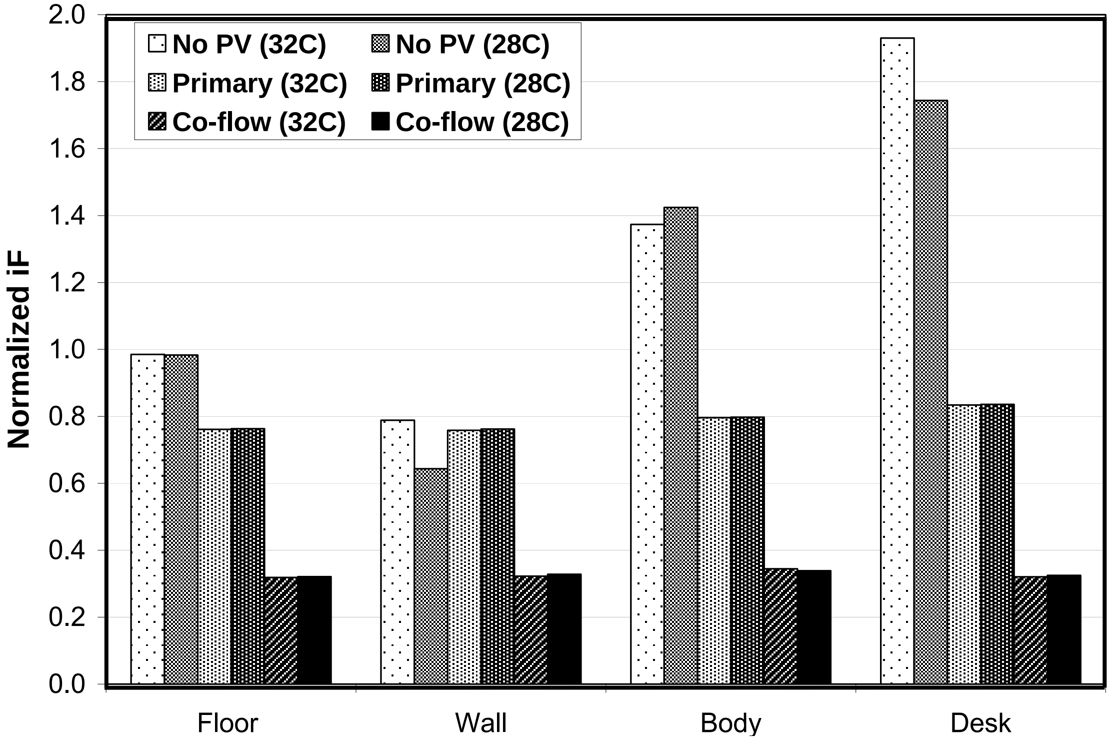

Figure 5.9: Normalized iF for 32°C and 28°C CSP surface temperature. A value = 1.0 corresponds to well-mixed air. A value >1.0/<1.0 correspond to more/less polluted air.

This figure shows a less than *10 %* change in *iF* for all sources without PV. For the two PV cases there is a change of *iF* of *1 %* or less. This shows that the changes in *iF* due to a *4 °C* surface body temperature changes are negligible. For the cases with PV, the lower momentum creates less of a disturbance for the PV jet and air is delivered to the BZ easier. This also shows the robustness of these PV systems. The two PV systems can deliver improved air quality to the BZ under a multitude of indoor pollutant emission scenarios, as well as for different body surface temperature (i.e., different clothing insulation). It should be noted that a *4 °C* change in body surface temperature results in a large *47 %* change in thermal plume momentum above the head, however, it only results in a negligible change of *iF* (at most *10 %*). For the case without PV, a deduction in the strength of the thermal plume changes the velocity of the air in the BZ which makes penetration of the BZ easier. However, in this case the thermal plume is undisturbed and the inhaled air comes from the same path line as the case with higher momentum making the change in results negligible. This implies that modeling the momentum of the thermal plume correctly is less significant than modeling the correct path of the inhaled air and transport of pollutants. However, for the Block CSP, both the momentum in the BZ and the path of the inhaled air are significantly changed compared with those of the Detailed CSP, resulting in an appreciable error in the estimation of *iF*.

5.2.5 Breathing method

Figure 5.10 shows the iF for four sources in a typically office space for four different breathing methods. This plot shows that there are negligible differences between modeling breathing as a volume of air in a hemisphere in the BZ, modeling steady state inhalation and modeling unsteady sinusoidal breathing. Using a nostril area average gives good results for all source locations except for a body source. This is because of the high gradient of species in the boundary layer around the CSP when the source is emitted from the body. From this, using a nostril are average should be used with great caution or not at all when modeling inhalation exposure.

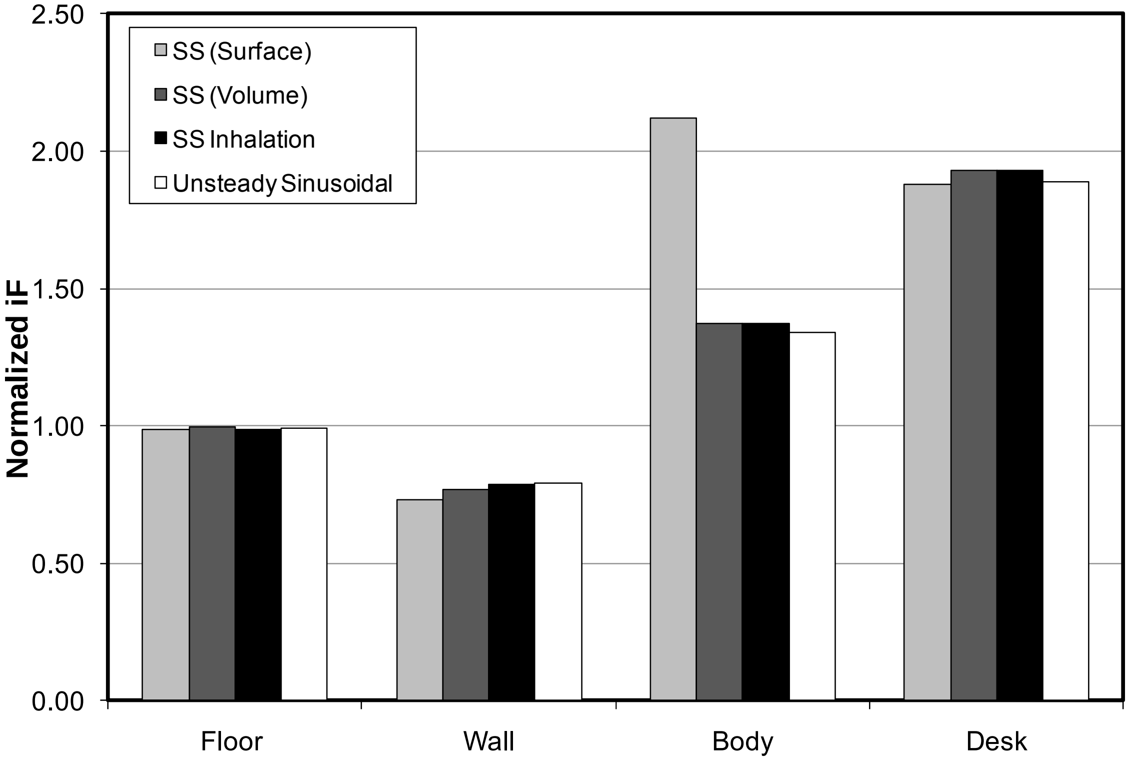

Figure 5.10: iF for four source locations and four different breathing methods.

5.2.6 Section Conclusions

The results for all cases show that pollutants from a source in a room do not exhibit well mixed behavior. In fact, it is shown that the *iF* can be more than twice as high as, or more than two times lower than that predicted by the well-mixed assumption. The results from the CSP geometry comparison show that using a Block CSP may overestimate or underestimate the predicted *iF* by more than a factor of 2, depending on the source location relative to the occupant and the supply air diffuser. This can be attributed to the distortion of the thermal plume by the sharp edges and the bluff objects in the Block CSP, especially in the vicinity of the head and the BZ. With a floor diffuser, the thermal plume acts as an effective transport mechanism to the BZ of pollutants emitted from the floor and the body, while acting as a buffer against pollutants emitted from sources away from the occupant (wall and desk).

Analysis of two PV systems demonstrates that, even with a little as *2.4 l/s* of fresh air delivered through the PV nozzle (plus *4.8 l/s* delivered through the floor diffuser), both PV systems can effect a significant reduction in *iF* compared with conventional general ventilation through a floor diffuser delivering *7.2 l/s* of fresh air. These results also show that the Co-flow PV nozzle is far superior to a single round PV nozzle, with the former achieving better than a *57 %* reduction in *iF* compared with the latter at the same *2.4 l/s* fresh air supply through either PV nozzle. The Co-flow PV system's advantage over general ventilation rages from *59 %* for the wall pollutant to *83 %* for the desk pollutant. An interesting feature of the PV systems is that, unlike the general ventilation system whose *iF* depends strongly on the location of the pollutant source, the iF values achieved by the two PV systems investigated are relatively insensitive to the pollutant source location. All three ventilation schemes (with and without PV) exhibited little sensitivity of *iF* to the body surface temperature (i.e., different clothing insulation).

Finally, it is recommended that, when using CFD to study the PμE and inhaled air quality, it is important that sufficient details of the CSP be included, especially such anatomical details as the separation of the legs, the shoulders, the chin and the roundedness of the human body parts, i.e., avoid the use of bluff, block objects with sharp corners. This is particularly true for CFD investigations of PV systems, where there is an intimate interaction between the PV jets and the body's thermal plume that is sensitive to the general morphology of the CSP.

The computational methodology utilized here lends itself to detailed analysis of other exposure scenarios, including those involving different geometries, or different phenomena such as chemical reactions of Ozone and VOCs in the personal micro-environment.

5.3 *Personal Ventilation vs. Conventional Ventilation Systems*

The idea of PV is to deliver fresh air directly to the BZ of the occupants in the space. A major argument against the use of PV is the question of how clean the air away from the PV system would be for a visitor. For all the work that is done for this research, all PV systems are used in conjunction with a floor diffuser that delivers the remainder of the fresh and/or recirculated air that is not dispersed by the PV system. The thought behind this approach is that the freshest air will be supplied directly to the occupant, while the rest of the space receives acceptable air quality. To test this line of thinking, the air quality at several locations in a space with PV systems and displacement ventilation has been compared with a setup with only displacement ventilation delivering the same total amount of fresh air as the combination of the PV system and floor diffuser. Basically, we are trying to determine if the air away from a PV system is 'just as good' as the air in the same location of a setup that is ventilated with a conventional ventilation system. The PV systems compared to the no-PV setup are the Co-flow PV system and the Primary (single jet) PV system.

5.3.1 Domain and Setup

The validated CFD model from Section 3 has been used to compare air quality in all regions in the room for a scenario with PV and a scenario without, i.e., with just the floor diffuser. A new grid was developed to test this concept with four cubicles, a hallway and four thermal CSPs with displacement ventilation and optional PV system in each cubicle corner. There were four floor diffusers and four ceiling exhausts in the entire space. The domain is shown in Figure 5.11 and 5.12. The grid shown in Figure's 3.9-3.11 were expanded to include both half's of a cubicle and a hallway. Only one cubicle was modeled with symmetry along two sides to represent four cubicles as shown in Figures 5.11 and 5.12. The total number of cells for one cubicle was a combination of 8.7 million structured and unstructured cells. This large number of cells is approximately twice as many as the validation grid because we are now modeling the entire cubicle instead of modeling one have side of the office space by applying symmetry along the CSP center plane. The same solver parameters that were used in section 3.1 were used here. The Navier-Stokes equations were solved using Fluent. The Realizable k-ε turbulence model was used along with the enhanced wall treatment option. Second-order accurate upwind schemes were employed to solve the momentum and energy equations, and a second-order accurate scheme was used for the pressure interpolation.

The BCs that were employed here were similar to those used in section 3.1. For the Co-flow case, the same velocity profile was used for the primary and secondary jets with a velocity magnitude of *~1.2 m/s* as for the validation cases. For the Primary PV system a velocity profile was used with a velocity magnitude of *~1.2 m/s* and the secondary jet was turned-off. In the case without PV, all fresh and recirculated air was delivered through the floor diffuser. To maintain the same air supply to the chamber in all cases, the air supply through the floor diffuser in the Primary and No PV case were increased to compensate for turning-off the secondary and/or primary jet. A pressure outlet was used at the exhausts with a value of *0* gage pressure in all cases. The CSP surface temperature was set to *28 ˚C* and the primary and secondary jet temperatures, the floor diffuser air supply temperature, the average chamber wall temperature, and the average floor temperature was set to match those of Case 1 from Section 3.

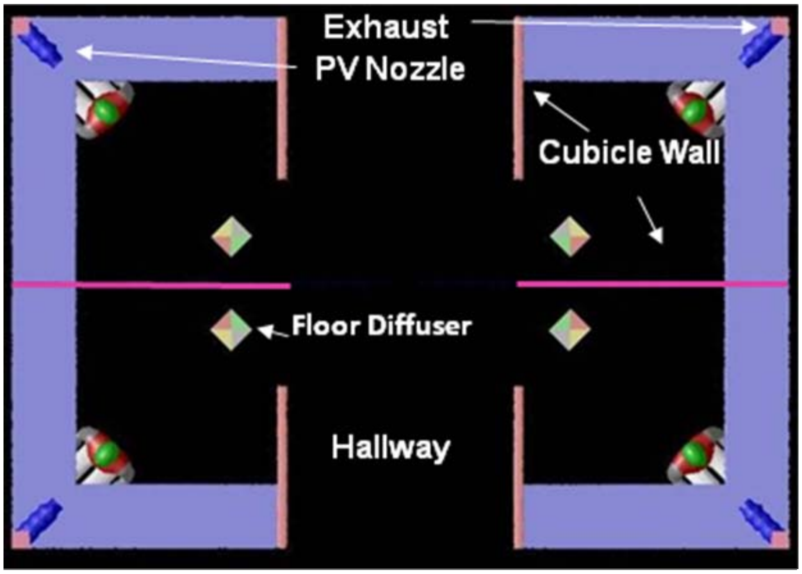

Figure 5.11: Four cubicle domain.

For the three cases compared (No PV, Primary only and Co-flow), iF was calculated at 6 locations: 1) BZ of the CSP modeled, 2) BZ height of a person standing behind the CSP in the cubicle, 3) BZ height of a person sitting behind the CSP in the cubicle, 4) BZ height of a person standing in the hallway, 5) BZ height of a person sitting in the hallway and 6) at a location under the desk. These 6 locations are shown in Figure 5.13 with the coordinates given in Table 5.2 where the origin is the CSP's nose (location 1). The use of iF in locations where a CSP is not located was chosen to represent the air quality that an individual would be exposed to if they were to enter the space for short periods of time, or just pass by the locations. Bjorn and Nielsen (2002) found that the protective effect of the thermal plume around the body disappears speeds as low as *0.2 m/s*, implying that a person is exposed to the same concentration as in the ambient air at the BZ height when moving at these speeds. It is accepted that the iF values in locations 2-6 would be different if a heated CSP was present there for significant periods of time. However, the concept of PV is to deliver fresh air directly to the locations of the room that is occupied for the majority of the time and to assume that other locations are occupied for the same length of time would be counterintuitive. Section 5.2.2 gives comparisons of AQI and iF for an occupied space and an unoccupied space.

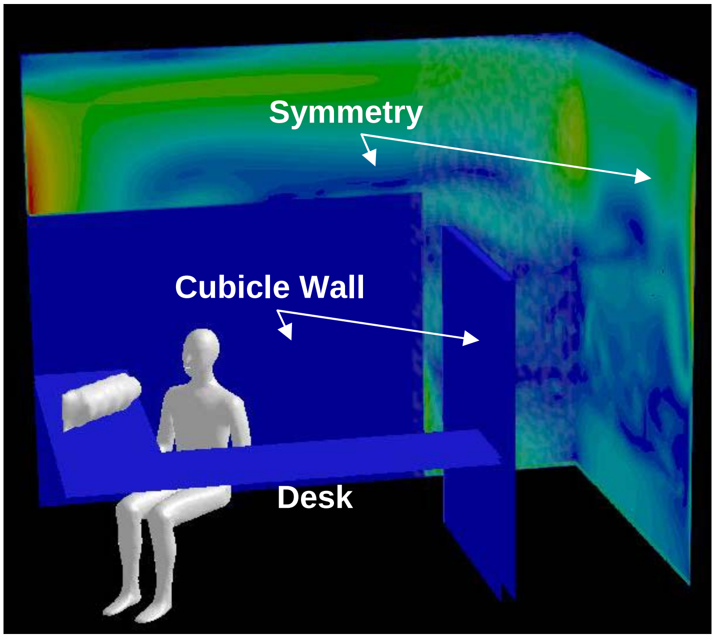

Figure 5.12: One cubicle setup and how it was used to model four cubicles.

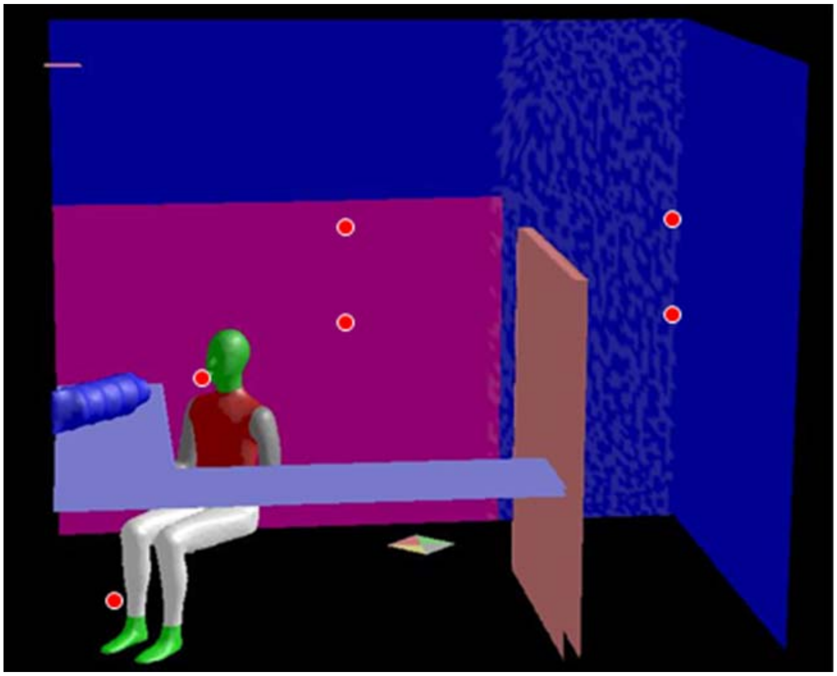

Figure 5.13: Assumed BZ locations for 1) seated CSP in front of the PV system, 2) standing CSP in the cubicle, 3) seated CSP in the cubicle away from the PV system, 4) standing CSP in the hallway, 5) seated CSP in the hallway and 6) a location under the desk.

Table 5.2: Coordinates for the 6 locations studied.

	x	y	z
1	0.00	0.00	0.00
2	0.90	0.50	0.00
3	0.90	0.00	0.00
4	2.68	0.50	0.68
5	1.21	0.00	0.68
6	-0.63	-0.85	0.00

iF was calculated for each location for four different contaminant sources. The first source is a body source that could represent any emissions from the body such as odor, aldehydes, ketones, carboxylic acids and secondary organic aerosols. Second, a desk source was modeled that could represent emissions from building materials and desk cleaners. A floor source was also modeled to represent emissions from floor cleaners and carpets. Finally, a wall source was modeled to represent emissions from paint, particle board, gypsum board or other building materials.

5.3.2 Species transport with and without a CSP

To determine the change of air quality in a location of the room with and without a CSP, two cases were compared. Using the grid from Section 5.1, two cases with four sources were simulated. Case 1 had a CSP and Case 2 did not (the CSP was filled in with instructed grids and all other sections of the grid remained the same). Figure 5.14 shows the concentration contours for a case with a CSP compared to a case without a CSP. From this figure it is clear that the thermal manikin changes air flow patterns in the room, therefore change species distributions.

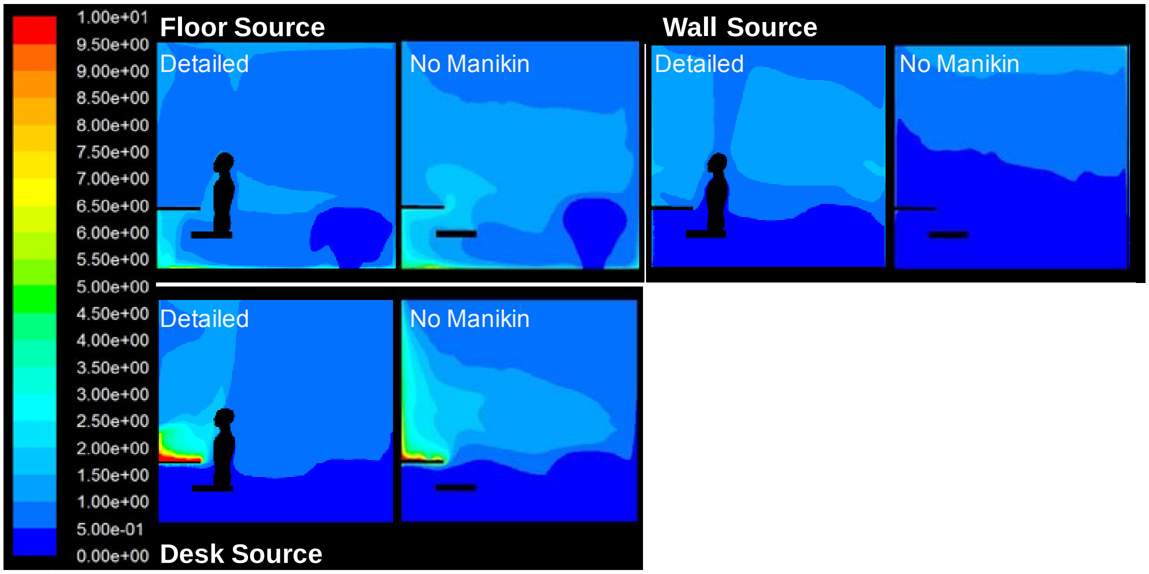

Figure 5.14: species contours for a detailed CSP compared to a case with no CSP.

To understand the severity of the change, iF was determined for both cases. For Case 2, the average concentration in a hemisphere located where the nose would be if a CSP was modeled was used as the inhaled volume of air as described in Section 8. These results are shown in Figure 5.15. Although the iF for each source location can change, the overall trend is captured it the case without a CSP. In fact, with the absences of a CSP the nature of the iF with regards to weather it is above or below well mixed levels is captured compared to a case with a CSP.

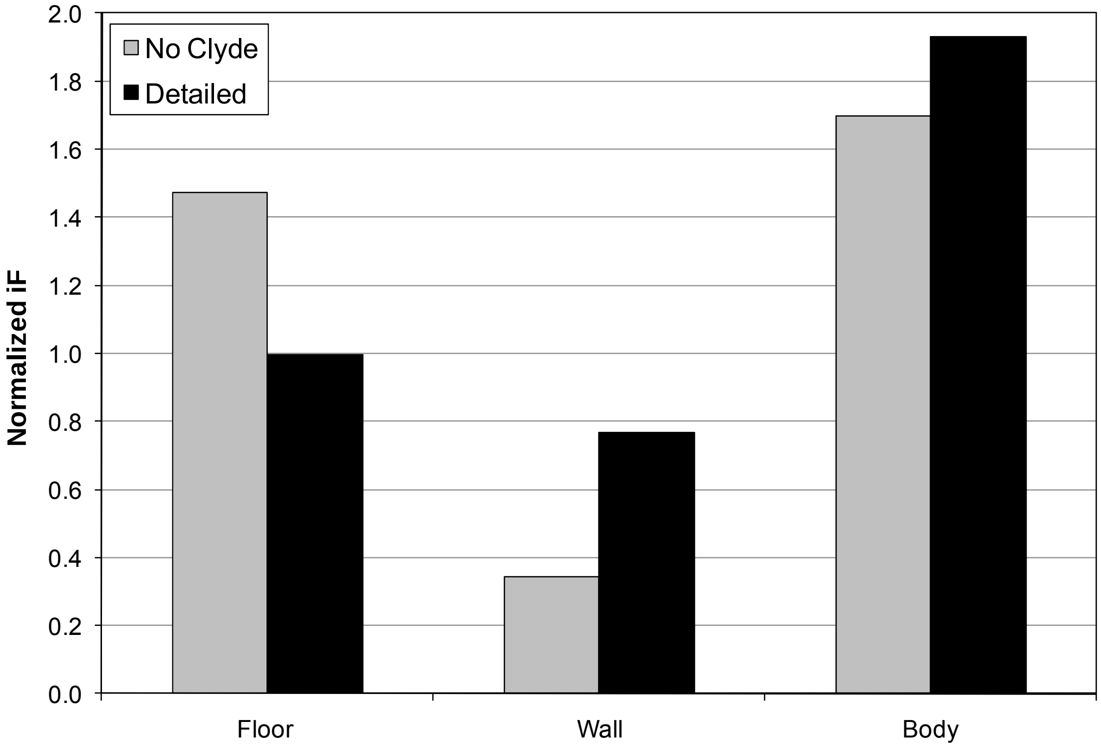

Figure 5.15: iF for a case with a CSP and a case without.

5.3.3 Air Quality Comparison

Figure 5.16 shows the normalized species contours for the case with PV turned off. The contours show a range from *0-2*. The concentration values have been normalized with the well mixed condition where a value of *1.0* corresponds to a perfectly mixed room. The dark blue region indicates cleaner than well mixed air and the red regions indicate dirtier air. For this ventilation system the concentration distribution is highly non-uniform with high gradients near the source for each source location and it is important to note that the freshest air is near the floor and away from the occupied BZ for all specie contours. Having the best air quality along the floor and below the BZ requires more air to be delivered to the space to achieve elevated air quality at the BZ height. The contours show that in the upper half of the space away from the sources, the concentration levels become well mixed (green).

Figure 5.17 shows the normalized species contours for the case with the Primary PV system. The contours shown range from *0-2* with *1.0* representing well mixed values (green). For this ventilation system the concentration distribution is highly non-uniform as in the case without PV and it is important to note that the freshest air is now split between the floor level and the occupied BZ for all species. This is the goal of PV, to deliver fresh air to a person without it becoming contaminated with all the pollutants that might exist in the space. Again, in the upper half of the space away from the sources and PV system, the concentration levels become well mixed.

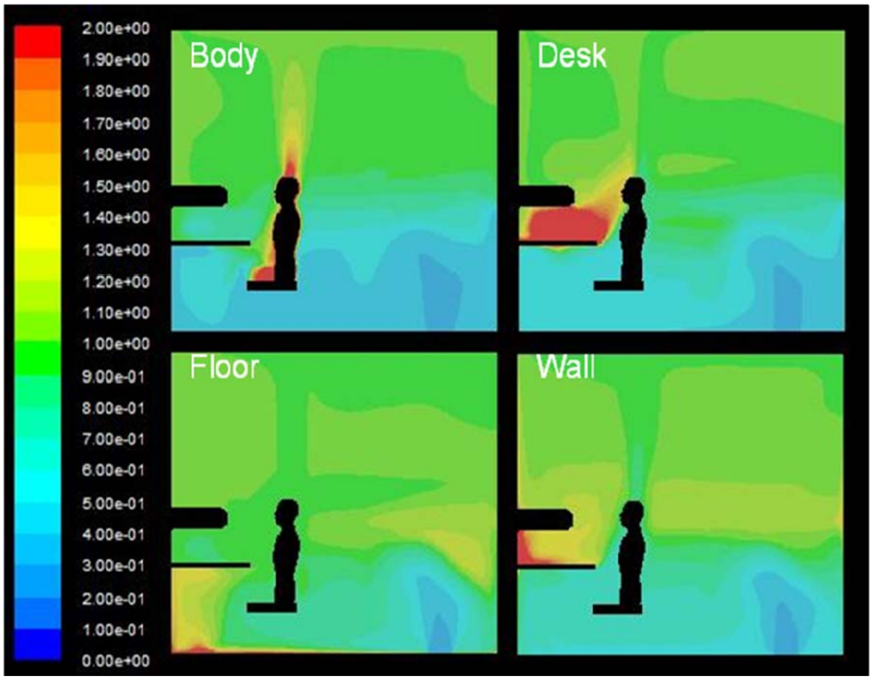

Figure 5.16: Species concentration contours normalized with the well mixed assumption when the PV system if off and all air is supplied through the floor diffuser.

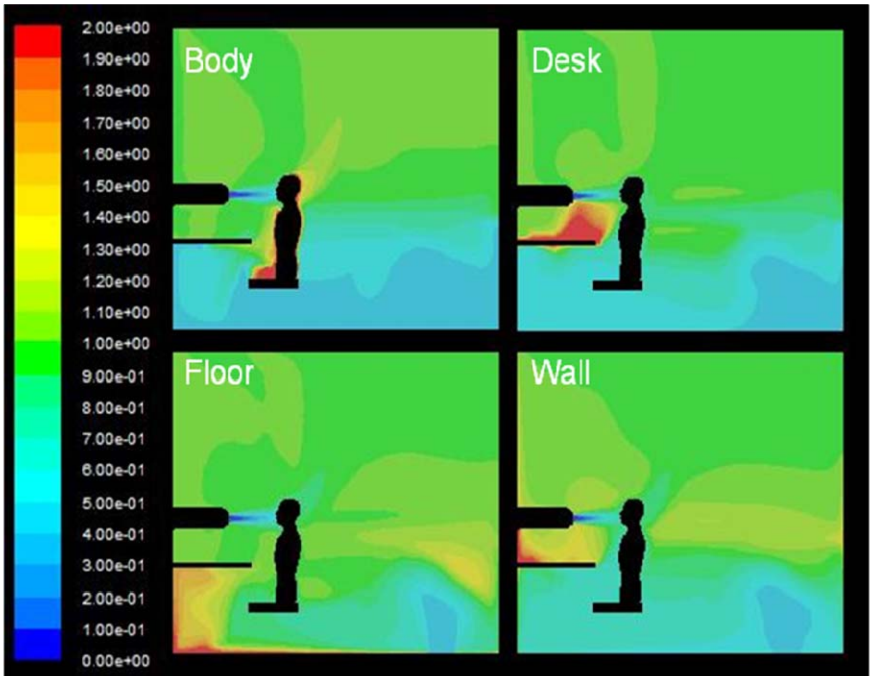

Figure 5.17: Species concentration contours normalized with the well mixed assumption when the Primary PV system where air is supplied through the primary jet of the PV system and through the floor diffuser.

Figure 5.18 shows the normalized species contours for the case with the Co-flow PV system. For this ventilation system the concentration distribution is non-uniform as in the other two cases and the freshest air is now delivered to the occupied BZ for all species. This is the main benefit of the Co-flow nozzle; to deliver fresh air to the regions of the room where people will breathe. These contours show a decreased air quality along the floor; however, people do not spend much of their time crawling during the work day so this is not seen as a disadvantage. For this case, the majority of the room away from the source locations (periodically occupied locations) shows that the air quality is well mixed which could be a secondary benefit to using the Co-flow PV system; i.e. delivering fresh air to highly occupied regions of the space while maintaining well mixed conditions elsewhere.

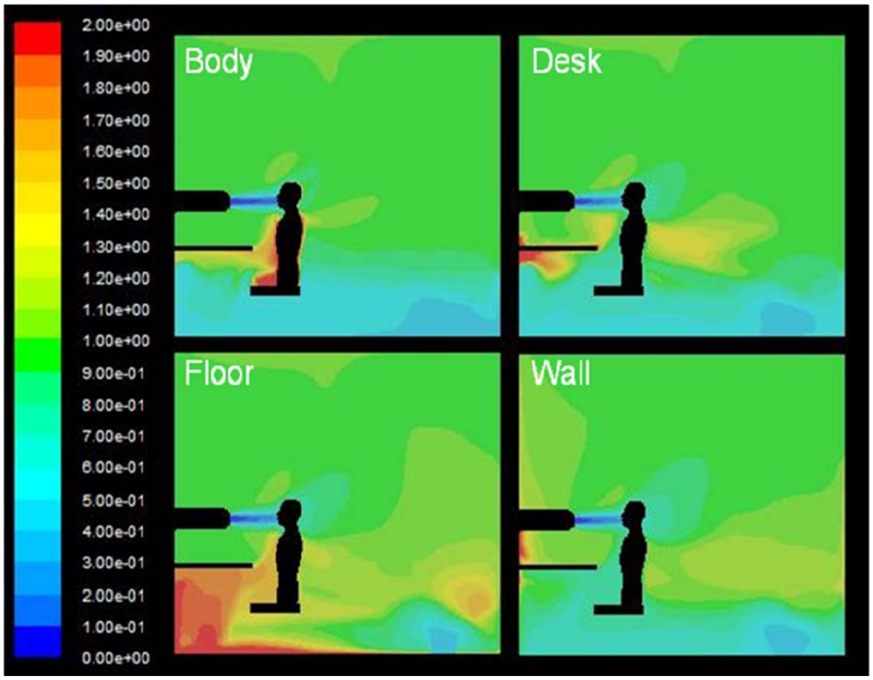

Figure 5.18: Species concentration contours normalized with the well mixed assumption when the Co-flow PV system where air is supplied through the primary and secondary jet of the PV system and through the floor diffuser.

To examine these results on a quantitative level, iF was calculated for 6 locations throughout the space. Figure 5.19 shows calculated iF for location 1 (thermal CSP's BZ) for each source normalized with the well mixed assumption. An iF of *1.0* represents well mixed inhaled air quality, a value greater than one shows dirtier than well mixed air is inhaled and a value less than one shows that cleaner than well mixed air is inhaled. The results show that the inhaled air quality is not well mixed for any of the ventilation cases modeled at location 1. For the case without PV, the iF is higher or lower than well mixed depending on the location of the source. For sources located near the CSP (body and desk sources), inhaled air quality is worse than well mixed and for sources away from the thermal CSP (floor and wall), the thermal plume acts as a protective barrier against the transport of contaminants into the BZ and the calculated inhaled air quality is better than well mixed. The figure also shows a decrease in *iF* for all sources for both PV systems with all iF's less than *1.0.* A greater decrease for the Co-flow case was found. The Co-flow PV system improves iF for a person seated directly in front of the nozzle up to ~5 times compared to a case without PV. It is clear that the Co-flow PV system is much more effective in removing pollutants from the occupants BZ than the single jet Primary case, but that both PV systems were able to decrease the *iF* and, therefore, increase the inhaled air quality compared to no PV.

For the standing height locations studied (locations 2 and 4), Figures 5.20 and 5.21 show the calculated iF for each source normalized with the well mixed assumption. Both figures show nearly well mixed conditions for all pollutants and ventilation configuration studied. This means that at a typical standing heights in a typical office space, a person entering an occupied office space will inhale air of well mixed quality whether a PV system is in use or not. This finding adds weight to the argument for the use of PV and shows that PV can redistribute air without worsening air for standing/walking heights.

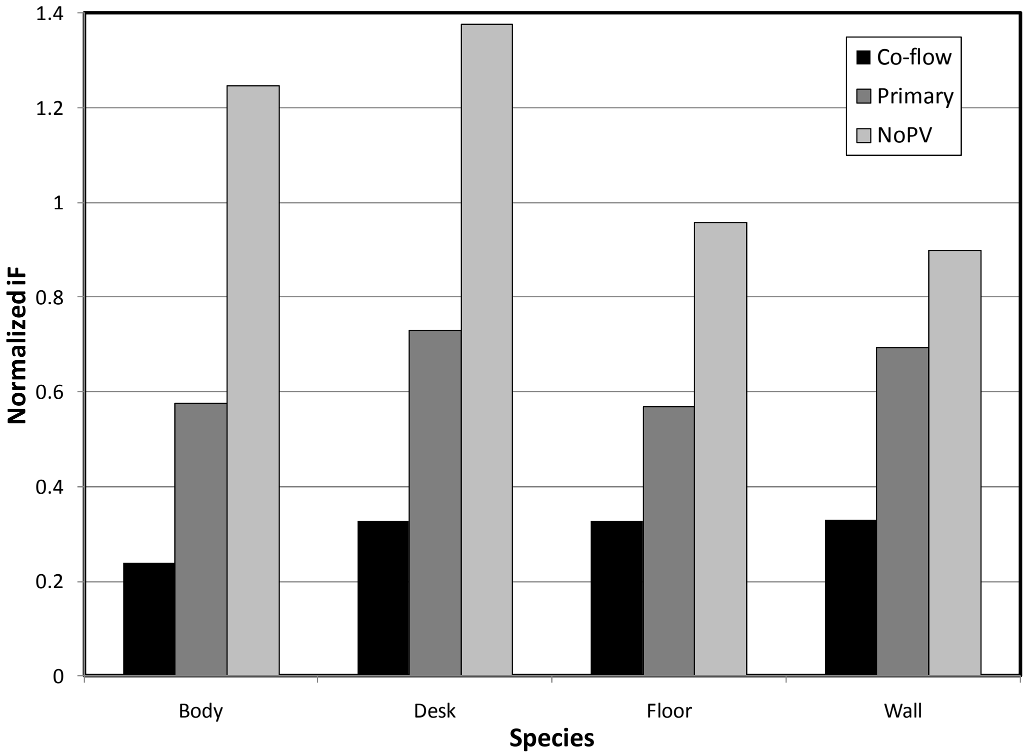

Figure 5.19: iF for location 1.

For the seated locations studied (locations 3 and 5), however, larger discrepancies were shown. Figure 5.22 and 5.23 show the calculated iF for each source normalized with the well mixed assumption for locations 3 and 5, respectively. Figure 5.20 shows that the iF of the ventilation configuration without PV, varies from *20 %* lower to *20 %* higher than the well mixed assumption, whereas the Primary and Co-flow PV system's show relatively well mixed results except for the wall source for the Primary PV system. Although the Primary PV system shows an iF of *20 %* higher than well mixed condition for the wall source, it is still delivering the same quality of air as the baseline case without PV. Figure 5.23 shows a similar trend with all systems resulting in nearly well mixed values except for the case with the wall sources where all systems give a normalized iF of ~*20 %* higher than well mixed condition.

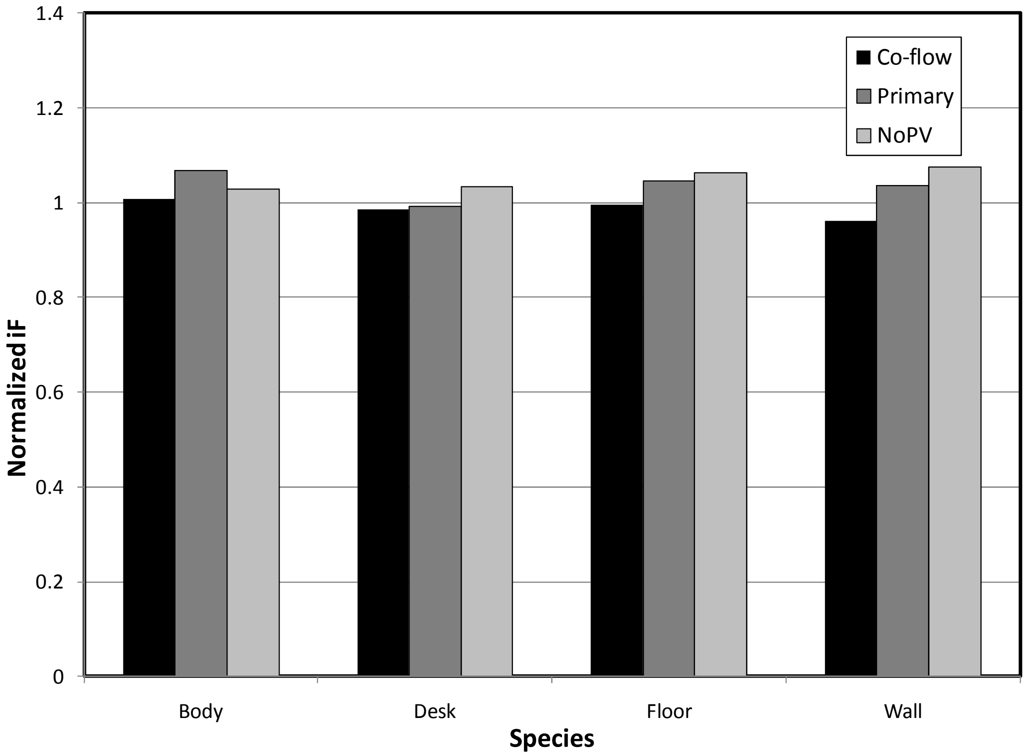

Figure 5.20: iF for location 2 (standing CSP in the cubicle).

To be thorough, iF was also compared for a location under the desk. Figure 5.22 shows the iF for location 6. This figure shows that the resulting inhaled air quality at this location is better than well mixed for the body, desk and wall sources. However, for the floor source, iF results were as high as two times the well mixed assumption. All three ventilation systems resulted in worse than well mixed iF's, with the Co-flow PV system the highest. This is not a surprising finding. The location chosen was near the floor, resulting in worse than well mixed results for the floor source, likewise it would be expected that a point near the wall would result in high iF levels for the wall source, a point near the desk would result in high iF levels for the desk source and similarly for the body source. The Co-flow PV system shows the worst results for the floor source because there is the lowest the amount of fresh air delivered by the floor diffuser for dilution for this ventilation configuration. However, as shown in Figure 5.19 the Co-flow PV system provides the most air near the body and results in the lowest iF. This redistribution of air is the goal of PV; to deliver fresh air to breathing zone heights to improve inhaled air quality instead of allowing fresh air to mix with indoor pollutants as it reaches breathing zone levels from floor or ceiling diffusers.

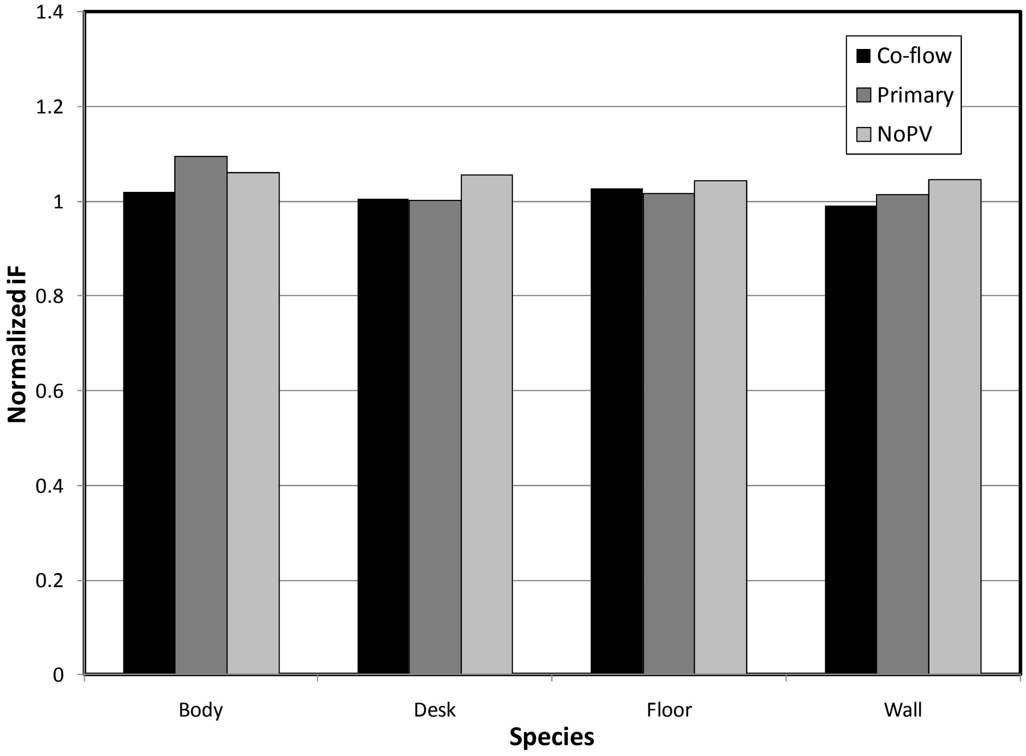

Figure 5.21: iF for location 4 (standing CSP in the hallway).

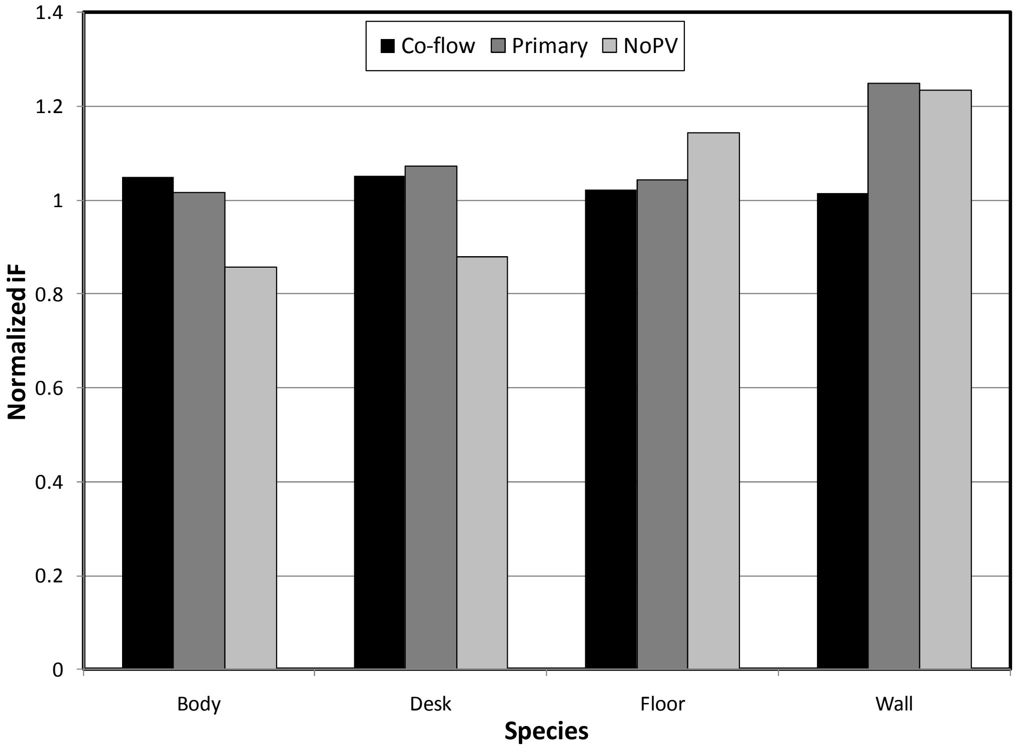

Figure 5.22: iF for location 3 (seated CSP in the cubicle away from the PV system).

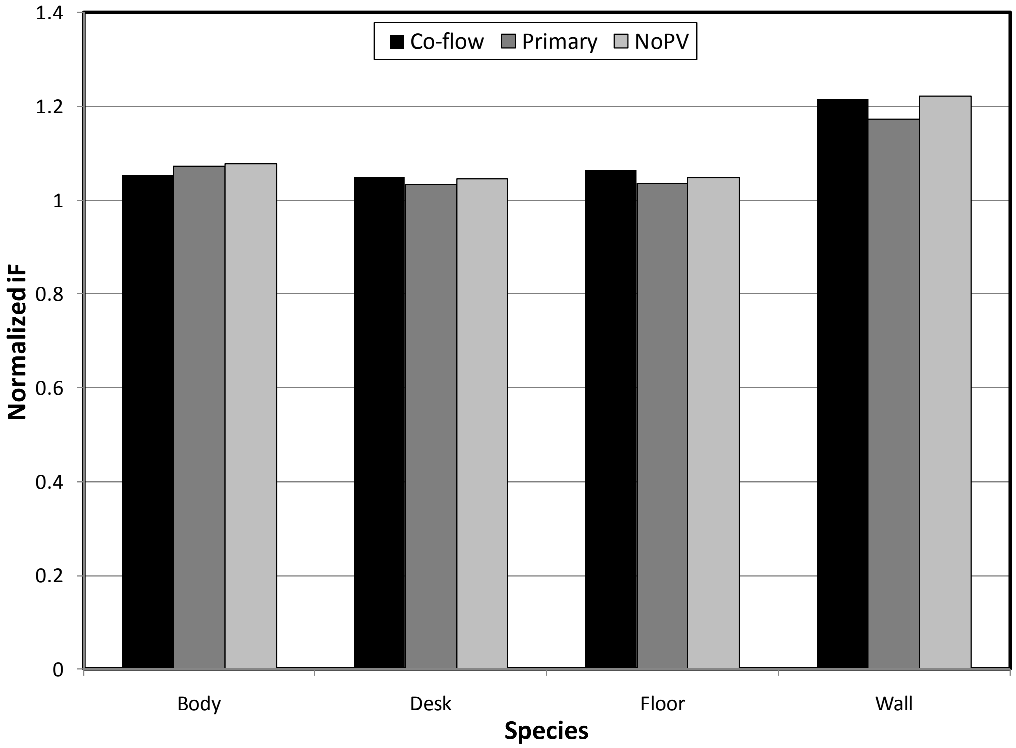

Figure 5.23: iF for location 5 (seated CSP in the hallway).

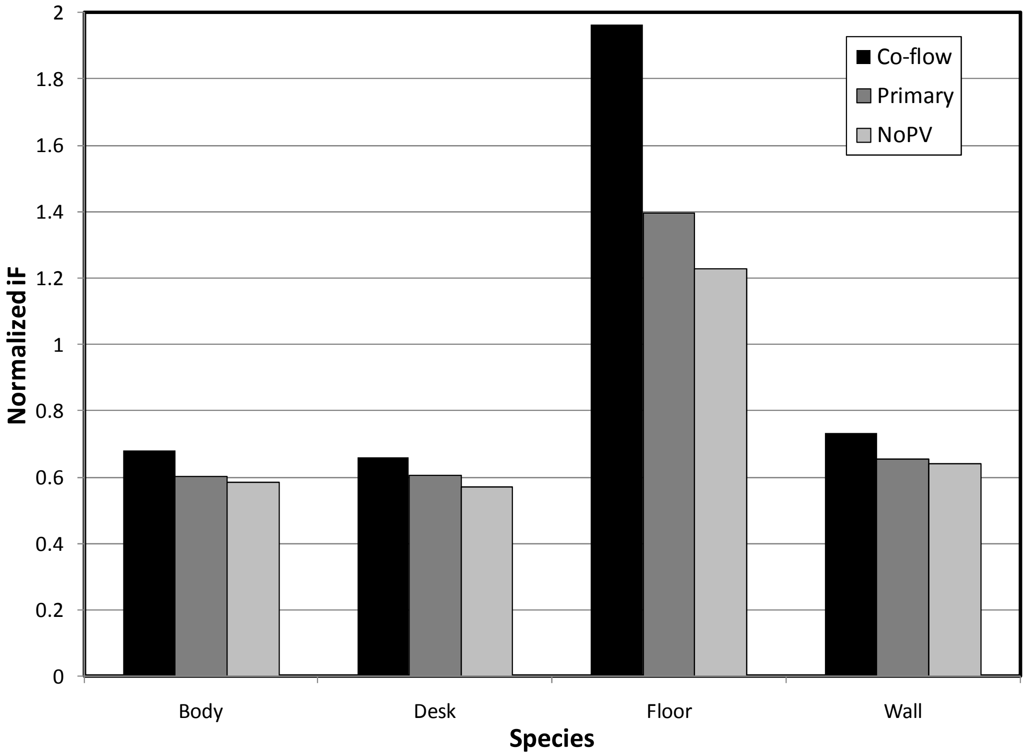

Figure 5.24: iF for location 6 (under the desk).

To examine the inhalation air quality for a typical sitting and standing height, iF was calculated along two planes using the local concentration for the inhalation value and is shown in Figures 5.25-5.30. From these figures it is clear that nearly well mixed conditions are achieved for the standing height plane with more variation shown for the seated plane and confirms the findings for the iF for the 6 locations in the room.

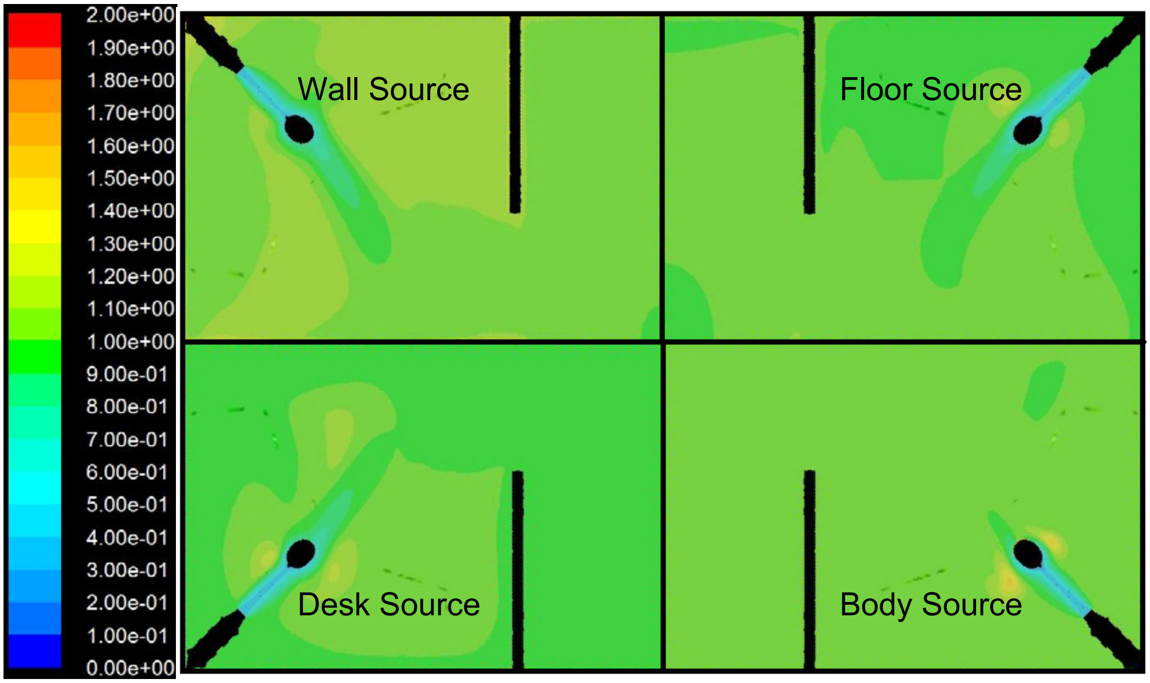

Figure 5.25: Normalized iF along a typical height for a seated person for the Co-flow PV system.

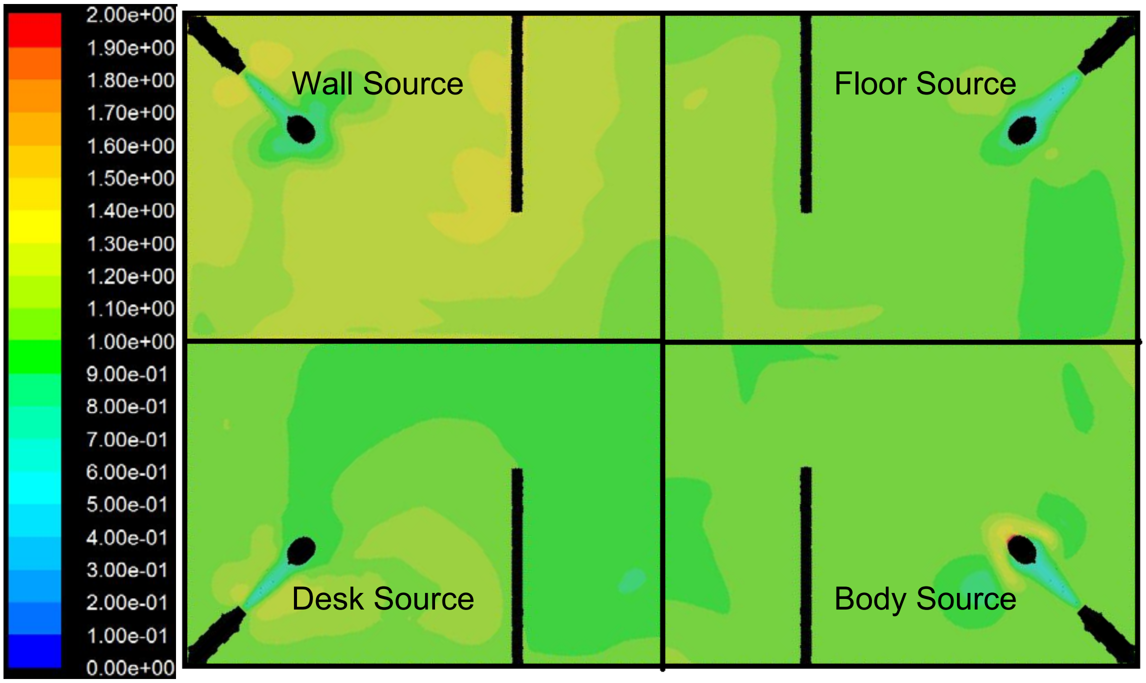

Figure 5.26: Normalized iF along a typical height for a seated person for the Primary PV system.

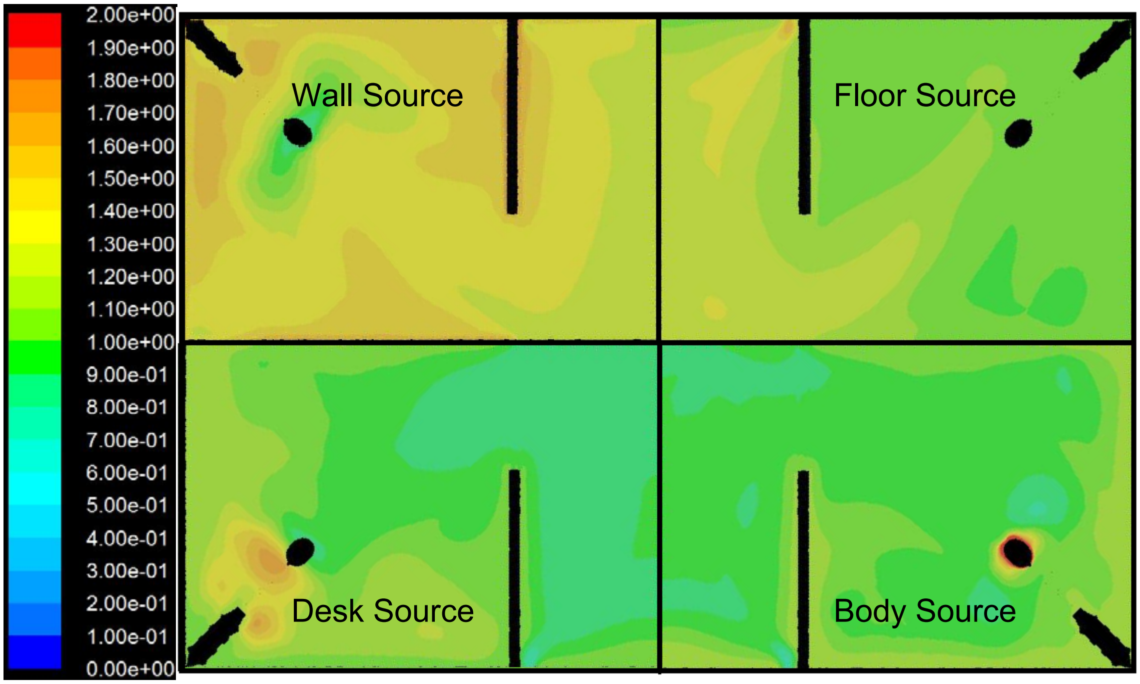

Figure 5.27: Normalized iF along a typical height for a seated person for a conventional ventilation system.

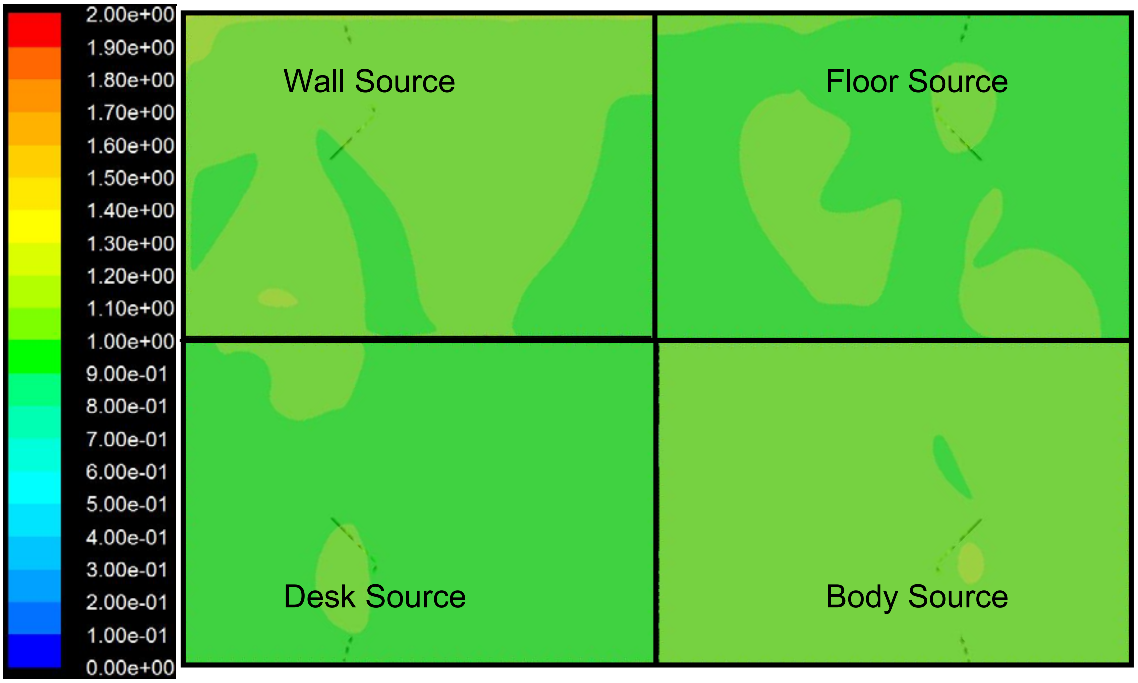

Figure 5.28: Normalized iF along a typical height for a standing person for the Co-flow PV system.

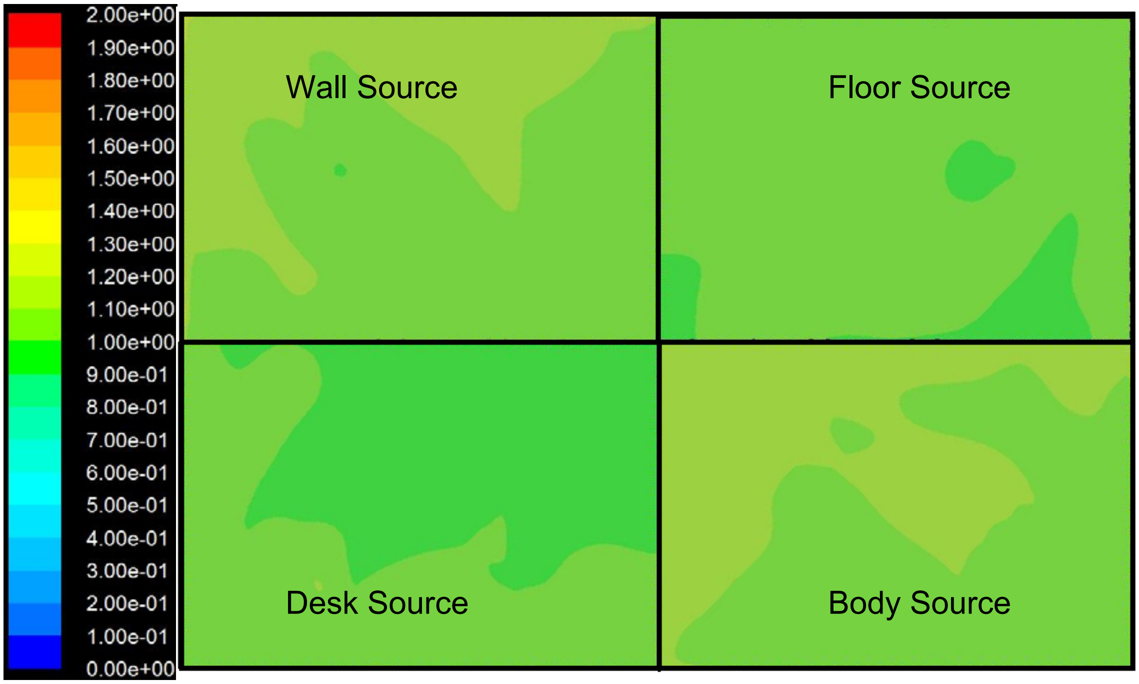

Figure 5.29: Normalized iF along a typical height for a standing person for the Primary PV system.

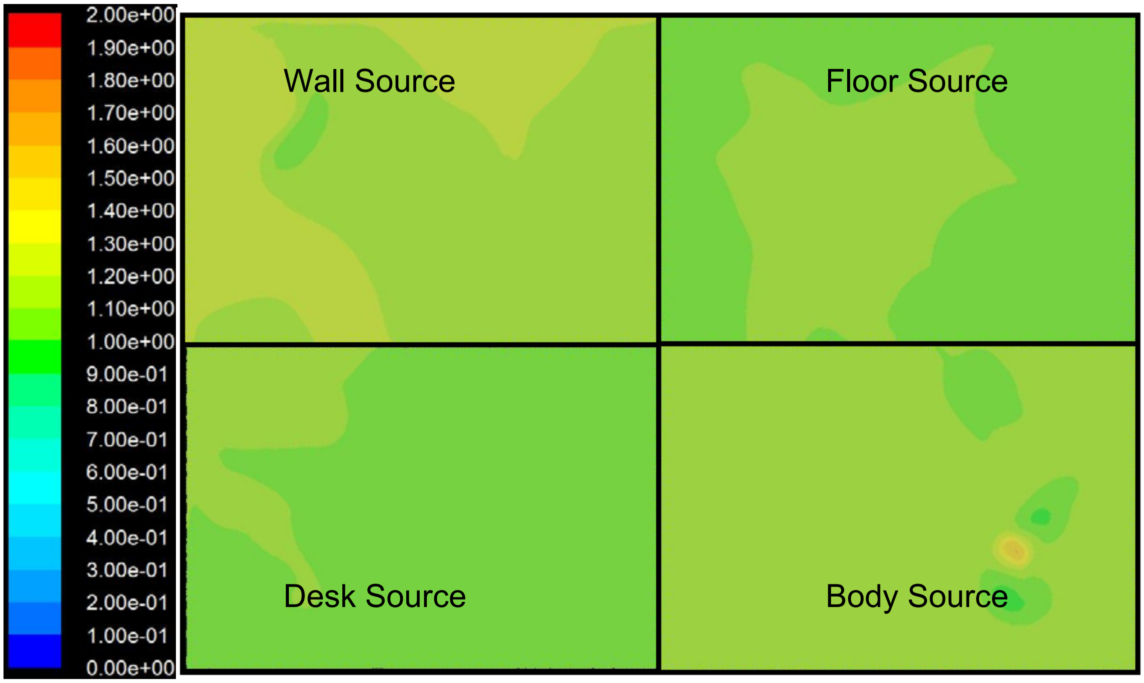

Figure 5.30: Normalized iF along a typical height for a standing person for a conventional ventilation system.

5.3.4 Section Conclusions

There is no disagreement that the use of PV will result in higher quality air in the BZ locations in the room while decreasing air quality in other locations of the room. This work found that PV improves air quality for a person seated in front of the system without drastically changing the air quality for others that may periodically occupy the space. Away from the ventilation systems it was found that well mixed values are achieved at standing heights for all systems and all species. For sitting heights, air quality was affected by the ventilation system, however the PV system did not deliver air that was worse than well mixed conditions or if it was worse than well mixed it was not notably worse than the case without PV for the locations tested. It was also found that certain locations in the room may result in poor quality of air with the use of PV, as shown in Figure 5.24; however, these locations are rarely occupied and should not be of concern. Alternatively, the goal of a ventilation system should be to deliver the freshest air to where it is needed instead of over diluting regions where no inhalation is present (as does the Co-flow PV system). With this information it is determined that the use of PV will improve the conditions of a typical office space for locations that are highly occupied without compromising the quality of the quality of the air beyond well mixed air for individuals who may come into the space periodically.

5.4 Cross Contamination from PV

Air quality in the BZ of a person depends strongly on both the ventilation system and the strength and location of sources. In a mixing ventilated system the goal is for everyone in a space to receive the same well mixed air and in a displacement ventilation system, the goal is to use the thermal plume to transport the fresh, cooler air distributed along the floor to the BZ. With PV the goal is to deliver the freshest air directly to a person's BZ. However, a concern with PV in occupied spaces with more than one occupant is that the momentum of the fresh air jet will cause cross contamination between the occupants by transporting contaminants emitted by an occupant to another. To investigate this, a CFD case was modeled with two occupants in a space with one using a PV jet and the other using a conventional system. Contaminant exposure, iF, was assessed for both occupants.

5.4.1 Domain and Setup

The validated CFD model from Section 4 was used to compare cross contamination for a scenario with PV and a scenario without. A new grid was developed to test this concept with two workstations at each corner of the space and two thermal CSPs with displacement ventilation and optional PV system in each cubicle. There were two floor diffusers and two ceiling exhausts in the entire space. Symmetry was applied through the center of each CSP bisecting plane, modeling only one half of each cubicle. The domain bounded by the front wall and two dashed lines is shown in Figure 5.29. The grid shown in Figure's 3.9-3.11 were expanded to include one half's of two cubicles with symmetry along two sides to represent two cubicles as shown in Figures 5.31. The total number of cells for this grid was a combination of 5.2 million structured and unstructured cells. The same solver parameters that were used in section 3.1 were used here. The Navier-Stokes equations were solved using Fluent. The Realizable k-ε turbulence model was used along with the enhanced wall treatment option. Second-order accurate upwind schemes were employed to solve the momentum and energy equations, and a second-order accurate scheme was used for the pressure interpolation. The BCs that were employed here were similar to section 3.1.

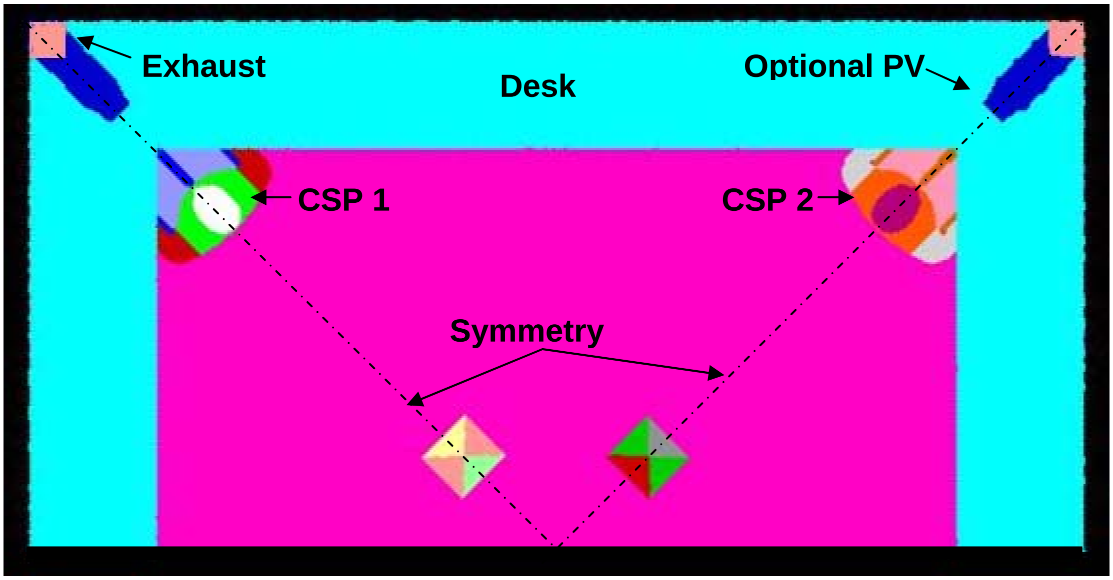

Figure 5.31: Domain for cross contamination.

For the three cases compared (No PV, Primary and Co-flow), the two PV systems in the simulated cubicles were not used simultaneously. That is, for the No PV case neither CSP had PV ventilation (Case 1). For the Primary setup, only CSP 1 had ventilation through the PV nozzle (Case 2) and similar for the Co-flow case (Case 3). iF was calculated for the two CSP's. iF was calculated for five different contaminant sources. The first source is a body source (modeled as 2 separate sources; one for CSP 1 and one for CSP 2) that could represent any emissions from the body such as odor, aldehydes, ketones, carboxylic acids and secondary organic aerosols. Third, a desk source was modeled that could represent emissions from building materials and desk cleaners. A floor source was also modeled to represent emissions from floor cleaners and carpets. Finally, a wall source was modeled to represent emissions from water based paint, oil based paint, particle board, gypsum board or other building materials.

5.4.2 Cross Contamination

First, the velocity fields in all three ventilation setups were compared to understand changes in the flow patters from the use of only one PV system. Figure 5.30 shows the velocity contours without any PV systems in use along the symmetry planes of each CSP and is considered the baseline flow patterns for the room. This contour is shown in perspective since the two symmetry planes are 90˚ from each other. Figure 5.32 shows air entering the cubicles through the two floor diffusers and spreading along the floor until the air reaches the CSP and is swept upward by the thermal plume. The thermal plume continues above each CSP until it reaches the ceiling and spreads outward. Figure 5.33 shows a similar pattern with the addition of air entering through the Primary PV system. In Case 2, the throw of the floor diffuser for CSP 1 is decreased compared to CSP 2 since less air is derived through the floor diffuser when used in conjunction with the PV system. The additional flow path for Case 2 starts at the Primary PV system and continues to CSP 1 where it interacts with the thermal plume and is diverted upward as it passes CSP 1. As the combined PV and CSP 1 thermal plume air extend toward the cubicle of CSP 2 it limits the spread of the thermal plume from CSP 2 across the ceiling. This is more noticeable for Case 3 when the Co-flow PV system is in use as shown in Figure 5.34. The throw of the floor diffuser for CSP 1 is significantly decreased with the use of the Co-flow nozzle because of the amount of air that is needed to operate the secondary jet of the system.

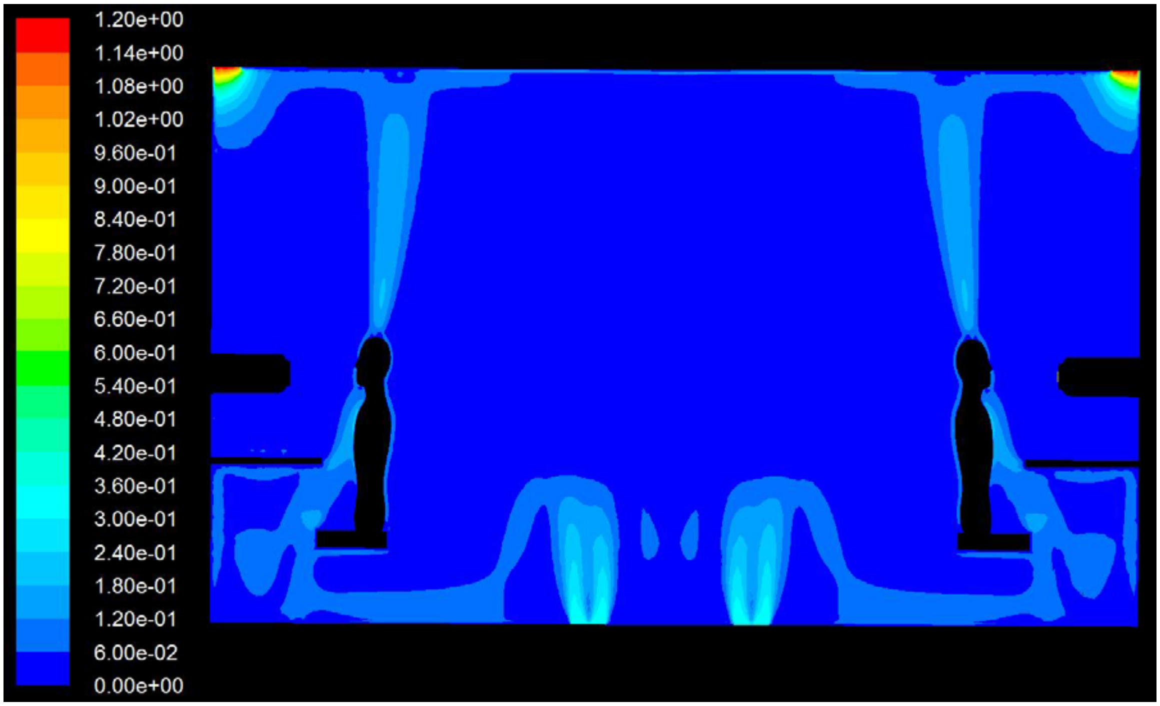

Figure 5.32: Velocity contours for Case 1.

iF was calculated for both CSP 1 and 2 and compared for Case 1, 2 and 3. Figure 5.33 shows the calculated iF for CSP 1 for Case 1, 2 and 3. The results show that the inhaled air quality is not well mixed for any of the ventilation cases modeled. For the case without PV, the iF is higher or lower than well mixed depending on the source location. For sources located near the CSP (body and desk sources), inhaled air quality is worse than well mixed and for sources away from the thermal CSP, the thermal plume acts as a protective barrier and the inhaled air quality is better than well mixed. The figure shows a decrease in *iF* for all sources for both PV systems with all iF's less than *1* with a greater decrease for the Co-flow case. The Co-flow PV system improves iF for a person seated directly in front of the nozzle up to ~4-5 times compared to a case without PV. It is clear that the Co-flow PV system is much more effective in removing pollutants from the occupants BZ than the single jet Primary case, but that both PV systems were able to decrease the *iF* and, therefore, increase the inhaled air quality compared to no PV.

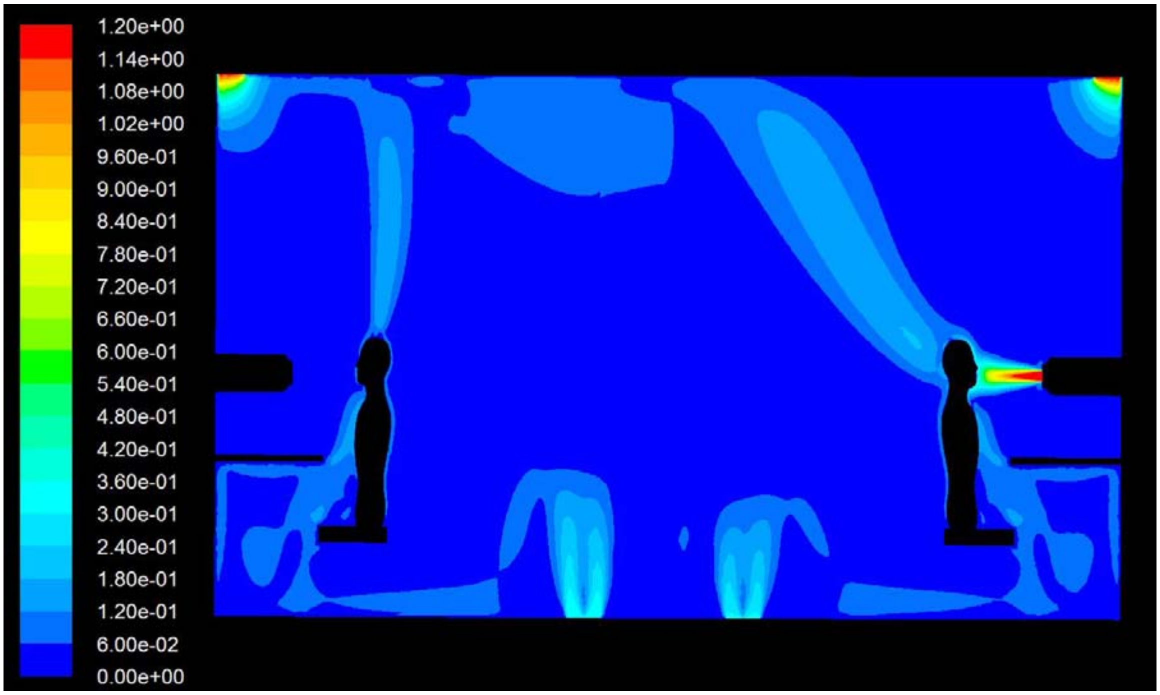

Figure 5.33: Velocity Contours for Case 2.

To determine cross contamination from the use of PV on an occupant that opted out of using a PV device, the iF was determined for CSP 2 for the same three ventilation setups (note: CSP 2 does not have air delivered to the BZ by any PV system in any case, the PV system shown only supplies CSP1). Figure 5.36 shows the calculated iF for CSP 2. Again, the results show that the inhaled air quality is not well mixed for the majority of the species. For all cases, the iF is higher or lower than well mixed depending on the source location. For sources located near CSP 2 (CSP 2 body source and desk source), inhaled air quality is worse than well mixed and for sources away from the thermal CSP (CSP 1 body source), the thermal plume acts as a protective barrier and the inhaled air quality is better than well mixed. The figure does not show a significant change in iF with the use of a PV system by a neighboring occupant or in a neighboring workstation.

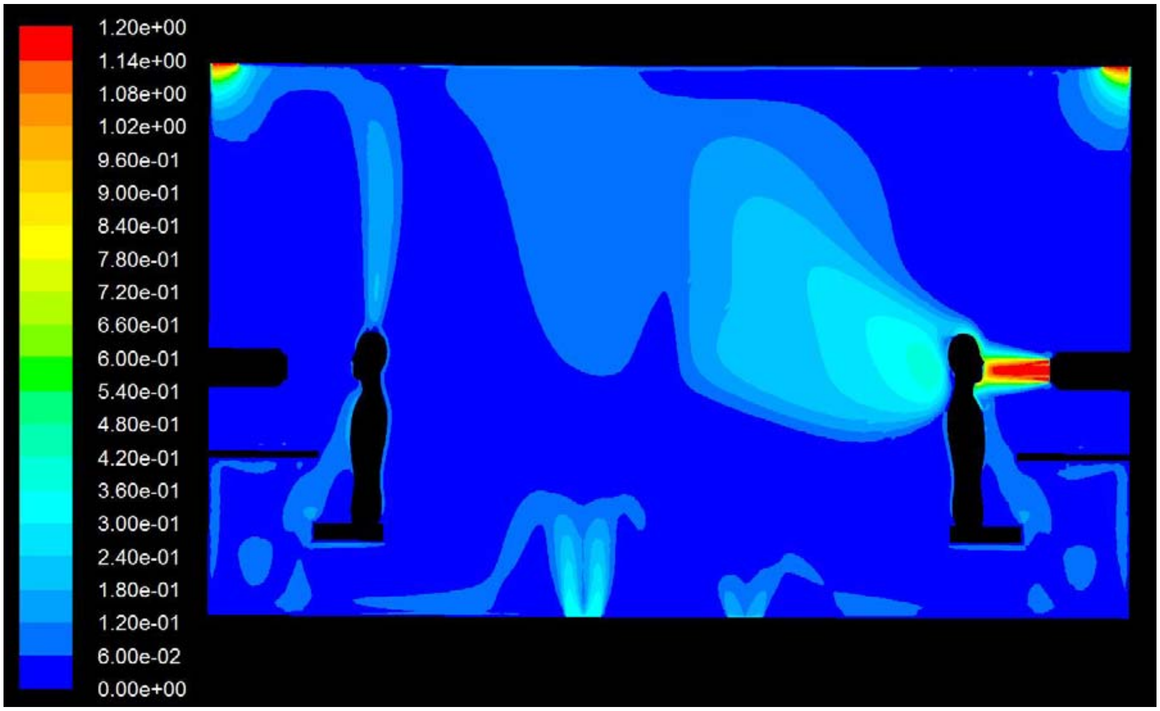

Figure 5.34: Velocity contours for Case 3.

To determine cross contamination from the use of PV on an occupant that opted out of using a PV device, the iF was determined for CSP 2 for the same three ventilation setups (note: CSP 2 does not have air delivered to the BZ by any PV system in any case, the PV system shown only supplies CSP1). Figure 5.36 shows the calculated iF for CSP 2. Again, the results show that the inhaled air quality is not well mixed for the majority of the species. For all cases, the iF is higher or lower than well mixed depending on the source location. For sources located near CSP 2 (CSP 2 body source and desk source), inhaled air quality is worse than well mixed and for sources away from the thermal CSP (CSP 1 body source), the thermal plume acts as a protective barrier and the inhaled air quality is better than well mixed. The figure does not show a significant change in iF with the use of a PV system by a neighboring occupant or in a neighboring workstation.

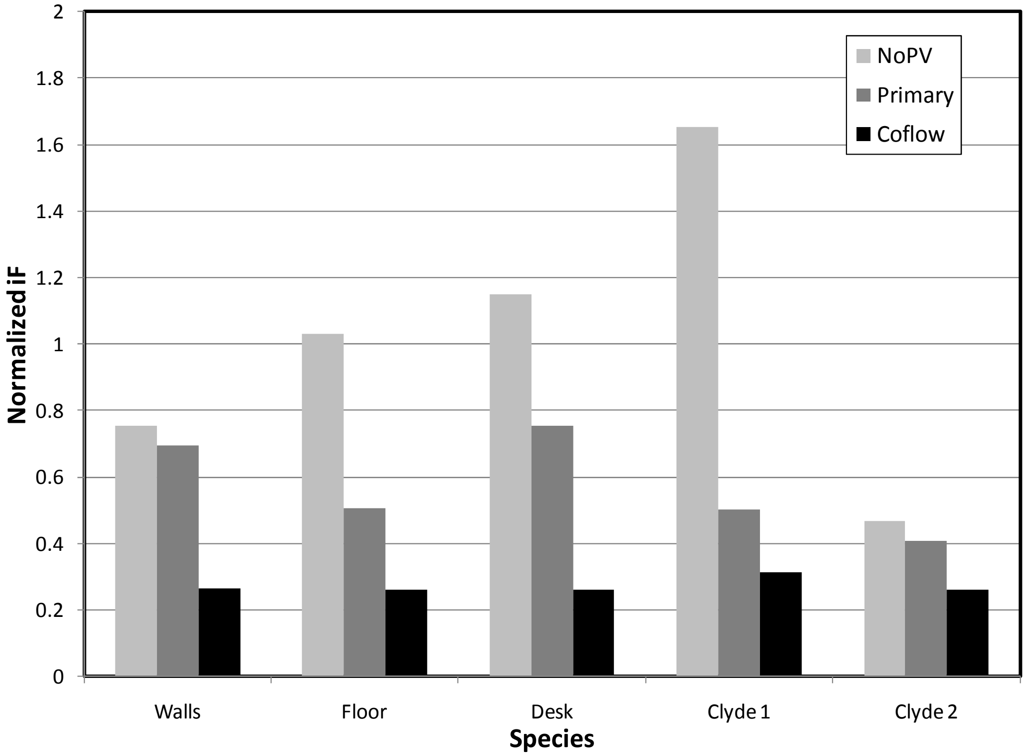

Figure 5.35: iF for CSP 1.

Cross contamination from CSP 1 to CSP 2 is low for the case without PV and results in the lowest iF for all sources studied. iF values for cross contamination without PV are only *~45 %* of well mixed values. With the use of the Primary PV system there was only a slight increase in iF for all sources and cross contamination from CSP 1 was increased to *50 %* of the well mixed value. While the Primary PV system increased cross contamination from CSP 1 to CSP 2 by *10 %,* it decreased cross contamination from CSP

2 to CSP 1 by *13 %*. Similar results were found for the Co-flow setup. With the use of the Co-flow PV system cross contamination from CSP 1 to CSP 2 was increased to *65 %* of the well mixed value and it decreased cross contamination from CSP 2 to CSP 1 by *~45 %*. Compared to the benefits of PV for sources that result in high iF (own body source), the increase in cross contamination is insignificant. The Primary PV system was able to decrease the iF of species Clyde 1 for CSP 1 *70 %* (from *~160 %* of the well mixed value to *~50 %*). Even more momentous results are shown for the Co-flow nozzle where a decrease of *~80 %* in iF was found (from *~160 %* of the well mixed value to *~30 %*). The personal benefits of a PV system outweigh the slight increase in already low iF for cross contamination. The use of PV to remove contaminants produced by the body is examined in detail in Section 7.2.

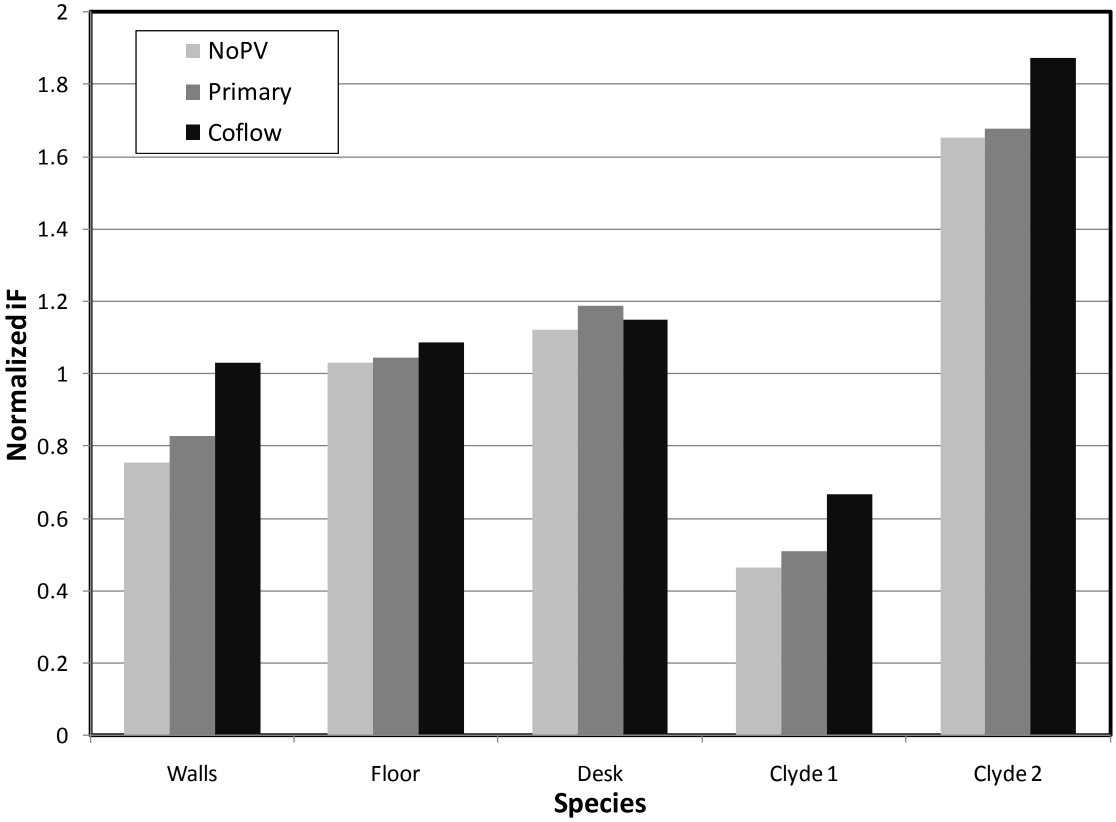

Figure 5.36: iF for CSP 2 (PV system is turned off).

5.4.3 Section Conclusions

With PV, the goal is to deliver the freshest air directly to a person's BZ, however the change in flow patters from the use of a PV system can lead to increased cross contamination between occupants. From this work, it was determined that the increase in cross contamination between occupants when only one is using a PV system was found to be small compared to the personal benefits a PV system can deliver.

5.5 *Alternate Ergonomic Placement of PV nozzles*

PV is intended to deliver fresh air to the BZ of a person to increase inhaled air quality. Fresh air is usually delivered to the BZ through nozzles placed in or in close proximity to a person's BZ, which leads to much higher air quality in the BZ. This method, however, may have limitations regarding implementation. The direct placement of a PV nozzle in the BZ would significantly improve the air quality in the BZ; however, this is an impractical setup. Moving the PV nozzle away from the BZ, but aiming the nozzle directly toward the BZ may be more sensible; however, it may also have its limitations. A study to determine practical and beneficial placements of PV systems in the indoor environment would be valuable to this line of work. CFD-based tools can be utilized to optimize the design of PV systems and their placement within the work space more efficiently and cost effectively than detailed experimental investigations.

Different configurations of PV systems were compared for this work. A baseline case consisted of a Co-flow nozzle aimed directly toward the BZ and this was compared to two impinging Co-flow nozzles on either side of a CSP (Side PV) and two impinging nozzles angled *45°* from the CSP's symmetry plane, meeting in the CSPs BZ (Corner PV). The same comparisons will also be made for a single jet PV system.

5.5.1 Domain and Setup

The domains used for all three configurations represents a chamber measuring *2.0 m* by *2.6 m* by *2.5 m*, in which there is a CSP, a Co-flow nozzle/nozzles, a floor diffuser and a ceiling exhaust vent. A symmetry BC was applied through the center of the CSP and floor diffuser; therefore, only half of the room was modeled in the CFD analysis. Three PV configurations are compared: 1) PV nozzle aimed directly toward the BZ (Baseline), 2) two impinging PV nozzles on either side of a CSP (Side) and 3) two PV nozzles angled 45° from the CSP's symmetry plane, meeting in the CSPs BZ (Corner) as shown in Figure 5.37.

The domain in Figure 5.37a represents the baseline domain which has been validated (Refer to Section 4 for more details on the validation cases). The domain in 5.37b has been modified to represent a more realistic configuration with two PV jets on either side of the CSP. The domain in Figure 5.37c is even more realistic with the CSP seated in the corner of the office space with a desk and two PV systems angled at *45°* from the CSP symmetry plan.

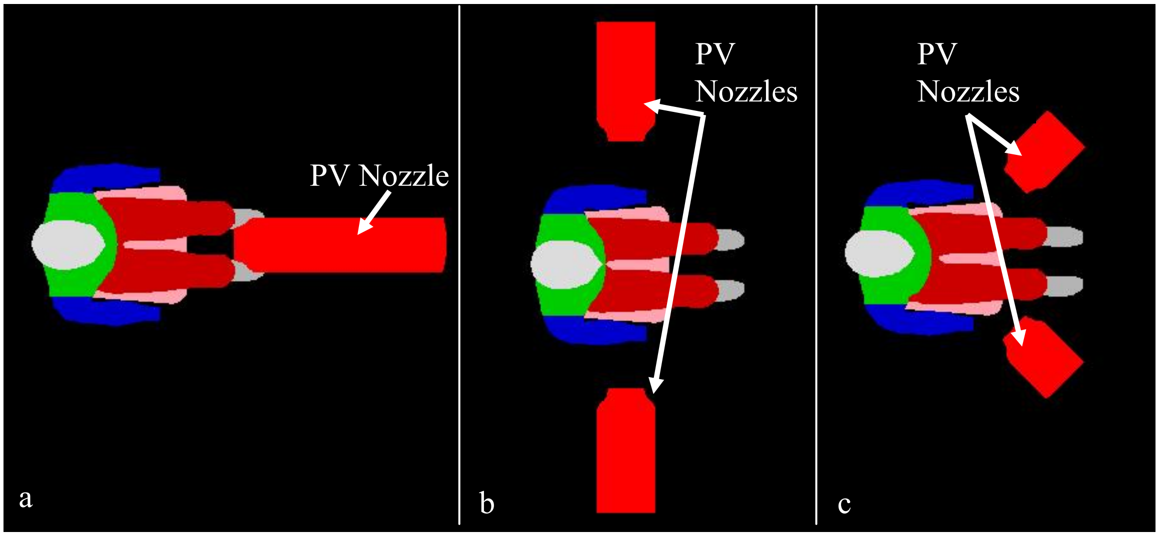

Figure 5.37: PV configurations used for this work, a) baseline configuration with PV nozzle aimed directly towards the BZ, b) side PV configuration with two impinging nozzles aimed toward the BZ, and c) corner PV configuration with two PV nozzles angles at 45˚ from the CSP's centerline aimed toward the BZ.

The grid development used for this work follows the same methods described in Section 3. All three domains have the same surface CSP grid (*20,000* elements) and total volume cell count (*4.2* million cells). Computational modeling follows the same parameters outlined in Section 3.2.

For species transport, a pollutant concentration was supplied through the floor diffuser and the secondary nozzle, while the primary air was kept free of the pollutant. For the cases used to compare PV configurations, the Co-flow PV system is assumed to deliver fresh air (zero pollutant) through the primary nozzle and recirculated and fresh air through the secondary nozzle. In this case there is a point source at the floor diffuser. For the Primary PV system, fresh air (zero pollutant) was also delivered through the primary nozzle and the secondary nozzle delivered no air. The point source at the floor diffuser was the main source of pollutant in this setup. The exhaust concentration was kept the same for all cases. Results of the pollutant concentration were normalized to give a profile of an AQI. AQI profiles located 10mm from the CSP's nose on the symmetry plane were generated and compared.

BCs employed for the three configurations and two PV nozzles are shown in Table 5.3. Other BC's are consistent with those used in the validation case (Section 4). To maintain the same air supply to the chamber in both the Co-Flow and Primary cases, a higher flow was set at the floor diffuser in the Primary case to compensate for turning-off the secondary jet.

Table 5.3: PV BCs for the three PV configurations (Baseline, Side and Corner) and for the two PV systems ('C' for the Co-flow nozzle and 'P' for the Primary nozzle).

Test Series	Baseline C	Baseline P	Side C	Side P	Corner C	Corner P
Number of PV nozzles	1	1	2	2	2	2
Primary Nozzle Air Flow, l/s	4.8	4.8	2.4	2.4	2.4	2.4
Secondary Nozzle Air Flow, l/s	15.2	0	7.6	0	7.6	0
Total PV Air Flow, l/s	20	4.8	20	4.8	20	4.8
Floor Diffuser Air Flow, l/s	0.7	15.9	0.7	15.9	0.7	15.9
Total Chamber Air Flow, l/s	20.7	20.7	20.7	20.7	20.7	20.7

5.5.2 Comparison of Personal Ventilation Configurations: 4.8 l/s

Figure 5.38 shows comparison of AQI contours at a plane through the CSP's mouth for the Co-flow and Primary baseline cases. The figure clearly shows that the Co-flow PV system is much more effective in delivering clean air to the occupant than the single jet

Primary case, as indicated by the much larger region of high values of AQI in the BZ. This is due to the Co-flow nozzles ability to extend the length of the potential core of the Primary jet by reducing mixing of the Primary jet with its surroundings by surrounding the Primary jet with an annular jet. Although this jet configuration is able to deliver very high quality of air (AQI~1) to the BZ, it is being done at a fresh air flow rate of *4.8 l/s* which results in velocities at the face that could be uncomfortable to a person. The velocity *2 cm* from the face for the Co-flow nozzle is ~*1.8 m/s* and for the Primary nozzle is ~*1.4 m/s*. Draught comfort is dependent on the velocity and turbulence of the jet as well as the temperature of the jet air. Cooler jets result in higher discomfort. It is thought that speeds of less than *1 m/s* are acceptable and considered comfortable since that is a typical walking pace of a person. The velocities of the primary and secondary jet may lead to an uncomfortable BZ velocity, which may lead to eye irritation when at or above *1 m/s* (Wyon & Arens, 1987). Wolkoff et al. (2005) showed that at high air velocities (>1m/s) increases the water evaporation from the eyes.

Figure 5.39 shows comparison of AQI contours at a plane through the CSP's mouth for the Side PV cases. This figure shows that neither system is as efficient at delivering fresh air to the BZ as the Baseline cases. Impinging jets create a radial jet which distributes fresh air over *360*° in a plane perpendicular to the centerline of the nozzles. The BZ air quality of the CSP is only affected by a small arc of the radial jet, resulting in a small fraction of the PV fresh air being delivered to the BZ. It has been shown that the impingement region (portion of the free jet affected by impingement) of a jet is ~*25 %* of the distance between the point of impingement and the nozzle (Awbi, 2003) and that when a jet approaches the point of impingement the centerline velocity will decrease to zero rapidly. With jets in close proximity to each other, the length of the potential core can be reduced by this effect resulting in lower BZ air quality. These two characteristics of impinging jets reduce the benefit of this ergonomic configuration; however, the figure shows that the Co-flow PV system is more effective in delivering clean air to the occupant than the single jet Primary case in this configuration.

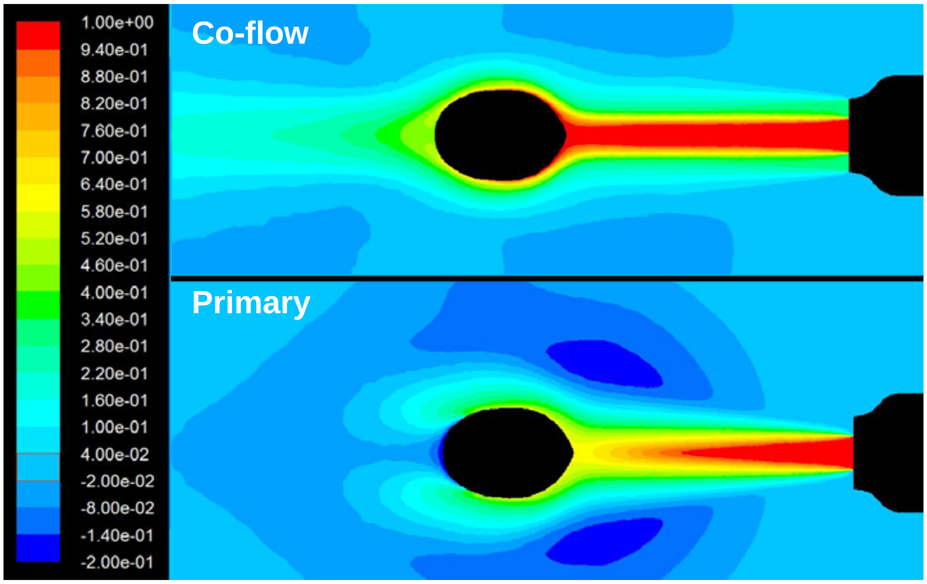

Figure 5.38: AQI contours for the Baseline configuration for the Co-flow and Primary PV systems.

Figure 5.40 shows comparison of AQI contours at a plane through the CSP's mouth for the Corner PV cases. Results of the Corner PV configuration show a similar trend as the Side PV configuration while achieving better results for both the Co-flow and Primary PV systems. The figure also shows that the Co-flow PV system is more effective in delivering clean air to the occupant than the single jet Primary case in this configuration. It is also clear that this configuration is able to deliver a higher level of air quality to the

BZ than the Side PV configurations over a larger region than the Baseline PV configuration. This benefit can be attributed to the mixing of the fresh air of the interacting jets to increase the region to which fresh air is delivered, while maintaining its directionality toward the BZ with its angular placement.

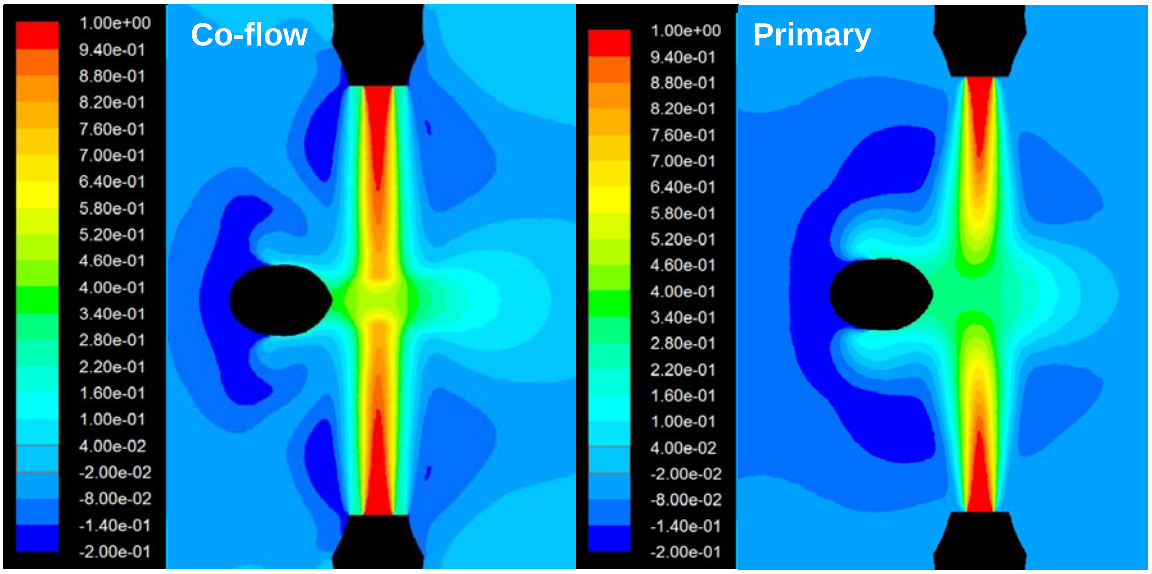

Figure 5.39: AQI contours for the Side configuration for the Co-flow and Primary PV systems.

Figure 5.41 shows AQI profile comparison of the Side PV and Corner PV system with the Baseline case for the Primary and Co-flow PV nozzles along a vertical line *1 cm* from the CSP's nose. This figure shows that the neither of the two realistic configurations can achieve the peak AQI value in the BZ that the Baseline configuration was able to reach. However, the area of improved air quality is much larger for the Side PV and Corner PV configurations than for the Baseline configuration. The results also show better performance of the Corner PV configuration than Side PV configuration for the reasons discussed previously. The AQI in the BZ for the corner PV system can be improved further by moving the PV system closer to the CSP (results shown in Appendix D).

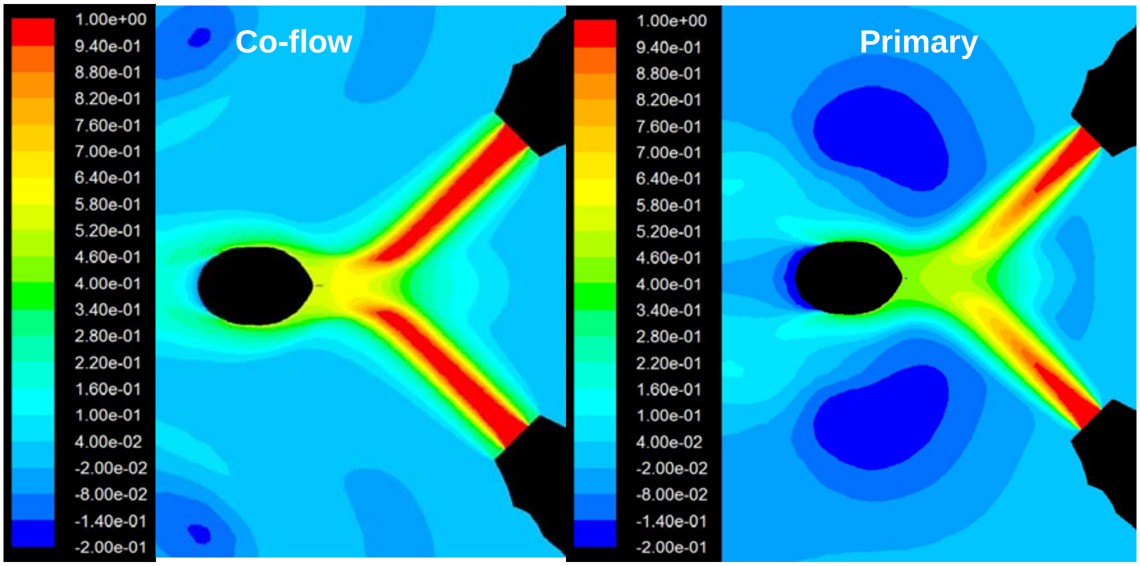

Figure 5.40: AQI Contours for the Corner configuration for the Co-flow and Primary PV systems.

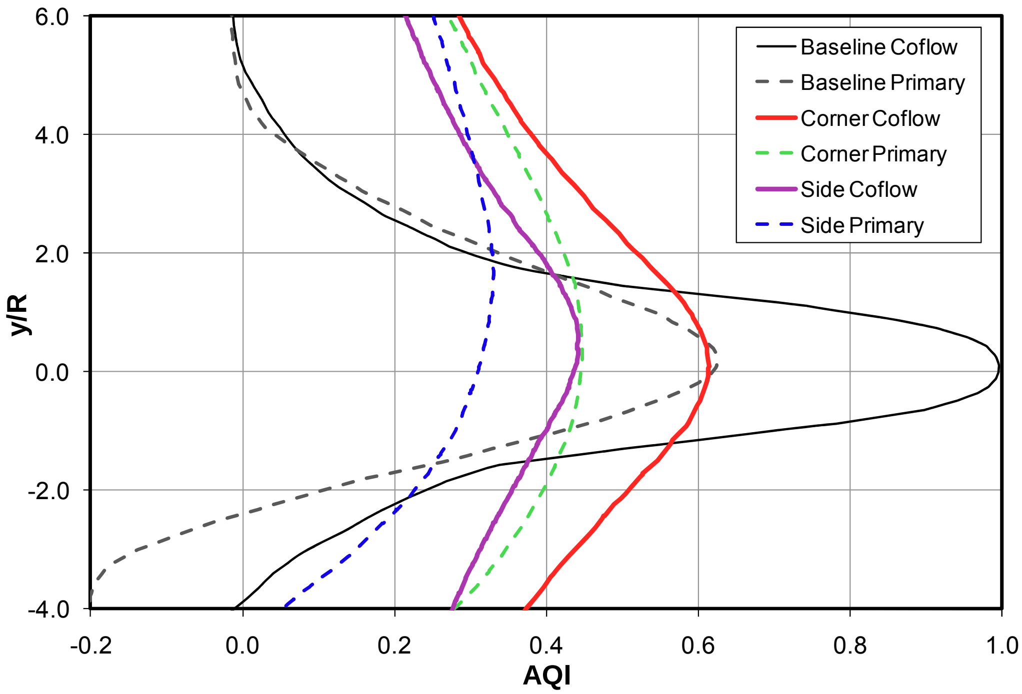

Figure 5.41: Comparison of the PV configurations with the Baseline configuration.

The use of PV is sensitive to its location relative to a person's BZ. The results so far have shown that the corner PV system is a very useful PV configuration that is shown to deliver better air quality to the BZ than the Primary PV system, while enlarging the area to which it is delivered compared to the Baseline Co-flow PV system. The benefits of the corner PV system can be further improved by moving closer to the PV system. A comparison was made when the CSP was moved into the impingement region of the two angled jets. Figure 5.42 shows the Normalized AQI contours for the two different locations. Figure 5.42a clearly shows better air quality in the BZ when the CSP is moved closer to the PV system than Figure 5.42b. Figure 5.43 shows this quantitatively. It is understood that a person will move relative to the PV system throughout the day, but it is important to optimize the location of PV systems to deliver fresh air to the region that is most often occupied.

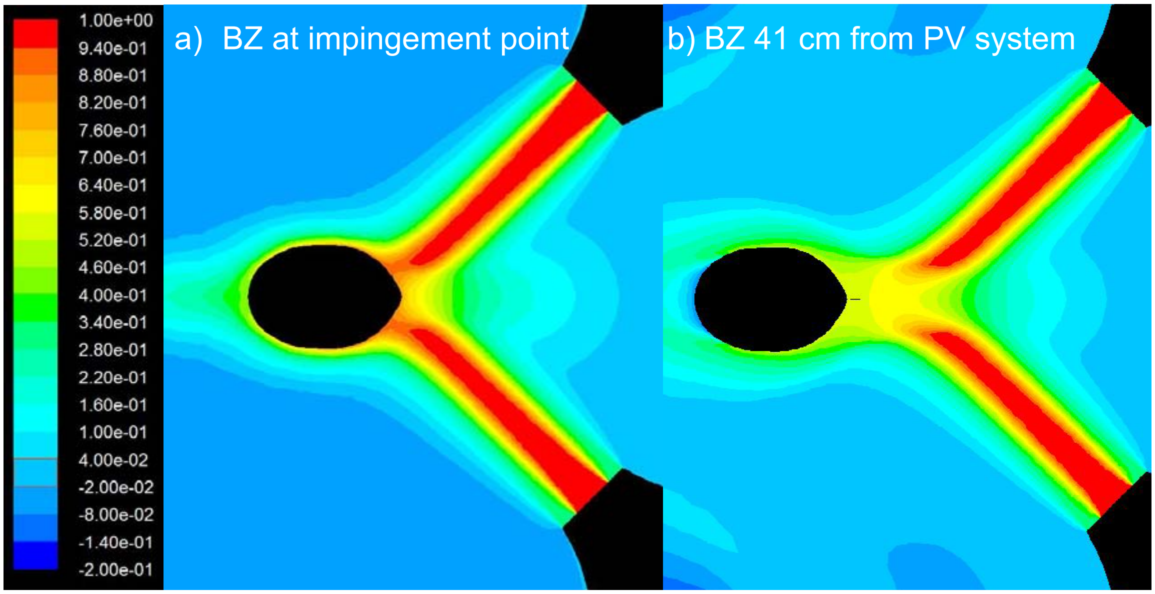

Figure 5.42: AQI contours for the corner PV with the CSP at two different locations relative to the PV system.

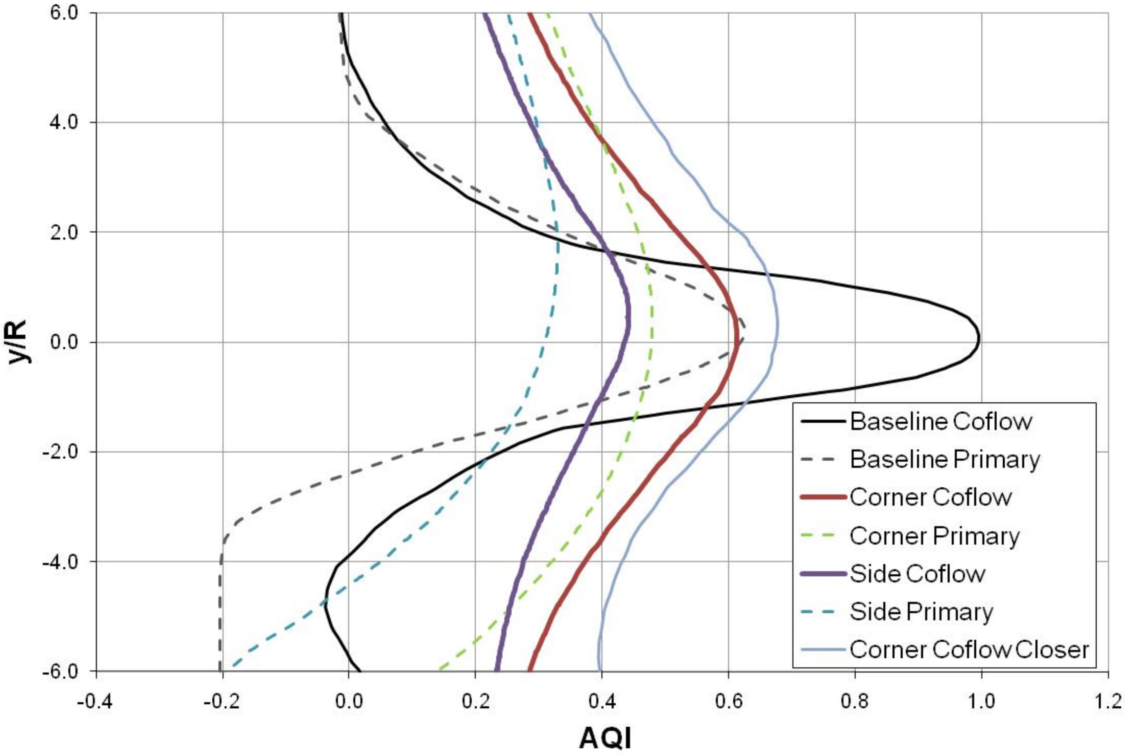

Figure 5.43: AQI profiles 1cm from the CSP nose.

5.5.3 Section Conclusions

These results show the usefulness of CFD when testing multiple PV configurations in the indoor environment. These results also reaffirm the advantages of a Co-flow nozzle when compared to a conventional single nozzle in realistic configurations. The use of the Corner Co-flow PV configurations is a practical PV configuration that is shown to deliver better air quality to the BZ than the Primary PV system, while enlarging the area to which it is delivered compared to the Baseline Co-flow PV system.

5.6 *Chapter Conclusions*

PV can be implemented in an ergonomic fashion while improving air quality delivered to an occupant of a typical office space while supplying satisfactory quality air to the rest of the space. This chapter shows that PV improves the air quality for a person seated in front of the PV system without considerably reducing the air quality for other occupants that may periodically enter the space. It is agreed that certain locations in the room may result in poor quality of air with the use of PV; however, this work has shown that these locations are rarely occupied and may not be of concern. Additionally, it was found that cross contamination between an occupant with and an occupant without PV is minimal compared to the benefits one could receive from using PV. This chapter also showed that PV is beneficial even when implemented in realistic and practical setups. The use of the Corner Co-flow PV configurations is a sensible PV configuration for a typical office cubicle that is able to deliver better air quality to the BZ than the Primary or no PV system, while enlarging the area to which it is delivered compared to the Baseline Co-flow PV system. These findings combat common misconceptions of the feasibility and implementation of PV across the field.

6 Develop and validate a CFD model for reacting flows

Chemical reactions can have a significant effect on indoor concentration levels by decreasing or increasing pollutant levels and producing products that would not be present otherwise. The formation of oxidation products have been shown to be more harmful to one's health than the reactants themselves (Weschler, 2000), making the understanding of chemical reactions and pollutant transport a major concern in the indoor environment.

Experimentally modeling detailed chemical reactions in the indoor environment is complex and expensive, which gives rise to the importance of a validated computational model to predict these reactions. Computational modeling is not without limitations and some chemical participants cannot be detected or quantified using commonly available analytical techniques (Weschler and Shields, 1997). One compartment mass-balance models have been constructed to include chemical reactions (Nazaroff and Cass, 1986; Weschler & Shields, 2000); however these models only predict overall room scales. They perform very well for well-mixed conditions, but lose accuracy for scales smaller than the room (Sorenson & Weschler, 2002). For this work, a CFD model that has been validated for flow field predictions will be improved to predict the concentrations of Ozone, Terpenes and their oxidation products.

6.1 *Ozone/D-limonene Reaction*

The validated CFD model was enhanced to be able to handle volumetric and surface reactions between Ozone and VOC's. When considering the oxidation of Terpenes (considered to be a VOC), Ozone removal through these reactions occurs on a timescale that can compete with typical indoor air exchange rates and surface adsorption. In the indoor environment, D-limonene is the most frequently detected Terpene (De Bortoli et al., 1986; Montgomery and Kalman, 1989; Wallace et al., 1991). Indoor levels were found to be, on average, *5-15 ppb* and over *80 ppb* when products containing D-limonene were used (Seifert et al., 1989; Fellin and Otson, 1994). These concentrations have been shown to be increasing over the past several years. In 2000, Wainman et al. reported that levels as high as *175 ppb* were measured after applying spray wax table cleaner. In 2006, Singer et al. found average levels to be close to *200 ppb* after using a pine-oil based cleaner. In 2007, Zuraimi et al. reported levels exceeding *50* and *220 ppb* in Singaporean offices. It has been reported that the volumetric reaction of O_3 with D-limonene results in an indoor half-life of Ozone of *60-500 minutes* (Kephalopoulos et al, 2007), which is on the same order as the half-life reported by Weschler (2000) of *21-210 minutes* for typical indoor air exchange rates.

With increased exposure to the oxidation of cleaning products and because these reactions occur fast enough to compete with normal air exchange rates it is important to understand the effect of these reactions on indoor air quality and health. Weschler (2004) has shown that being exposed to the products of Ozone reacting with D-Limonene for *20 minutes* at realistic indoor concentrations increases the rate of blinking in human subjects (blinking is an indication of eye irritation). A significant increase in blink frequency due to exposure to Ozone/D-Limonene reaction was also shown by Kleno and Wolkoff (2004). Tamas et al. (2006) showed that more than *50 %* of people were dissatisfied with the perceived air quality in offices when Ozone and D-Limonene were present together compared to *10 %* when neither were present in the room or where only one of the reactants was present. It has also been shown that Terpene oxidation products are more irritating to the upper airways of mice than the Terpenes or Ozone alone (Rohr et al. 2002; Wolkoff et al. 1999), and the oxidation of D-limonene has also been shown to produce contact allergens (Karlberg et al., 1994).

Several authors studied chemical reactions in the indoor environment both experimentally and numerically without the presence of a person (Nicolas et al. (2007), Weschler et al. (2007), Lai et al. (2004), Sarwar et al. (2003), Ito et al. (2003), Ito et al. (2004) Weschler & Shields (2000)), however, modeling the oxidation of D-limonene using CFD in the indoor environment with the presence of a thermal manikin has not been investigated.

6.1.1 Validation

Before room simulations are carried out, the use of wall adsorption and volumetric reactions in Fluent was validated by comparison with experimental data by Ito (2007b). Ito studied the Ozone and Terpene distributions in a stainless steel chamber with a turbulent flow field to investigate Ozone distributions alone, D-limonene distributions alone, and reaction of Ozone and D-limonene. Ito also conducted CFD investigations for the aforementioned three experimental test cases and confirmed that CFD and experimental results were in reasonable agreement.

6.1.2 Domain and Setup

A 2D domain *1.5 m* x *1.0 m* with one inlet and one outlet similar to that modeled by Ito, was created for validation and three validation cases were conducted for the Ozone/D-limonene reaction. For all cases Fluent was used with second-order accurate upwind schemes to solve the momentum and energy equations, and a second-order accurate scheme for the pressure interpolation. The Realizable k-ε turbulence model was used along with the enhanced wall treatment option. The species transport equation was included to compute the concentration of each pollutant. The inflow velocity for the three cases was *3.0 m/s*. First, Case A was computed with the wall adsorption for Ozone only. In this case Ozone entered the room through the ventilation system at *0.3 ppm*. The mass accommodation coefficient for stainless steel was taken as $\gamma=3.4x10^{-6}$ (Ito, 2007b). The mass accommodation coefficient (or reaction probability) is defined as the fraction of pollutant molecular collisions with a surface that result in irreversible removal. Case B simulates the wall adsorption of D-limonene only. D-limonene was released from the floor along a line source at a rate of *15 μg/s*. The location of the source is shown in Figure 6.1. The mass accommodation coefficient for D-limonene on stainless steel is $\gamma=2.1x10^{-5}$ (Ito, 2007b). Case C, includes wall adsorption of Ozone and D-limonene and a volumetric reaction occurring between the two species. The mass accommodation coefficients for wall adsorption are those previously mentioned. The volumetric reaction rate was taken as $k=0.0184\ ppb^{-1}\ h^{-1}$ (Atkinson et al., 1990). Horizontal and vertical centerline profiles for concentration distribution were compared to experimental measurements. A summary of the cases modeled for validation is given in Table 6.1.

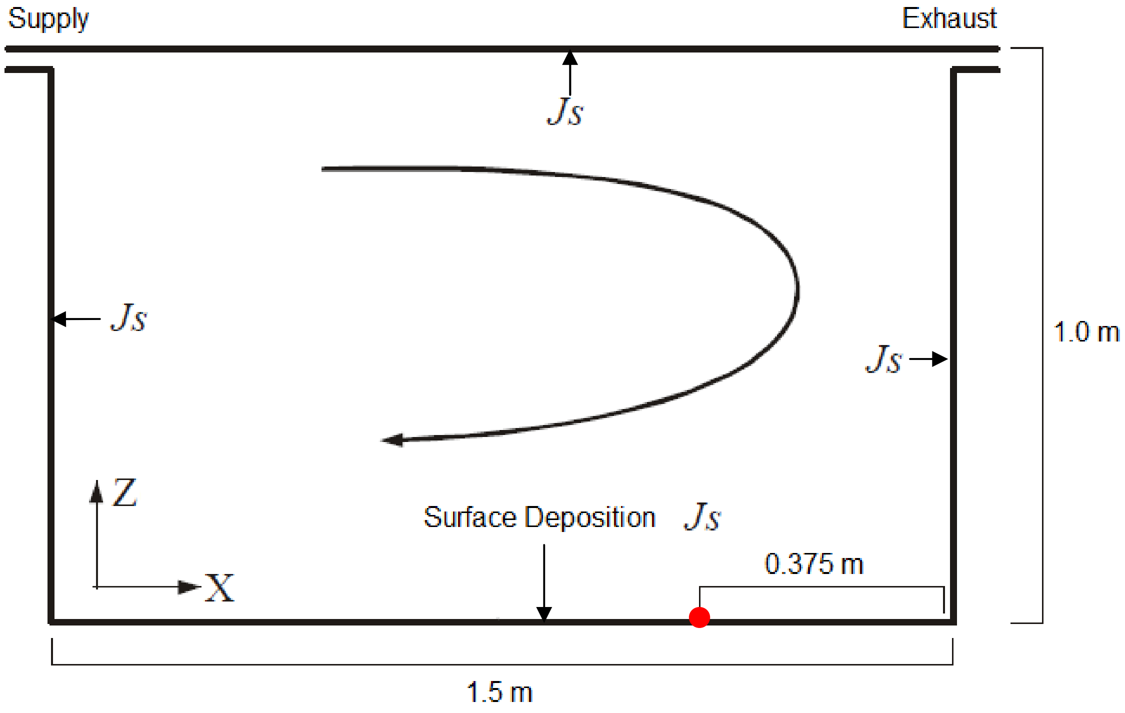

Figure 6.1: Setup of 2D domain for validation. The red circle indicates the location where D-Limonene was released.

Table 6.1: Summary of chemical BCs used for validation cases.

	Case A	Case B	Case C
Inflow	$C_{ozone} = 300$ ppb	-	$C_{ozone} = 300$ ppb $C_{d\text{-limonene}} = 0$ ppb
Line Source	-	$S_{d\text{-limonene}} = 15$ μg/s	$S_{d\text{-limonene}} = 15$ μg/s
Reaction Probability at Surfaces	$\gamma_{ozone} = 3.4\text{x}10^{-6}$	$\gamma_{d\text{-limonene}} = 2.1\text{x}10^{-5}$	$\gamma_{ozone} = 3.4\text{x}10^{-6}$ $\gamma_{d\text{-limonene}} = 2.1\text{x}10^{-5}$
Volumetric Reaction	-	-	$k = 0.0184$ ppb^{-1} h^{-1}

The adsorption of Ozone and D-Limonene by interior surfaces (walls, ceiling and desk) was modeled as a surface flux based on the grid size given by Cano-Ruiz et al. (1993) written as:

$$J_s = \frac{-\gamma\langle v\rangle/4}{1+\left(\gamma < v > /4/D_m\right)\Delta y_1} C\left(\Delta y_1\right) \tag{6.1}$$

where D_m is the binary diffusion coefficient, Δy_1 is the grid height at the wall, $<v>$ is the Boltzmann velocity, $C(\Delta y_1)$ is the concentration at the first cell height, and γ is the mass accommodation coefficient.

6.1.2.1 Experimental Comparison

Figure 6.2 shows the Ozone and D-limonene distribution with wall adsorption only, respectively. Modeling the wall adsorption shows a non-uniform concentration distribution within the 2D domain for both Ozone and D-limonene. Ozone concentrations varied from *227 ppb* to *300 ppb* and D-limonene concentrations varied from *0* to *500 ppb*.

Figures 6.3 and 6.4 show the predicted Ozone and D-limonene concentration profiles compared to the experimental results by Ito (2007b) along the horizontal and vertical centerline, respectively. For the Ozone comparison the maximum difference is *2 %* between the experimental results and CFD results. For the D-limonene comparison the maximum difference is *30 %* between the experimental results and CFD results and an average difference of about *~7 %*. Near the walls, the CFD model tended to under predict the species concentration, therefore over predicting wall adsorption. However, in the center of the room reasonable agreement was achieved for most data points. The occurance of heterogenous reactions between Ozone and adsorbed D-Limonene (Tirkkonene and Saarela, 1997) is possible and could increase the sink effect of the material surfaces and the probability of oxidative reactions.

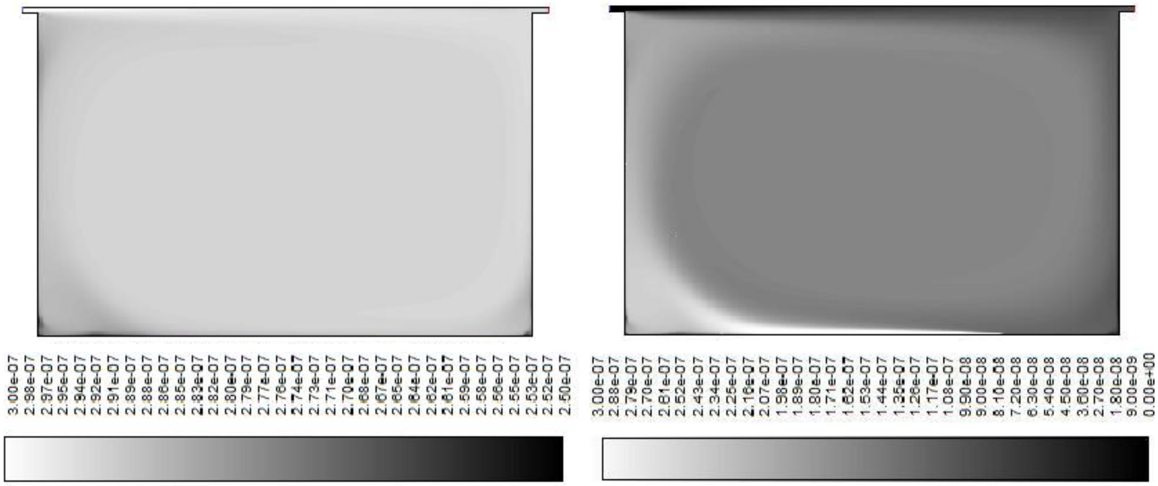

Figure 6.2: Left: Ozone distribution in 2D case with wall adsorption only. Right: D-limonene distribution in 2D case with wall adsorption only.

Figures 6.5 shows the Ozone and D-limonene distribution within the domain with wall adsorption and volumetric reactions. This figures show high non-uniformity for both Ozone and D-limonene when wall adsorption and volumetric reactions are modeled. Ozone concentrations vary from *224* to *300 ppb*. D-limonene concentrations vary from *0* to *500 ppb*.

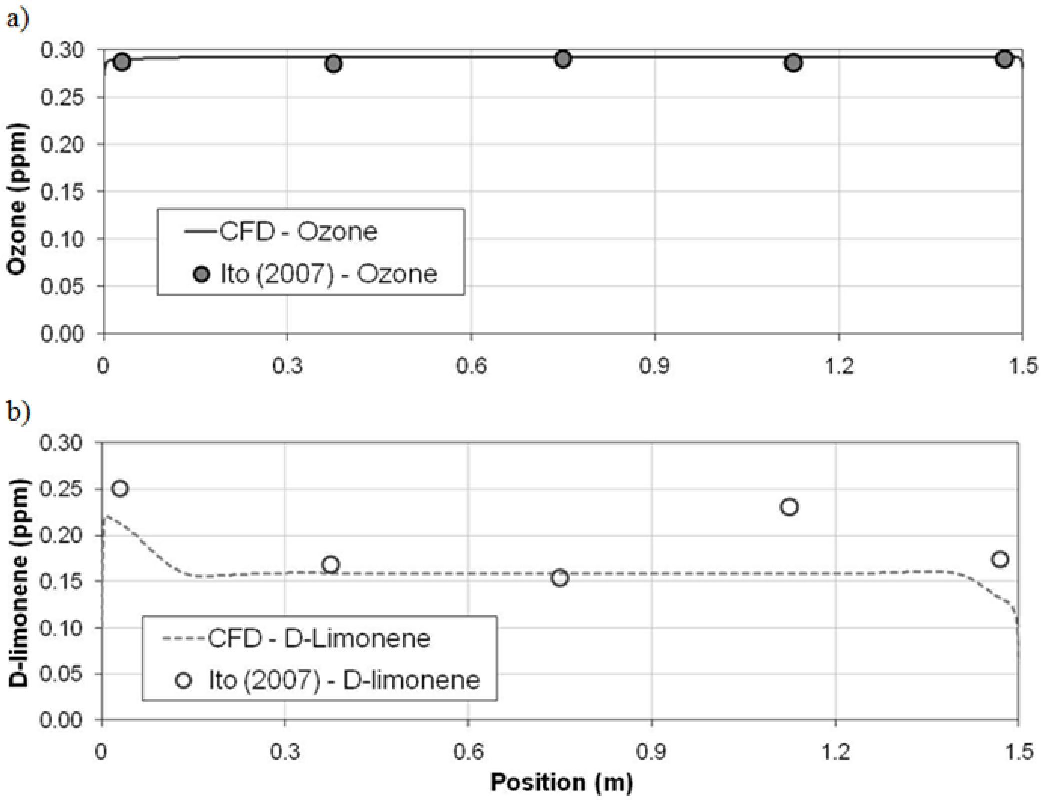

Figure 6.3: a) Comparison of Ozone levels along the horizontal centerline with adsorption only. b) Comparison of D-limonene levels along the horizontal centerline with adsorption only.

Figures 6.6 and 6.7 show the computational Ozone and D-limonene concentration profiles compared to the experimental results obtained by Ito (2007b) along the horizontal and vertical centerline, respectively. Near the walls, in Figures 6.6 the maximum difference is *~40 %* between the experimental results and CFD results with an average difference of about *~10 %.* Throughout the domain the CFD results achieved reasonable agreement with the experimental results and tended to slightly over predict the concentration values, therefore slightly under predicting volumetric reactions.

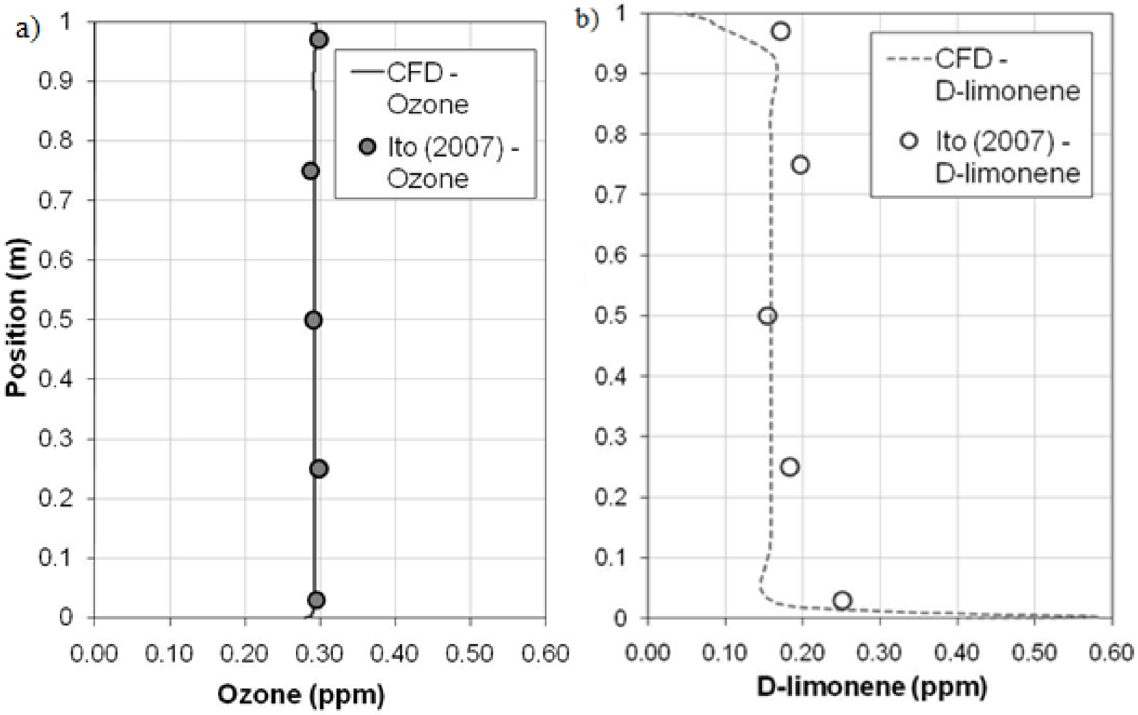

Figure 6.4: a) Comparison of Ozone levels along the vertical centerline with wall adsorption only. b) Comparison of D-limonene levels along the vertical centerline wall adsorption.

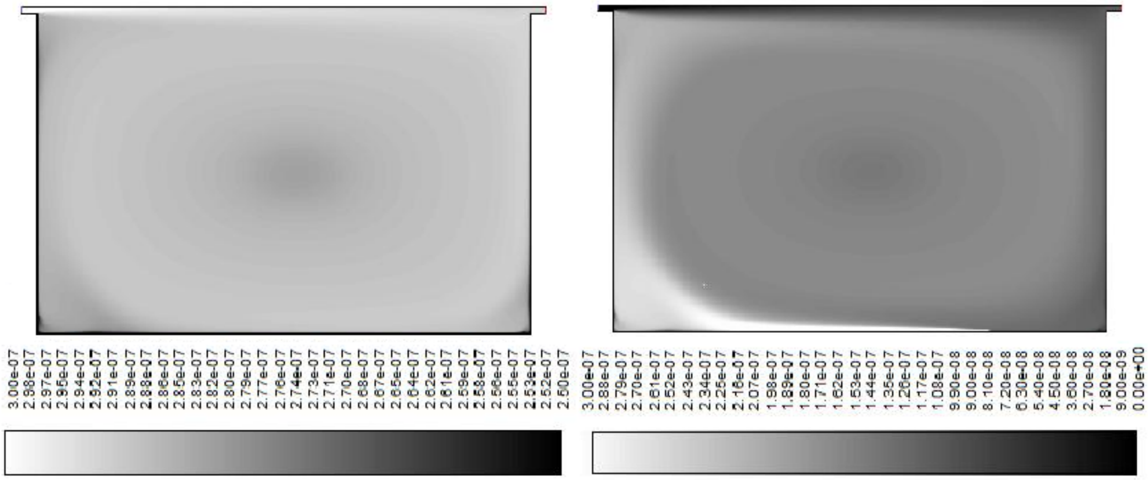

Figure 6.5: Left: Ozone distribution in a 2D case with wall adsorption and volumetric reaction with D-limonene. Right: D-limonene distribution in a 2D case with wall adsorption and volumetric reactions with Ozone.

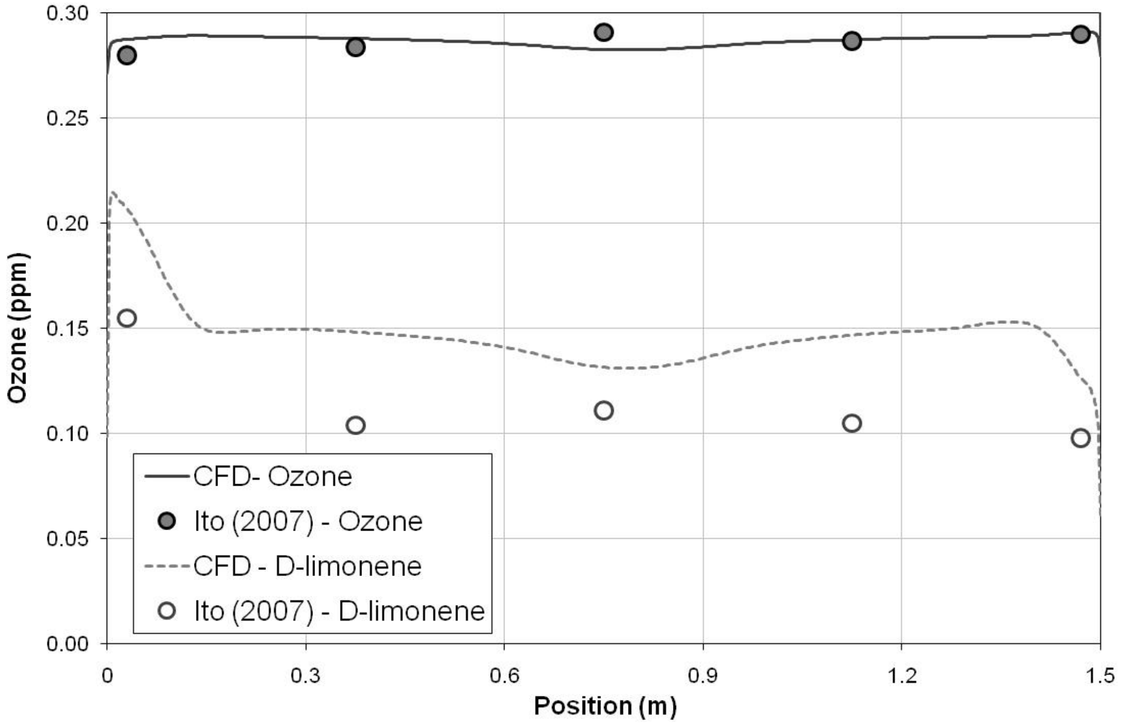

Figure 6.6: Comparison of Ozone and D-limonene levels along the horizontal centerline of the CFD results and the experimental values given by Ito (2007).

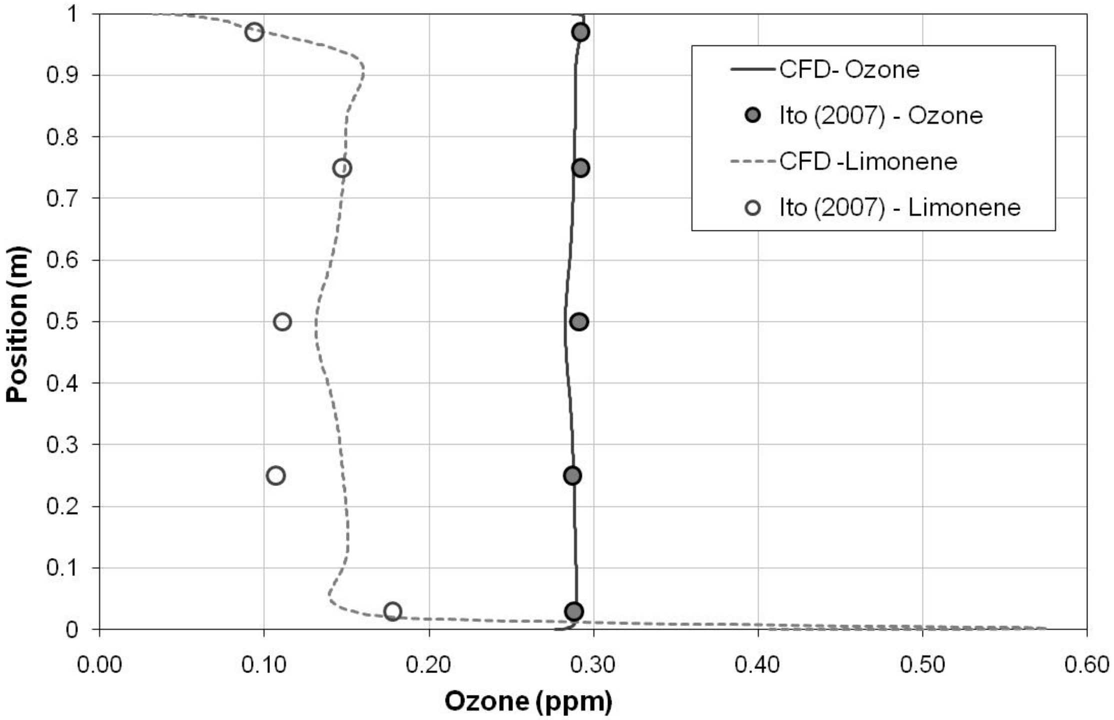

Figure 6.7 : Comparison of Ozone and D-limonene levels along the vertical centerline of the CFD results and the experimental values given by Ito (2007).

6.1.3 Typical Office Space

6.1.3.1 Domain and Setup

After validation, a typical office space was simulated with wall adsorption and volumetric reactions between Ozone and D-limonene. Three cases were compared including 1) displacement ventilation (No PV), 2) a single round jet PV system and 3) a novel low-mixing Co-flow PV system (Khalifa & Glauser, 2006) that directs fresh air toward the BZ. The domain and setup that were used were the same as the domain described in Section 6.1.

For these cases, the Ozone/D-limonene reaction was modeled as $O_3 + C_{10}H_{16} =$ Hypothetical Product. Ozone is prevalent in outdoor air and is the main source of Ozone indoors and is delivered into the indoor environment through the ventilation systems. Before 1990, common Ozone levels found indoors range from *20-40 ppb*, but were found to exceed *100 ppb* in extreme cases (Sabersky et al., 1973; Weschler et al., 1998). In 1996, increased Ozone levels of *28-60 ppb* were reported in a naturally ventilated building in Mexico City (Gold et al., 1996). In 2000, Weschler reported that indoor Ozone levels often exceeded *20 ppb*, levels above *40 ppb* in the summer months and levels above *50 ppb* were not uncommon in well ventilated buildings in the United States. Based on this, Ozone is assumed to be a component of fresh outdoor air and will enter the domain through the ventilation system at an elevated outdoor concentration of *80 ppb* (recirculated air was a mixture of outdoor concentrations and exhaust concentrations) to represent an above average case. Adsorption of Ozone was modeled with a mass accommodation coefficient of $\gamma=2.0x10^{-5}$ (Reiss et al., 1994) on the walls, ceiling and desk to represent typical indoor Ozone characteristics for indoor spaces with latex paint.

D-limonene was modeled as a floor source with a source strength of $1.89\ mg/m^2\cdot h$ over the entire floor (Sorensen and Weschler, 2002). Adsorption of D-limonene was modeled with a mass accommodation coefficient of $\gamma=2.1x10^{-5}$ on the walls, ceiling and desk given by Ito (2007b) for D-limonene adsorption in a test chamber (The adsorption of D-Limonene on painted walls is likely to be different that this, however additional data was not available).

The volumetric reaction occurred between Ozone and D-limonene was modeled with a second order rate constant of $k=0.0184\ ppb^{-1}\ h^{-1}$ (Atkinson et al. 1990). Surface reactions and other volumetric reactions of Ozone with any other species were ignored in this work. A summary of chemical BC's are given in Table 6.2.

Recirculated air was a mixture of exhaust concentrations and fresh air concentrations. The primary nozzle of the two PV systems delivered fresh air only at a small fraction (*2.4 l/s*) of the fresh air recommended by ASHRAE Standard 62.1-2004. The rest of the fresh air for the cases with PV and all of the fresh air for the case without PV is mixed with the recirculated air from the room and is delivered through the secondary nozzle and/or the floor diffuser.

Table 6.2: Chemical reaction BC's for typical office simulation.

	Case C
Inflow (fresh air)	C_{ozone} = 80 ppb $C_{d\text{-}limonene}$ = 0 ppb
Line Source	$S_{d\text{-}limonene}$ = 1.89 mg/m^2•h
Reaction Probability at Surfaces	$\gamma_{ozone} = 2.0\text{x}10^{-6}$ $\gamma_{d\text{-}limonene} = 2.1\text{x}10^{-5}$
Volumetric Reaction	k = 0.0184 ppb^{-1} h^{-1}

For the cases studied in this work the mass balance of species involved in the hypothetical reaction, $A + B = P$ are,

$$ACH(C_A)_{in} = ACH(C_A)_{out} - k_{f,r}(C_A)_{in}(C_B)_{in} - v_{d,A}\frac{A}{V}(C_A)_{in} \tag{6.2}$$

$$ACH(C_B)_{in} = ACH(C_B)_{out} - k_{f,r}(C_A)_{in}(C_B)_{in} - v_{d,B}\frac{A}{V}(C_B)_{in} \tag{6.3}$$

$$ACH(C_P) = k_{f,r}(C_A)_{in}(C_B)_{in} \tag{6.4}$$

Personalized ventilation benefits were assessed under conditions where the total amount of fresh air recommended by ASHRAE 61.1-2004 is split between the floor diffuser and a PV nozzle such as that described by Khalifa et al. (2009). The concentrations of the various contaminants in the inhaled air were computed. We then compared the results of these simulations with those obtained without PV with the same total amount of clean air, using the concept of iF in all cases.

6.1.3.2 Intake Fraction and Removal Ratios

Figure 6.8 shows the normalized concentration distribution for Ozone for the three cases studied where Ozone was delivered to the room through the ventilation system. The figure shows that Ozone concentration distributions do not exhibit well mixed behavior due to imperfect mixing, wall adsorption and chemical reactions. The Ozone concentrations vary throughout the room and BZ concentration values are *35*, *51* and *64 ppb* for Case 1, 2 and 3, respectively. While the Co-flow nozzle delivers the highest levels of Ozone to the BZ, it is noted that the levels of Ozone are not above EPA allowable standards. In 2008 the EPA published guidelines for Ozone Air Quality Standards stating that Ozone levels should not to exceed *75 ppb* averaged for an eight hour period. The concentration of Ozone is largest near the ventilation system and is reduced in the regions of the room where mixing and volumetric reactions occur and there are large concentration gradients near the wall due to the surface adsorption. These patterns are similar for all three cases. Since the primary nozzle of the PV systems deliver only fresh air, Figure 6.8a shows the highest concentration of Ozone exiting the primary nozzle of the PV system and extending to the BZ for the Co-flow nozzle. Figure 6.8b shows a similar trend, however, the concentration of Ozone decreases more rapidly toward the BZ for the primary nozzle. Figure 6.8c shows the highest concentration of Ozone along the floor and at the floor diffuser for the case without PV.

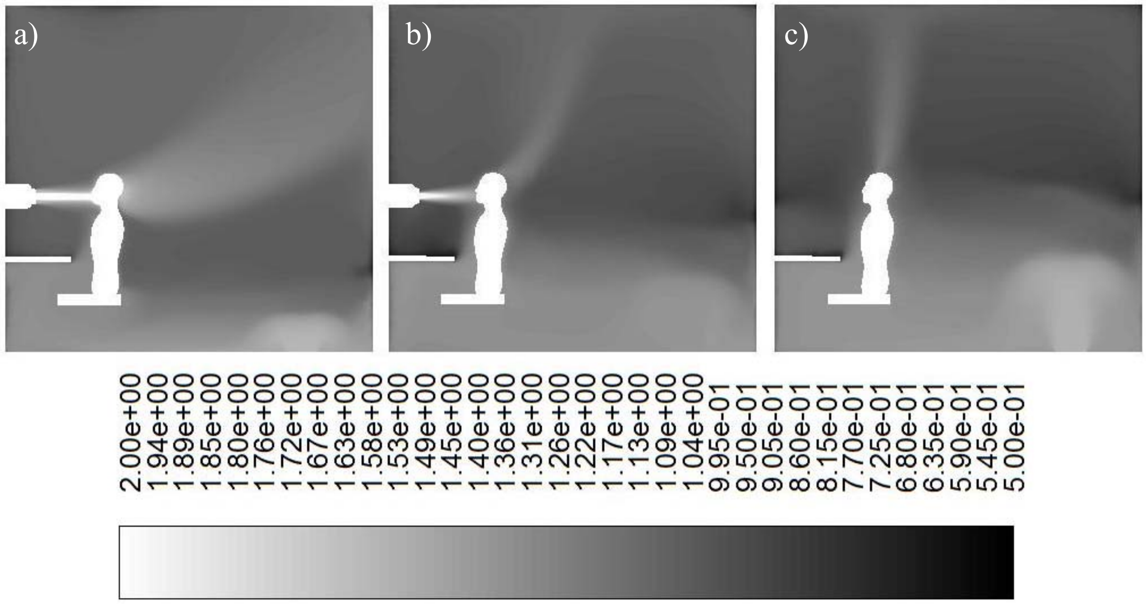

Figure 6.8: Ozone contours for a) the Co-flow PV system, b) the Primary jet PV system and c) no PV system. All contours are normalized with the well mixed condition so that a value of 1 equals well mixed.

Figure 6.9 shows the normalized concentration distribution for D-limonene for the three cases studied where D-limonene was emitted from a floor source. The figure shows that D-limonene concentration distributions do not exhibit well mixed behavior due to imperfect mixing, wall adsorption and chemical reactions. The D-limonene concentrations vary throughout the room and BZ concentration values are *96, 34* and *21 ppb* for Case 1, 2 and 3, respectively (within normal range when products contain D-limonene are used). The concentration of D-limonene is largest near the floor and under the desk. The flow direction at the floor is towards the left wall and creates a recirculating region under the desk where the concentration of D-limonene is very high. D-limonene concentrations are reduced in the regions of the room where mixing and volumetric reactions occur. There are also large concentration gradients near the wall due to the surface adsorption. These patterns are similar for all three cases. Since the primary nozzle of the PV systems deliver only fresh air, Figure 6.9a shows the lowest concentration of D-limonene exiting the primary nozzle of the PV system and extending to the BZ for the Co-flow nozzle. Figure 6.9b shows a similar trend, however, the concentration of D-limonene increases more rapidly toward the BZ for the primary PV system. Figure 6.9c shows the lowest concentration of D-limonene exiting the floor diffuser for the case without PV.

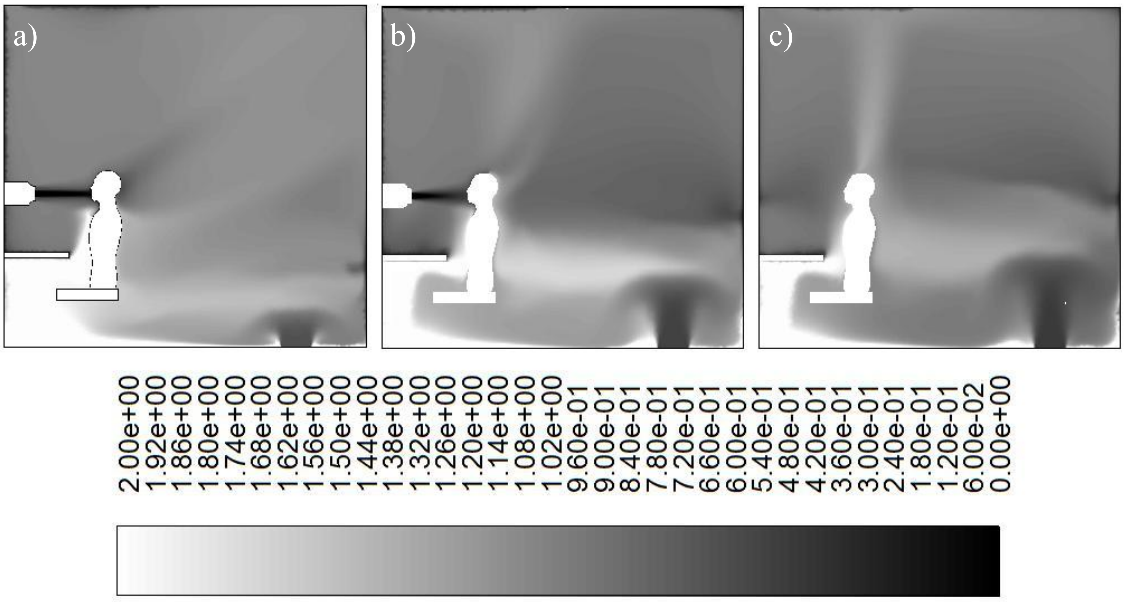

Figure 6.9: D-limonene contours for a) the Co-flow PV system, b) the Primary jet PV system and c) no PV system. All contours are normalized with the well mixed condition so that a value of 1 equals well mixed.

Figure 6.10 shows the normalized concentration distribution for the hypothetical product from the volumetric reaction for the three cases studied. The figure shows that product concentration distributions do not exhibit well mixed behavior due to imperfect mixing and chemical reactions. The product concentrations vary throughout the room and BZ concentration values are *11, 6*, and *3* ppb for Case 1, 2 and 3, respectively. The concentration of the product is largest in the region of the rooms were recirculation occurs and there is more time for the reaction to occur. The product concentrations are reduced near the ventilation systems where the fluid velocities are fast. These patterns are similar for all three cases. Since the primary nozzle of the PV systems deliver only fresh air, Figure 6.10a shows the lowest concentration of the product exiting the primary nozzle of the PV system and extending to the BZ for the Co-flow nozzle. Figure 6.10b shows a similar trend, however, the concentration of the product increases more rapidly toward the BZ for the primary PV system. Figure 6.10c shows the lowest concentration of the product exiting the floor diffuser for the case without PV.

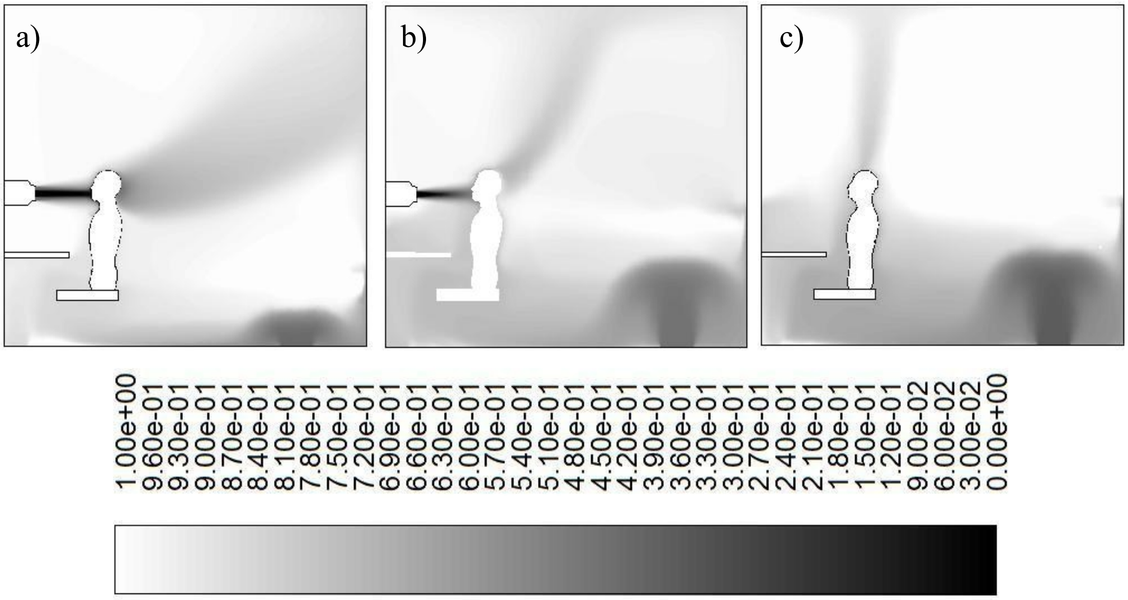

Figure 6.10: Hypothetical product contours for a) the Co-flow PV system, b) the Primary jet PV system and c) no PV system. All contours are normalized with the well mixed condition so that a value of 1 equals well mixed.

Figure 6.11 shows the iF normalized with the well mixed condition for each species for the Co-flow, Primary and no PV cases when adsorption and volumetric reactions were modeled. The results show that these species distribution do not exhibit well mixed behavior, and further support the idea that the well mixed assumption should not be used when there are indoor sources or chemical reactions present in a room especially with PV. It is shown that the iF can be more than or ~5 times lower than a case that assumes well mixed conditions. The Co-flow nozzle produces the highest levels of Ozone in the BZ which results in the highest iF, followed by the primary nozzle and no PV system. For D-limonene and the hypothetical product the trend is reversed. The Co-flow nozzle reduces the iF values by a factor of ~5 in both instances.

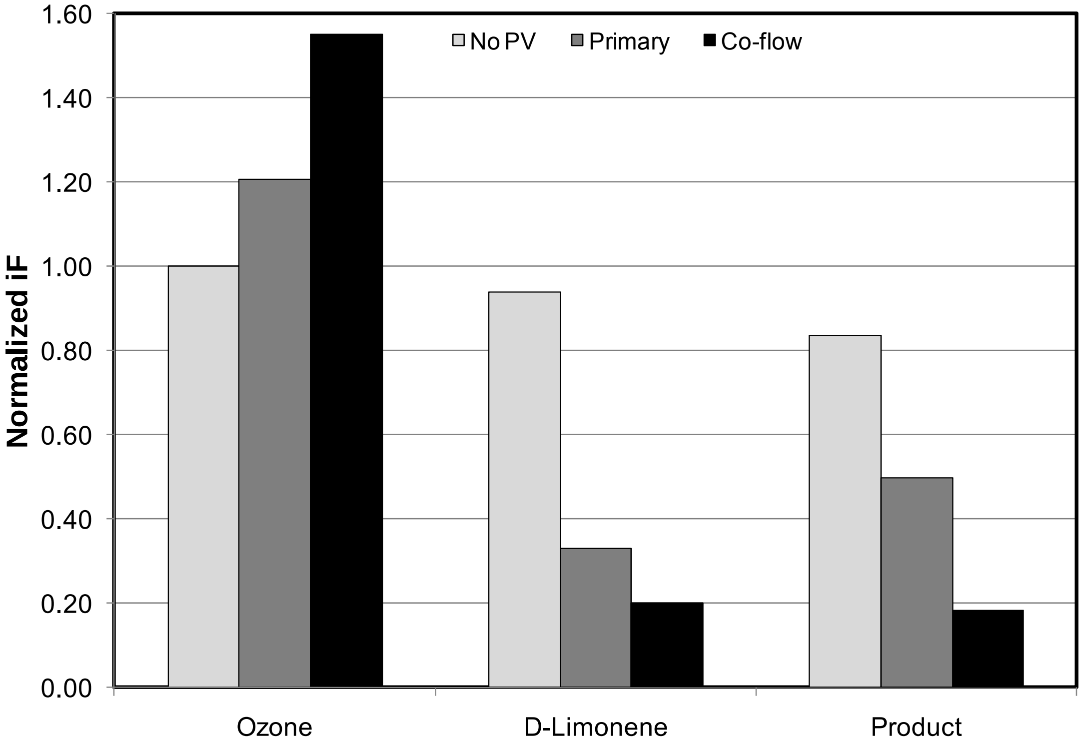

Figure 6.11: iF comparison for the 2 PV systems and a case without PV. All iF values were normalized with the well mixed condition so that a value of 1 is equal to well mixed.

Table 6.3 gives the removal ratios for ventilation, adsorption and volumetric reaction for the three ventilation configurations. Removal ratios were calculated as a percentage of the species that was removed by ventilation, adsorption and volumetric reaction for Ozone and D-limonene. The removal ratio of Ozone in the first case (no PV system) was: *51 %* by ventilation, *47 %* by adsorption and *2 %* by volumetric reaction with D-limonene. The removal ratio of D-limonene in the first case (no PV system) was: *46 %* by ventilation, *51 %* by adsorption and *3 %* by the volumetric reaction with Ozone. The removal ratios with PV are very similar to the case without PV. Under these conditions the removal ratio of Ozone and D-limonene from volumetric chemical reaction was relatively low because of the high air exchange rate and low age of air in the room. At lower air exchange rates there would be more time for the volumetric reaction to occur which would result in higher removal ratios from the reaction. Sorensen and Weschler (2002) found that the removal of Ozone that was consumed by the volumetric reaction with D-Limonene was much larger (37.5 %) for an ACH of $0.5\ h^{-1}$ and that this decreased significantly with an increase of ACH to $2.0\ h^{-1}$ (7.3 %). The ACH of the work here was $\sim 5\ h^{-1}$. This trend was also found for D-Limonene which confirmed the influence of the decreased time available for the reaction.

The removal of Ozone by adorption and the ventilation system are expected to be on the same order. Typical values for deposition velocity of Ozone in office spaces are ~1 *m/h* (Weschler et al., 1989, and Shair& Heitner, 1974) and typical office area to volume ratios are ~3 m^{-1} resulting in typical deposition removal rates of ~3 h^{-1}. This is on the same order as the removal rate for ventilation. The ACH used for this work was ~5 h^{-1} with a fresh air ACH of ~1.67 h^{-1}. Since Ozone is a constituent of fresh air, the ACH for air that is not polluted with Ozone is ~3.33 which is on the same order as the deposition removal rate.

Table 6.3: Removal ratios of Ozone and D-limonene in percentages of the amount introduced into the room.

		Removal Ratio (%)		
		No PV	Primary	Co-flow
Ozone	Ventilation	51	51	52
	Adsorption	47	47	45
	Reaction	2	2	3
D-Limonene	Ventilation	46	46	46
	Adsorption	51	51	52
	Reaction	3	3	2

6.1.4 Section Conclusions

A 2D CFD model that accounts for volumetric reactions and wall adsorption was validated with experimental results of Ito (2007b). The results show that the developed model agrees reasonably well with the experimental data with an average error of *~10 %*. The CFD model was able to predict species concentrations in the test chamber accurately and can be used as a reliable tool to optimize the design and placement of PV systems, and to investigate chemically reacting flows more cost-effectively and faster than laboratory testing. With these results a 3D computational domain was created that can be used to study chemical reactions in a typical office space.

The 3D computational investigation models the complex chemically reacting flow patterns in the personal microenvironment of a detailed CSP with wall adsorption of Ozone and D-limonene in a typical office space. The results show that, for each case and for each species, the concentration distribution is not well mixed with significant variations in the species distributions at different locations in the room. This non-uniform distribution in the indoor environment is attributed to imperfect mixing, concentration variations leading to different reaction rates at different locations in the room and the age of air is different at different locations in the room which allows more time for reaction to occur. For situations where indoor sources or chemically reacting flows are present in the indoor environment, like the one outlined in this work, assuming the concentration distributions are well mixed can lead to significant over or under prediction of inhalation exposure.

When comparing the three cases, the Co-flow nozzle (Case 3) is superior at removing D-limonene and reaction products from the inhalation air than the single jet PV system and both PV systems have lower D-limonene and product concentrations in the BZ than the case without PV. The reduction of oxidation products in the BZ from the use of PV is a significant result because the reaction products have been shown to be more irritating than there precursors. However, Co-flow nozzle delivers the highest levels of Ozone to the BZ, which is not favorable. The levels of Ozone in the BZ could be reduced by using an Ozone filter in the primary nozzle of the PV system to reduce the Ozone level from outdoor air that is being delivered in the fresh air supply. Ozone filters have been studied

(Lee and Davidson, 1999; Metts and Batterman, 2006; Zhao et al., 2007; Shelton et al., 2008) and could make significant improvements on indoor Ozone levels.

6.2 Ozone/Squalene Reaction

The common reaction between Ozone from the outdoors and Terpenes found on clothing, in the oils produced by the skin and in hair oil/products is of significant importance in the indoor environment. Because these reactions occur within the thermal plume of the human body, the effect on the air quality in the BZ should be understood to a greater depth. Reactions with human skin oils and clothing reduces the total amount of Ozone near a person; it has been shown that Ozone/human reactions can contribute to more than half of the total loss of Ozone in a densely populated aircraft cabin (Tamas et al., 2006). It has also been shown that a single person in a residential room can be responsible for about *10 %* of the total Ozone removal. Hair is another significant sink of Ozone, and it has been shown that the uptake of Ozone is limited by the transport of Ozone through the boundary layer rather than by the reaction probability of Ozone on the surfaces (Pandrangi and Morrison, 2008). This is also the case for Ozone/clothing reactions (Coleman et al., 2008).

As a result, the removal of Ozone from indoor air increases the amount of oxidation products that are more harmful than the Ozone itself. The reaction of Ozone and Squalene, found in the oils of the skin, produce 4-oxopentanal, 6-methyl-5-hepten-2-one, geranyl acetone, acetone, nonanal, and decanal (Fruekilde et al., 1997). These products have been shown to be respiratory irritants and can act as a sensitizer (Anderson et al., 2007). Other reaction products from Ozone/human oil reactions include aldehydes, ketones, carboxylic acids and secondary organic aerosols. These products have been shown to be eye and airway irritants (Wolkoff et al., 1999; Kleno and Wolkoff, 2004, Tamas et al., 2006; Rohr et al., 2002). The Ozone/human body reaction has been studied both experimentally and computationally (Coleman et al., 2008; Rim et al., 2009), however, a detailed analysis of the Ozone/Squalene reaction using CFD has not been made in the presence of a detailed CSP in the indoor environment.

6.2.1 Validation

The validated CFD model was extended to handle surface reactions between Ozone and Squalene. Before room simulations are carried out, the use of surface reactions in Fluent were validated by comparison with experimental data of Rim et al. (2009) who studied the Ozone/human body reaction on a cylinder in a stainless steel chamber. The domain for this study is shown in Figure 6.12. The influence of chemical interactions at the human surface on BZ levels of reactants and products were modeled experimentally and computationally. Rim et al (2009) studied different ventilation rates that ranged from *0.7* and *0.9* ACH and the Ozone concentration was measured. For the experimental setup the Ozone decay rate, air exchange rate, Ozone removal rate and deposition velocity of Ozone were determined. An Ozone generator was used to inject the chamber until a well-mixed condition was achieved for a setup with the cylinder in the center of the room and a setup without the human simulator cylinder. The cylinder was fit with a snug-fitting sleeve that was made of cotton and soaked in a solution to represent the transport limited uptake of Ozone on an occupant. Ozone samples were then collected every one minute and the Ozone decay rate was quantified by a best fit to the exponential decay. The difference between the Ozone decay rate and the air exchange rate was defined as the Ozone decay rate for surface consumption. The difference between the Ozone decay rate with and without the human simulator is defined as the human simulator-specific Ozone decay rate. The Ozone deposition velocity was then found by multiplying the ratio of the volume of the room to the area of the cylinder with the Ozone decay rate associated with the cylinder. The deposition velocity was found for the same CFD setup using a zero mass fraction BC at the cylinder surface for three different grids (the size of the first cell height varied) and the differences between the CFD and experimental deposition velocities were found. For the CFD calculations the heated cylinder is assumed to be a perfect sink of Ozone. The percent difference varied from *15-38 %* between the experimental and CFD calculations. It was found that the cell size distribution moderately affects the velocity and concentration profiles when Neumann thermal BCs are used. It is noted that the deposition velocity differences between the experimental and CFD are greater than the experimental error but were judged to be sufficiently accurate to give insight into Ozone mass transfer in the vicinity of an occupant. With the results of the validation setup a more detailed CSP was used to determine the BZ Ozone and product concentrations. It was found that large concentration gradients occur between BZ and bulk air with a ceiling supply. It was concluded that micro-environment measurements alone should not be used to assess the intake of Ozone.

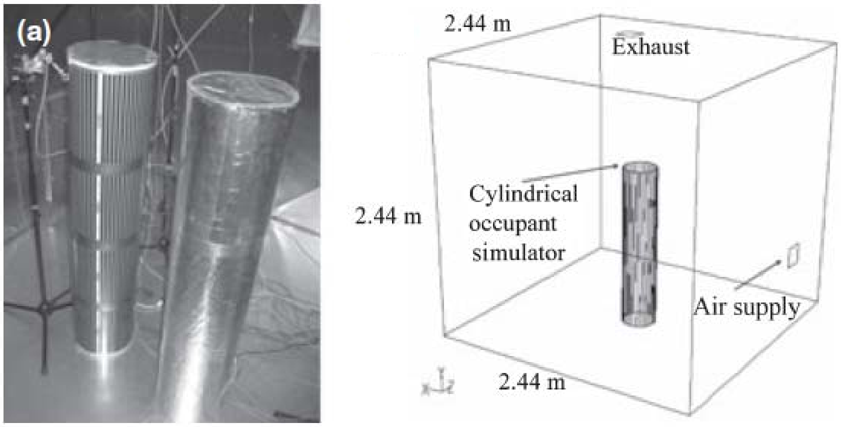

Figure 6.12: Domain used in Rim et al. (2009) (Rim et al., 2009).

6.2.1.1 Domain and Setup

A 3D domain *2.44 m* x *2.44 m* x *2.44 m* with one inlet and one outlet was created for validation which matched the dimensions of the chamber in the experimental paper (Rim et al., 2009) as shown in Figure 6.12. In the room a *1.5 m* tall cylinder with a *0.3 m* diameter was located off center; therefore, symmetry was not applied. The ACH was modeled as *0.79* and Ozone entered through the ventilation system on a wall at *0.03 ppm* and was exhausted at the ceiling. The grid developed for validation followed the same guidelines as Section 3.1. The total number of cells in the domain were ~*4.5* million with a starting size of *0.5 mm* ($y^+ = 0.4$) on the cylinder surface, which is half the size as the smallest starting grid size used by Rim et al. (2009). The grid is shown in Figure 6.13. For all cases, Fluent was used with second-order accurate upwind schemes to solve the momentum and energy equations, and a second-order accurate scheme for the pressure interpolation. The species transport equation was included to compute the concentration of each pollutant.

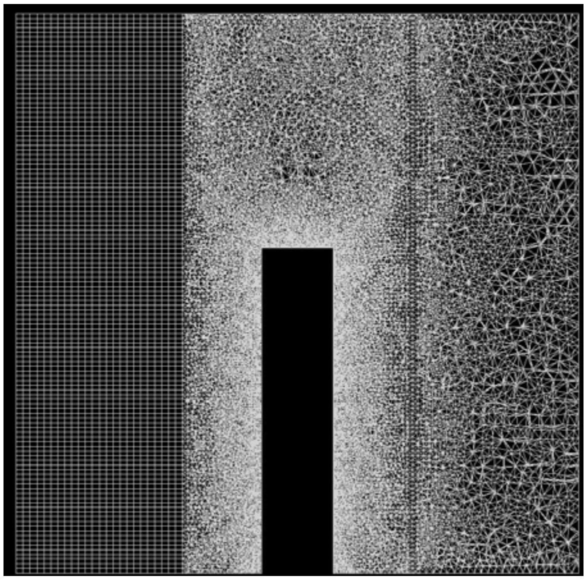

Figure 6.13: Grid used for Ozone/Human Body reaction validation.

For validation three cases were analyzed. For Case 1, it was assumed that the cylinder was a perfect sink of Ozone (set the mass fraction of Ozone to zero on the surface of the cylinder as in Rim et al. (2009)). It has been shown that Ozone deposition occurs at the transport limited rate when $\gamma>\sim 3x10\text{-}4$ for typical indoor air flow conditions (Cano-Ruiz et al. 1993) and Ozone deposition can be predicted by surface kinetics alone if $\gamma<\sim 5x10\text{-}7$. The Ozone/Squalene reaction has mass accommodation coefficients ranging from $\gamma=5e\text{-}4$ to $\gamma=2e\text{-}3$ (Wisthaler & Weschler, 2009) which indicates that the deposition velocity is limited by the transport deposition velocity only. This has led some authors (Rim et al., 2009) to model the reaction of Ozone/Squalene using a BC of zero mass fraction of Ozone at the body surface. The temperature of the cylinder was set to match the average temperature of the cylinder from the experiment (*27.5 ˚C*) and the thermal BCs on the walls (average surface temperature of *24.8 ˚C*) were determined by matching the CFD exhaust temperature to the experimental exhaust temperature. This is believed to be an improvement on the CFD modeling methods used by Rim et al. (2009) where the convective flux from the cylinder was modeled based on the findings is Section 2.4. To improve on these results, for Case 2, a flux of Ozone was determined from the Ozone removal rate of $0.57\ h^{-1}$ from Rim et al. (2009) and used as a BC at the cylinder surface. Finally, for Case 3 a reaction was set at the cylinder surface representing an Ozone/Squalene reaction with a mass accommodation coefficient ranging from $\gamma=5x10^{-4}$ to $\gamma=2x10^{-3}$ (Wisthaler & Weschler, 2009). Squalene is a major component of human skin lipid and is the single most abundant Ozone-reactive constituent (Nicolaides, 1974) and, therefore, a reasonable reaction to be studied. All other BC for Case 2 and 3 were the same as Case 1.

For all three steps, computational deposition velocity results were compared to experimental deposition velocity of Ozone (Experimental $v_d = 5.83 +/- 0.85\ m/h$ (Rim et al., 2009)). Deposition velocity was determined by,

$$v_d = \frac{ACH(C_S - C_E)}{\frac{A_C}{V} C_E} \tag{6.5}$$

where, ACH is the air change per hour, C_S is the supply concentration of Ozone, C_E is the exhaust concentration of Ozone, A_C is the area of the cylinder and V is the volume of the room.

6.2.1.2 Experimental Comparison

Figure 6.14 shows Ozone contours for Case 1, 2 and 3. For Case 1, where a zero mass fraction BC was set at the cylinder surface, this contour shows high concentration gradients near the cylinder, with a plume of depleted Ozone rising above the cylinder. The highest levels of Ozone are in the lower half of the room where the Ozone is supplied through the ventilation air. Contours for Case 2 and 3 show similar overall patters as Case 1, however, the contours show higher levels of Ozone present in the room; indicating less removal by the cylinder surface. Concentration levels were not given in the experimental data, so no comparison was made.

To examine these cases on a quantitative level, deposition velocity was computed for all three cases and shown in Figure 6.15. The deposition velocity of Ozone to the surface of the human body is sensitive to air movements around the body (Pandrangi & Morrison, 2008) and the experimental deposition velocity was found experimentally to be *5.83 +/- 0.85 m/h*. For the experimental setup, air movement around the body is driven by the thermal plume only and air movement from the ventilation system is almost a non-factor. Figure 6.15 shows that Case 1 was able to predict the overall deposition velocity from the Ozone removal ratio of the cylinder to within *10 %*. This result is noticeably better than what was reported by Rim et al. (2009) for the same setup where a percent difference of *20 %* was found. The improvement in the comparison with this work can be attributed to grid refinement as well as a change in the thermal BC applied to the CFD model.

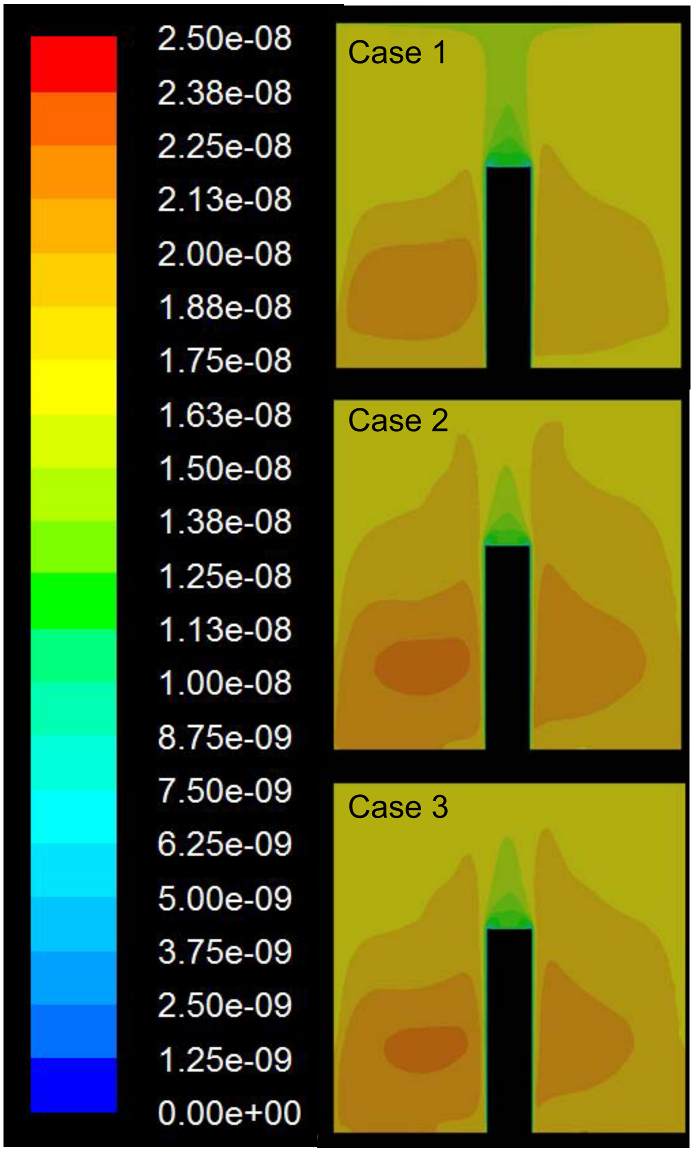

Figure 6.14: Ozone contours (mass fraction) for Case 1 (zero mass fraction boundary condition on cylinder surface), Case 2 (ozone flux boundary condition set at the cylinder surface) and Case 3 (ozone/squalene reaction boundary condition set at the cylinder surface).

Further improvement in the modeling of the reaction at the surface was achieved with Case 2 and 3. Modeling the Ozone flux, as determined from the experimental results, at the cylinder surface was able to achieve the closest comparison of less than *5 %* different. This is not a surprising result, however, this is not useful for modeling different scenarios since the BC determined was based on a specific experimental setup with a particular flow pattern and would change with any change to the domain. However, Case 3 used the reaction probability of Squalene to model the removal of Ozone at the cylinder surface. With the range of reported reaction probabilities, it was found that the deposition velocity of Ozone was predicted to within *4-6 %*. This is a successful finding and modeling the Ozone/Squalene reaction can be implemented in different indoor scenarios without losing validity.

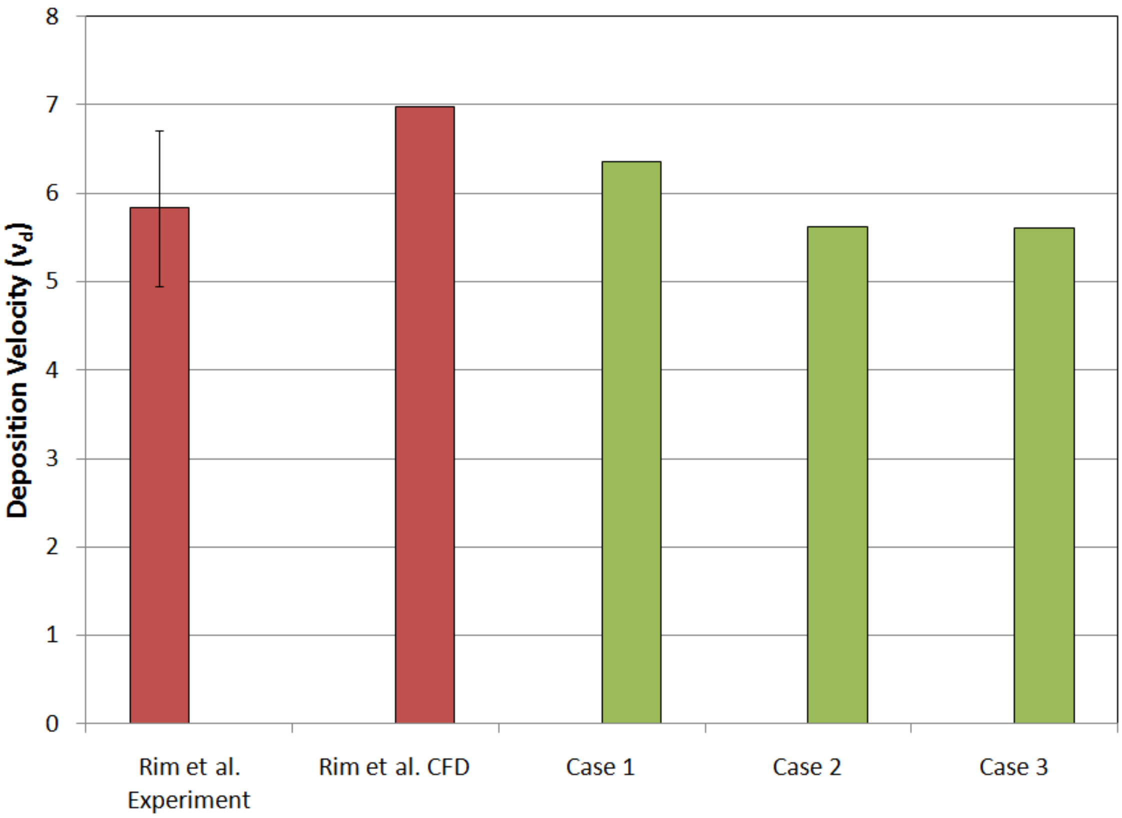

Figure 6.15: Computed deposition velocity compared to Rim et al. (2009).

To better understand the differences between the CFD results found in this work (Case 1) and those produced by Rim et al. (2009) additional CFD cases were simulated. A summary of the setup for both Rim et al. (2009) and this work are given in Table 6.3. The main difference between the CFD simulations was the way thermal boundary conditions imposed on the body and walls. For Rim et al. (2009) a convective heat flux was defined at the cylinder surface, where as an average surface temperature from the experimental results was used for this work. For the wall BCs, an average surface temperature was determined by matching the CFD exhaust temperature to the experiment. It is not stated in Rim et al. (2009) what the BC on the walls were. We believe this may be the reason for discrepancy between the results. Also, the height of the first cell at the heated cylinder surface was half of the size that was used in Rim et al. (2009).

The differences in simulation method resulted in different deposition velocity results. The deposition velocity results for this work are compared to Rim et al. (2009) experimental and computational results and were shown in Figure 6.15. With the same species BC, the results were improved from 20 % different to 9% different with the simulation changes. To examine the effect of thermal BCs further, three additional cases were simulated with different modeled heat flux from the cylinder surface ranging from 9W to 15W and with all other BCs the same. The results of these simulations are shown in Table 6.5. With this range of cylinder thermal BCs, error from the experimental results ranged 15%. This coupled with different thermal wall BCs could lead to a 10% difference between Rim et al. (2009) CFD and the computational work studied here.

Table 6.4: Summary of CFD cases

	Rim et al. CFD	Russo CFD Case 1	Russo CFD Case 2	Russo CFD Case 3
Room Geometry (m)	2.4 x 2.4 x 2.4	2.4 x 2.4 x 2.4	2.4 x 2.4 x 2.4	2.4 x 2.4 x 2.4
Manikin Geometry (m)	Cylinder 1.5 x 0.3	Cylinder 1.5 x 0.3	Cylinder 1.5 x 0.3	Cylinder 1.5 x 0.3
Thermal BC on Cylinder	calculated convective heat flux: 12W	average surface temperature: 27.5˚C	average surface temperature: 27.5˚C	average surface temperature: 27.5˚C
Species BC on Cylinder	0 mass fraction	0 mass fraction	Ozone flux: determined from experiment	first order reaction: ozone/squalene reaction probablity
Thermal BC on Walls	Not stated (stated that the only heat source is the cylinder)	average surfae temperature: 24.8˚C; determined by matching CFD exhaust temperature to experiment	average surfae temperature: 24.8˚C; determined by matching CFD exhaust temperature to experiment	average surfae temperature: 24.8˚C; determined by matching CFD exhaust temperature to experiment
Ventilation Rate (ACH)	~0.8	0.79	0.79	0.79
Surface adjacent grid cell height (mm)	1	0.5	0.5	0.5
y^+	not stated	0.4	0.4	0.4
Total Number of Cells	not stated	4.5 Million	4.5 Million	4.5 Million
Turbulence Model	RNG *k*-□	Realizable *k*-□	Realizable *k*-□	Realizable *k*-□
Wall Treatment	not stated	Enhanced Wall Treatment	Enhanced Wall Treatment	Enhanced Wall Treatment

Table 6.5: Additional cases studied

BC Set for Cylinder	Average Heat Flux (W)	Average Surface Temperature (˚C)	v_d	% Diff from Experiment
Surface Temp 27.5˚C	11.17	27.50	6.36	9
Heat Flux 9W	9.00	27.02	5.85	0
Heat Flux 12W	12.00	27.55	6.27	8
Heat Flux 15W	15.00	28.14	6.62	14

6.2.2 Typical Office Space

With the knowledge gained from computationally modeling the experimental setup from Rim et al. (2009), this work proceeded to modeling a more realistic setup with a detailed CSP using the Ozone/Squalene reaction at the CSP surface. This was the final step in creating a validated computational model for chemically reacting flow and was used to assess PV under an array of reaction scenarios.

6.2.2.1 Domain and Setup

After validation, a typical office space was simulated with wall adsorption and surface reactions for the two PV systems and without PV for comparison (Case 1). The domain that was used was a *2 m* by *2.6 m* by *2.5 m* domain (for more details on the domain refer to Section 5.1). The grid and the CFD strategy that was used for this work follow the same methods described in Section 5.1

The Ozone/Squalene reaction was modeled as O_3 + Sq = Hypothetical Product. Known products of this reaction include 4-Oxopentanal (4-OPA), 6-methyl-5-hepten-2-one (6-MHO), Geranyl Acetone, Acetone, Nonanal and Decanal. Ozone is assumed to be a component of fresh outdoor air and entered the domain through the ventilation system at *80 ppb* (recirculated air was a mixture of outdoor concentrations and exhaust concentrations). Adsorption of Ozone was modeled with a mass accommodation coefficient of $\gamma=2x10^{-5}$ (Reiss et al., 1994) on the walls, ceiling and desk. A surface reaction was modeled between Ozone and Squalene and was represented with a first order reaction with a first order reaction constant of $2.0\ h^{-1}$ (Wisthaler & Weschler, 2009), which is used for all surface reaction rates between Ozone and Squalene. A summary of chemical BC's is given in Table 6.6. Recirculated air consisted of a mixture of exhaust concentrations and fresh air concentrations. Surface reactions of Ozone with any other species were ignored in this work.

Personalized ventilation benefits were assessed under conditions where the total amount of fresh air recommended by ASHRAE 61.1-2004 is split between the floor diffuser and a PV nozzle such as that described by Khalifa et al. (2009). In all cases, fresh air is mixed with recirculated air for the ventilation air introduced through the floor diffuser. The primary nozzle of the two PV systems will deliver fresh air only at a small fraction of the fresh air recommended by ASHRAE Standard 62.1-2004. The rest of the fresh air for the cases with PV and all of the fresh air for the case without PV is mixed with the recirculated air from the room and is delivered through the secondary nozzle and/or the floor diffuser. The concentration of the various contaminants in the inhaled air was computed. The results of these simulations were compared with those obtained without PV with the same total amount of clean air, using the concept of iF in all cases.

A series of reactions were studied for this work. First, Ozone reacted with Squalene and produced a gas phase product (Case 'a') modeled as $O_3 + C_{30}H_{50} \rightarrow A$. Case 'a' represents a simplistic, hypothetical reaction between Ozone and Squalene. Second, for Case 'b', Ozone reacted with Squalene and produced gas and liquid phase products, representing the next level of hypothetical reactions between Ozone and Squalene and was modeled as $O_3 + C_{30}H_{50} \rightarrow A + B$. For Case 'c', the reactions were improved so that

Ozone reacted with Squalene to produce 6-MHO and a hypothetical liquid phase product modeled as $4O_3 + C_{30}H_{50} \rightarrow C_8H_{14}O + B$. Also for this case, the gas phase 6-MHO was modeled to react with the gas phase Ozone as a secondary volumetric reaction to produce 4-OPA and was modeled as $5O_3 + 5(C_8H_{14}O) \rightarrow 4(C_5H_8O_2) + C$. Stoichimetric coefficients for these reactions are not fully known, however, there is information about the yield of these products. Yield is defined as moles of product of a species *i* formed per mole of ozone consumed. The yield of 6-MHO from the Ozone/Squalene reaction *~16-27 %* (Wisthaler & Weschler, 2009; Fruekilde et al., 1998) or *0.16-0.27 moles* of 6-MHO for every mole of Ozone consumed. The yield of 4-OPA from the Ozone/6-MHO reaction is ~80% (Wisthaler & Weschler, 2009) or *0.8 moles* produced for every mole of Ozone consumed. The volumetric reaction was modeled with a second order reaction a rate of $k=3.8x10^{-16}\ cm^3\ mol^{-1}\ s^{-1}$ (Fruekilde et al., 1997), which is very similar to other reported values ($k=4.1x10^{-16}\ cm^3\ mol^{-1}\ s^{-1}$ found by Grosjean et al. 1996). For Case ‘d’, the affect of uniform vs. non-uniform distribution of Squalene was determined. Finally for Case ‘e’, Ozone filters were modeled in the PV systems to study the benefit of Ozone removal in the PV ventilation ducts. These reaction cases are summarized in Table 6.6, the chemical BC’s are given in Table 6.7 and comparisons of the results from reaction Cases ‘a’-‘e’ are discussed in Section 6.2.4.

Table 6.6: Cases simulated for the Ozone/Squalene reaction.

	Reaction
Case 'a'	$O_3 + C_{30}H_{50} \rightarrow A$ (gas)
Case 'b'	$O_3 + C_{30}H_{50} \rightarrow A$ (gas) + B (Liquid)
Case 'c'	$4O_3 + C_{30}H_{50} \rightarrow C_8H_{14}O + B$ (liquid); $5O_3 + 5(C_8H_{14}O) \rightarrow 4(C_5H_8O_2) + C$ (gas)
Case 'd'	Uniform vs. Non-uniform Squalene Distribution
Case 'e'	$4O_3 + C_{30}H_{50} \rightarrow C_8H_{14}O + B$; $5O_3 + 5(C_8H_{14}O) \rightarrow 4(C_5H_8O_2) + C$ with ozone filter

Table 6.7: Chemical BC's for typical office simulation.

	Case C
Inflow (fresh air)	C_{ozone} = 80 ppb $C_{products}$ = 0 ppb
Reaction Probability at Surfaces	$\gamma_{ozone} = 2.0\text{x}10^{-6}$
Surface Reaction	$k = 2.0\ h^{-1}$
Volumetric Reaction	$k=3.8\text{x}10^{-16}\ cm^3\ mol^{-1}\ s^{-1}$

6.2.2.2 Intake Fraction and Removal Ratios

6.2.2.2.1 O3 + Sq → A (gas)

Figure 6.16 shows the normalized concentration distribution for Ozone for the three ventilation cases studied where Ozone was delivered to the room through the ventilation system. The figure shows that Ozone concentration distributions do not exhibit well mixed behavior due to imperfect mixing, wall adsorption and chemical reactions. The Ozone concentrations vary throughout the room and BZ concentration values are *27*, *48* and *67 ppb* for ventilation Case 1, 2 and 3, respectively. Although the Co-flow nozzle delivers the highest levels of Ozone to the BZ for above average outdoor Ozone levels, it is noted that the levels of Ozone in the BZ are not above EPA standards for above average outdoor Ozone levels. The concentration of Ozone is largest near the ventilation system and is reduced in the regions of the room where mixing and volumetric reactions occur and there are large concentration gradients near the wall due to the surface adsorption. These patterns are similar for all three cases. Since the primary nozzle of the PV systems deliver only fresh air, Figure 6.16c shows the highest concentration of Ozone exiting the primary nozzle of the PV system and extending to the BZ for the Co-flow nozzle. Figure 6.16b shows a similar trend, however, the concentration of Ozone decreases more rapidly toward the BZ for the Primary nozzle. High levels of Ozone in the BZ are undesirable and methods considered to reduce Ozone levels are discussed in Section 6.2.2.2.5. Figure 6.16a shows the highest concentration of Ozone along the floor and at the floor diffuser for the case without PV.

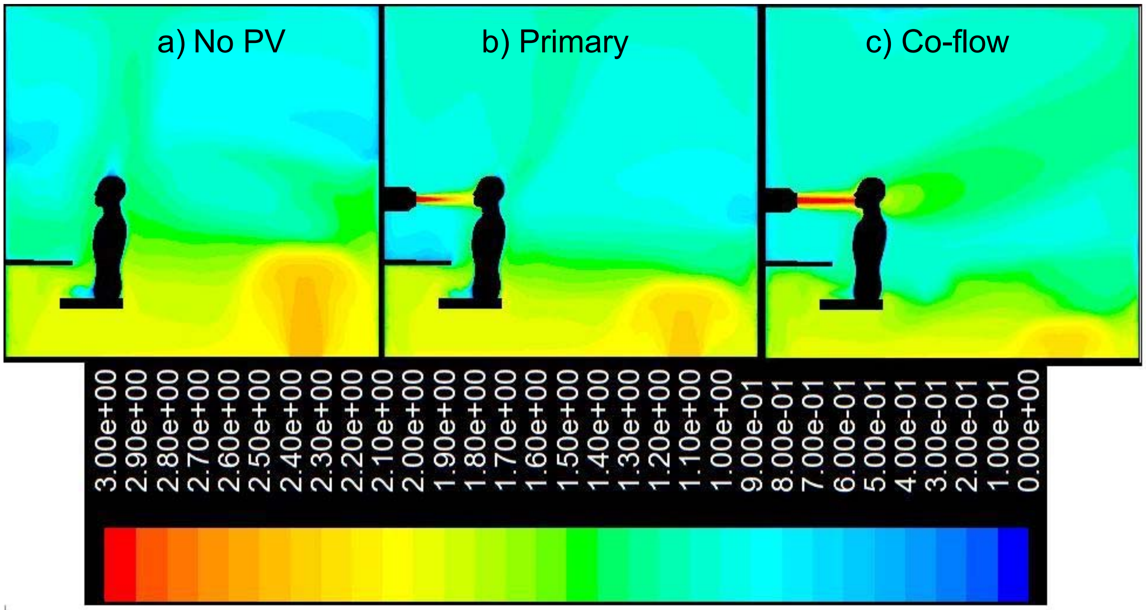

Figure 6.16: Normalized ozone contours for reaction Case ‘a’

Figure 6.17 shows the normalized concentration distribution for the hypothetical product ‘A’ for the three ventilation cases. The figure shows that product ‘A’ concentration distributions do not exhibit well mixed behavior due to imperfect mixing, wall adsorption and chemical reactions. Product ‘A’ concentrations vary throughout the room and BZ concentration values are *67, 31* and *16 ppb* for ventilation Case 1, 2 and 3, respectively. The concentration of ‘A’ is largest near the body and is transported away from the body by the thermal plume. Product ‘A’ concentrations are reduced in the regions of the room where mixing occurs. These patterns are similar for all three cases. Since the primary nozzle of the PV systems deliver only fresh air, Figure 6.17c shows the lowest concentration of ‘A’ exiting the primary nozzle of the PV system and extending to the BZ for the Co-flow nozzle. Figure 6.17b shows a similar trend, however, the concentration of ‘A’ increases more rapidly toward the BZ for the primary PV system. Figure 6.17a shows the lowest concentration of ‘A’ exiting the floor diffuser for the case without PV.

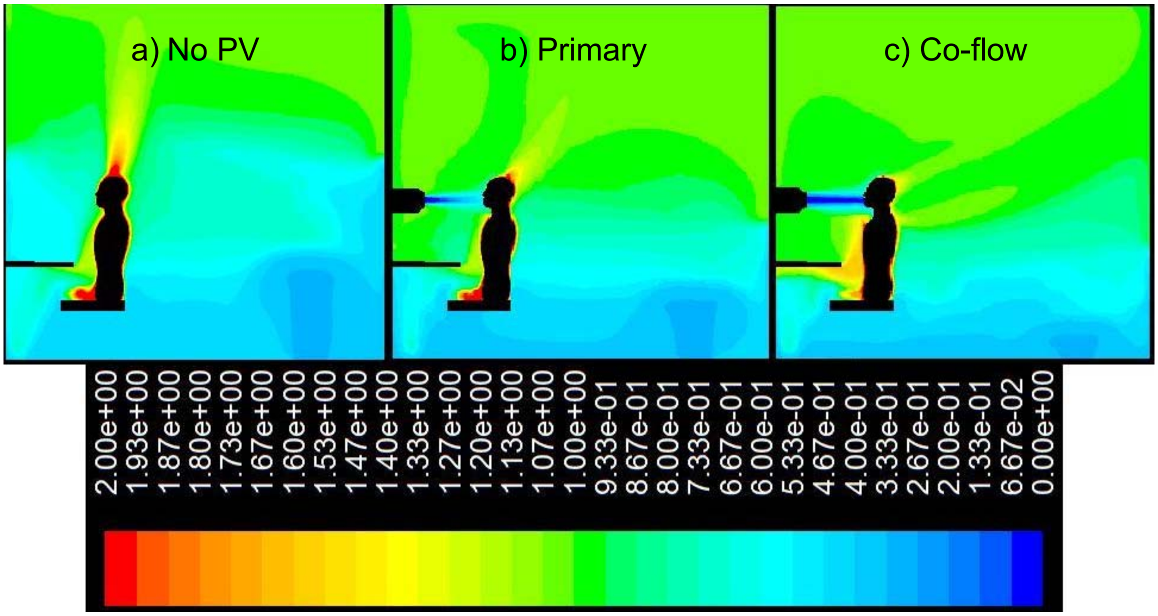

Figure 6.17: Normalized hypothetical product ‘A’ contours for reaction Case ‘a’.

The flux of ozone to the body surface and, therefore, the flux of ‘A’ from the body surface is equal to the rate of molecular collisions with the wall, as predicted by the molecular theory of gases, multiplied by the reaction probability. This quantity can be utilized to determine the amount of pollutant produced by the uptake of Ozone during the Ozone/Squalene reaction and in combination with iF to determine risk assessment of the products. It was found that $2.4\ mg/m^2 \cdot h$ of Product 'A' was produced from the Ozone/Squalene reaction.

Figure 6.18 shows the iF normalized with respect to with the well mixed condition for each species for the Co-flow, Primary and no PV cases when adsorption of Ozone and surface reactions between Ozone and Squalene were modeled. It is shown that the iF can be more than or ~*4* times lower than a case predicted by the well-mixed assumption. The Co-flow nozzle produces the highest levels of Ozone in the BZ which resulted in the highest iF followed by the primary nozzle and no PV system. For the hypothetical product 'A' the trend is reversed. The Co-flow nozzle reduces the iF values by a factor of ~*4*. This is the goal of PV in this simulation; to remove oxidation products from the CSP BZ.

Table 6.8 gives the removal ratios for ventilation, adsorption and surface reaction for the three ventilation configurations. Removal ratios were calculated as a percentage of the species that were removed by ventilation, adsorption and surface reaction for Ozone. The removal ratio of Ozone in the first case (no PV system) was: *41 %* by ventilation, *47 %* by adsorption and 1*2 %* by surface reaction with Squalene. The removal ratios with PV are very similar to the case without PV. Under these conditions the removal ratio of Ozone from surface chemical reaction was in agreement with Pandrangi and Morrison

(2008) where they estimated that a single occupant of a typical residential room was responsible for approximately 10% of the total ozone removal.

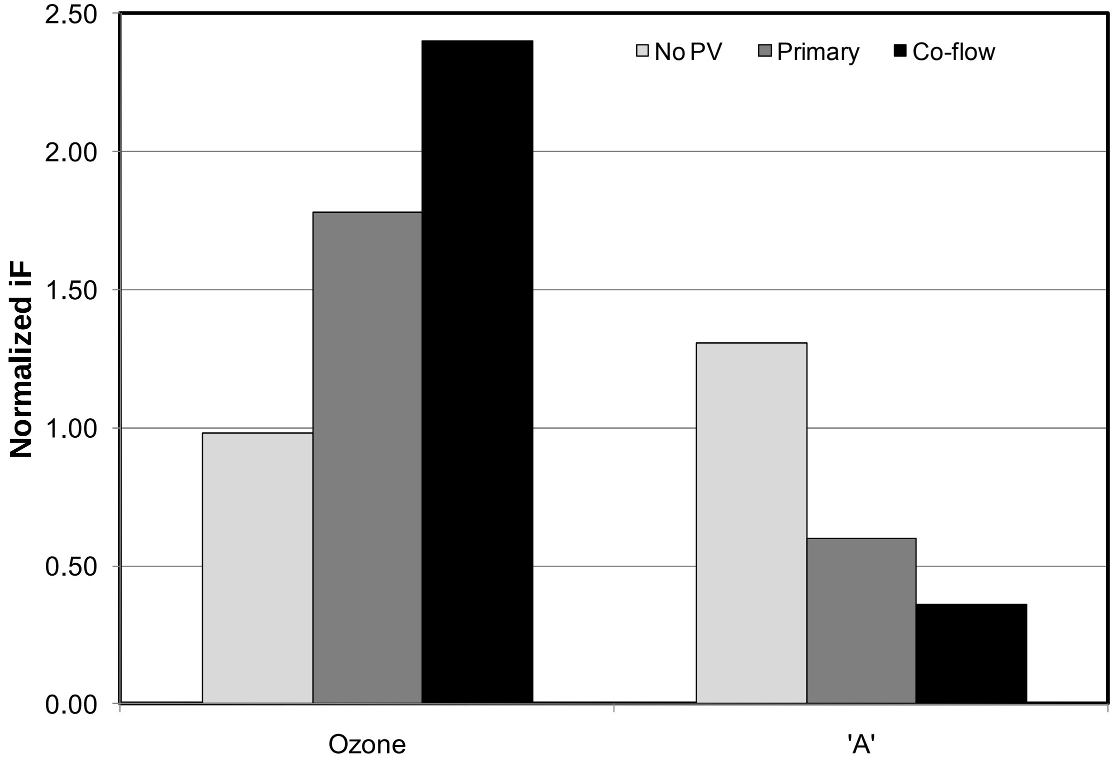

Figure 6.18: iF results for Case 'a'.

Table 6.8: Removal Ratios of ozone.

		Removal Ratio (%)		
		No PV	Primary	Co-flow
Ozone	Ventilation	41	42	42
	Adsorption	47	47	45
	Reaction	12	11	13

6.2.2.2.2 $O_3 + C_{30}H_{50} \rightarrow A$ *(gas) + B (liquid on skin)*

When examining the results from Case 'b', insignificant changes were found when comparing normalized contours and iF to Case 'a'. This is an expected result since the reaction rate for the Ozone/Squalene reaction remained the same (therefore, the removal of Ozone would be the same), the same ratio of reactants and products were inhaled (resulting in the same iF) and for this scenario, the liquid phase product does not affect the inhalation air quality. Concentration contours and iF results are not shown for this case. Although Case B does not offer any new information, it represents a more realistic reaction between Ozone and Squalene with both gas and liquid phase products. This improvement was implemented in the next reaction scenarios.

.

6.2.2.2.3 $4O_3 + C_{30}H_{50} \rightarrow C_8H_{14}O + B$ *(liquid)*; $5O_3 + 5(C_8H_{14}O) \rightarrow 4(C_5H_8O_2) + C$ *(gas)*

Figure 6.19 shows the normalized concentration distribution for Ozone for the three ventilation cases studied where Ozone was delivered to the room through the ventilation system for Case 'c'. Again, the figure shows that Ozone concentration distributions do not exhibit well mixed behavior due to imperfect mixing, wall adsorption and chemical reactions. The Ozone concentrations vary throughout the room and BZ concentration values are *22*, *47* and *63 ppb* for Case 1, 2 and 3, respectively. The concentration of Ozone is largest near the ventilation system and is reduced in the regions of the room where mixing and volumetric reactions occur and there are large concentration gradients near the wall due to the surface adsorption. These patterns are similar for all three cases.

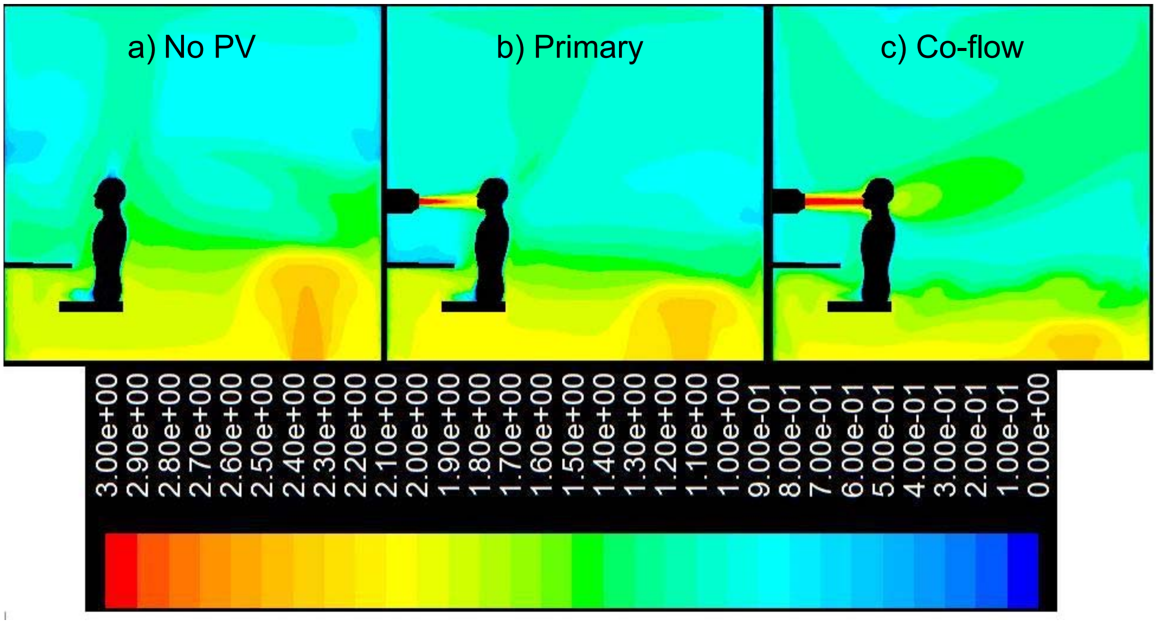

Figure 6.19: Normalized Ozone contours for Case 'c'.

Figure 6.20 shows the normalized concentration distribution for 6-MHO for the three ventilation cases. 6-MHO concentrations vary throughout the room and BZ concentration values are *25, 7* and *6 ppb* for Case 1, 2 and 3, respectively. The concentration of 6-MHO is largest near the body and the thermal plume transports 6-MHO away from the body. 6-MHO concentrations are reduced in the regions of the room where mixing occurs. These patterns are similar for all three cases. For the Co-flow PV system, the primary nozzle deliver only fresh air, Figure 6.20c shows the lowest concentration of 6-MHO near the primary nozzle of the PV system and extending to the BZ. Figure 6.20b shows a similar trend, however, the concentration of 6-MHO increases more rapidly toward the BZ for the primary PV system. Figure 6.20a shows the lowest concentration of 6-MHO exiting the floor diffuser for the case without PV.

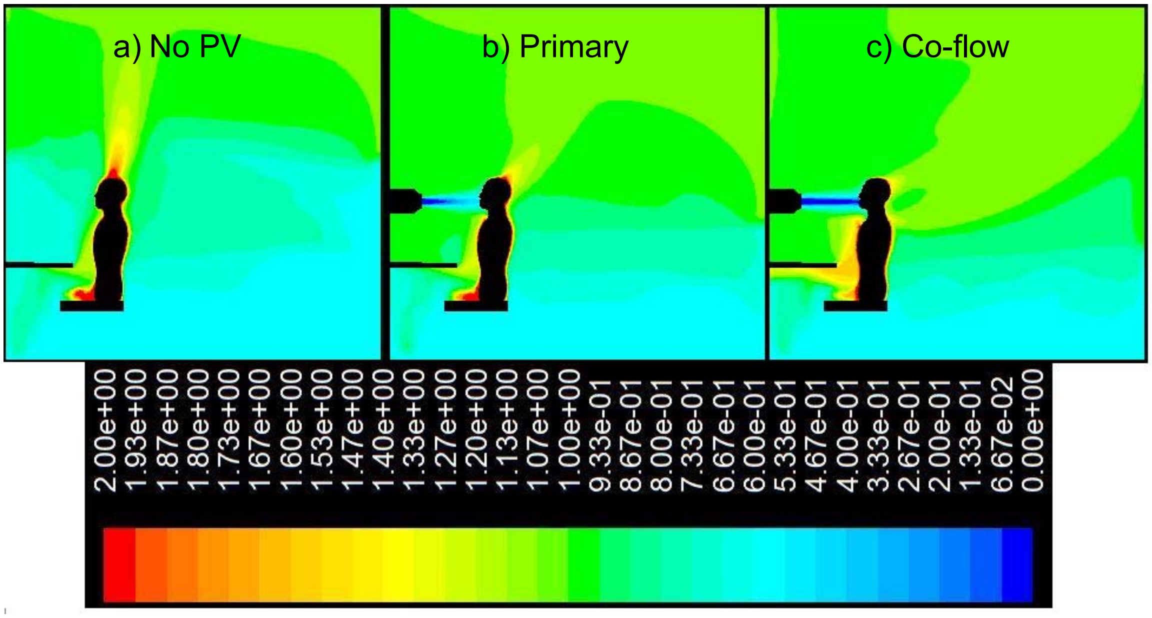

Figure 6.20: Normalized 6-MHO contours for Case 'c'.

Figure 6.21 shows the normalized concentration distribution for 4-OPA for the three ventilation cases. 4-OPA concentrations vary throughout the space and BZ concentration values are *6, 2* and *<1 ppb* for ventilation Case 1, 2 and 3, respectively. The volumetric reaction of Ozone and 6-MHO produced levels of 4-OPA an order of magnitude lower than their existing concentrations due to the ACH in the simulation. At lower air exchange rates there would be more time for the volumetric reaction to occur, resulting in higher 4-OPA concentrations. The concentration of 4-OPA is highest in the recirculation regions of the room. Recirculation zones allow more time for the volumetric reaction to occur, leading to elevated levels. This pattern is similar for all three cases.

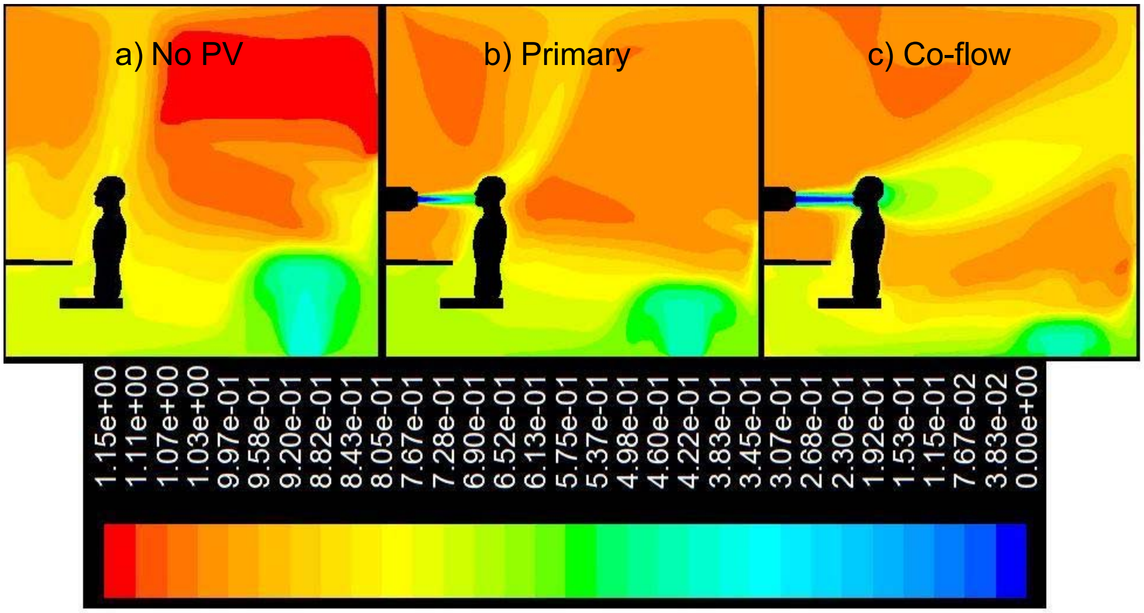

Figure 6.21: Normalized 4-OPA contours for Case 'c'.

Figure 6.22 shows the iF normalized with the well mixed condition for each species for the Co-flow, Primary and no PV cases when adsorption of Ozone, surface reactions between Ozone and Squalene and volumetric reactions with Ozone and 6-MHO were modeled. The results show that these species distribution do not exhibit well mixed behavior. It is shown that the iF can be more than or *~5* times lower than a case that assumes well mixed conditions. The Co-flow nozzle produces the highest levels of Ozone in the BZ which results in the highest iF, followed by the primary nozzle and no PV system. For 6-MHO and 4-OPA the trend is reversed. The Co-flow nozzle reduces the iF values by a factor of *~4*. For all three ventilation systems, iF results for 4-OPA are less than well mixed, due to the location of the source. Since 4-OPA is mostly created in the recirculated regions of the room airflow (away from the CSP BZ) only low levels are inhaled compared to what is released into the space.

Table 6.9 gives the removal ratios for ventilation, adsorption, surface and volumetric reaction for the three ventilation configurations. The removal ratio of Ozone in the first case (no PV system) was: *40 %* by ventilation, *47 %* by adsorption, 1*2 %* by surface reaction with Squalene and *1 %* by volumetric reaction with 6-MHO. The removal ratios with PV are very similar to the case without PV. Again, these results are in agreement with Pandrangi and Morrison (2008) where they estimated that a single occupant of a typical residential room was responsible for approximately 10% of the total ozone removal.

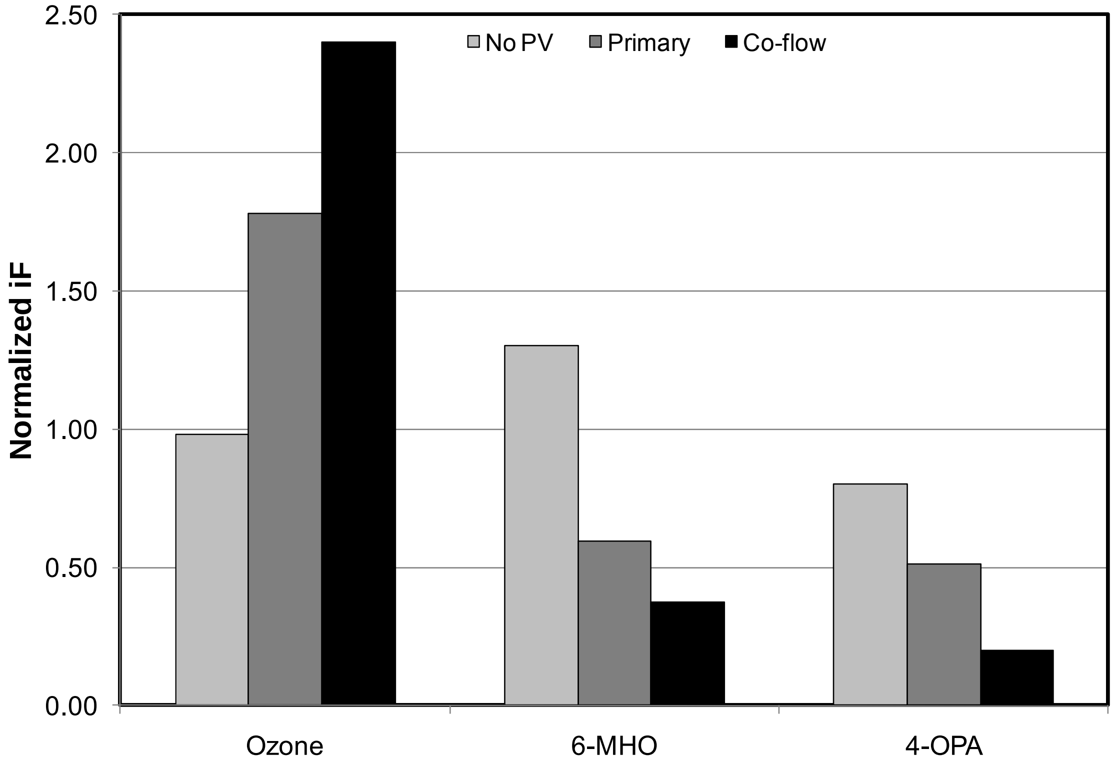

Figure 6.22: iF results for Case ‘c’.

Table 6.9: Ozone removal ratios for Case ‘c’.

		Removal Ratio (%)		
		No PV	Primary	Co-flow
Ozone	Ventilation	40	41	41
	Adsorption	47	47	45
	Surface Reaction	12	11	13
	Volumetric Reaction	1	1	1

6.2.2.2.4 Uniform vs. Non-uniform Squalene Distribution

Squalene is a major constituent in human skin oils; however, it is produced unevenly by the body. Squalene is more prevalent in the oils on the face, ears and scalp than the rest of the body. Based on this, the effect of an uneven distribution of Squalene on Ozone removal and product creation was found in Case ‘d’. For this comparison, Squalene was only covering the neck and head of the CSP for Case ‘d’ instead of the entire body and all other simulation conditions remained the same.

Figure 6.23 shows the normalized concentration distribution for Ozone for the three ventilation cases studied where Ozone was delivered to the room through the ventilation system for Case ‘d’. In this figure, the contours show a lower Ozone concentration gradient in the room. However, the lower concentration gradients for Case ‘d’ are misleading; the contours appear to have lower levels of Ozone (less red) in the space than Case ‘a’, ‘b’ and ‘c’, but this is not the case. Because there are less surface reactions with Squalene, less Ozone is being removed through surface reactions resulting in lower gradients (the exhaust concentration value is closer to the ventilation concentration). This change in Squalene distribution results in Ozone BZ concentration values are *33*, *50* and

67 ppb for Case 1, 2 and 3, respectively. The concentrations of Ozone follow the same pattern as Case ‘a’, ‘b’ and ‘c’.

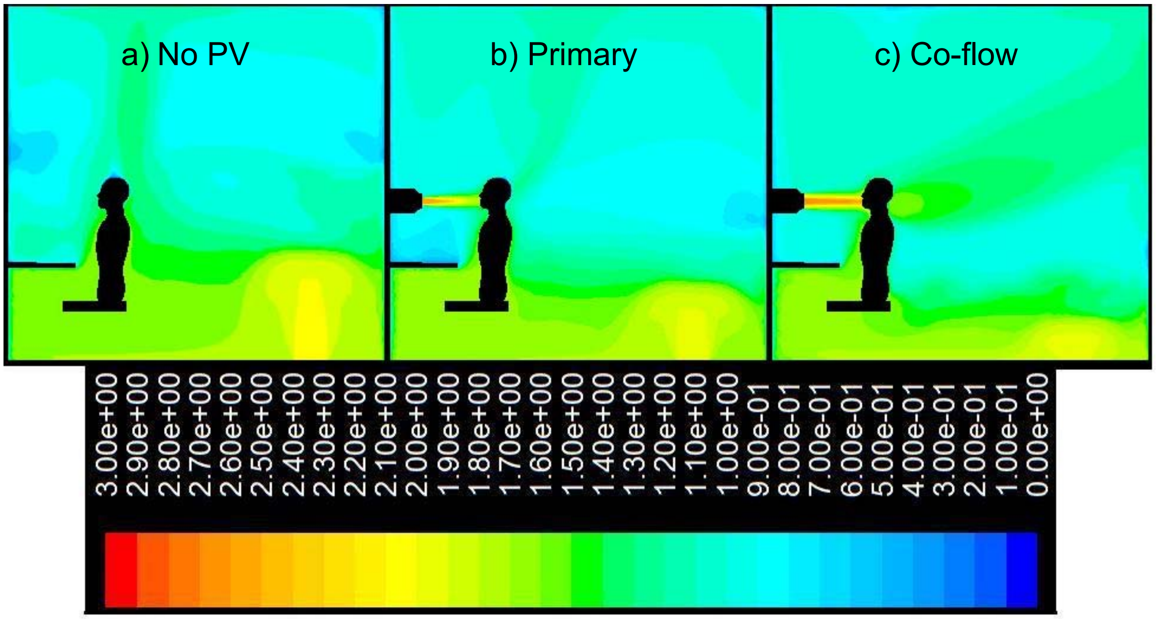

Figure 6.23: Normalized Ozone contours for Case ‘d’.

Figure 6.24 shows the normalized concentration distribution for 6-MHO for the three ventilation cases. The figure shows that 6-MHO concentration distributions do not exhibit well mixed behavior due to imperfect mixing, wall adsorption and chemical reactions as in Case ‘a’, ‘b’ and ‘c’. For Case ‘d’, the contours show the highest levels of 6-MHO around the head and it is important to note that there is no gradient of 6-MHO in the thermal plume below the neck level. That is, there is no high concentration gradient where most inhaled air originates from. 6-MHO BZ concentration values are *19, 7* and *6 ppb* for Case 1, 2 and 3, respectively which is lower than Case ‘a’, ‘b’ and ‘c’. The differences in Figure 24a, b and c follow the same pattern as Case ‘a’, ‘b’ and ‘c’.

Figure 6.25 shows the normalized concentration distribution for 4-OPA for the three ventilation cases. 4-OPA concentrations show the same trend as Case 'c' and BZ concentration values are *2, 1* and <*1 ppb* for Case 1, 2 and 3, respectively. The change in BZ concentration levels is due to the decrease in Squalene/Ozone surface reactions. The volumetric reaction of Ozone and 6-MHO produced levels of 4-OPA an order of magnitude lower than their existing concentrations. The concentration of 4-OPA is highest in the recirculation regions of the room. Recirculation zones allow more time for the volumetric reaction to occur, leading to elevated levels. This pattern is similar for all three cases.

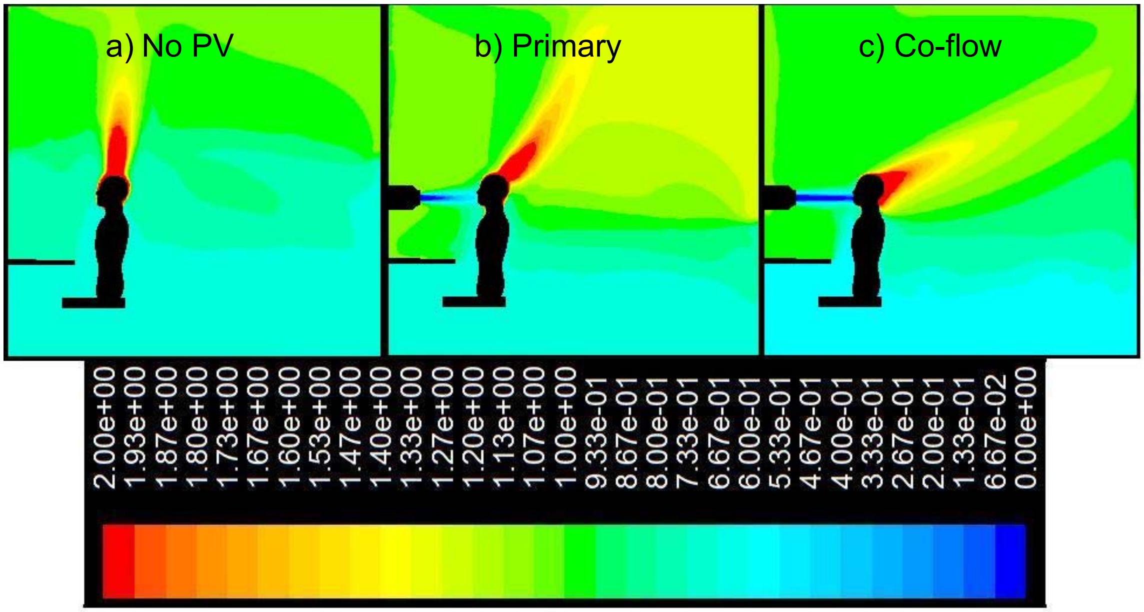

Figure 6.24: Normalized 6-MHO contours for Case 'd'.

Figure 6.26 shows the iF normalized with the well mixed condition for each species for the Co-flow, Primary and no PV cases when adsorption of Ozone, surface reactions between Ozone and Squalene on the neck and head region and volumetric reactions with

Ozone and 6-MHO were modeled. It is shown that the iF can be ~2.5 times higher or more than or ~*5* times lower than a case that assumes well mixed conditions. The Co-flow nozzle produces the highest levels of Ozone in the BZ which results in the highest iF, followed by the primary nozzle and no PV system. For 6-MHO and 4-OPA the trend is reversed. The Co-flow nozzle reduces the iF values by a factor of ~3-*4*. For all three ventilation systems, iF results for 4-OPA are less than well mixed, due to the location of the source. Since 4-OPA is mostly created in the recirculated regions of the room airflow (away from the CSP BZ) only low levels are inhaled compared to what is released into the space.

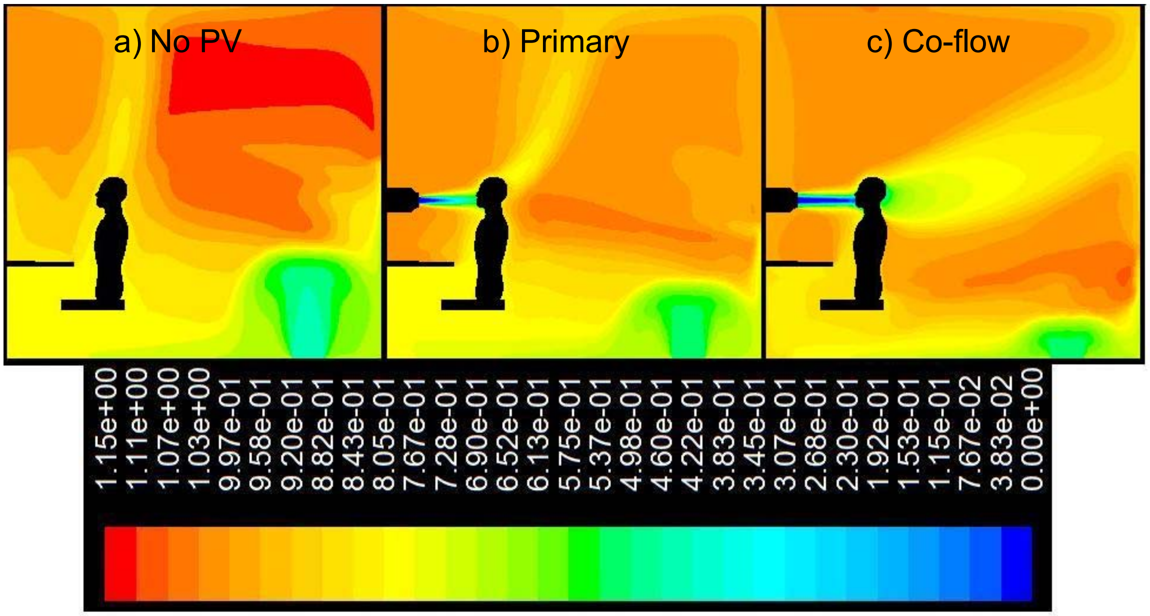

Figure 6.25: Normalized 4-OPA contours for Case 'd'.

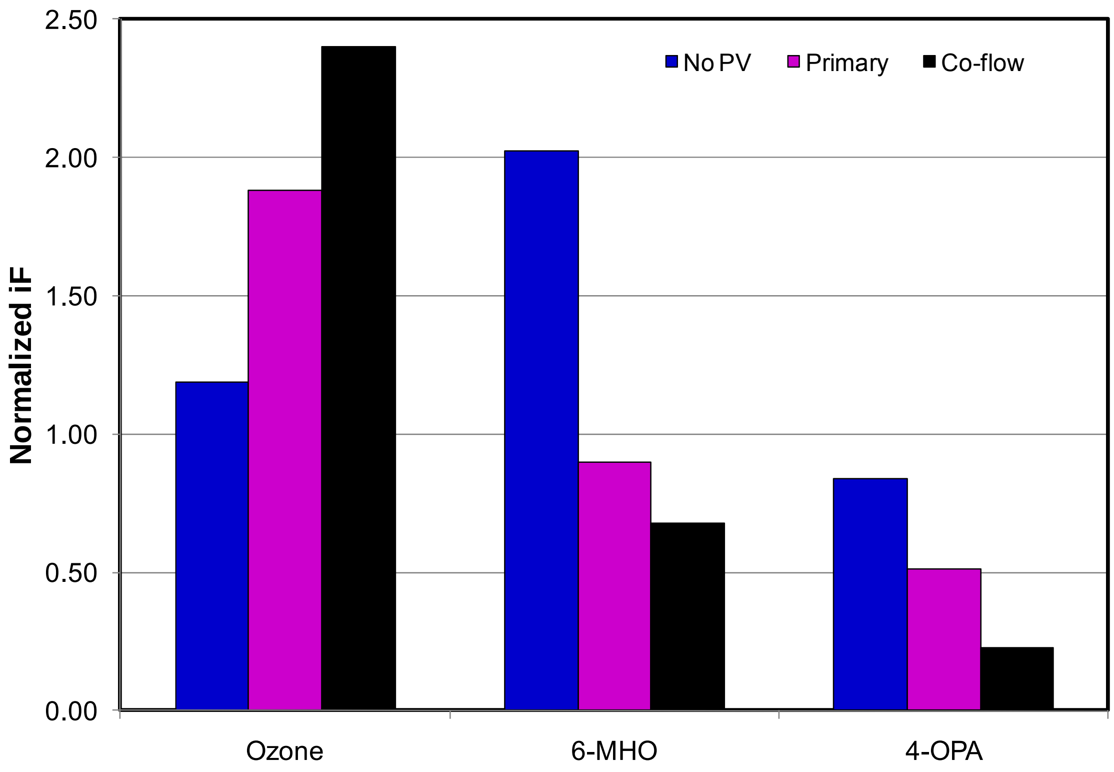

Figure 6.26: iF for Case ‘d’.

6.2.3 PV with Ozone Filter

PV has been shown to be beneficial in many situations throughout this work. With the addition of PV to a space comes the opportunity of additional benefits besides delivering fresh air to the BZ. Ozone filters can be very effective at removing Ozone from ventilation air and implementing one into the PV duct can add significant benefits to the system. Activated carbon filters are one of many types of Ozone filter that could be used and it has been shown that these filters can remove up to 98% of Ozone from the air initially (Lee and Davidson, 1999). The removal rate decreases with constant exposure to Ozone over time, but when removed from Ozone-laden air the removal percentage will increase again. It has shown that over long periods of time, activated carbon filters will remove ~85% of Ozone (Lee and Davidson, 1999; Metts and Batterman, 2006; Zhao et al., 2007; Shelton et al., 2008). To study this extra benefit, Case 'c' was simulated with an 85% reduction in Ozone concentration levels in the PV ducts for Case 'e'. Placing the filters in the PV systems only is practical application since filters would not have to be positioned in all the ductwork into the room and no modifications to existing ductwork would have to be made.

Figure 6.27 shows a comparison of Ozone distribution for a Case 'c' without a filter and Case 'e' with an Ozone filter. For both cases the contours are normalized with the well mixed condition of Case 'c' for comparison purposes where a value of 1 represents well mixed for Case 'c'. Decreases in concentration levels for Case 'e' are improvements over Case 'c' due to the use of the Ozone filter. From Figure 6.27 there is significant enhancement with the use of an Ozone filter in the PV system regarding Ozone levels in the room. More notably, the Ozone levels near the BZ are greatly improved, and it is apparent that the Co-flow PV system benefits more from the filter since more Ozone passes through the system. BZ concentration levels of *50* (Primary) and *67 ppb* (Co-flow) from Case 'c' are improved to *13* (Primary) and *7 ppb* (Co-flow) for Case 'e'. This is a significant reduction in the BZ levels of Ozone For the case without PV, there would be no change in concentrations levels in the BZ since there is no Ozone filter added to the system.

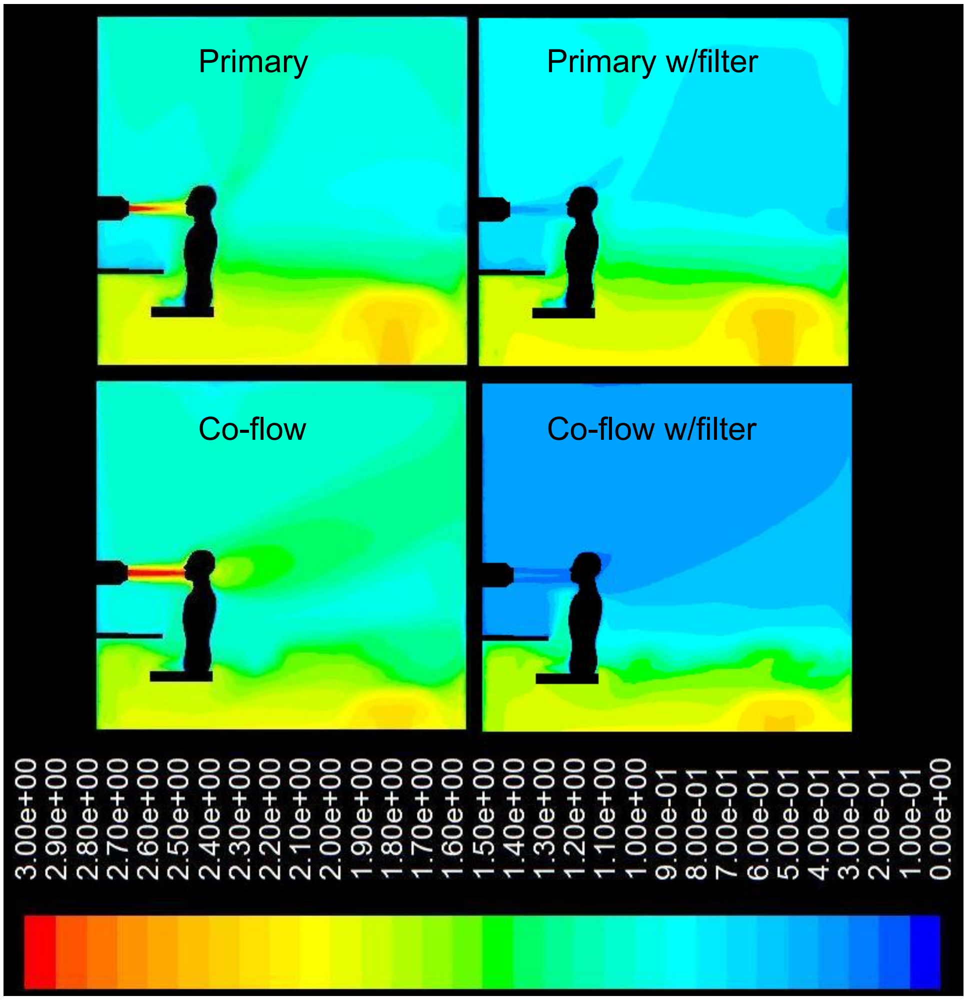

Figure 6.27: Ozone contours for Case ‘c’ and ‘e’ normalized with the well mixed assumption of Case ‘c’.

Figure 6.28 shows a comparison of 6-MHO distribution for a Case C without a filter and Case E with an Ozone filter. For both cases the contours are normalized with the well mixed condition of Case ‘c’ for comparison purposes where a value of *1* represents well mixed for Case ‘c’. Decreases in 6-MHO concentration levels for Case ‘e’ are improvements over Case ‘c’ due to the use of the Ozone filter. From Figure 6.28 there is significant improvement with the used of an Ozone filter in the PV system. More remarkably, the 6-MHO levels near the BZ are greatly improved. With the reduction of

Ozone entering the office space, there are fewer reactions occurring at the CSP surface resulting in less 6-MHO production. The contours show a vast reduction in the concentration gradient near the body of the CSP where inhaled air originates from. For the case without PV, there would be no change in concentrations levels in the BZ since there is no Ozone filter added to the system.

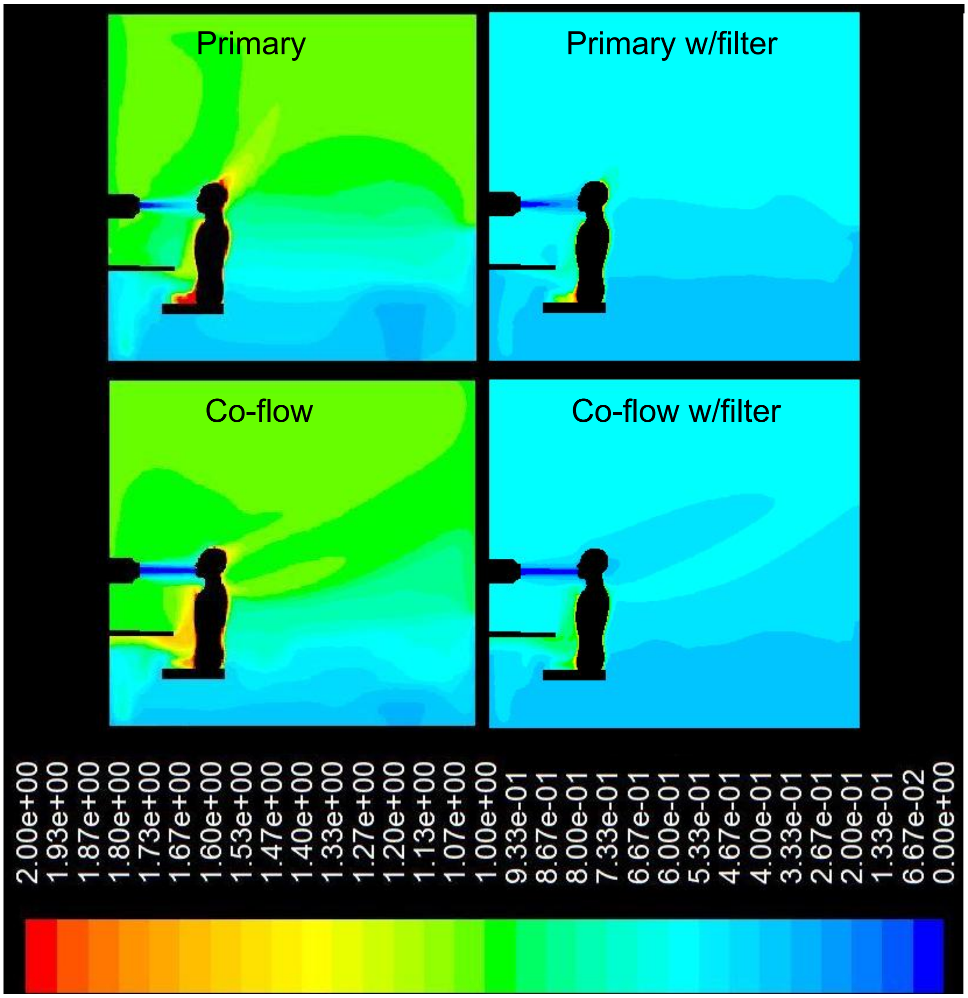

Figure 6.28: 6-MHO contours for Case ‘c’ and ‘e’ normalized with the well mixed assumption of Case ‘c’.

Figure 6.29 shows Case ‘e’ iF normalized with the well mixed condition (from Case ‘c’) for each species for the Co-flow, and Primary cases when adsorption of Ozone, surface reactions and volumetric reactions with Ozone and 6-MHO were modeled with an Ozone filter. It is shown that the iF can be ~5 times lower than a case that assumes well mixed conditions. The Co-flow nozzle produced the highest levels of Ozone for Case ‘c’; however this is drastically reduced for Case ‘e’ with an Ozone filter and actually delivers the lowest levels of ozone to the BZ. This is a significant benefit of adding an Ozone filter to PV systems. In fact, the Ozone filter not only lowers levels of Ozone in the BZ it also lowers the levels of harmful products. Figure 6.29shows a decrease in iF for 6-MHO with the addition of an Ozone filter.

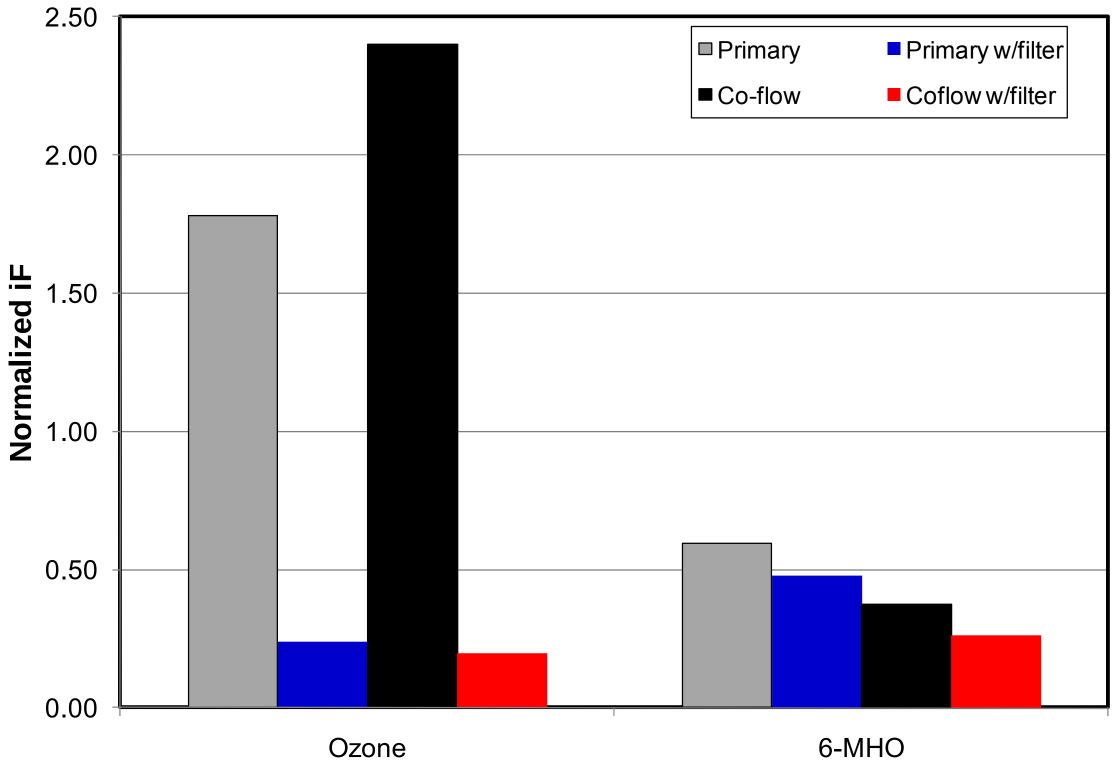

Figure 6.29: iF for Case ‘c’ and ‘e’ normalized with the well mixed assumption of Case ‘c’.

6.2.4 Comparison of Cases

In Section 6.2 there were many cases studied involving Ozone and Squalene and their resulting products. To examine the results from Case ‘a’, ‘c’, ‘d’ and ‘e’ more closely, comparisons of iF for each species were made. Figure 6.30 shows the Ozone comparison for the different cases. Case ‘a’ and ‘c’ show very similar results as expected. Without PV, the increase for Case ‘d’ was due to an increase in the amount of Ozone inhaled. For Case ‘d’, Ozone is only reacting on the neck and head of the CSP; therefore less Ozone is removed from the thermal plume creating higher levels of Ozone in the inhalation region. This effect decreases with the use of PV because high levels of Ozone were already being delivered to the BZ. This figure also shows a considerable decrease in iF for the two PV systems for Case ‘e’. The use of a PV Ozone filter significantly reduces the amount of Ozone in the BZ, with a greater decrease shown for the Co-flow PV system.

Figure 6.31 shows the 6-MHO comparison for the different cases. Case ‘a’ and ‘c’ show very similar results as expected. Without PV, the increase for Case ‘d’ was due to a decrease in the denominator that defines iF. For Case ‘d’, Ozone is only reacting on the neck and head of the CSP; therefore less 6-MHO is released into the indoor environment, but it is being emitted directly in the CSP BZ. This results in the ratio of inhaled 6-MHO to released 6-MHO to increase. This effect is also shown for the two PV systems. The use of a PV Ozone filter slightly decreased the iF for Case ‘e’. The use of a PV Ozone filter significantly reduces the amount of Ozone in the BZ which decreased the amount of 6-MHO created in the BZ resulting in a lower iF.

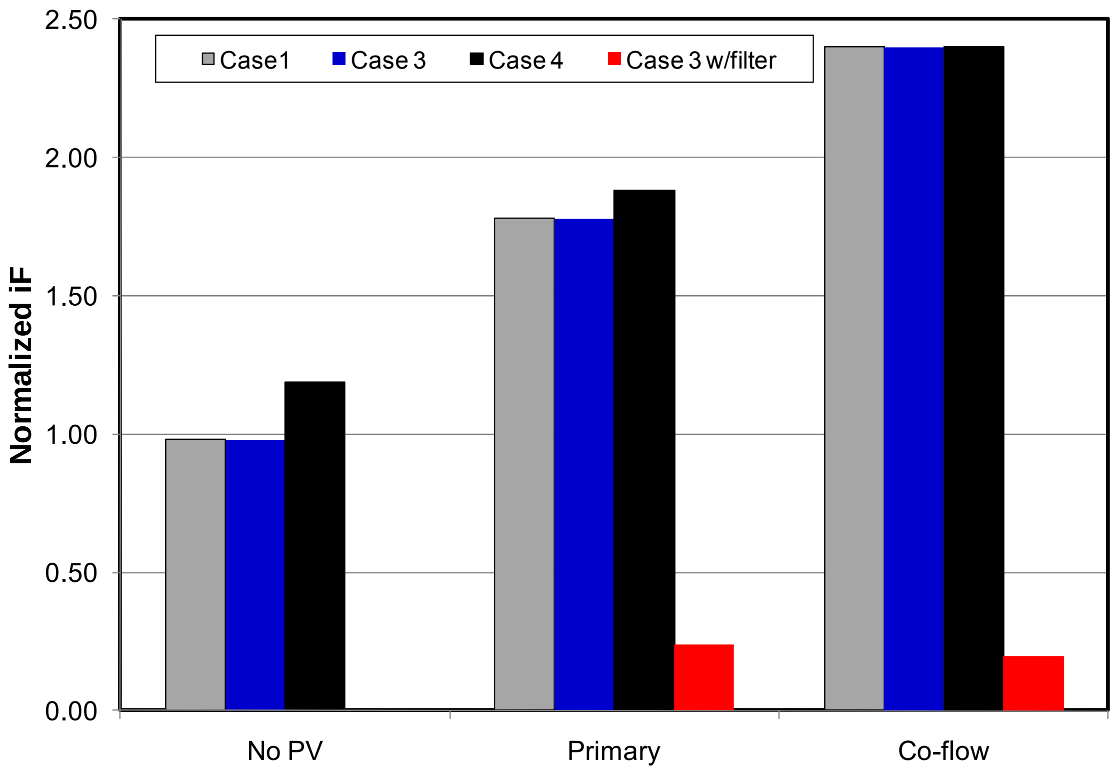

Figure 6.30: Comparison of Ozone iF.

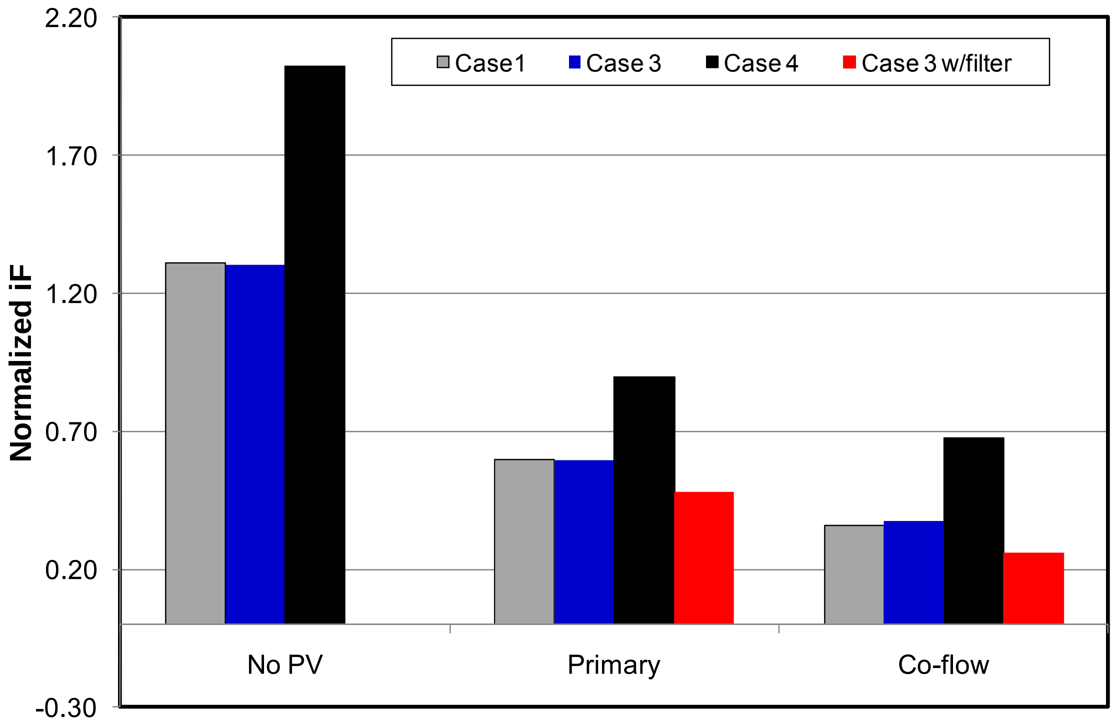

Figure 6.31: iF for 6-MHO comparison.

Figure 6.32 shows a comparison of 4-OPA for the cases studied. This figure shows no significant changes in the 4-OPA results. The source (volumetric reaction of Ozone and 6-MHO) of 4-OPA was mainly in recirculation regions away from the BZ and the changes made for each case had little effect on the overall iF of 4-OPA.

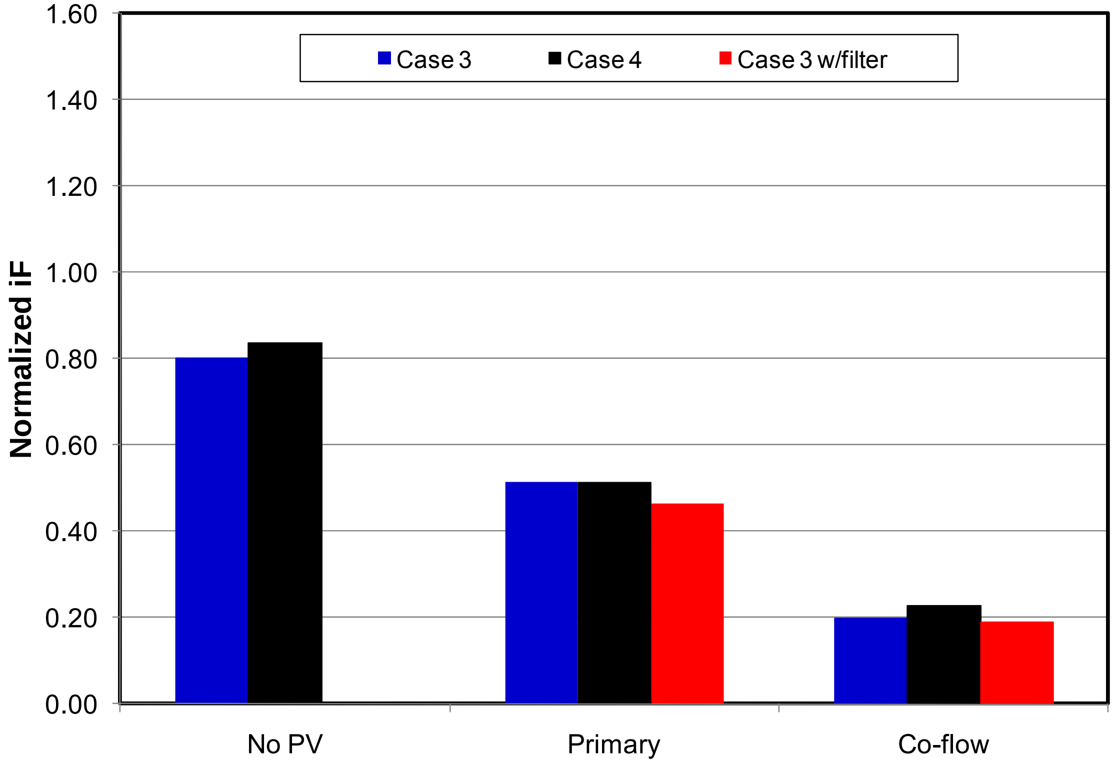

Figure 6.32: iF for 4-OPA comparison.

6.2.5 Section Conclusions

A 3D CFD model that accounts for surface reactions was validated with experimental results of Rim et al. (2009). The results show that our model agrees reasonably well with the experimental data with errors ranging from 4-10%, which is well within the experimental uncertainty. The CFD model was able to predict Ozone deposition velocity in the test chamber accurately and can be used as a reliable tool to optimize the design and placement of PV systems, and to investigate chemically reacting flows more cost-effectively and faster than laboratory testing.

The validated 3D model from Section 4 was improved to computationally investigate the complex chemically reacting flow patterns in the personal microenvironment of a detailed CSP with wall adsorption of Ozone and the surface reaction of Ozone and Squalene on the human skin in a typical office space. The results show that, for each case and for each species, the concentration distribution is not well mixed with noteworthy variations in the species distributions at different locations in the room. Imperfect mixing, concentration variations leading to different reaction rates at different locations in the room and the age of air is different at different locations in the room which allows more time for volumetric reaction to occur are the cause of the high non-uniformity. For circumstances where indoor sources or chemical reactions are present in the indoor environment, assuming well mixed distributions can lead to significant over or under prediction of inhalation exposure.

When comparing the three ventilation configurations, the Co-flow nozzle is superior at removing 6-MHO and 4-OPA concentrations from the inhalation air than the single jet PV system and both PV systems are superior to the configuration without PV. With the exception of Case ‘e’, the opposite trend is shown for Ozone. Case ‘e’ shows extended possible benefits of PV systems, and the results show that the use of an Ozone filter in the

PV system can decrease the Ozone concentration levels in the room while simultaneously decreasing the reaction products in the BZ. The reduction of oxidation products in the BZ from the use of PV is a significant result because the reaction products have been shown to be more irritating than there precursors.

6.3 *Chapter Conclusions*

The work in this chapter improves the CFD model from Section 4 to be able to accurately predict typical indoor chemical reactions. Chemical reactions can have a significant effect on indoor concentration levels by decreasing or increasing pollutant levels and producing products that would not be otherwise present. A validated computational model that can accurately predict chemical reactions is a significant accomplishment since experimentally modeling detailed chemical reactions in the indoor environment is complex and expensive. This validated model can explore other PV nozzle configurations and orientations, ventilation arrangements, and the effect of the presence of other objects and contaminant sources in the occupied space on BZ air quality more feasibly than experimental modeling.

7 Conclusions

The two main objectives of this work were to create a validated computational model for chemically reacting flows and to use this model to assess PV in a typical office space while modeling indoor chemical reactions between Ozone and Terpenes. When assessing PV, key developments were made.

1. It has been shown that PV is advantageous over conventional ventilation systems when analyzing inhaled air quality. Beyond that, the Co-flow nozzle exhibited superior performance and robustness over a single jet PV system. Chapter 4 details the two PV systems studied and the results show that the Co-flow PV system can deliver more than double the air quality in the BZ than a conventional single nozzle at clean air supply rate as low as *2.4 l/s*. This is an important finding in the sense that the air quality in the BZ of an occupant can be close to 100% fresh air at a fraction of the required fresh air supply by ASHRAE standard 62.1-2004. Also, the Co-flow nozzle maintains advantageous with slight temperature changes, with an increase or decrease in flow rate and over a range of different clothing and skin moisture values as shown in Chapter 5. Another advantage to PV is, unlike the general ventilation system whose inhaled air quality depends strongly on the location of the pollutant source, the inhaled air quality achieved by the two PV systems investigated are relatively insensitive to

the pollutant source location (not including sources within the PV system). This finding broadens the applicability of the results to other situations when considering the risk factor of pollutants.

2. PV can be implemented in an ergonomic and aesthetically pleasing way while improving air quality delivered to an occupant of a typical office space and supplying satisfactory quality air to the rest of the space. Chapter 5 shows that PV improves the air quality for a person seated in front of the PV system without severely changing the air quality for others that may periodically occupy the space. In addition, cross contamination between an occupant with and an occupant without PV is not a major concern in a typical office setup. Lastly, PV has been shown to be beneficial even when implemented in realistic and practical setups. The use of the Corner Co-flow PV configurations is a sensible PV configuration for a typical office cubicle that is able to deliver better air quality to the BZ than the Primary or no PV system, while enlarging the area to which it is delivered compared to the Baseline Co-flow PV system. These findings combat common misconceptions of the feasibility and implementation of PV across the field.

3. For the cases studied, it was found that well mixed behavior is not exhibited and should not be assumed for inhalation air quality in the indoor environment. This finding is even more apparent in cases dealing with high velocity and concentration gradients that are developed by the use of PV and/or when indoor

> sources or chemical reactions are present. It has been shown that for situations where indoor sources or chemically reacting flows are present in the indoor environment, like the one outlined in this work, assuming the concentration distributions are well mixed can lead to significant over or under prediction of inhalation exposure. It is common practice to assume well mixed conditions in the indoor environment and the conclusions of this work strongly oppose this assumption.

Not only are the results of the PV assessment study significant to this line of work, but also, the validated computational model is momentous on its own. Although there are several studies that use CFD to investigate the indoor environment, there has not been a complete study that examines and validates a computational model with chemical reactions in a typical indoor office space. The validated computational model can further be used to investigate other indoor configurational and exposure scenarios easily and cost effectively to examine indoor interactions to a greater depth. Along with the validated model, several contributions were produced from the validation process.

1. A new method of specifying a pollutant mass flux at a wall was introduced. Before this work, there was no direct way of specifying a species mass flux in Fluent. A *Fictitious Surface Reaction Method* was developed where a pollutant mass flux at the surface can be created by introducing a *fictitious* surface reaction that converts "air" into a pollutant at the wall. This method allows the user to specify the thermo-physical properties of the emitted species, not just the

diffusion coefficient as required by other methods which enables the user to solve the species transport equations as a coupled (or an uncoupled) set, along with the continuity, momentum and energy equations. This method also allows the inclusion of the full density effect when buoyancy is present, and not resort to the simplified Boussinesq approximation and its well known pitfalls. In addition, it allows the straightforward inclusion of surface or volume chemical reactions of the pollutants with other species such as ozone.

2. When modeling the indoor environment, certain computational parameters showed to be detrimental to the validation results and cannot be ignored or simplified. These included grid resolution, CSP geometry, the inclusion of radiation effects and far field BCs. The grid resolution in the indoor environment is key for reliable and accurate results. The validation process has shown that too coarse of a grid can result in the under prediction of the strength of the thermal plume and could lead to incorrect deflection of PV jets that interact with the thermal plume. This effect becomes even more significant when dealing with low momentum jets. The validation process also reinforced the notion that a detailed CSP geometry must be used for precise simulations. Using a simplified CSP geometry may overestimate or underestimate the predicted inhaled iF by more than a factor of 2, depending on the source location relative to the occupant and the supply air diffuser. The results show that there is a significant dependence on the wall thermal BC's and determining the correct thermal BC on the body is not enough when dealing with radiation and modeling the effects of

radiation is needed for accurate results. This work has demonstrated that it is important to handle all BCs with care, not just near field BCs, in order to properly simulate cases involving strong interactions between PV jets and the thermal plume.

3. In contrast, this work also outlined a few computational simplifications that can be made when modeling the indoor environment including simplified breathing methods, skin wittedness and simplifying radiation modeling. It was found that adding complex, realistic features, such as unsteady breathing or sweating, to a CFD model of the BZ of a CSP does not improve the inhaled air quality results of the solution. For the five breathing methods compared in Chapter 5, no significant differences were found between them and it is recommended that steady state inhalation should be used as the modeled breathing method since it does not increase the complexity of the simulation compared to unsteady methods and makes post processing easier compared to using a presumed volume of air method. It is understood that modeling breathing is necessary when studying re-inhaled air and for the transport of exhaled contaminants between people, neither of which were studied in this work. The results show that simplified modeling of the thermal BC's can account for radiation effects and in situations where modeling radiation is difficult, modeling surface temperatures is shown to be easily implemented and gives very similar results compared to modeling radiation.

While this work has shown success in the study and use of PV for a typical office setup, it highlights certain issues that would provide useful for continuing work. First, the domain used for this study consisted of minimalistic detail. The effect of the inclusion of other indoor furniture and appliances, specifically other indoor heat sources (computers and lighting), should be determined. Also, the thermal BCs on the CSP were considered to be ideal, that is, the temperature on the CSP surface was always modeled as uniform. This is not the case and, along with modeling other heat sources in the space, could alter some of the conclusions found in this work.

With the promise of PV shown for a typical office space, studying the benefits in additional indoor scenarios is encouraged. In other settings with stationary occupants, like auditoriums, theaters, call centers, busses, etc, the benefits could be significant and the use of PV is appropriate. Exploring other possible applications of PV will broaden its function and widen its acceptance in the indoor ventilation community.

Appendix A: 2D Jet Study to Determine Grid Size

In order to determine the grid strategy in the jet region, 2D jet calculations were modeled to determine the level of grid refinement in this region needed to capture the jet characteristics. The computational domain that was used for this work is shown in Figure A.1. Four computational grids were created to evaluate the effects of grid clustering and grid topology on the jet spreading rate as shown in Figure A.2. The four grids had 10 cells across the inlet radius, two were structured grids and two were unstructured grids. A distinction was made between a uniform grid vs. a clustered grid at the jet shear layer. The trials were run using the Realizable *k-ε* model (Shih et al., 1995) with *2.0 %* turbulent intensity and a *1 mm* length scale. The inlet velocity profile was a "top-hat" profile with a velocity magnitude of *~1 m/s*, yielding a Reynolds number of *~3,400* for the nozzle studied here.

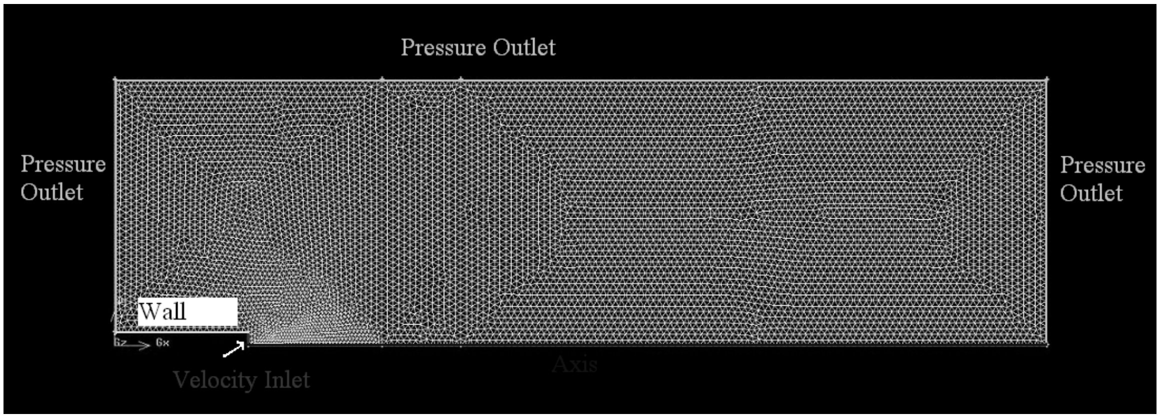

Figure A.1: Computational domain.

The resulting velocity contours are shown in Figure A.3. From this figure, only differences in the far field velocity can be seen and these differences are only slight. To examine these results further, the jet spread and centerline velocity decay were determined. Jet spread is defined as,

$$\frac{r(1/2)}{d} = S(\frac{x}{d})$$

and is found by determining the slope of a r(1/2)/d vs. x/d plot. The spread rates for the 4 cases are shown in Figure A.4. Figure A.4 shows the jet spread for different x/d based on the region of concern for PV studies. A person is typically located approximately *40 cm* from the PV nozzle which results in an x/d of *8* for the diameter tested. This region is extended to an x/d of *20* and *25* to be thorough.

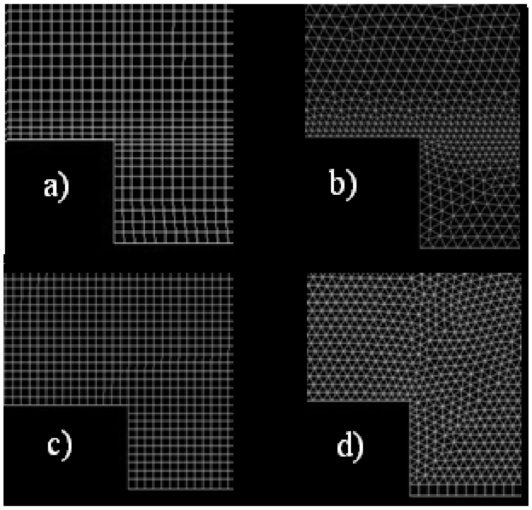

Figure A.2: Grid spacing across jet inlet a) Structured Clustered, b) Unstructured Clustered, c) Structured Uniform, and d) Unstructured Uniform.

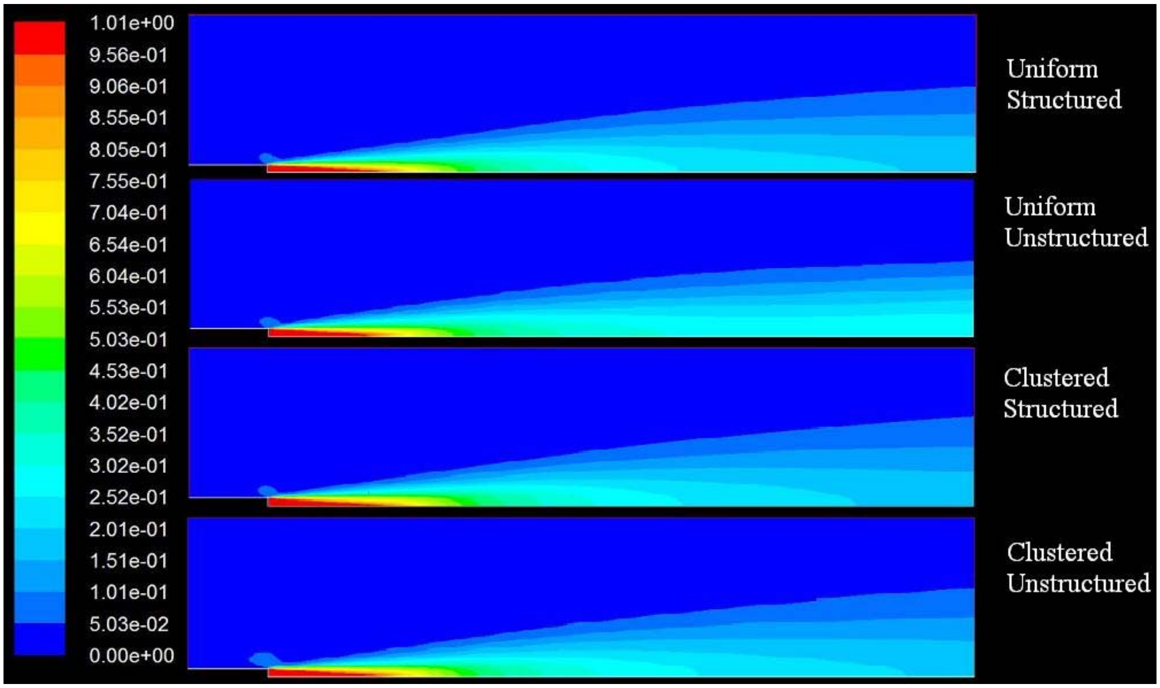

Figure A.3: Velocity Contours for the 4 grids studied.

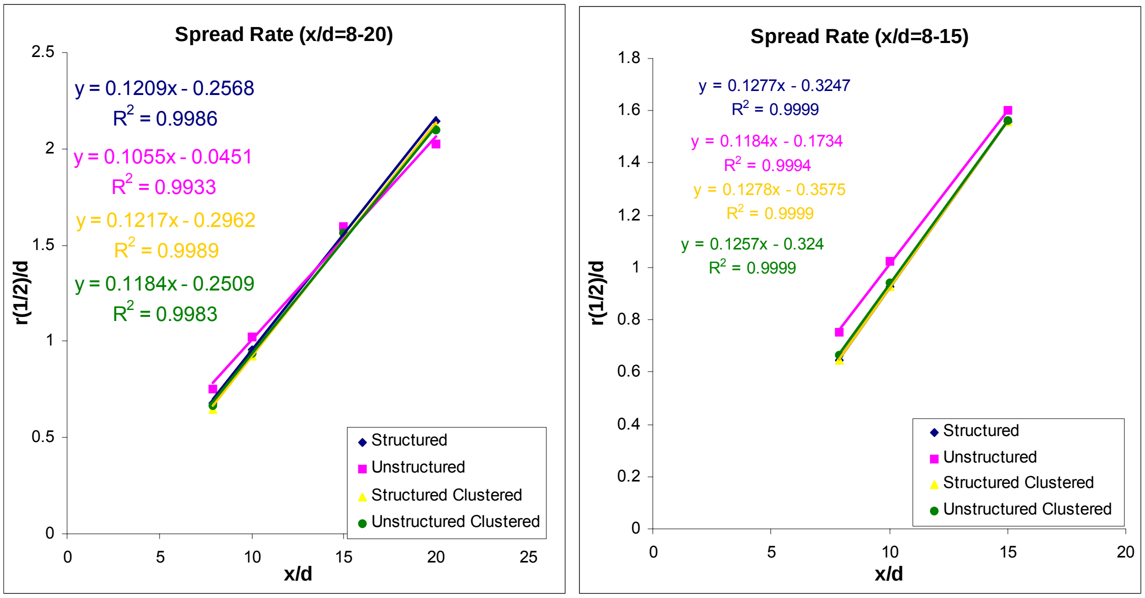

Figure A. 4: Jet spread rate for 2D jet.

The centerline velocity decay was also examined. Centerline velocity decay is defined as,

$$\frac{U_x}{U_o} = B(\frac{d}{x})$$

and can be found by determining the slope of a U_x/U_o vs. x/d plot. Figure A.5 shows the centerline velocity decay for an x/d of 20 and 25 to be thorough. All values for the jet spread rate (S) and centerline velocity decay (B) fall within the range of reported values given by Mi et al. (2001) and Malmstrom et al. (1997) as summarized in Table A.1. The obvious grid strategy would be to cluster the grids at the interface between the jet outer diameter and the surrounding air. However, since our problem involves relatively low-momentum jets interacting with a heated solid boundary (the manikin) in the presence of a rising thermal plume, the jet deflection can be large and hence the trajectories of the jets are unknown. For this reason, it was decided that a uniform mesh should be used in the mixing region between the PV jet and the manikin's face.

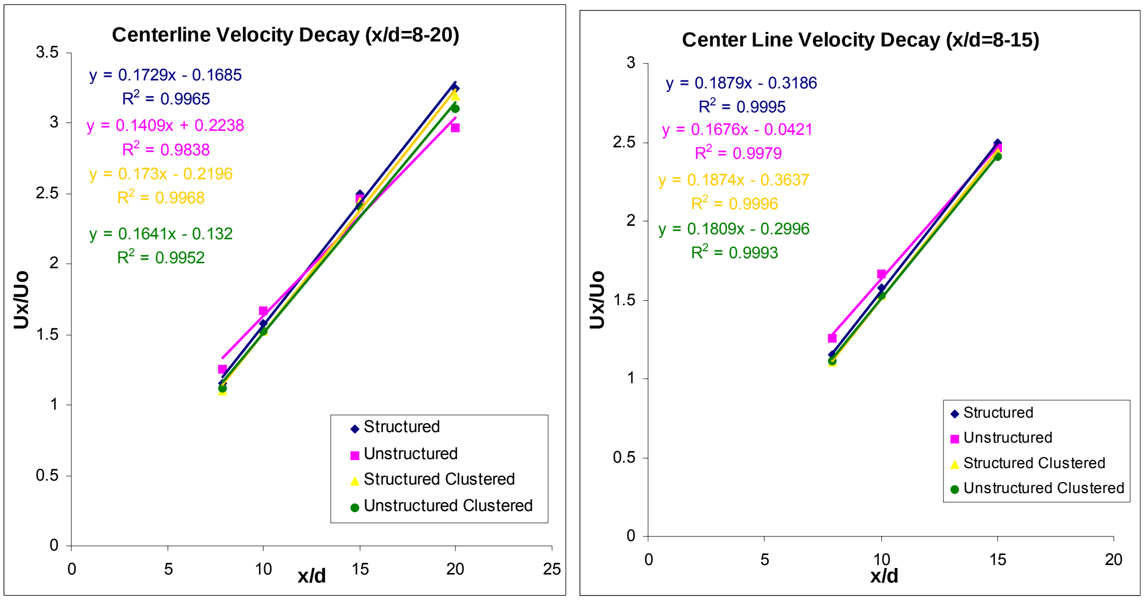

Figure A.5: Centerline velocity decay for 2D jets.

Table A.1: Corresponding jet spread rate (S) and centerline velocity decay (B) for each grid strategy.

	D (m)	Re	S	B	x/d
a	0.0508	3400	0.128	5.34	8-15
b	0.0508	3400	0.126	5.53	8-16
c	0.0508	3400	0.128	5.32	8-17
d	0.0508	3400	0.118	5.97	8-18

Appendix B: Graphs as Tables

For future comparison purposes validation profiles are listed as tables.

Table B.1:Primary Validation Experimental Cases

Primary Jet Temp., °C		23.5		23.5		20.0		26.0		23.5
Profile Distance from Nose, mm		10.0		25.0		10.0		10.0		10.0
Primary Nozzle Air Flow, l/s		2.40		2.40		2.40		2.40		2.40
Secondary Nozzle Air Flow, l/s		0.00		0.00		0.00		0.00		0.00
Nose Distance from Nozzle, m		0.41		0.41		0.41		0.41		0.41
	AQI		AQI		AQI		AQI		AQI	
		Primary 1S		Primary 2S		Primary 3S		Primary 4S		Primary 5S
	-0.116	-3.500	-0.114	-3.500	-0.096	-3.500	-0.108	-3.500	-0.149	-3.500
	-0.124	-3.303	-0.116	-3.303	-0.096	-3.303	-0.100	-3.303	-0.138	-3.303
	-0.136	-3.106	-0.104	-3.106	-0.092	-3.106	-0.103	-3.106	-0.149	-3.106
	0.364	-0.500	0.264	-0.500	0.307	-0.500	0.205	-0.500	0.448	-0.500
	0.454	-0.402	0.315	-0.402	0.251	-0.402	0.335	-0.402	0.483	-0.402
	0.431	-0.303	0.259	-0.303	0.316	-0.303	0.364	-0.303	0.514	-0.303
	0.406	-0.205	0.292	-0.205	0.322	-0.205	0.359	-0.205	0.544	-0.205
	0.400	-0.106	0.420	-0.106	0.312	-0.106	0.313	-0.106	0.541	-0.106
	0.292	2.500	0.233	2.500	0.285	2.500	0.297	2.500	0.254	2.500
	0.286	2.598	0.222	2.598	0.233	2.598	0.282	2.598	0.246	2.598
	0.297	2.697	0.157	2.697	0.241	2.697	0.281	2.697	0.171	2.697
	0.303	2.795	0.172	2.795	0.248	2.795	0.282	2.795	0.188	2.795
	0.249	2.894	0.193	2.894	0.208	2.894	0.263	2.894	0.137	2.894
	-0.030	5.500	-0.005	5.500	-0.023	5.500	0.016	5.500	-0.140	5.500
	-0.030	5.697	-0.007	5.697	0.022	5.697	-0.010	5.697	-0.066	5.697
	0.000	5.894	0.002	5.894	0.004	5.894	0.005	5.894	-0.153	5.894
	-0.096	-4.000	-0.114	-4.000	-0.092	-4.000	-0.108	-4.000	-0.129	-4.000
	-0.116	-3.803	-0.115	-3.803	-0.097	-3.803	-0.100	-3.803	-0.117	-3.803
	-0.123	-3.606	-0.106	-3.606	-0.097	-3.606	-0.101	-3.606	-0.124	-3.606
	0.216	-1.000	0.141	-1.000	0.139	-1.000	0.162	-1.000	0.322	-1.000
	0.239	-0.902	0.126	-0.902	0.212	-0.902	0.141	-0.902	0.341	-0.902
	0.233	-0.803	0.130	-0.803	0.220	-0.803	0.120	-0.803	0.408	-0.803
	0.298	-0.705	0.179	-0.705	0.219	-0.705	0.188	-0.705	0.421	-0.705
	0.267	-0.606	0.265	-0.606	0.201	-0.606	0.190	-0.606	0.450	-0.606
	0.369	2.000	0.327	2.000	0.356	2.000	0.401	2.000	0.354	2.000
	0.337	2.098	0.297	2.098	0.361	2.098	0.380	2.098	0.328	2.098
	0.321	2.197	0.326	2.197	0.308	2.197	0.334	2.197	0.278	2.197
	0.326	2.295	0.298	2.295	0.305	2.295	0.329	2.295	0.262	2.295
	0.267	2.394	0.276	2.394	0.303	2.394	0.326	2.394	0.282	2.394
	-0.017	5.000	0.056	5.000	0.016	5.000	0.061	5.000	-0.151	5.000
	0.041	5.197	0.016	5.197	0.014	5.197	0.064	5.197	-0.159	5.197
	0.061	5.394	-0.028	5.394	0.043	5.394	0.019	5.394	-0.155	5.394

-0.108	-4.500	-0.115	-4.500	-0.094	-4.500	-0.109	-4.500	-0.124	-4.500
-0.126	-4.303	-0.113	-4.303	-0.095	-4.303	-0.103	-4.303	-0.111	-4.303
-0.131	-4.106	-0.108	-4.106	-0.096	-4.106	-0.104	-4.106	-0.109	-4.106
0.088	-1.500	-0.040	-1.500	0.065	-1.500	0.027	-1.500	0.120	-1.500
0.119	-1.402	0.087	-1.402	0.056	-1.402	0.028	-1.402	0.188	-1.402
0.167	-1.303	0.086	-1.303	0.111	-1.303	0.077	-1.303	0.230	-1.303
0.186	-1.205	0.067	-1.205	0.127	-1.205	0.130	-1.205	0.188	-1.205
0.153	-1.106	0.058	-1.106	0.155	-1.106	0.124	-1.106	0.288	-1.106
0.417	1.500	0.422	1.500	0.411	1.500	0.461	1.500	0.443	1.500
0.415	1.598	0.408	1.598	0.389	1.598	0.452	1.598	0.420	1.598
0.399	1.697	0.369	1.697	0.376	1.697	0.415	1.697	0.412	1.697
0.412	1.795	0.347	1.795	0.350	1.795	0.420	1.795	0.386	1.795
0.373	1.894	0.365	1.894	0.349	1.894	0.403	1.894	0.378	1.894
0.094	4.500	-0.005	4.500	0.045	4.500	0.069	4.500	-0.039	4.500
0.035	4.697	0.001	4.697	0.045	4.697	0.036	4.697	-0.084	4.697
0.070	4.894	0.069	4.894	0.046	4.894	0.076	4.894	-0.117	4.894
-0.140	-5.000	-0.115	-5.000	-0.095	-5.000	-0.110	-5.000	-0.127	-5.000
-0.137	-4.803	-0.114	-4.803	-0.098	-4.803	-0.103	-4.803	-0.095	-4.803
-0.126	-4.606	-0.106	-4.606	-0.094	-4.606	-0.103	-4.606	-0.111	-4.606
-0.101	-2.000	-0.068	-2.000	-0.074	-2.000	-0.097	-2.000	-0.070	-2.000
-0.058	-1.902	-0.071	-1.902	-0.060	-1.902	-0.076	-1.902	-0.023	-1.902
0.022	-1.803	-0.026	-1.803	-0.024	-1.803	-0.071	-1.803	-0.001	-1.803
0.034	-1.705	-0.052	-1.705	0.023	-1.705	-0.052	-1.705	0.072	-1.705
0.036	-1.606	-0.049	-1.606	0.025	-1.606	-0.050	-1.606	0.090	-1.606
0.481	1.000	0.449	1.000	0.402	1.000	0.476	1.000	0.549	1.000
0.454	1.098	0.456	1.098	0.447	1.098	0.494	1.098	0.534	1.098
0.478	1.197	0.501	1.197	0.383	1.197	0.497	1.197	0.522	1.197
0.447	1.295	0.436	1.295	0.403	1.295	0.464	1.295	0.473	1.295
0.404	1.394	0.418	1.394	0.398	1.394	0.474	1.394	0.474	1.394
0.159	4.000	0.084	4.000	0.047	4.000	0.105	4.000	-0.050	4.000
0.044	4.197	0.047	4.197	0.066	4.197	0.088	4.197	-0.075	4.197
0.077	4.394	0.027	4.394	0.009	4.394	0.085	4.394	-0.080	4.394
-0.136	-5.500	-0.116	-5.500	-0.095	-5.500	-0.109	-5.500	-0.089	-5.500
-0.139	-5.303	-0.116	-5.303	-0.096	-5.303	-0.101	-5.303	-0.097	-5.303
-0.141	-5.106	-0.108	-5.106	-0.096	-5.106	-0.103	-5.106	-0.123	-5.106
-0.114	-2.500	-0.094	-2.500	-0.088	-2.500	-0.101	-2.500	-0.156	-2.500
-0.100	-2.402	-0.108	-2.402	-0.086	-2.402	-0.113	-2.402	-0.101	-2.402
-0.082	-2.303	-0.093	-2.303	-0.082	-2.303	-0.109	-2.303	-0.108	-2.303
-0.080	-2.205	-0.101	-2.205	-0.096	-2.205	-0.113	-2.205	-0.074	-2.205
-0.075	-2.106	-0.053	-2.106	-0.073	-2.106	-0.114	-2.106	-0.031	-2.106
0.456	0.500	0.498	0.500	0.382	0.500	0.401	0.500	0.612	0.500
0.435	0.598	0.436	0.598	0.396	0.598	0.441	0.598	0.619	0.598
0.487	0.697	0.485	0.697	0.452	0.697	0.484	0.697	0.589	0.697
0.485	0.795	0.508	0.795	0.419	0.795	0.490	0.795	0.559	0.795
0.479	0.894	0.418	0.894	0.422	0.894	0.519	0.894	0.568	0.894
0.179	3.500	0.114	3.500	0.135	3.500	0.184	3.500	0.018	3.500
0.104	3.697	0.101	3.697	0.131	3.697	0.126	3.697	0.033	3.697
0.104	3.894	0.072	3.894	0.073	3.894	0.123	3.894	-0.021	3.894

-0.139	-6.000	-0.119	-6.000	-0.096	-6.000	-0.110	-6.000	-0.060	-6.000
-0.138	-5.803	-0.118	-5.803	-0.098	-5.803	-0.101	-5.803	0.000	-5.803
-0.140	-5.606	-0.106	-5.606	-0.094	-5.606	-0.105	-5.606	-0.042	-5.606
-0.130	-3.000	-0.101	-3.000	-0.088	-3.000	-0.108	-3.000	-0.155	-3.000
-0.120	-2.902	-0.109	-2.902	-0.087	-2.902	-0.122	-2.902	-0.143	-2.902
-0.121	-2.803	-0.105	-2.803	-0.091	-2.803	-0.120	-2.803	-0.181	-2.803
-0.120	-2.705	-0.107	-2.705	-0.094	-2.705	-0.132	-2.705	-0.154	-2.705
-0.092	-2.606	-0.114	-2.606	-0.086	-2.606	-0.119	-2.606	-0.133	-2.606
0.471	0.000	0.385	0.000	0.381	0.000	0.384	0.000	0.579	0.000
0.456	0.098	0.412	0.098	0.356	0.098	0.390	0.098	0.573	0.098
0.435	0.197	0.401	0.197	0.410	0.197	0.437	0.197	0.593	0.197
0.472	0.295	0.465	0.295	0.402	0.295	0.407	0.295	0.597	0.295
0.442	0.394	0.541	0.394	0.418	0.394	0.432	0.394	0.580	0.394
0.271	3.000	0.162	3.000	0.198	3.000	0.247	3.000	0.142	3.000
0.189	3.197	0.114	3.197	0.181	3.197	0.218	3.197	0.038	3.197
0.143	3.394	0.139	3.394	0.133	3.394	0.165	3.394	0.025	3.394

Table B.2: Co-flow Experimental Validation Cases

Primary Jet Temp., °C	23.5		23.5		20.0		26.0		23.5
Profile Distance from Nose, mm	10.0		25.0		10.0		10.0		10.0
Primary Nozzle Air Flow, l/s	2.4		2.4		2.4		2.4		4.7
Secondary Nozzle Air Flow, l/s	6.7		6.7		6.7		6.7		13.4
Nose Distance from Nozzle, mm	0.41		0.41		0.41		0.41		0.41
AQI		AQI		AQI		AQI		AQI	
	Co-Flow 1C		Co-Flow 2C		Co-Flow 3C		Co-Flow 4C		Co-Flow 5C
-0.047	-3.500	-0.070	-3.500	-0.023	-3.500	-0.045	-3.500	-0.050	-3.500
-0.045	-3.303	-0.069	-3.303	-0.059	-3.303	-0.056	-3.303	-0.063	-3.303
-0.061	-3.106	-0.069	-3.106	-0.043	-3.106	-0.063	-3.106	-0.080	-3.106
0.510	-0.500	0.452	-0.500	0.472	-0.500	0.469	-0.500	0.522	-0.500
0.535	-0.402	0.525	-0.402	0.440	-0.402	0.459	-0.402	0.600	-0.402
0.712	-0.303	0.565	-0.303	0.578	-0.303	0.519	-0.303	0.697	-0.303
0.698	-0.205	0.643	-0.205	0.641	-0.205	0.643	-0.205	0.792	-0.205
0.722	-0.106	0.673	-0.106	0.719	-0.106	0.752	-0.106	0.870	-0.106
-0.029	2.500	-0.042	2.500	-0.047	2.500	-0.013	2.500	-0.188	2.500
-0.018	2.598	-0.030	2.598	-0.044	2.598	-0.021	2.598	-0.183	2.598
-0.025	2.697	-0.041	2.697	-0.052	2.697	-0.016	2.697	-0.175	2.697
-0.027	2.795	-0.051	2.795	-0.031	2.795	-0.028	2.795	-0.181	2.795
-0.045	2.894	-0.044	2.894	-0.052	2.894	-0.039	2.894	-0.178	2.894
-0.055	5.500	0.002	5.500	-0.030	5.500	-0.003	5.500	-0.006	5.500
-0.023	5.697	-0.008	5.697	-0.007	5.697	-0.005	5.697	0.001	5.697
-0.006	5.894	0.010	5.894	-0.028	5.894	-0.001	5.894	-0.008	5.894
-0.044	-4.000	-0.065	-4.000	-0.027	-4.000	-0.041	-4.000	-0.022	-4.000
-0.061	-3.803	-0.077	-3.803	-0.055	-3.803	-0.049	-3.803	-0.022	-3.803
-0.068	-3.606	-0.071	-3.606	-0.046	-3.606	-0.060	-3.606	-0.054	-3.606

0.226	-1.000	0.142	-1.000	0.167	-1.000	0.079	-1.000	0.045	-1.000
0.345	-0.902	0.250	-0.902	0.223	-0.902	0.202	-0.902	0.134	-0.902
0.363	-0.803	0.268	-0.803	0.232	-0.803	0.251	-0.803	0.253	-0.803
0.416	-0.705	0.358	-0.705	0.300	-0.705	0.346	-0.705	0.308	-0.705
0.458	-0.606	0.315	-0.606	0.334	-0.606	0.324	-0.606	0.428	-0.606
0.041	2.000	-0.001	2.000	0.040	2.000	0.104	2.000	-0.114	2.000
0.028	2.098	-0.017	2.098	0.004	2.098	0.058	2.098	-0.121	2.098
-0.003	2.197	-0.003	2.197	-0.013	2.197	0.024	2.197	-0.157	2.197
-0.004	2.295	-0.022	2.295	0.005	2.295	0.032	2.295	-0.159	2.295
-0.024	2.394	-0.044	2.394	-0.034	2.394	-0.004	2.394	-0.167	2.394
-0.034	5.000	-0.007	5.000	-0.029	5.000	-0.016	5.000	-0.012	5.000
-0.020	5.197	-0.014	5.197	-0.026	5.197	-0.004	5.197	-0.008	5.197
-0.017	5.394	-0.017	5.394	-0.030	5.394	-0.010	5.394	-0.020	5.394
-0.043	-4.500	-0.061	-4.500	-0.034	-4.500	-0.041	-4.500	-0.016	-4.500
-0.049	-4.303	-0.054	-4.303	-0.039	-4.303	-0.048	-4.303	-0.020	-4.303
-0.064	-4.106	-0.072	-4.106	-0.036	-4.106	-0.053	-4.106	-0.018	-4.106
0.023	-1.500	-0.030	-1.500	-0.017	-1.500	-0.040	-1.500	-0.167	-1.500
0.074	-1.402	0.025	-1.402	-0.003	-1.402	0.014	-1.402	-0.160	-1.402
0.096	-1.303	0.057	-1.303	0.034	-1.303	0.022	-1.303	-0.121	-1.303
0.169	-1.205	0.116	-1.205	0.074	-1.205	0.047	-1.205	-0.100	-1.205
0.229	-1.106	0.123	-1.106	0.090	-1.106	0.100	-1.106	-0.039	-1.106
0.210	1.500	0.168	1.500	0.227	1.500	0.331	1.500	0.187	1.500
0.197	1.598	0.122	1.598	0.127	1.598	0.214	1.598	0.117	1.598
0.095	1.697	0.115	1.697	0.090	1.697	0.196	1.697	0.053	1.697
0.080	1.795	0.055	1.795	0.050	1.795	0.136	1.795	-0.009	1.795
0.064	1.894	0.058	1.894	0.060	1.894	0.133	1.894	-0.035	1.894
-0.040	4.500	-0.021	4.500	-0.051	4.500	-0.030	4.500	-0.034	4.500
-0.027	4.697	-0.017	4.697	-0.045	4.697	-0.029	4.697	-0.042	4.697
-0.027	4.894	-0.012	4.894	-0.051	4.894	-0.019	4.894	-0.024	4.894
-0.042	-5.000	-0.059	-5.000	-0.018	-5.000	-0.035	-5.000	-0.014	-5.000
-0.052	-4.803	-0.064	-4.803	-0.046	-4.803	-0.038	-4.803	-0.011	-4.803
-0.043	-4.606	-0.060	-4.606	-0.028	-4.606	-0.051	-4.606	-0.021	-4.606
-0.040	-2.000	-0.056	-2.000	-0.050	-2.000	-0.052	-2.000	-0.184	-2.000
-0.036	-1.902	-0.076	-1.902	-0.058	-1.902	-0.060	-1.902	-0.194	-1.902
-0.006	-1.803	-0.058	-1.803	-0.058	-1.803	-0.033	-1.803	-0.190	-1.803
-0.001	-1.705	-0.061	-1.705	-0.023	-1.705	-0.017	-1.705	-0.194	-1.705
0.025	-1.606	-0.003	-1.606	-0.045	-1.606	-0.034	-1.606	-0.201	-1.606
0.521	1.000	0.496	1.000	0.568	1.000	0.664	1.000	0.682	1.000
0.515	1.098	0.439	1.098	0.542	1.098	0.614	1.098	0.624	1.098
0.310	1.197	0.425	1.197	0.339	1.197	0.488	1.197	0.512	1.197
0.317	1.295	0.333	1.295	0.231	1.295	0.443	1.295	0.415	1.295
0.226	1.394	0.284	1.394	0.242	1.394	0.493	1.394	0.367	1.394
-0.054	4.000	-0.037	4.000	-0.056	4.000	-0.038	4.000	-0.094	4.000
-0.043	4.197	-0.018	4.197	-0.053	4.197	-0.034	4.197	-0.074	4.197
-0.056	4.394	-0.032	4.394	-0.049	4.394	-0.027	4.394	-0.059	4.394
-0.034	-5.500	-0.066	-5.500	-0.016	-5.500	-0.040	-5.500	-0.022	-5.500
-0.064	-5.303	-0.066	-5.303	-0.046	-5.303	-0.033	-5.303	-0.012	-5.303
-0.049	-5.106	-0.058	-5.106	-0.022	-5.106	-0.038	-5.106	-0.019	-5.106

-0.065	-2.500	-0.088	-2.500	-0.062	-2.500	-0.064	-2.500	-0.135	-2.500
-0.057	-2.402	-0.063	-2.402	-0.077	-2.402	-0.056	-2.402	-0.140	-2.402
-0.052	-2.303	-0.080	-2.303	-0.074	-2.303	-0.066	-2.303	-0.157	-2.303
-0.047	-2.205	-0.066	-2.205	-0.066	-2.205	-0.057	-2.205	-0.165	-2.205
-0.038	-2.106	-0.062	-2.106	-0.063	-2.106	-0.052	-2.106	-0.184	-2.106
0.830	0.500	0.832	0.500	0.848	0.500	0.919	0.500	0.982	0.500
0.759	0.598	0.812	0.598	0.775	0.598	0.839	0.598	0.963	0.598
0.725	0.697	0.771	0.697	0.689	0.697	0.849	0.697	0.921	0.697
0.728	0.795	0.632	0.795	0.579	0.795	0.810	0.795	0.859	0.795
0.614	0.894	0.580	0.894	0.586	0.894	0.768	0.894	0.804	0.894
-0.053	3.500	-0.047	3.500	-0.062	3.500	-0.041	3.500	-0.132	3.500
-0.047	3.697	-0.033	3.697	-0.062	3.697	-0.039	3.697	-0.116	3.697
-0.051	3.894	-0.032	3.894	-0.058	3.894	-0.040	3.894	-0.121	3.894
-0.007	-6.000	-0.053	-6.000	-0.057	-6.000	-0.048	-6.000	-0.047	-6.000
-0.030	-5.803	-0.052	-5.803	-0.025	-5.803	-0.031	-5.803	-0.035	-5.803
-0.047	-5.606	-0.053	-5.606	-0.027	-5.606	-0.042	-5.606	-0.019	-5.606
-0.067	-3.000	-0.074	-3.000	-0.059	-3.000	-0.062	-3.000	-0.101	-3.000
-0.050	-2.902	-0.077	-2.902	-0.074	-2.902	-0.042	-2.902	-0.117	-2.902
-0.060	-2.803	-0.071	-2.803	-0.077	-2.803	-0.054	-2.803	-0.122	-2.803
-0.050	-2.705	-0.067	-2.705	-0.066	-2.705	-0.053	-2.705	-0.129	-2.705
-0.057	-2.606	-0.075	-2.606	-0.057	-2.606	-0.061	-2.606	-0.141	-2.606
0.826	0.000	0.816	0.000	0.773	0.000	0.812	0.000	0.936	0.000
0.856	0.098	0.878	0.098	0.899	0.098	0.838	0.098	0.965	0.098
0.855	0.197	0.884	0.197	0.909	0.197	0.888	0.197	0.977	0.197
0.848	0.295	0.920	0.295	0.869	0.295	0.870	0.295	0.989	0.295
0.797	0.394	0.873	0.394	0.806	0.394	0.900	0.394	0.981	0.394
-0.037	3.000	-0.037	3.000	-0.044	3.000	-0.024	3.000	-0.166	3.000
-0.043	3.197	-0.037	3.197	-0.057	3.197	-0.044	3.197	-0.160	3.197
-0.053	3.394	-0.041	3.394	-0.059	3.394	-0.039	3.394	-0.146	3.394

Table B.3: Primary CFD Validation CFD Cases

Primary Jet Temp., °C	23.5		23.5						20.0		26.0		23.5
Profile, mm	10.0		25.0						10.0		10.0		10.0
Primary Nozzle Air Flow, l/s	2.40		2.40						2.40		2.40		4.80
Primary Turbulent Intensity, %	1.7		1.7						2.0		2.0		1.7
Primary Length Scale, mm	3.0		3.0						3.0		3.0		3.0
Secondary Nozzle Air Flow, l/s	0.00		0.00						0.00		0.00		0.00

Nose Distance from Nozzle, m	0.41		0.41						0.41		0.41		0.41
AQI		AQI		AQI		AQI		AQI		AQI		AQI	
	Primary 1S		Primary 2S		Primary 2S		Primary 2S		Primary 3S		Primary 4S		Primary 5S
-0.086	-4.011	-0.112	-4.007	0.4366	0.0201	0.0425	3.6199	-0.078	-4.011	-0.086	-4.011	-0.203	-4.011
-0.085	-3.826	-0.112	-3.997	0.4410	0.0498	0.0383	3.6823	-0.073	-3.826	-0.085	-3.826	-0.201	-3.826
-0.085	-3.781	-0.112	-3.992	0.4425	0.0598	0.0365	3.7083	-0.072	-3.781	-0.085	-3.781	-0.200	-3.781
-0.085	-3.744	-0.112	-3.988	0.4503	0.1095	0.0325	3.7646	-0.071	-3.744	-0.085	-3.744	-0.200	-3.744
-0.084	-3.578	-0.112	-3.933	0.4546	0.1338	0.0312	3.7855	-0.065	-3.578	-0.084	-3.578	-0.196	-3.578
-0.082	-3.407	-0.111	-3.829	0.4581	0.1608	0.0305	3.7968	-0.052	-3.407	-0.081	-3.407	-0.185	-3.407
-0.081	-3.322	-0.111	-3.768	0.4592	0.1696	0.0290	3.8182	-0.047	-3.322	-0.080	-3.322	-0.181	-3.322
-0.081	-3.284	-0.111	-3.742	0.4680	0.2293	0.0276	3.8360	-0.044	-3.284	-0.080	-3.284	-0.178	-3.284
-0.080	-3.226	-0.111	-3.666	0.4694	0.2388	0.0247	3.8718	-0.038	-3.226	-0.078	-3.226	-0.172	-3.226
-0.073	-3.007	-0.110	-3.581	0.4701	0.2439	0.0175	3.9803	-0.011	-3.007	-0.071	-3.007	-0.139	-3.007
-0.068	-2.901	-0.110	-3.544	0.4707	0.2485	0.0154	4.0202	0.005	-2.901	-0.065	-2.901	-0.117	-2.901
-0.059	-2.748	-0.110	-3.538	0.4739	0.2786	0.0147	4.0426	0.027	-2.748	-0.057	-2.748	-0.086	-2.748
-0.053	-2.651	-0.109	-3.440	0.4744	0.2842	0.0137	4.0707	0.040	-2.651	-0.050	-2.651	-0.065	-2.651
-0.041	-2.520	-0.109	-3.405	0.4756	0.2978	0.0110	4.1442	0.061	-2.520	-0.039	-2.520	-0.034	-2.520
-0.016	-2.313	-0.108	-3.335	0.4796	0.3497	0.0104	4.1571	0.096	-2.313	-0.015	-2.313	0.020	-2.313
-0.014	-2.295	-0.107	-3.271	0.4814	0.3730	0.0093	4.1823	0.099	-2.295	-0.013	-2.295	0.025	-2.295
-0.007	-2.247	-0.107	-3.244	0.4842	0.4077	0.0071	4.2823	0.108	-2.247	-0.006	-2.247	0.038	-2.247
0.022	-2.062	-0.106	-3.181	0.4847	0.4133	0.0069	4.2932	0.142	-2.062	0.021	-2.062	0.087	-2.062
0.028	-2.023	-0.104	-3.101	0.4870	0.4394	0.0061	4.3208	0.149	-2.023	0.027	-2.023	0.097	-2.023
0.069	-1.799	-0.102	-3.045	0.4885	0.4561	0.0057	4.3393	0.193	-1.799	0.065	-1.799	0.160	-1.799
0.079	-1.750	-0.102	-3.023	0.4894	0.4674	0.0056	4.3414	0.204	-1.750	0.075	-1.750	0.177	-1.750
0.135	-1.524	-0.099	-2.937	0.4898	0.4723	0.0049	4.3708	0.261	-1.524	0.128	-1.524	0.261	-1.524
0.144	-1.481	-0.095	-2.871	0.4913	0.4969	0.0049	4.3729	0.270	-1.481	0.137	-1.481	0.275	-1.481
0.158	-1.408	-0.095	-2.863	0.4920	0.5089	0.0026	4.4625	0.284	-1.408	0.150	-1.408	0.296	-1.408
0.181	-1.294	-0.090	-2.762	0.4973	0.5881	0.0019	4.4993	0.306	-1.294	0.172	-1.294	0.330	-1.294
0.206	-1.166	-0.087	-2.718	0.4996	0.6389	0.0013	4.5336	0.329	-1.166	0.196	-1.166	0.365	-1.166
0.222	-1.090	-0.079	-2.599	0.5002	0.6802	-0.0006	4.6382	0.343	-1.090	0.212	-1.090	0.388	-1.090
0.231	-1.056	-0.078	-2.594	0.5009	0.7161	-0.0010	4.6599	0.351	-1.056	0.221	-1.056	0.401	-1.056
0.279	-0.832	-0.076	-2.562	0.5014	0.7475	-0.0014	4.6764	0.391	-0.832	0.267	-0.832	0.466	-0.832
0.280	-0.827	-0.076	-2.559	0.5018	0.7845	-0.0017	4.6998	0.392	-0.827	0.268	-0.827	0.468	-0.827
0.280	-0.827	-0.073	-2.523	0.5018	0.7883	-0.0017	4.7050	0.392	-0.827	0.268	-0.827	0.468	-0.827
0.281	-0.821	-0.072	-2.516	0.5019	0.7967	-0.0021	4.7319	0.393	-0.821	0.269	-0.821	0.469	-0.821
0.309	-0.663	-0.071	-2.507	0.5017	0.8108	-0.0022	4.7365	0.414	-0.663	0.296	-0.663	0.505	-0.663
0.319	-0.606	-0.0596	-2.4212	0.5011	0.8699	-0.0023	4.7484	0.422	-0.606	0.305	-0.606	0.518	-0.606
0.332	-0.541	-0.0483	-2.3289	0.5009	0.8873	-0.0035	4.8701	0.431	-0.541	0.318	-0.541	0.534	-0.541
0.351	-0.440	-0.0406	-2.2735	0.5002	0.9485	-0.0037	4.8879	0.444	-0.440	0.336	-0.440	0.556	-0.440
0.352	-0.433	-0.0371	-2.2485	0.4958	1.0410	-0.0043	4.9403	0.444	-0.433	0.337	-0.433	0.557	-0.433
0.357	-0.404	-0.0142	-2.0845	0.4951	1.0549	-0.0046	4.9783	0.447	-0.404	0.342	-0.404	0.563	-0.404
0.375	-0.301	-0.0135	-2.0792	0.4944	1.0687	-0.0059	5.1105	0.459	-0.301	0.360	-0.301	0.582	-0.301
0.378	-0.281	-0.0132	-2.0774	0.4927	1.0983	-0.0064	5.1674	0.461	-0.281	0.363	-0.281	0.585	-0.281

0.395	-0.187	-0.0036	-2.0083	0.4918	1.1087	-0.0064	5.1681	0.470	-0.187	0.379	-0.187	0.599	-0.187
0.405	-0.127	-0.0035	-2.0079	0.4908	1.1187	-0.0064	5.1684	0.475	-0.127	0.389	-0.127	0.606	-0.127
0.414	-0.075	-0.0033	-2.0067	0.4888	1.1415	-0.0064	5.1687	0.479	-0.075	0.397	-0.075	0.613	-0.075
0.419	-0.036	0.0121	-1.9327	0.4757	1.2723	-0.0070	5.2339	0.481	-0.036	0.403	-0.036	0.616	-0.036
0.432	0.064	0.0352	-1.8210	0.4753	1.2767	-0.0070	5.2421	0.487	0.064	0.416	0.064	0.622	0.064
0.438	0.106	0.0361	-1.8163	0.4741	1.2871	-0.0071	5.2567	0.489	0.106	0.421	0.106	0.623	0.106
0.447	0.197	0.0446	-1.7712	0.4692	1.3273	-0.0084	5.4407	0.491	0.197	0.430	0.197	0.625	0.197
0.452	0.243	0.0455	-1.7669	0.4662	1.3495	-0.0089	5.4957	0.493	0.243	0.435	0.243	0.625	0.243
0.454	0.259	0.0461	-1.7645	0.4653	1.3557	-0.0091	5.5207	0.493	0.259	0.437	0.259	0.625	0.259
0.458	0.299	0.0462	-1.7638	0.4588	1.4018	-0.0094	5.5813	0.494	0.299	0.441	0.299	0.624	0.299
0.469	0.403	0.0559	-1.7209	0.4490	1.4770	-0.0097	5.6621	0.495	0.403	0.452	0.403	0.620	0.403
0.478	0.519	0.0902	-1.5558	0.4402	1.5403	-0.0102	5.7931	0.493	0.519	0.462	0.519	0.609	0.519
0.481	0.556	0.0936	-1.5397	0.4392	1.5472	-0.0104	5.8215	0.492	0.556	0.464	0.556	0.606	0.556
0.484	0.612	0.0990	-1.5118	0.4315	1.6023	-0.0105	5.8638	0.491	0.612	0.467	0.612	0.599	0.612
0.490	0.720	0.0992	-1.5107	0.4292	1.6178	-0.0107	5.9063	0.487	0.720	0.474	0.720	0.585	0.720
0.493	0.852	0.1011	-1.5013	0.4276	1.6258	-0.0109	5.9346	0.480	0.852	0.478	0.852	0.565	0.852
0.495	0.932	0.1346	-1.3527	0.4211	1.6602	-0.0110	5.9617	0.476	0.932	0.481	0.932	0.554	0.932
0.496	0.992	0.1348	-1.3518	0.4079	1.7317	-0.0115	6.1074	0.471	0.992	0.482	0.992	0.544	0.992
0.491	1.196	0.1417	-1.3208	0.3996	1.7764			0.449	1.196	0.481	1.196	0.502	1.196
0.487	1.270	0.1524	-1.2784	0.3916	1.8195			0.438	1.270	0.479	1.270	0.484	1.270
0.479	1.420	0.1527	-1.2774	0.3900	1.8279			0.422	1.420	0.473	1.420	0.458	1.420
0.478	1.433	0.1528	-1.2770	0.3873	1.8396			0.420	1.433	0.473	1.433	0.456	1.433
0.463	1.568	0.1528	-1.2767	0.3816	1.8671			0.398	1.568	0.462	1.568	0.426	1.568
0.445	1.707	0.1670	-1.2131	0.3648	1.9481			0.376	1.707	0.449	1.707	0.398	1.707
0.436	1.764	0.1960	-1.0794	0.3539	1.9913			0.366	1.764	0.443	1.764	0.386	1.764
0.426	1.817	0.1971	-1.0746	0.3382	2.0649			0.356	1.817	0.435	1.817	0.374	1.817
0.407	1.931	0.1978	-1.0705	0.3251	2.1202			0.335	1.931	0.421	1.931	0.350	1.931
0.385	2.070	0.2047	-1.0373	0.3113	2.1742			0.313	2.070	0.404	2.070	0.326	2.070
0.375	2.121	0.2056	-1.0327	0.3088	2.1840			0.303	2.121	0.396	2.121	0.315	2.121
0.346	2.275	0.2106	-1.0136	0.2868	2.2708			0.276	2.275	0.374	2.275	0.286	2.275
0.344	2.283	0.2129	-1.0039	0.2734	2.3351			0.275	2.283	0.372	2.283	0.285	2.283
0.309	2.433	0.2221	-0.9670	0.2644	2.3760			0.245	2.433	0.345	2.433	0.254	2.433
0.302	2.469	0.2245	-0.9575	0.2618	2.3898			0.239	2.469	0.339	2.469	0.247	2.469
0.2863	2.5672	0.2520	-0.8493	0.2464	2.4686			0.2254	2.5672	0.3264	2.5672	0.2339	2.5672
0.2699	2.6632	0.2591	-0.8209	0.2441	2.4777			0.2117	2.6632	0.3131	2.6632	0.2203	2.6632
0.2577	2.7237	0.2669	-0.7901	0.2345	2.5156			0.2017	2.7237	0.3029	2.7237	0.2104	2.7237
0.2303	2.8586	0.2735	-0.7660	0.2137	2.6064			0.1793	2.8586	0.2803	2.8586	0.1880	2.8586
0.2132	2.9409	0.2948	-0.6779	0.2059	2.6416			0.1654	2.9409	0.2656	2.9409	0.1741	2.9409
0.1917	3.0617	0.2974	-0.6671	0.2003	2.6664			0.1480	3.0617	0.2469	3.0617	0.1568	3.0617
0.1781	3.1511	0.3035	-0.6307	0.1948	2.6908			0.1372	3.1511	0.2348	3.1511	0.1458	3.1511
0.1550	3.3004	0.3144	-0.5742	0.1855	2.7389			0.1196	3.3004	0.2129	3.3004	0.1265	3.3004
0.1421	3.3798	0.3191	-0.5519	0.1703	2.8181			0.1098	3.3798	0.2008	3.3798	0.1158	3.3798
0.1217	3.5146	0.3234	-0.5355	0.1663	2.8383			0.0951	3.5146	0.1802	3.5146	0.0974	3.5146
0.1166	3.5608	0.3335	-0.4972	0.1575	2.8836			0.0915	3.5608	0.1747	3.5608	0.0926	3.5608

0.0985	3.7131	0.3353	-0.4898	0.1295	3.0070			0.0792	3.7131	0.1540	3.7131	0.0743	3.7131
0.0815	3.8807	0.3368	-0.4831	0.1260	3.0230			0.0676	3.8807	0.1333	3.8807	0.0559	3.8807
0.0777	3.9357	0.3411	-0.4646	0.1230	3.0368			0.0650	3.9357	0.1273	3.9357	0.0512	3.9357
0.0619	4.1138	0.3519	-0.4169	0.1200	3.0530			0.0536	4.1138	0.1027	4.1138	0.0307	4.1138
0.0571	4.2060	0.3544	-0.4050	0.1140	3.0879			0.0498	4.2060	0.0932	4.2060	0.0241	4.2060
0.0481	4.4092	0.3610	-0.3782	0.1121	3.0991			0.0430	4.4092	0.0781	4.4092	0.0121	4.4092
0.0478	4.4189	0.3695	-0.3432	0.1093	3.1168			0.0427	4.4189	0.0775	4.4189	0.0118	4.4189
0.0397	4.6221	0.3813	-0.2945	0.1002	3.1769			0.0357	4.6221	0.0624	4.6221	0.0029	4.6221
0.0357	4.7524	0.3949	-0.2305	0.0917	3.2335			0.0321	4.7524	0.0548	4.7524	-0.0008	4.7524
0.0312	4.8733	0.3967	-0.2191	0.0851	3.2788			0.0282	4.8733	0.0468	4.8733	-0.0050	4.8733
0.0276	5.0641	0.4041	-0.1754	0.0772	3.3330			0.0247	5.0641	0.0397	5.0641	-0.0081	5.0641
0.0268	5.0972	0.4104	-0.1384	0.0687	3.3976			0.0240	5.0972	0.0384	5.0972	-0.0088	5.0972
0.0246	5.2636	0.4149	-0.1131	0.0665	3.4140			0.0220	5.2636	0.0339	5.2636	-0.0104	5.2636
0.0230	5.3699	0.4211	-0.0740	0.0633	3.4450			0.0205	5.3699	0.0309	5.3699	-0.0115	5.3699
0.0213	5.5182	0.4221	-0.0681	0.0514	3.5366			0.0191	5.5182	0.0277	5.5182	-0.0124	5.5182
0.0192	5.6643	0.4281	-0.0326	0.0504	3.5432			0.0173	5.6643	0.0238	5.6643	-0.0138	5.6643
0.0184	5.7720	0.4302	-0.0187	0.0467	3.5699			0.0167	5.7720	0.0223	5.7720	-0.0141	5.7720
0.0170	5.9570	0.4331	0.0002	0.0458	3.5802			0.0155	5.9570	0.0197	5.9570	-0.0148	5.9570
0.0165	6.0480	0.4350	0.0129	0.0437	3.6033			0.0152	6.0480	0.0190	6.0480	-0.0149	6.0480

Table B.4: Co-flow CFD Validation Cases

Primary Jet Temp., °C		23.5		23.5		20.0		26.0		23.5
Profile Distance from Nose, mm		10.0		25.0		10.0		10.0		10.0
Primary Nozzle Air Flow, l/s		2.4		2.4		2.4		2.4		4.8
Primary Turbulent Intensity, %		1.7		1.7		1.7		1.7		1.7
Secondary Nozzle Air Flow, l/s		6.7		6.7		6.7		6.7		13.4
Secondary Turbulent Intensity, %		1.7		1.7		1.7		1.7		1.7
Nose Distance from Nozzle, mm		0.41		0.41		0.41		0.41		0.4
	AQI		AQI		AQI		AQI		AQI	
		Co-Flow 1C		Co-Flow 2C		Co-Flow 3C		Co-Flow 4C		Co-Flow 5C
	-0.057	-4.013	-0.060	-4.649	-0.054	-4.013	-0.058	-4.013	-0.031	-4.013
	-0.056	-3.777	-0.060	-4.644	-0.052	-3.777	-0.057	-3.777	-0.044	-3.777
	-0.056	-3.775	-0.059	-4.353	-0.052	-3.775	-0.057	-3.775	-0.044	-3.775
	-0.056	-3.775	-0.059	-4.353	-0.052	-3.775	-0.057	-3.775	-0.044	-3.775
	-0.055	-3.590	-0.059	-4.344	-0.051	-3.590	-0.056	-3.590	-0.053	-3.590
	-0.055	-3.589	-0.059	-4.343	-0.051	-3.589	-0.056	-3.589	-0.053	-3.589
	-0.055	-3.545	-0.059	-4.343	-0.050	-3.545	-0.056	-3.545	-0.055	-3.545
	-0.054	-3.508	-0.059	-4.324	-0.050	-3.508	-0.056	-3.508	-0.056	-3.508
	-0.054	-3.508	-0.059	-4.324	-0.050	-3.508	-0.056	-3.508	-0.056	-3.508
	-0.053	-3.343	-0.058	-4.031	-0.049	-3.343	-0.055	-3.343	-0.064	-3.343

-0.053	-3.342	-0.058	-4.031	-0.049	-3.342	-0.055	-3.342	-0.064	-3.342
-0.053	-3.342	-0.057	-3.799	-0.049	-3.342	-0.055	-3.342	-0.064	-3.342
-0.052	-3.171	-0.057	-3.798	-0.047	-3.171	-0.053	-3.171	-0.075	-3.171
-0.052	-3.171	-0.057	-3.788	-0.047	-3.171	-0.053	-3.171	-0.075	-3.171
-0.052	-3.170	-0.057	-3.787	-0.047	-3.170	-0.053	-3.170	-0.075	-3.170
-0.051	-3.086	-0.057	-3.772	-0.046	-3.086	-0.053	-3.086	-0.080	-3.086
-0.051	-3.048	-0.056	-3.576	-0.045	-3.048	-0.052	-3.048	-0.082	-3.048
-0.050	-2.991	-0.056	-3.575	-0.044	-2.991	-0.052	-2.991	-0.086	-2.991
-0.050	-2.990	-0.056	-3.574	-0.044	-2.990	-0.052	-2.990	-0.086	-2.990
-0.046	-2.772	-0.056	-3.574	-0.040	-2.772	-0.049	-2.772	-0.105	-2.772
-0.046	-2.771	-0.056	-3.455	-0.040	-2.771	-0.049	-2.771	-0.105	-2.771
-0.046	-2.770	-0.055	-3.320	-0.040	-2.770	-0.049	-2.770	-0.105	-2.770
-0.044	-2.665	-0.055	-3.320	-0.037	-2.665	-0.047	-2.665	-0.115	-2.665
-0.041	-2.512	-0.055	-3.320	-0.033	-2.512	-0.044	-2.512	-0.126	-2.512
-0.041	-2.512	-0.054	-3.202	-0.033	-2.512	-0.044	-2.512	-0.126	-2.512
-0.038	-2.415	-0.054	-3.201	-0.030	-2.415	-0.042	-2.415	-0.132	-2.415
-0.038	-2.414	-0.053	-3.088	-0.030	-2.414	-0.042	-2.414	-0.132	-2.414
-0.034	-2.284	-0.052	-2.986	-0.025	-2.284	-0.039	-2.284	-0.140	-2.284
-0.034	-2.284	-0.052	-2.985	-0.025	-2.284	-0.039	-2.284	-0.140	-2.284
-0.034	-2.283	-0.052	-2.985	-0.025	-2.283	-0.039	-2.283	-0.140	-2.283
-0.026	-2.077	-0.051	-2.844	-0.014	-2.077	-0.032	-2.077	-0.151	-2.077
-0.026	-2.077	-0.050	-2.745	-0.014	-2.077	-0.032	-2.077	-0.151	-2.077
-0.025	-2.060	-0.050	-2.745	-0.013	-2.060	-0.031	-2.060	-0.152	-2.060
-0.025	-2.059	-0.050	-2.744	-0.013	-2.059	-0.031	-2.059	-0.152	-2.059
-0.022	-2.012	-0.048	-2.652	-0.009	-2.012	-0.029	-2.012	-0.152	-2.012
-0.022	-2.010	-0.048	-2.652	-0.009	-2.010	-0.029	-2.010	-0.152	-2.010
-0.022	-2.009	-0.046	-2.507	-0.009	-2.009	-0.028	-2.009	-0.152	-2.009
-0.011	-1.826	-0.046	-2.506	0.006	-1.826	-0.019	-1.826	-0.152	-1.826
-0.011	-1.826	-0.043	-2.344	0.006	-1.826	-0.019	-1.826	-0.152	-1.826
-0.008	-1.787	-0.043	-2.344	0.010	-1.787	-0.017	-1.787	-0.151	-1.787
0.017	-1.565	-0.043	-2.343	0.043	-1.565	0.004	-1.565	-0.123	-1.565
0.017	-1.564	-0.042	-2.304	0.043	-1.564	0.005	-1.564	-0.123	-1.564
0.017	-1.563	-0.042	-2.303	0.043	-1.563	0.005	-1.563	-0.123	-1.563
0.025	-1.514	-0.040	-2.232	0.053	-1.514	0.011	-1.514	-0.112	-1.514
0.025	-1.514	-0.040	-2.231	0.053	-1.514	0.011	-1.514	-0.111	-1.514
0.085	-1.288	-0.035	-2.072	0.137	-1.288	0.061	-1.288	0.066	-1.288
0.085	-1.288	-0.035	-2.071	0.137	-1.288	0.061	-1.288	0.066	-1.288
0.085	-1.288	-0.033	-2.015	0.137	-1.288	0.061	-1.288	0.066	-1.288
0.095	-1.246	-0.033	-2.013	0.150	-1.246	0.069	-1.246	0.097	-1.246
0.095	-1.245	-0.023	-1.811	0.150	-1.245	0.069	-1.245	0.097	-1.245
0.1183	-1.1723	-0.0234	-1.8099	0.1837	-1.1723	0.0879	-1.1723	0.1771	-1.1723
0.1187	-1.1712	-0.0217	-1.7803	0.1843	-1.1712	0.0883	-1.1712	0.1784	-1.1712
0.1612	-1.0578	-0.0123	-1.6885	0.2426	-1.0578	0.1232	-1.0578	0.3008	-1.0578
0.2341	-0.9309	-0.0123	-1.6877	0.3360	-0.9309	0.1840	-0.9309	0.4407	-0.9309
0.2346	-0.9301	-0.0121	-1.6862	0.3367	-0.9301	0.1844	-0.9301	0.4417	-0.9301
0.2350	-0.9295	0.0012	-1.5506	0.3371	-0.9295	0.1847	-0.9295	0.4424	-0.9295
0.2790	-0.8536	0.0013	-1.5500	0.3949	-0.8536	0.2211	-0.8536	0.5332	-0.8536
0.2794	-0.8531	0.0063	-1.5041	0.3953	-0.8531	0.2214	-0.8531	0.5338	-0.8531

0.3127	-0.8201	0.0064	-1.5036	0.4344	-0.8201	0.2497	-0.8201	0.5818	-0.8201
0.3132	-0.8196	0.0395	-1.2957	0.4350	-0.8196	0.2501	-0.8196	0.5824	-0.8196
0.3529	-0.7742	0.0399	-1.2934	0.4759	-0.7742	0.2870	-0.7742	0.6255	-0.7742
0.5092	-0.5954	0.0421	-1.2826	0.6371	-0.5954	0.4320	-0.5954	0.7952	-0.5954
0.5126	-0.5918	0.0422	-1.2821	0.6405	-0.5918	0.4351	-0.5918	0.7989	-0.5918
0.5130	-0.5913	0.0935	-1.0903	0.6409	-0.5913	0.4355	-0.5913	0.7994	-0.5913
0.5133	-0.5910	0.0935	-1.0903	0.6412	-0.5910	0.4358	-0.5910	0.7996	-0.5910
0.5133	-0.5910	0.0936	-1.0900	0.6412	-0.5910	0.4358	-0.5910	0.7996	-0.5910
0.5137	-0.5904	0.0938	-1.0895	0.6416	-0.5904	0.4363	-0.5904	0.7999	-0.5904
0.5167	-0.5862	0.1111	-1.0397	0.6443	-0.5862	0.4392	-0.5862	0.8021	-0.5862
0.5176	-0.5848	0.1113	-1.0391	0.6451	-0.5848	0.4401	-0.5848	0.8028	-0.5848
0.5184	-0.5836	0.1122	-1.0373	0.6458	-0.5836	0.4410	-0.5836	0.8034	-0.5836
0.5215	-0.5794	0.1966	-0.8650	0.6485	-0.5794	0.4440	-0.5794	0.8056	-0.5794
0.6322	-0.4269	0.2237	-0.8052	0.7471	-0.4269	0.5548	-0.4269	0.8860	-0.4269
0.6327	-0.4263	0.2242	-0.8044	0.7475	-0.4263	0.5554	-0.4263	0.8863	-0.4263
0.6722	-0.3704	0.2351	-0.7913	0.7787	-0.3704	0.5972	-0.3704	0.9085	-0.3704
0.7221	-0.3057	0.2354	-0.7908	0.8178	-0.3057	0.6502	-0.3057	0.9359	-0.3057
0.7223	-0.3055	0.2356	-0.7906	0.8180	-0.3055	0.6504	-0.3055	0.9360	-0.3055
0.7226	-0.3051	0.2953	-0.7362	0.8182	-0.3051	0.6507	-0.3051	0.9361	-0.3051
0.7856	-0.2043	0.2954	-0.7361	0.8608	-0.2043	0.7219	-0.2043	0.9627	-0.2043
0.7858	-0.2040	0.4428	-0.5990	0.8610	-0.2040	0.7222	-0.2040	0.9628	-0.2040
0.7861	-0.2035	0.4432	-0.5987	0.8611	-0.2035	0.7224	-0.2035	0.9629	-0.2035
0.7893	-0.1971	0.4435	-0.5984	0.8632	-0.1971	0.7262	-0.1971	0.9642	-0.1971
0.8018	-0.1689	0.4952	-0.5589	0.8698	-0.1689	0.7416	-0.1689	0.9680	-0.1689
0.8024	-0.1676	0.6464	-0.4143	0.8701	-0.1676	0.7423	-0.1676	0.9682	-0.1676
0.8488	-0.0650	0.6465	-0.4141	0.8947	-0.0650	0.7996	-0.0650	0.9827	-0.0650
0.8489	-0.0648	0.6847	-0.3568	0.8948	-0.0648	0.7997	-0.0648	0.9827	-0.0648
0.8491	-0.0645	0.6852	-0.3562	0.8948	-0.0645	0.7999	-0.0645	0.9827	-0.0645
0.8558	-0.0451	0.7322	-0.2865	0.8973	-0.0451	0.8092	-0.0451	0.9843	-0.0451
0.8834	0.0469	0.7323	-0.2863	0.9048	0.0469	0.8489	0.0469	0.9896	0.0469
0.8839	0.0485	0.7327	-0.2858	0.9049	0.0485	0.8496	0.0485	0.9897	0.0485
0.8840	0.0489	0.7738	-0.2321	0.9050	0.0489	0.8498	0.0489	0.9897	0.0489
0.8841	0.0493	0.7743	-0.2313	0.9050	0.0493	0.8499	0.0493	0.9898	0.0493
0.8938	0.1087	0.7930	-0.1966	0.9028	0.1087	0.8682	0.1087	0.9904	0.1087
0.8941	0.1105	0.8338	-0.1186	0.9027	0.1105	0.8688	0.1105	0.9904	0.1105
0.9029	0.1615	0.8890	-0.0162	0.9009	0.1615	0.8850	0.1615	0.9910	0.1615
0.9041	0.1992	0.8892	-0.0157	0.8954	0.1992	0.8906	0.1992	0.9897	0.1992
0.9041	0.1999	0.8895	-0.0151	0.8953	0.1999	0.8907	0.1999	0.9897	0.1999
0.9041	0.2000	0.9008	0.0426	0.8953	0.2000	0.8907	0.2000	0.9897	0.2000
0.9018	0.2998	0.9009	0.0430	0.8751	0.2998	0.8991	0.2998	0.9841	0.2998
0.9017	0.3004	0.9010	0.0434	0.8749	0.3004	0.8991	0.3004	0.9841	0.3004
0.8981	0.3414	0.9146	0.1129	0.8634	0.3414	0.9001	0.3414	0.9801	0.3414
0.8980	0.3418	0.9198	0.2204	0.8632	0.3418	0.9001	0.3418	0.9801	0.3418
0.8980	0.3420	0.9199	0.2225	0.8632	0.3420	0.9001	0.3420	0.9801	0.3420
0.8812	0.4327	0.9205	0.2340	0.8313	0.4327	0.8935	0.4327	0.9670	0.4327
0.8812	0.4331	0.9205	0.2345	0.8311	0.4331	0.8935	0.4331	0.9669	0.4331
0.8736	0.4784	0.9198	0.2427	0.8156	0.4784	0.8911	0.4784	0.9608	0.4784
0.8735	0.4789	0.9197	0.2432	0.8153	0.4789	0.8911	0.4789	0.9607	0.4789

0.8693	0.4949	0.9082	0.3768	0.8083	0.4949	0.8889	0.4949	0.9577	0.4949
0.8532	0.5344	0.9082	0.3771	0.7848	0.5344	0.8783	0.5344	0.9456	0.5344
0.8527	0.5358	0.9081	0.3773	0.7840	0.5358	0.8780	0.5358	0.9452	0.5358
0.8073	0.6390	0.9081	0.3774	0.7187	0.6390	0.8476	0.6390	0.9105	0.6390
0.8072	0.6392	0.8779	0.4800	0.7185	0.6392	0.8475	0.6392	0.9104	0.6392
0.8070	0.6395	0.8778	0.4801	0.7184	0.6395	0.8474	0.6395	0.9102	0.6395
0.7360	0.7548	0.8723	0.5001	0.6314	0.7548	0.7908	0.7548	0.8511	0.7548
0.7356	0.7555	0.8722	0.5003	0.6310	0.7555	0.7905	0.7555	0.8508	0.7555
0.7157	0.7917	0.8721	0.5007	0.6072	0.7917	0.7743	0.7917	0.8336	0.7917
0.7152	0.7922	0.8475	0.5534	0.6067	0.7922	0.7739	0.7922	0.8332	0.7922
0.6749	0.8472	0.8461	0.5565	0.5637	0.8472	0.7376	0.8472	0.7940	0.8472
0.6743	0.8480	0.8014	0.6549	0.5630	0.8480	0.7370	0.8480	0.7933	0.8480
0.5900	0.9557	0.8011	0.6554	0.4731	0.9557	0.6609	0.9557	0.7106	0.9557
0.5895	0.9564	0.7911	0.6722	0.4726	0.9564	0.6604	0.9564	0.7101	0.9564
0.5894	0.9565	0.7907	0.6728	0.4725	0.9565	0.6603	0.9565	0.7099	0.9565
0.4879	1.0882	0.7907	0.6728	0.3772	1.0882	0.5594	1.0882	0.5832	1.0882
0.4316	1.1676	0.7592	0.7124	0.3235	1.1676	0.5038	1.1676	0.5139	1.1676
0.4314	1.1679	0.7591	0.7126	0.3233	1.1679	0.5037	1.1679	0.5137	1.1679
0.4308	1.1686	0.6477	0.8515	0.3228	1.1686	0.5031	1.1686	0.5129	1.1686
0.3857	1.2277	0.6472	0.8520	0.2838	1.2277	0.4553	1.2277	0.4452	1.2277
0.3852	1.2282	0.5513	0.9556	0.2834	1.2282	0.4548	1.2282	0.4445	1.2282
0.3852	1.2283	0.5499	0.9571	0.2834	1.2283	0.4547	1.2283	0.4444	1.2283
0.2324	1.4323	0.4939	1.0195	0.1596	1.4323	0.2864	1.4323	0.1902	1.4323
0.2322	1.4327	0.4934	1.0200	0.1595	1.4327	0.2861	1.4327	0.1899	1.4327
0.1861	1.5058	0.4461	1.0703	0.1242	1.5058	0.2331	1.5058	0.1074	1.5058
0.1853	1.5081	0.4454	1.0711	0.1235	1.5081	0.2321	1.5081	0.1058	1.5081
0.1304	1.6554	0.4452	1.0713	0.0834	1.6554	0.1665	1.6554	0.0027	1.6554
0.1301	1.6559	0.3425	1.1732	0.0832	1.6559	0.1662	1.6559	0.0023	1.6559
0.1300	1.6563	0.2155	1.3271	0.0831	1.6563	0.1661	1.6563	0.0021	1.6563
0.1258	1.6698	0.2154	1.3273	0.0801	1.6698	0.1610	1.6698	-0.0052	1.6698
0.1256	1.6703	0.2147	1.3282	0.0799	1.6703	0.1608	1.6703	-0.0055	1.6703
0.0831	1.8041	0.2056	1.3398	0.0493	1.8041	0.1087	1.8041	-0.0761	1.8041
0.0551	1.9425	0.2053	1.3403	0.0290	1.9425	0.0745	1.9425	-0.1109	1.9425
0.0549	1.9431	0.2010	1.3498	0.0290	1.9431	0.0743	1.9431	-0.1110	1.9431
0.0548	1.9437	0.1110	1.5232	0.0289	1.9437	0.0742	1.9437	-0.1112	1.9437
0.0443	1.9998	0.1076	1.5297	0.0212	1.9998	0.0613	1.9998	-0.1222	1.9998
0.0364	2.0522	0.1074	1.5303	0.0155	2.0522	0.0517	2.0522	-0.1278	2.0522
0.0362	2.0536	0.0919	1.5834	0.0154	2.0536	0.0515	2.0536	-0.1279	2.0536
0.0188	2.1675	0.0916	1.5845	0.0028	2.1675	0.0303	2.1675	-0.1416	2.1675
0.0188	2.1680	0.0597	1.7028	0.0027	2.1680	0.0302	2.1680	-0.1416	2.1680
0.0074	2.3054	0.0416	1.8021	-0.0054	2.3054	0.0163	2.3054	-0.1449	2.3054
0.0017	2.3565	0.0416	1.8021	-0.0095	2.3565	0.0094	2.3565	-0.1473	2.3565
0.0016	2.3568	0.0415	1.8030	-0.0095	2.3568	0.0093	2.3568	-0.1473	2.3568
0.0016	2.3570	0.0304	1.8720	-0.0095	2.3570	0.0093	2.3570	-0.1473	2.3570
-0.0083	2.5105	0.0303	1.8726	-0.0164	2.5105	-0.0029	2.5105	-0.1457	2.5105
-0.0084	2.5110	0.0129	2.0067	-0.0164	2.5110	-0.0029	2.5110	-0.1457	2.5110
-0.0089	2.5191	0.0128	2.0072	-0.0168	2.5191	-0.0035	2.5191	-0.1455	2.5191
-0.0089	2.5197	0.0128	2.0076	-0.0168	2.5197	-0.0036	2.5197	-0.1455	2.5197

-0.0089	2.5200	0.0089	2.0437	-0.0168	2.5200	-0.0036	2.5200	-0.1455	2.5200
-0.0158	2.6693	0.0040	2.0942	-0.0212	2.6693	-0.0122	2.6693	-0.1376	2.6693
-0.0172	2.7045	-0.0063	2.2120	-0.0221	2.7045	-0.0139	2.7045	-0.1359	2.7045
-0.0191	2.8028	-0.0063	2.2128	-0.0231	2.8028	-0.0164	2.8028	-0.1306	2.8028
-0.0191	2.8030	-0.0064	2.2133	-0.0231	2.8030	-0.0164	2.8030	-0.1306	2.8030
-0.0192	2.8044	-0.0113	2.3078	-0.0231	2.8044	-0.0164	2.8044	-0.1306	2.8044
-0.0208	2.8991	-0.0113	2.3083	-0.0239	2.8991	-0.0186	2.8991	-0.1251	2.8991
-0.0208	2.8996	-0.0165	2.3935	-0.0239	2.8996	-0.0186	2.8996	-0.1250	2.8996
-0.0213	2.9598	-0.0165	2.3936	-0.0239	2.9598	-0.0193	2.9598	-0.1205	2.9598
-0.0228	3.0942	-0.0212	2.5271	-0.0243	3.0942	-0.0215	3.0942	-0.1104	3.0942
-0.0228	3.0944	-0.0212	2.5278	-0.0243	3.0944	-0.0215	3.0944	-0.1104	3.0944
-0.0228	3.0949	-0.0230	2.5952	-0.0243	3.0949	-0.0215	3.0949	-0.1103	3.0949
-0.0233	3.1767	-0.0230	2.5954	-0.0241	3.1767	-0.0223	3.1767	-0.1038	3.1767
-0.0233	3.1771	-0.0247	2.7192	-0.0241	3.1771	-0.0223	3.1771	-0.1038	3.1771
-0.0233	3.1775	-0.0247	2.7193	-0.0241	3.1775	-0.0223	3.1775	-0.1037	3.1775
-0.0231	3.2974	-0.0247	2.7197	-0.0233	3.2974	-0.0224	3.2974	-0.0954	3.2974
-0.0231	3.2982	-0.0258	2.8904	-0.0233	3.2982	-0.0224	3.2982	-0.0954	3.2982
-0.0229	3.3873	-0.0259	2.8913	-0.0227	3.3873	-0.0224	3.3873	-0.0901	3.3873
-0.0229	3.3877	-0.0262	2.9270	-0.0227	3.3877	-0.0224	3.3877	-0.0900	3.3877
-0.0218	3.5364	-0.0261	2.9733	-0.0211	3.5364	-0.0216	3.5364	-0.0809	3.5364
-0.0218	3.5369	-0.0261	2.9745	-0.0211	3.5369	-0.0216	3.5369	-0.0809	3.5369
-0.0213	3.6157	-0.0261	2.9753	-0.0204	3.6157	-0.0213	3.6157	-0.0760	3.6157
-0.0213	3.6161	-0.0258	3.1016	-0.0204	3.6161	-0.0213	3.6161	-0.0760	3.6161
-0.0213	3.6162	-0.0258	3.1020	-0.0204	3.6162	-0.0213	3.6162	-0.0760	3.6162
-0.0200	3.7505	-0.0243	3.2709	-0.0186	3.7505	-0.0202	3.7505	-0.0681	3.7505
-0.0200	3.7510	-0.0243	3.2711	-0.0186	3.7510	-0.0202	3.7510	-0.0681	3.7510
-0.0196	3.7962	-0.0243	3.2715	-0.0181	3.7962	-0.0198	3.7962	-0.0661	3.7962
-0.0195	3.7970	-0.0242	3.2834	-0.0181	3.7970	-0.0198	3.7970	-0.0660	3.7970
-0.0195	3.7975	-0.0240	3.2970	-0.0181	3.7975	-0.0198	3.7975	-0.0660	3.7975
-0.0195	3.7975	-0.0240	3.2979	-0.0181	3.7975	-0.0198	3.7975	-0.0660	3.7975
-0.0179	3.9494	-0.0222	3.4858	-0.0163	3.9494	-0.0184	3.9494	-0.0587	3.9494
-0.0162	4.1165	-0.0222	3.4864	-0.0145	4.1165	-0.0169	4.1165	-0.0516	4.1165
-0.0162	4.1166	-0.0211	3.5674	-0.0145	4.1166	-0.0169	4.1166	-0.0516	4.1166
-0.0162	4.1171	-0.0211	3.5679	-0.0145	4.1171	-0.0169	4.1171	-0.0516	4.1171
-0.0162	4.1178	-0.0199	3.6596	-0.0144	4.1178	-0.0169	4.1178	-0.0516	4.1178
-0.0157	4.1711	-0.0199	3.6598	-0.0139	4.1711	-0.0164	4.1711	-0.0497	4.1711
-0.0157	4.1720	-0.0199	3.6601	-0.0139	4.1720	-0.0164	4.1720	-0.0496	4.1720
-0.0134	4.3493	-0.0179	3.7877	-0.0117	4.3493	-0.0144	4.3493	-0.0411	4.3493
-0.0134	4.3497	-0.0179	3.7878	-0.0117	4.3497	-0.0144	4.3497	-0.0411	4.3497
-0.0134	4.3504	-0.0179	3.7884	-0.0117	4.3504	-0.0144	4.3504	-0.0410	4.3504
-0.0124	4.4417	-0.0172	3.8302	-0.0108	4.4417	-0.0135	4.4417	-0.0375	4.4417
-0.0124	4.4422	-0.0172	3.8308	-0.0108	4.4422	-0.0135	4.4422	-0.0375	4.4422
-0.0109	4.6449	-0.0156	3.9722	-0.0094	4.6449	-0.0122	4.6449	-0.0314	4.6449
-0.0109	4.6450	-0.0149	4.0313	-0.0094	4.6450	-0.0122	4.6450	-0.0314	4.6450
-0.0109	4.6454	-0.0149	4.0318	-0.0094	4.6454	-0.0122	4.6454	-0.0314	4.6454
-0.0108	4.6547	-0.0149	4.0325	-0.0093	4.6547	-0.0122	4.6547	-0.0311	4.6547
-0.0108	4.6555	-0.0148	4.0424	-0.0093	4.6555	-0.0122	4.6555	-0.0310	4.6555
-0.0092	4.8579	-0.0145	4.0642	-0.0079	4.8579	-0.0108	4.8579	-0.0235	4.8579

-0.0092	4.8583	-0.0145	4.0647	-0.0079	4.8583	-0.0108	4.8583	-0.0235	4.8583
-0.0092	4.8585	-0.0145	4.0650	-0.0079	4.8585	-0.0108	4.8585	-0.0235	4.8585
-0.0084	4.9884	-0.0119	4.2560	-0.0072	4.9884	-0.0101	4.9884	-0.0192	4.9884
-0.0076	5.1088	-0.0119	4.2564	-0.0064	5.1088	-0.0094	5.1088	-0.0148	5.1088
-0.0076	5.1091	-0.0119	4.2566	-0.0064	5.1091	-0.0094	5.1091	-0.0148	5.1091
-0.0076	5.1097	-0.0119	4.2569	-0.0064	5.1097	-0.0094	5.1097	-0.0148	5.1097
-0.0067	5.2999	-0.0106	4.3955	-0.0056	5.2999	-0.0086	5.2999	-0.0103	5.2999
-0.0067	5.3006	-0.0106	4.3963	-0.0056	5.3006	-0.0086	5.3006	-0.0102	5.3006
-0.0065	5.3328	-0.0104	4.4149	-0.0055	5.3328	-0.0085	5.3328	-0.0095	5.3328
-0.0065	5.3336	-0.0096	4.5447	-0.0055	5.3336	-0.0085	5.3336	-0.0095	5.3336
-0.0065	5.3339	-0.0095	4.5494	-0.0055	5.3339	-0.0085	5.3339	-0.0094	5.3339
-0.0060	5.4997	-0.0095	4.5519	-0.0049	5.4997	-0.0079	5.4997	-0.0072	5.4997
-0.0056	5.6056	-0.0095	4.5641	-0.0046	5.6056	-0.0076	5.6056	-0.0058	5.6056
-0.0056	5.6060	-0.0094	4.5645	-0.0046	5.6060	-0.0076	5.6060	-0.0058	5.6060
-0.0056	5.6064	-0.0094	4.5665	-0.0046	5.6064	-0.0076	5.6064	-0.0058	5.6064
-0.0052	5.7543	-0.0094	4.5673	-0.0042	5.7543	-0.0072	5.7543	-0.0045	5.7543
-0.0047	5.9000	-0.0080	4.7248	-0.0037	5.9000	-0.0068	5.9000	-0.0031	5.9000
-0.0047	5.9003	-0.0080	4.7251	-0.0037	5.9003	-0.0068	5.9003	-0.0031	5.9003
-0.0047	5.9007	-0.0080	4.7255	-0.0037	5.9007	-0.0068	5.9007	-0.0031	5.9007
-0.0045	6.0080	-0.0069	4.9138	-0.0035	6.0080	-0.0066	6.0080	-0.0027	6.0080
		-0.0069	4.9143						
		-0.0068	4.9343						
		-0.0068	4.9348						
		-0.0067	4.9482						
		-0.0067	4.9489						
		-0.0061	5.1272						
		-0.0061	5.1274						
		-0.0061	5.1279						
		-0.0059	5.1911						
		-0.0052	5.4109						
		-0.0052	5.4115						
		-0.0051	5.4300						
		-0.0051	5.4304						
		-0.0051	5.4420						
		-0.0051	5.4427						
		-0.0049	5.4999						
		-0.0044	5.7025						
		-0.0044	5.7065						
		-0.0043	5.7070						
		-0.0042	5.7654						
		-0.0042	5.7660						
		-0.0042	5.7668						
		-0.0038	6.0348						

References

Abdel-Rahman, A.A., Al-Fahed, S.F., and Chakroun, W. 1996. The Near-Field Characteristics of Circular Jets at Low Reynolds Numbers. *Mechanics Research Communications*, Vol. 23, pp. 313-324.

Alkandry, H., Sideroff, C., Dang, T. 2008. Computational study of the personal micro-environment in an aircraft cabin. Indoor Air 2008, paper ID 622.

ANSI/ASHRAE Standard 62.1-2004. “Ventilation for Acceptable Indoor Air Quality” 2004.

Anderson, S.E., Wells, J.R., Fedorowicz, A., Butterworth, L.F., Meade, B.J. and Munson, A.E. 2007. Evaluation of the Contact and Respiratory Sensitization Potential of Volatile Organic Compounds Generated by Simulated Indoor Air Chemistry, *Toxicol. Sci*., Vol. 97, pp. 355-363.

Atkinson, R., Hasegawa, D. and Aschmann, S.M. 1990. Rate Constants for the Gas-Phase Reactions of O_3 with a Series of MonoTerpenes and Related Compounds at 296 ±2K.

Awbi, H. 2003. Ventilation of Buildings. Taylor & Francis Group: Spon Press, London, UK.

Bauman, F.S., Zhang, H., Arens, E.A., Benton, C.C. 1993. Localized comfort control with a desktop task conditioning system: laboratory and field measurements. ASHRAE Transactions, Vol. 99 (2), pp. 733-749.

Bell, M., Peng, R.D. and Dominici, F. 2006. The Exposure-Response Curve for Ozone and Risk of Mortality and the adequacy of Current Ozone Regulations, *Environ. Health Perspect.*, Vol. 114, pp. 532-536.

Bennett, D.H., McKone, T.E., Evans, J.S., Nazaroff, W.W., Margni, M.D., Jolliet, O., and Smith, K.R. 2002. Defining Intake Fraction, *Environmental Science & Technology*, 3-5.

Bjorn, E., and Nielsen, P.V. 2002. Dispersal of Exhaled Air and Personal Exposure in Displacement Ventilated Rooms. *Indoor Air*, Vol. 12, pp. 147-164.

Bogey, C. and Bailly, C. 2006. Large Eddy Simulations of Transitional Round Jets: Influence of the Reynolds Number on Flow Development and Energy Dissipation, *Phys. Fluids*, Vol. 18, pp. 1–14.

Bolashikov, Z.D., Nagano, H., Melikov, A.K., Meyer, K.E., and Kato, S. 2009. Control of the Free Convection Flow within the Breathing Zone by Confluent Jets for Improved Performance of Personalized Ventilation: Part 2 – Inhaled Air Quality. *Proceedings of Healthy Buildings 2009.*

Bolashikov, Z., Nikolaev, L., Melikov, A., Kaczmarczyk, J., and Fanger, P.O. 2003. New air terminal devices with high efficiency for personalized ventilation application. *Healthy Buildings 2003*, pp. 850-855.

Brohus, H., Hyldig, M.L., Kamper, S.K. and Vachek, U.M. 2008. Influence of Persons' Movements on Ventilation Effectiveness. *Proceedings of Indoor Air*, Paper ID: 665.

Burattini, P., Antonia, R.A., Rajagopalan, S. and Stephens, M. 2004. Effect of Initial Conditions on the Near-Field Development of a Round Jet. *Exp. Fluids*, Vol. 37, pp. 56-64.

Cano-Ruiz, J.A., Kong, D., Balas, R.B., and Nazaroff, W.W. 1993. Removal of Reactive Gases at Indoor Surfaces: Combining Mass Transport and Surface Kinetics. *Atmospheric Environment*, Vol. 27A, pp. 2039-2050.

Cermak, R., Melikov, A.K., and Forejt, L. 2006. Performance of personalized ventilation in conjunction with mixing and displacement ventilation. *HVAC&R Research*, Vol. 12, Number 2, pp. 295-311.

Chao, C.Y.H., Wan, M.P., Morawska, L., Johnson, G.R., Ristovski, Z.D., Hargreaves, M., Mengersen, K., Corbett, S., Li, Y., and Katoshevski, D. 2009. Characterization of Exhaled Air Jets and Droplet Size Distributions Immediately at the Mouth Opening. *Aerosol Science*, Vol. 40, pp. 1222-133.

Coleman, B.K., Destaillats, H., Hodgson, A.T. and Nazaroff, W.W. 2008. Ozone Consumption and Volatile Byproduct Formation from Surface Reactions with

Aircraft Cabin Materials and Clothing Fabrics, *Atmos. Environ*., Vol. 42, pp. 642-654.

Corsi, R.L., and Morrison, G.C. 2009. Tradeoffs between Energy Conservation and Adverse Outcomes of Indoor Chemistry in Residential Buildings. *Proceedings of Healthy Buildings*, paper 454.

De Bortoli, M., Knoppel, H., Pecchio, E., Peil, A., Rogora, L., Schauenburg, H., Schlitt, H., Vissers, H. 1986. Concentrations of Selected Organic Pollutants in Indoor and Outdoor Air in Northern Italy. *Environment International*, Vol. 12, pp. 343-350.

Deevy, M., Sinai, Y., Everitt, P., Voigt, L., and Gobeau, N. 2008. Modeling the Effect of an Occupant on Displacement Ventilation with Computational Fluid Dynamics. *Energy and Buildings*, Vol. 40, pp. 255-264.

Devos, M., Patte, F., Rouault, J., Laffort, P. and Gemert, L.J.V. 1990. Standardized Human Oldfactory Thresholds. Oxford University Press, New York.

Dygert, R., Russo, J., Dang, T. and Khalifa, H.E.. 2009. Modeling of the Human Body to Study the Personal Micro-environment. *ASHRAE Transactions*, Vol. 115(2).

Fellin, P. and Otson, R. 1994. Assessment of the Influence of Climatic Factors on Concentation Levels of Volatile Organic Compounds (VOCs) in Canadian Homes. *Atmos. Environ*., Vol. 28, pp. 3581-3586.

Faulkner, D., Fisk, W.J., Sullivan, D.P., Lee, S.M. 2003. Ventilation efficiencies and thermal comfort results of a desk-edge-mounted task ventilation system. Report #LBNL-53798, Lawrence Berkeley National Lab., Berkeley, CA (USA).

Faulkner, D., Fisk, W.J., Sullivan, D.P., and Lee, S.M. 2002. Ventilation efficiencies of a desk-edge-mounted task ventilation system. Indoor Environmental Dept., Lawrence Berkeley National Lab., Berkeley, CA (USA).

Faulkner, D., Fisk, W.J., Sullivan, D.P., and Wyon, D.P. 2000. Ventilation efficiencies of desk-mounted task/ambient conditioning systems. Report #LBNL-42700, Indoor Environmental Dept., Lawrence Berkeley National Lab, Berkeley, CA (USA).

Faulkner, D., Fisk, W.J., Sullivan, D.P., and Wyon, D.P. 1999. Ventilation efficiencies of task/ambient conditioning systems with desk-mounted air supplies. Report #LBNL-42597, Indoor Environmental Dept., Lawrence Berkeley National Lab, Berkeley, CA (USA).

Fruekilde, P., Hjorth, J., Jensen, N.R., Kotzias, D., and Larsen, B. 1998. Ozonolysis at Vegetation Surfaces: A Source of Acetone, 4-Oxopentanal, 6-Methyl-5-Hepten-2-One, and Geranyl Acetone in the Troposphere. *Atmospheric Environment*, Vol. 32, pp. 1893-1902.

Gadgil, A.J., Lobscheid, C., Abadie, M.O., and Finlayson, E.U. 2003. Indoor Pollutant Mixing Time in an Isothermal Closed Room: an Investigation using CFD. *Atmospheric Environment*, Vol. 37, pp. 5577-5586.

Gao, N., and Niu, J. 2006. Transient CFD Simulation of the Respiration Process and Inter-Person Exposure Assessment. *Building and Environment*, Vol. 41, pp. 1214-1222.

Gao, N., and Niu, J. 2004. CFD Study on Micro-Environment around Human Body and Personalized Ventilation. *Building and Environment*, Vol. 39, pp. 795-805.

Gao, Z. Ph.D. Thesis. Study of Particle and Ozone Penetration through the Building Envelope. Syracuse University, 2010.

Grosjean, D., Williams II, E.L., Grosjean, E., Andino, J.M. and Seinfeld, J.H. 1993. Atmospheric Oxidation of Biogenic Hydrocarbons: Reaction of Ozone with Beta-Pinene, D-Limonene and Trans-Caryophyllene. *Environmental Science and Technology*, Vol. 27, pp. 2754-2758.

Grosjean, E., Grosjean, D. and Seinfeld, J.H. 1996. Gas-Phase Reaction of Ozone with Trans-2-Hexenal, Trans-2-Hexenyl Acetate, Ethylvinyl Keytone, and 6-Methyl-5-Hepten-2-one. *Int. J. Chem. Kinet.,* Vol. 28, pp. 373-382.

Gold, D.R., Damokosh, A., Pope, C.A., Dockery, D.W., McDonnel, W.F., Serrano, P., Retama, A. and Castillejos, M. 1999. Particulate and Ozone Effects on the Respiratory Function of Children's in Southwest Mexico City. *Epidemiology*, Vol. 10, pp. 8-16.

Halvonova, B., and Melikov, A.K. 2009. Performance of "ductless" Personalized Ventilation in Conjunction with Displacement Ventilation: Impact of Disturbances due to Walking Persons. *Building and Environment*, in press.

Hayashi, T., Kato, S., Murakami, S. and Yang, J.H. 2002. CFD Analysis on Rising Stream Around a Human Body and its Effect on Inhalation Air Quality. ASHRAE Transactions, Vol. 108(2), pp. 1173-1178.

Hayashi, T., Ishizu, Y., Kato, S., and Murakami, S. 2002. CFD Analysis on Characteristics of Contaminated Indoor Air Ventilation and its Application in the Evaluation of the Effects of Contaminant Inhalation by a Human Occupant. *Building and Environment*, Vol. 37, pp. 219-230.

Incropera, F.P, DeWitt, D.P., Bergman, T.L and Lavine, A.S. 2007. Fundamentals of Heat and Mass Transfer, 6th Ed., John Wiley & Sons, Hoboken, NJ, USA.

Ito, K. 2007. Experimental and CFD Analysis Examining Ozone Distribution in Model Rooms with Laminar and Turbulent Flow Fields. Journal of Asian Architecture and Building Engineering, pp. 387-394.

Ito, K., Sorensen, D.N., and Weschler, C.J. 2004. Experimental and CFD Analyses Examining Ozone Distribution in a Model Room with a Two-Dimensional Flow Field. RoomVent, 9th International Conference.

Ito, K., Abuku, M., Kato, S., and Murakami, S. 2003. CFD and Model Experiment with Chemical Reaction. *International Symposium on Indoor Air Quality and Health Hazards, Japan*, Vol. 1, pp 305-311.

Karlberg, A.T., Shao, L.P., Nilsson, U., Gafvert, E. and Nilsson, J.L.G. 1994. Hydroperoxides in Oxidized D-limonene Identified as Potent Contact Allergens. Arch Dermatol. Res., Vol. 286, pp. 97-103.

Kays, W.M. and Crawford, M.E. 1980. Convective Heat Transfer and Mass Transfer, McGraw-Hill, New York.

Kephalopoulos, S., Kotzias, D., and Koistinen, K. 2007. Impact of Ozone-Initiated Terpene Chemistry on Indoor Air Quality and Human Health, EUR 23052 EN

Khalifa, H.E., Janos, M.I., and Dannenhoffer, J.F, “Energy-Neutral Personal Ventilation,” *Proceedings of Indoor Air 2008*, Copenhagen, Denmark, 2008.

Khalifa, H., Janos, M., Dannenhoffer III, J. 2009. Experimental Investigation of Reduced-mixing Personal Ventilation Jets. Building and Environment. Vol. 44 (8), pp.1551-1558.

Khalifa, H. E. and Glauser, M. N. 2006. Low-Mixing Nozzle for Personal Ventilation, US Provisional Patent Application No. 60/826,829.

Khalifa, H.E. Prescod, S.J, Dannenhoffer III, J.F. and Elhadidi, B. 2006. "Computation of Occupant Exposure in an Office Cubicle", Proceedings of AWMA/EPA Conference: Indoor Air Quality-Problems, Research and Solutions, Durham, NC, July 17-19, 2006.

Kilic, M., and Sevilgen, G. 2008. Modeling Airflow, Heat Transfer and Moisture Transport Around a Standing Human Body by Computational Fluid Dynamics. *International Communications in Heat and Mass Transfer*, Vol. 35, pp. 1159-1164.

Kleno, J., and Wolkoff, P. 2004 Changes in eye blink frequency as a measure of trigeminal stimulation by exposure to limonene oxidation products, isoprene oxidation products and nitrate radicals. *Int Arch Occup Environ Health*, Vol. 77, pp. 235-243.

Klepeis, N.E., Nelson, W.C., Ott, W.R., Robinson, J.P., Tsang, A.M., Switzer, Paul., Behar, J.V., Hern, S.C. and Engelmann, W.H. 2001. The National Human Activity Pattern Survey (NHAPS): A Resource for Assessing Exposure to Environmental Pollutants, *J. Expo. Anal. Environ. Epidemiol.*, Vol. 11, pp. 231-252.

Kuethe, A.M. and Schetzer, J.D. 1959. Foundations of Aerodynamics, 2nd ed. (New York: Wiley & Sons).

Kwon, S.J. and Seo, I.W. 2005. Reynolds Number Effects on the Behaviour of a Nonbuoyant Round Jet, *Exp. Fluids,* Vol. 38, pp. 801–812.

Lai, H.K., Kendall, M., Ferrier, H., Lindup, I., Alm, S., Hanninen, O., Jantunen, M., Mathys, P., Colvile, R., Ashmore, M.R., Cullinan, P., and Nieuwenhuijsen, M.J., 2004. Personal Exposure and Microenvironment Concentrations of $PM_{2.5}$, VOC, NO_2 and CO in Oxford, UK. *Atmospheric Environment*, Vol. 38, pp. 6399-6410.

Lai, A.C.K., Thatcher, T.L., and Nazaroff, W.W. 2000. Inhalation Transfer Factors for air Pollution Health Risk Assessment. *Journal of the Air & Waste Management Association*, Vol. 50, pp. 1688-1699.

Lee, P. and Davidson, J. 1999. Evaluation of activated carbon filters for removal of ozone at the ppb level. *Am. Ind. Hyg. J.,* Vol. 60, pp. 589-600.

Malmstrom, T.G., Kirkpatrick, A.T., Christensen, B., and Knappmiller K.D. 1997, “Centerline Velocity Decay Measurements in Low-Velocity Axisymmetric Jets,” *J. Fluid Mech.* Vol. 246, pp. 363-377.

Marr, D.R. 2007 Length Scale Propagation Along a Joint Inlet and Thermal Buoyancy Driven Flow. PhD Thesis, *Syracuse University, Dept. of Mechanical Engineering.*

Melikov, A. and Kaczmarczyk, J. 2007. Measurement and Prediction of Indoor Air Quality Using a Breathing Thermal Manikin. *Indoor Air*, Vol. 17, pp. 50-59.

Melikov, A., and Kaczmarczyk, J. 2006. Measurement and prediction of indoor air quality using a breathing thermal manikin. *Proceedings of Indoor Air 2007*, Vol. 17, pp. 50-59.

Melikov, A.K. 2004. Personalized Ventilation. *Indoor Air*, Vol. 14, pp. 157-167.

Melikov, A. 2004. Breathing Thermal Manikins for Indoor Environment Assessment: Important Characteristics and Requirements. *Eur J Appl Physiol*, Vol. 92, pp. 710-713.

Melikov, A.K., Cermak, R., and Majer, M. 2002. Personalized Ventilation: Evaluation of Different Air Terminal Devices. *Energy and Buildings*, Vol. 34, pp. 829-836.

Metts, T.A. and Batterman, S.A. 2005. Effect of VOC loading on the Ozone Removal Efficiency of Activated Carbon Filters. *Chemosphere*, Vol. 62, pp. 34-44.

Mi, J., Nobes, D.S., and Nathan, G.J., Influence of Jet Exit Conditions on the Passive Scalar Field of an Axisymmetric Free Jet. *J. Fluid Mech*. Vol. 432, pp. 91-125.

Montgomery, D., Kalman, D.A. 1989. Indoor/Outdoor Air Quality: Reference Pollutant Concentrations in Compliant-Free Residences. *Applied Industrial Hygiene*, Vol. 4, pp. 17-20.

Morrison, G. 2008. Interfacial Chemistry in Indoor Environments. *Environmental Science & Technology*, pp. 3495-3499.

Morrison, G.C. and Wiseman, D.J. 2006. Temporal Considerations in the Measurement of Indoor Mass Transfer Coefficients. *Atmospheric Environment*, Vol. 40, pp. 3389-3395.

Morrison, G.C., Zhao, P. and Kasthuri, L. 2006. The Spatial Distribution of Pollutant Transport to and from Indoor Surfaces. *Atmospheric Environment*, Vol. 40, pp. 3677-3685.

Morrison, G.C., Ping, Z., Wiseman, D.J., Ongwandee, M.. Chang, H., Portman, J. and Regmi, S. 2003. Rapid Measurement of Indoor Mass-Transfer Coefficients. *Atmospheric Environment*, Vol. 37, pp. 5611-5619.

Murakami, S. 2004. Analysis and Design of Micro-Climate Around the Human Body with Respiration by CFD. *Indoor Air*, Vol. 14, pp. 144-156.

Murakami, S., Kato, S., and Zeng, J. 1998. "Numerical Simulation of Contaminant Distribution Around a Modeled Human Body: CFD Study on Computational Thermal Manikin – Part II" *ASHRAE Transactions*, Vol. 104.

Nagano, H., Bolashikov, Z.D., Melikov, A.K., Kato, S., and Meyer, K.E. 2009. Control of the Free Convection Flow within the Breathing Zone by Confluent Jets for Improved Performance of Personalized Ventilation: Part 1 – Thermal Influence. *Proceedings of Healthy Buildings 2009.*

National Research Council. 2008. *Estimating Mortality Risk Reduction and Economic Benefits from Controlling Ozone Air Pollution*, Report by National Research Council, Committee on Estimating Mortality Risk Reduction Benefits from Decreased Tropospheric Ozone Exposure. Washington, DC, The national Academic Press, ISBN-10: 0-309-11994-4.

Nazaroff, W.W. 2008. Inhalation Intake Fraction of Pollutants from Episodic Indoor Emissions. *Building and Environment*, Vol. 43, pp. 269-277.

Nazaroff, W.W. and Weschler, C.J. 2004. Cleaning Products and Air Fresheners: Exposure to Primary and Secondary Air Pollutants. *Atmospheric Environment*, Vol. 38, pp. 2841-2865.

Nicolaides, N. 1974. Skin Lipids: Their Biochemical Uniqueness. *Science*, Vol. 186, pp. 19-26.

Nicolas, M., Ramalho, O., and Maupetit, F., 2007. Reactions between Ozone and Building Products: Impact on Primary and Secondary Emissions. *Atmospheric Environment*, Vol. 41, pp. 3129-3138.

Nielsen, P.V., Hyldgaard, C.E., Melikov, A., Andersen, H., and Soennichsen, M. 2005. Personal exposure between people in a room ventilated by textile terminals – with and without personalized ventilation. *Proceedings of Indoor Air 2005*, pp. 2522-2526.

Nielsen, P.V. 2004. Computational Fluid Dynamics and Room Air Movement. *Indoor Air*, Vol. 14, pp. 134-143.

Nielsen, P.V., Bjorn, E., and Brohus, H. 2002. Contaminant Flow and Personal Exposure. HPAC Engineering, pp. 40-44.

Niu, J., Gao, N., Phoebe, M., and Huigang, Z. 2007. Experimental Study on a Chair-Based Personalized Ventilation System. *Building and Environment*, Vol. 42, pp. 913-925.

Pandrangi, L. and Morrison, G.C. 2008. Ozone Interactions with Human Hair: Ozone Uptake Rates and Product Formation, *Atmos. Environ.*, Vol. 42, pp. 5079-5089.

Papodopoulos, G., and Pitts, W.M. 1999. A Generic Centerline Velocity Decay Curve for Initially Turbulent Axisymmetric Jets. *Transactions of the ASME*, Vol. 121, pp. 80-85.

Pope, C.A. III and Dockery, D.W. 2006. Health Effects of Fine Particulae Air Pollution: Lines that Connect. *J. Air & Waste Manage. Assoc.*, Vol. 56, pp. 709-742.

Reiss, R., Ryan, P.B., Koutrakis, P. 1994. Modeling Ozone Deposition onto Indoor Residential Surfaces. *Environ. Sci. Technol*., Vol. 28, pp. 504-513.

Rim, D., Novoselec, A. and Morrison, G. 2009. The Influence of Chemical Interactions at the Human Surface on Breathing Zone Levels of Reactants and Products.

Rohr, A.C., Wilkins, C.K, Clausen, P.A. Hammer M., Neilsen, G.D., Wolkoff, P., et al. 2002. Upper Airway and Pulmonary Effects of Oxidation Products of (+)-alpha-pinene, D-limonene and isoprene in BALB/c Mice. Inhalation Toxicology, Vol. 14, pp. 663-684.

Russo, J.S., Dang, T.Q. and Khalifa, H.E. 2009. Computational Analysis of Reduced-Mixing Personal Ventilation Jets. *Building and Environment*, Vol. 44, pp. 1559-1567.

Sabersky, R., Sinema, D., and Shair, F. 1973. Concentrations, Decay Rates and Removal of Ozone and Their Relation to Establishing. *Indoor Air*, Vol. 7, pp. 347-353.

Sarwar, G., Corsi, R., Allen, D., and Weschler, C. 2003. The Significance of Secondary Organic Aerosol Formation and Growth in Buildings: Experimental and Computational Evidence. *Atmospheric Environment*, Vol. 37, pp. 1365-1381.

Seifert, B., Mailahn, W., Schulz, C. and Ullrich, D. 1989. Seasonal Variation of Concentrations of Volatile Organic Compounds in Selected German Homes. *Environmental International*, Vol. 15, pp. 397-408.

Shelton, G., Zhoa, P., Corsi, R.L. and Siegel, J. "Ozone Removal on HVAC Filters: Underlying Mechanisms, Model development and Parameter Estimation." *Proceedings of Indoor Air 2008*. Copenhagen, Denmark, 2008.

Shih, T.H., Liou, W.W., Shabbir, A., Yang, Z., and Zhu, J. 1995. A New k-ε Eddy Viscosity Model For High Reynolds Number Turbulent Flows. *Computer Fluids* Vol. 24, pp. 227-238.

Sideroff, C. and Dang T., 2008, "Verification and Validation of CFD for the Personal Micro-Environment," to be published in *ASHRAE Transactions*.

Sideroff, C. Thesis. Detailed Examination of the Human Micro-Environment by CFD. Syracuse University, 2009.

Sidheswaran, M; Tavlarides, L. L., Gas and Particle Phase Chemistry of Linalool Ozone Reactions and Analysis of Reactive Oxygen Species, presented and published as a proceeding at The AIChE Annual Meeting 2008, Philadelphia, PA, November 2008.

Singer, B.C., Destaillats, H., Hodgson, A.T. and Nazaroff, W.W. 2006. Cleaning Products and Air Fresheners: Emissions and Resulting Concentrations of Glycol Ethers and Terpenoids. *Indoor Air*, Vol. 16(3), pp. 179-191.

Sorensen, D.N., and Nielsen, P.V. 2003. Quality Control of Computational Fluid Dynamics in Indoor Environments. *Indoor Air*, Vol. 13, pp. 2-17.

Sorensen, D.N. and Voigt, L.K. 2003. Modeling Flow and Heat Transfer around a Seated Human Body by Computational Fluid Dynamics. *Building and Environment*, Vol. 38, pp. 753-762.

Sorensen, D.N., and Weschler, C.J. 2002. Modeling-gas phase reactions in indoor environments using computational fluid dynamics. *Atmospheric Environment*, Vol. 36 pp. 9-18.

Symons, E.P. and Labus, T.L. 1971. Experimental Investigation of an Axisymmetric Fully Developed Laminar Free Jet. NASA TN D-6304.

Tamas, G., Weschler, C.J., Toftum, J., and Fanger, P.O. 2006. Influence of Ozone-Limonene Reactions on Perceived Air Quality. 2006. *Indoor Air*, Vol. 6, pp. 168-178.

Thornberry, T. and Abbatt, J.P.D. 2004. Heterogeneous Reaction of Ozone with Liquid Unsaturated Fatty Acids: Detailed Kinetics and Gas-Phase Product Studies. *Phys. Chem. Chem. Phys*., Vol. 6, pp. 84-93.

Tirkkonen, T. and Saarela, K. 1997. Adsorption of VOC's on interior surfaces in a full scale building. *Healthy Buildings*, Vol. 3, pp. 551-556.

Tsuzuki, K., Arens, E.A., Bauman, F.S., Wyon, D.P. 1999. Individual thermal comfort control with desk-mounted and floor-mounted task/ambient conditioning (TAC) systems. *Proceedings of Indoor Air 1999*, Edinburgh, Scotland, pp. 368-373.

Todde, V., Spazzini, P.G. and Sandberg, M. 2009. Experimental Analysis of Low-Reynolds Number Free Jets. *Exp. Fluids*, Vol. 47, pp. 279-294.

Topp, C., Nielsen, P.V., and Sorensen, D.N. 2002. "Application of Computer Simulated Persons in Indoor Environmental Modeling" *ASHRAE Transactions*.

Venkatachari, P. and Hopke, P.K. 2008. Characterization of Products Formed in the Reaction of Ozone with Alpha-Pinene: Case for Organic Peroxides. *J. Environ. Monit.,* Vol. 10(8), pp. 966-974.

Wainman, T., Zhang, J., Weschler, C.J., and Lioy, P.J. 2000. Ozone and Limonene in Indoor Air: A Source of Submicron Particle Exposure. *Environmental Health Perspectives*, Vol. 108, pp. 1139-1145.

Wallace, L., Nelson, W., Zeigenfus, R., Pellizzari, E., Michael, L., Whitmore, R., Zelon, H., Hartwell, T., Perritt, R., Westerdahl, D. 1991. The Los Angeles Team Study: Personal Exposures, Indoor-Outdoor Air Concentrations, and Breath Concentrations of 25 Volatile Compounds. *Journal of Exposure Analysis and Environmental Epidemiology*, Vol. 2, pp. 157-192.

Weschler, C.J., Wisthaler, A., Cowlin, S., Tamas, G., Strom-Tejsen, P., Hodgson, A.T., Destaillats, H., Herrington, J., Zhang, J., and Nazaroff, W.W., 2007. Ozone-Initiated Chemistry in an Occupied Simulated Aircraft Cabin. *Environ. Sci. Technol*., Vol. 41, pp. 6177-6184.

Weschler, C.J. 2006. Ozone's Impact on Public Health: Contributions from Indoor Exposures to Ozone and Products of Ozone-Initiated Chemistry. *Environmental Health Perspectives*, Vol. 114, pp. 1489-1496.

Weschler, C.J., Wells, J.R., Poppendieck, D., Hubbard, H., and Pearce, T.A. 2006. Workgroup Report: Indoor Chemistry and Health. Environmental Health Perspectives, Vol. 114, pp. 442-446.

Weschler, C.J. 2004. New Directions: Ozone-Initiated Reaction Products Indoors May be More Harmful than Ozone Itself. *Atmospheric Environment*, Vol. 38, pp. 5715-5716.

Weschler, C.J. 2000. Ozone in Indoor Environments: Concentration and Chemistry. *Indoor Air*, Vol. 10, pp. 269-288.

Weschler, C.J., and Shields, H.C., 2000. The Influence of Ventilation on Reactions Among Indoor Pollutants: Modeling and Experimental Observations. Indoor Air, Vol. 10, pp. 92-100.

Weschler, C.J., and Shields, H.C., 1999. Indoor Ozone/Terpene reactions as a source of indoor particles. *Atmospheric Environment*, 33, 2301-2312.

Weschler, C.J., and Shields, H.C. 1997. Potential Reactions Among Indoor Pollutants. *Atmospheric Environment*, Vol. 31, pp. 3487-3495.

Weschler, C.J., Shields, H.C. and Naik, D.V. 1989. Indoor Ozone Exposure. *J. Air Pollut. Control Assoc.*, Vol. 39, pp. 1562-1568.

Wiley, J.A., Robinson, J.P., Piazza, T., Garrett, K., Cirksena, K., Cheng, Y.T. and Martin, G. 1991. Activity Patterns of California Residents. Final Report Contract No. A6-177-33. California Air Resource Board, Sacramento, CA.

Wisthaler, A. and Weschler, C.J. 2009. Reactions of Ozone with Human Skin Lipids: Source of Carbonyls, Dicarbonyls, and Hydroxycarbonyls in Indoor Air. *Environmental Sciences*, PNAS Early Edition, pp. 1-8.

Wolkoff, P., Nojgaard, J.K., Troiano, P. and Piccoli, B. 2005. Eye Complaints in the Office Environment: Precorneal Tear Film Integrity Influenced by Eye Blinking Efficiency. *Occup. Environ. Med.*, Vol. 62, pp. 4-12.

Wolkoff, P., Clausen, P.A., Wilkins, C.K, Hougaard K.S., and Nielsen, G.D. 1999. Formation of Strong Airway Irritants in a Model Mixture of (+)-alpha-pinene/Ozone. Atmospheric Environment, Vol. 33, pp. 693-698.

Wyon, N.M., and Wyon, D.P. 1987. Measurement of Acute Response to Draught in the Eye. Acta Ophthalmologica, Vol. 65, pp. 385–392.

Xia, L.P. and Lam, K.M. 2009. Velocity and Concentration Measurements in Initial Region of Submerged Round Jets in Stagnant Environment and In Coflow. *Hydro-environment Research*, Vol. 3, pp. 21-34.

Xu, G., and Antonia, R.A. 2002. Effect of Different Initial Conditions on a Turbulent Round Free Jet. *Experiments in Fluids*, Vol. 33, pp. 667-683.

Yang, X., Chen, Q., and Zhang, J.S. 1998, Impact of Early Stage Incomplete Mixing on Estimating VOC Emissions in Small Test Chambers. *Indoor Air*, Vol. 8, pp. 180-189.

Yang, X., Chen, Q., Zeng, J., Zhang, J.S., Nong, G., and Shaw, C.Y. 2001, "Effects of Airflow on VOC Emissions from 'Wet' Coating materials: Experimental Measurements and Numerical Simulations," *ASHRAE Transactions*, Vol. 107, pp. 1-11.

Zhao, P., Siegel, J.A. and Corsi, R.L. 2007. Ozone Removal by HVAC Filters. Atmospheric Environment, Vol. 41, pp. 3151-3160.

Zhao, B., Zhang, Z., and Li, X. 2005. Numerical Study of the Transport of Droplets or Particles Generated by Respiratory System Indoors. *Building and Environment*, Vol. 40, pp. 1032-1039.

Zhu, S., Kato, S., and Yang, J.H. 2006. Study on Transport Characteristics of Saliva Droplets Produced by Coughing in a calm indoor environment. Building and Environment, Vol. 41, pp. 1691-1702.

Zhu, S., Kato, S., Murakami, S., and Hayashi, T. 2005. Study on Inhalation Region by Means of CFD Analysis and Experiment. *Building and Environment*, Vol. 40, pp. 1329-1336.

Zuaimi, M.S., Tham, K.W., Chew, F.T. and Ooi, P.L. 2007. The Effect of Ventilation Strategies of Child Care Centers on Indoor Air Quality and Respiratory Health of Children in Singapore. *Indoor Air*, Vol. 17(4), pp. 317-327.